

Surface roughness evolution in adhesive wear processes

Présentée le 18 septembre 2020

à la Faculté de l'environnement naturel, architectural et construit
Laboratoire de simulation en mécanique des solides
Programme doctoral en mécanique

pour l'obtention du grade de Docteur ès Sciences

par

Enrico MILANESE

Acceptée sur proposition du jury

Prof. M. E. S. Violay, présidente du jury
Prof. J.-F. Molinari, directeur de thèse
Prof. N. Fillot, rapporteur
Prof. D. Bonamy, rapporteur
Dr S. Mischler, rapporteur

Sospecho, sin embargo, que no era muy capaz de pensar. Pensar es olvidar diferencias, es generalizar, abstraer. En el abarrotado mundo de Funes no había sino detalles, casi inmediatos.

— *Funes el memorioso*,
Jorge Luis Borges

To Gigi.

Acknowledgements

Maybe that's all family really is:
a group of people that miss the same
imaginary place.

— Large, *Garden State*

The end of a Ph.D. is often a good time to take a deep breath and look back at what life has been during these years – in particular for the many to whom the commitment came with significant life changes. Like a pandemic. I soon realized that a fast-moving environment, like EPFL and Lausanne, implies that people come and go, which made the full list of people to acknowledge much longer than expected, and I had to cut it down. If we have met and your name is not below, know that I am thankful for sharing a moment together – it brought me here today.

I will always be grateful to Jean-François for welcoming me in the lab twice: for my Master thesis in 2013 and again for my Ph.D. studies in 2016. Not only your knowledge of mechanics and your ability to get people engaged when sharing it have always been inspirational, but also your human side and your caring for each person in the team are remarkable. I am also grateful that you were nine time zones away when France won the football world cup.

I am thankful to the jury of my oral exam – Prof. Marie Violay, Prof. Nicolas Fillot, Prof. Daniel Bonamy, and Dr. Stefano Mischler – for the time and passion they put into thoughtfully evaluating my work, and for the stimulating discussion that emerged during the defense. Special thanks go to Prof. Daniel Bonamy and Dr. Alizée Dubois for the long and inspiring discussion on surface growth models that we had just before Christmas 2017 – I remember that day fondly.

The years at EPFL would have not been that good and profitable without the LSMS family. Okan, Ramin, Tobias, Lucas, Fabian, Mohit, Emil, Thibault, Son, Manon,

Acknowledgements

Nicolas, Guillaume, Roozbeh, Aurelia, Jaehyun, Valentine, Jérémy, Tom, Gianluca, Mauro, Fatima, Birgitte, Emma, Anne-Françoise: thanks for the countless memories, and it was an honour to see everyone's remarkable achievements. And thank you all for putting up with my avoidant moods and relentlessly asking me to join for coffee even if I would not join often – it means a lot.

I will always be thankful to Giulia, for supporting me when I decided to pursue a Ph.D. abroad, to Francesco for the help during some tough times, and to Cristina, for the meaningful conversations.

I am grateful for the flatmates I have had – you are all awesome. Thanks in particular to Greg for all the melted cheese, Roxane for picking up my pieces heartbreak after heartbreak, and Connor for the friendship and support during the lockdown period.

I grew a lot by joining the Catalyst – a scicomm collective populated by a bunch of fools: thanks a ton for making me feel less out of place and less weird. The Catalyst also contributed to kicking off the project that has become SciFilmIt, which I am proud of being part of – thanks to Aurélie, Eleo, Kat, Kerstin, Robbie, Theo and all the volunteers and people involved in taking over the world together, one science film at a time.

Thanks to Federico, Matteo and Andrea for the mutual support and the loads of laughs and fun, from the Montreux Jazz Festival to the Barcelona Primavera Sound: you always make my day.

Of course, this great achievement would not have been possible without the support of Mamma, Papà and Fratello. The endless trust you have in me and my life choices is unbelievable, and I am looking forward to the opening of the borders to come visit again.

I will always be in debt with Marta and Carlotta for their unconditional support when my mood goes south, and with Ann-Kristin for using her wit to help me get a grip on it – I am grateful to have all of you in my life.

Finally, I am extremely thankful to Michela, Marta, Giulio, Luca, Fra, Luca, Sabrina and Enrica. No matter where we meet – at Marta and Giulio's wedding, at a pub in Lausanne, or playing Monopoly over zoom during a pandemic – you always feel like home.

Lausanne, Spring 2020

E. M.

Abstract

Geological faults movements generating earthquakes, a vehicles' tyres rolling on the pavement, and a chalk writing on a blackboard are all different examples of frictional systems. In these systems, which are everywhere around us, two separate bodies are in contact and in relative motion, interacting with one another. Under these conditions, several phenomena arise at the interface: friction, wear, and lubrication being the main ones. Wear, in particular, is the loss of material from the surface of one (or both) the moving bodies. This phenomenon is of interest as it leads to loss of usefulness of manufactured objects and health concerns for patients with implants, to name just a few of important consequences due to material degradation. Yet, our knowledge on the topic of wear is still scattered, with many observations and models that are system dependent. How the surface morphology changes during wear processes is one of those aspects that are not well understood, and that at the same time affect significantly wear itself. Therefore, the aim of this dissertation is to investigate the role of surface roughness in wear processes upon dry sliding. The work focuses on wear of the adhesive type, as it is the most common one (together with the abrasive type).

The first part of the thesis addresses the topic with numerical investigations. Two-dimensional systems are modelled with a discrete approach, where two surfaces are rubbed against one another. In this setup, a wear debris particle is eventually formed and it is constrained to roll between the sliding surfaces. It is shown that the method reproduces the evolution of the surface roughness into the self-affine morphology that is observed for different frictional surfaces. Furthermore, the interplay between surface roughness, adhesion, and wear debris particle size is investigated, and a minimum size for the debris particle is determined, based on a critical length scale recently derived for adhesive wear processes. These sets of simulations bring further observations on the wear process, like the evolution of the work due to the tangential forces and of the wear volume. The latter in particular displays an overall increase: debris particle accretion is favoured over its break down. This leads to the second part of the dissertation, where an analytical framework is presented that allows to

Abstract

explain the tendency of the debris particle to grow in volume, instead of depositing material onto the mating surfaces.

The general approach of the work aims at uncovering underlying mechanisms of wear processes, and it is not restrained to some specific application. While on one hand this means that the work cannot cover the specificity of some frictional systems, on the other hand it leads to fundamental insights that are relevant from the nano- to the geological-scale.

Key words: adhesive wear, surface roughness, tribology, critical length scale, particle size, wear volume, ductile-to-brittle transition, rolling contact, adhesive contact, frictional contact

Riassunto

Movimenti di faglie geologiche che danno origine a terremoti, gli pneumatici di un veicolo che ruotano sull'asfalto e un gesso che scrive su una lavagna sono tutti esempi diversi di sistemi dove l'attrito è fondamentale. In questi sistemi, che possiamo trovare ovunque attorno a noi, due corpi distinti sono in contatto e in moto relativo, interagendo l'uno con l'altro. In queste condizioni, diversi fenomeni si manifestano lungo all'interfaccia e i principali sono l'attrito, l'usura e la lubrificazione. L'usura in particolare è la perdita di materiale da parte della superficie di uno dei due corpi (o entrambi). L'interesse per tale fenomeno è dovuto al fatto che il deterioramento di materiali ha importanti conseguenze, per esempio nei casi di degrado di diversi prodotti manifatturieri e di protesi in ambito biomedico. Nonostante ciò, la nostra conoscenza dell'argomento è tuttora frammentata, con diverse osservazioni e modelli che dipendono dal sistema considerato. Uno degli aspetti del fenomeno che ancora non sono compresi è la modalità con cui la morfologia delle superfici cambia durante i processi d'usura, la quale a sua volta influenza notevolmente il processo d'usura stesso. Di conseguenza, l'obiettivo di questa tesi è quello di studiare il ruolo della rugosità delle superfici nei processi d'usura in assenza di lubrificanti. Il lavoro si concentra sull'usura di tipo adesivo, essendo il tipo più comune (assieme all'usura di tipo abrasivo).

La prima parte della tesi affronta l'argomento con simulazioni numeriche. Sistemi bi-dimensionali sono modellati con un approccio discreto, dove due superfici sono fatte scivolare l'una contro l'altra. In tali sistemi viene a formarsi una particella d'usura che è costretta a rotolare tra le due superfici che sono in moto relativo. Viene mostrato che il metodo numerico riproduce la stessa evoluzione della rugosità delle superfici che è osservata sperimentalmente in numerose superfici sottoposte ad attrito, ovvero la loro geometria diviene auto-affine. Inoltre, viene anche studiata l'influenza reciproca di adesione, rugosità delle superfici e dimensioni della particella d'usura: viene quindi identificata la dimensione minima di una particella d'usura, sulla base di una scala di lunghezza critica in processi d'usura di tipo adesivo derivata recentemente. Questi set di simulazioni portano ad ulteriori osservazioni

Riassunto

sul processo d'usura, come l'evoluzione del lavoro compiuto dalle forze tangenziali e del volume d'usura. Quest'ultimo in particolare mostra una tendenza a crescere: un aumento del volume della particella d'usura è favorito rispetto ad una sua rottura. Quest'osservazione porta alla seconda parte della tesi, dove viene presentato un approccio analitico che permette di spiegare tale tendenza della particella d'usura di aumentare di volume, invece di depositare materiale sulla superficie opposta.

L'approccio generale dello studio mira a svelare meccanismi fondamentali dei processi d'usura e non è ridotto ad applicazioni particolari. Mentre da un lato questo significa che il lavoro non può affrontare le specificità di alcuni sistemi, dall'altro porta a osservazioni fondamentali che sono rilevanti a tutte le scale, da quella nanoscopica a quella geologica.

Parole chiave: usura adesiva, rugosità delle superfici, tribologia, scala di lunghezza critica, dimensione delle particelle d'usura, volume d'usura, transizione duttile-fragile, contatto adesivo, contatto tangenziale, contatto con rotolamento

Contents

Acknowledgements	i
Abstract	iii
Riassunto	v
List of figures	xi
List of tables	xv
1 Introduction	1
1.1 Objectives	5
1.2 Approach	5
1.3 Outline	7
2 State of the art	11
2.1 Early studies in tribology	11
2.2 Wear across scales	12
2.2.1 Wear models	14
2.2.2 AWM critical length scale	17
2.2.3 Third body	18
2.3 Surface morphology	19
2.3.1 Equilibrium roughness	19
2.3.2 Self-affine surfaces	20
2.3.3 Surface characterization	22
2.3.4 Surface growth concepts	25
3 Numerical framework	29
3.1 Numerical methods in wear modelling	30
3.2 Atomistic simulations	32

Contents

3.2.1	Sampling	32
3.2.2	Monte Carlo methods	34
3.2.3	Molecular dynamics	36
3.2.4	Potential energy	39
3.3	Discrete element method	44
3.3.1	Formulation	44
3.3.2	Comparison between DEM and MD	45
4	Emergence of self-affine surfaces during adhesive wear	47
4.1	Introduction	48
4.2	Results	49
4.2.1	Simulation set-up	49
4.2.2	Self-affine description	51
4.2.3	Evolution of a debris particle	56
4.2.4	Influence of heterogeneity and limitations	59
4.3	Discussion	61
4.4	Methods	62
4.4.1	Interaction potentials	62
4.4.2	Simulation geometry and boundary conditions	62
4.4.3	Self-affine surfaces	63
4.4.4	Spectral analysis	64
4.4.5	Height–height correlation analysis	65
4.4.6	Average roughness quantification	66
4.4.7	Data analysis	66
4.5	Supplementary materials	69
4.5.1	Supplementary figures	69
4.5.2	Supplementary discussion	78
5	The role of interfacial adhesion on minimum wear particle size and roughness evolution	81
5.1	Introduction	82
5.2	Materials and methods	83
5.2.1	Interaction potentials	84
5.2.2	Simulation geometry and boundary conditions	85
5.2.3	Self-affine surfaces	86
5.2.4	Surface analysis	86
5.2.5	Data analysis	88
5.3	Results	89

5.3.1	Particle formation	90
5.3.2	Long timescale self-affine morphology	96
5.3.3	Wear rate	100
5.4	Discussion	102
5.5	Supplementary materials	103
5.5.1	Supplementary methods	103
5.5.2	Supplementary figures	107
5.5.3	Supplementary Tables	112
6	A mechanistic model for the growth of cylindrical debris particles in the presence of adhesion	121
6.1	Introduction	122
6.2	Theory	128
6.2.1	Approach	128
6.2.2	Framework	128
6.2.3	Adhesive forces: Maugis model	132
6.2.4	Tractive rolling forces: Carter model	133
6.2.5	Stress field	134
6.2.6	Crack propagation angle	137
6.3	Calculation	139
6.4	Results and discussion	140
6.4.1	Effect of cylinder radius	144
6.4.2	Effect of Maugis parameter	145
6.4.3	Effect of load	145
6.4.4	Effect of friction	146
6.4.5	Effect of pre-existing surface flaws	148
6.4.6	Further considerations	149
6.4.7	Numerical validation	149
6.5	Conclusions	151
6.6	Further cases	152
6.6.1	Calculation	153
6.6.2	Results and discussion	156
6.7	Maugis formalism	158
6.7.1	Theory	158
6.7.2	Calculation	160

Contents

7	Conclusions and outlook	163
7.1	Summary	163
7.2	Outlook	165
A	A geometrical model as a tool for surface roughness evolution investigations	169
A.1	Introduction	170
A.2	Model	170
A.2.1	Local geometry update	171
A.2.2	Asperity interaction	174
A.3	Preliminary results	176
A.4	Conclusions	178
	Bibliography	199

List of Figures

2.1	Model of a tribo-system.	13
2.2	Example of fractal profiles.	21
2.3	Comparison between fractal profiles and a non-fractal one.	28
3.1	Examples of interaction potentials.	41
3.2	Family of interaction potentials adopted in the simulations of Chapters 4 and 5.	43
4.1	Ductile-to-brittle transition, simulation setup, and evolution.	54
4.2	Steady-state surface morphology analysis.	57
4.3	Evolution of equivalent roughness σ_{eq} , frictional work W_t , and wear volume V	58
S4.4	Steady-state surface morphology analysis.	69
S4.5	Scaling of the root mean square of heights σ with system size.	70
S4.6	Height distribution for top and bottom surfaces of simulation S1 at sliding distance $29950 r_0$ after minimization to avoid effects due to temperature fluctuations.	71
S4.7	Height distribution for top and bottom surfaces of simulation G1 at sliding distance $29750 r_0$ after minimization to avoid effects due to temperature fluctuations.	71
S4.8	Evolution of tangential force F_t with the sliding distance s	72
S4.9	Evolution of the wear rate with the sliding distance s	72
S4.10	Evolution of the ratio V/W_t between the wear volume V and the tangential work W_t with the sliding distance s	73
S4.11	Evolution of equivalent roughness σ_{eq} , frictional work W_t , and wear volume V	74
S4.12	Evolution of equivalent roughness σ_{eq} , frictional work W_t , and wear volume V	75
S4.13	Comparison between simulations run at different temperatures.	76

List of Figures

5.1	Short timescale evolution	91
5.2	Scenario 1: debris particle formation and initial volume V_0	93
5.3	Effect of interfacial adhesion $\tilde{\gamma}$ and surface morphology on the initial debris particle volume V_0	94
5.4	Long timescale evolution and effect of adhesion on debris particle motion	98
5.5	Surface morphology analysis	99
5.6	Evolution of the equivalent roughness σ_{eq} and of the wear volume V	101
S5.7	Ductile-to-brittle transition and simulation setup	107
S5.8	Steady-state surface morphology analysis	108
S5.9	Evolution of the equivalent roughness σ_{eq} and of the wear volume V	109
S5.10	Distance s_t travelled by the debris particle as a function of the sliding distance	109
S5.11	Effect of roughness on debris particle formation and d^*	110
6.1	Example of particle accretion observed in 2D molecular dynamics simulations	124
6.2	Frame of reference for a body in contact with a half-space and stress directions taken as positive for a small representative square element at a random point within the bodies	130
6.3	Tractions and stress distributions	136
6.4	Construction of the tangential tractions and relative stresses	138
6.5	Mohr diagram for a generic stress state and principal stresses directions	139
6.6	Stress $\bar{\bar{\sigma}}_{xx}(\xi)$ in the case of tractive rolling with adhesion	141
6.7	Maximum principal stress $\bar{\bar{\sigma}}_1(\xi)$ and crack propagation angle θ_c along the interface in the case of tractive rolling with adhesion	143
6.8	Maximum principal stress $\bar{\bar{\sigma}}_1(\xi)$ and crack propagation angle θ_c along the interface in the case of tractive rolling with adhesion, with adhesive friction	148
6.9	Discretized geometry for the phase-field simulations and damage evolution	153
6.10	Stress $\bar{\bar{\sigma}}_{xx}(\xi)$ in the case of tractive rolling without adhesion	155
6.11	Maximum principal stress $\bar{\bar{\sigma}}_1(\xi)$ and crack propagation angle θ_c along the interface in the case of tractive rolling without adhesion	157
A.1	Local geometry update: ductile damage	173
A.2	Local geometry update: ductile damage and pile-up	174
A.3	Local geometry update: brittle damage	175

A.4	Local geometry update: brittle damage with asperity interaction . . .	176
A.5	Profile evolution for the simulation GM1	179
A.6	Profile evolution for the simulation GM2	180
A.7	Height-height correlation and contact area evolution for the simulations GM1 and GM2	181
A.8	Evolution of root mean square of heights σ for simulations GM1 and GM2	182

List of Tables

4.1	Summary of the simulations.	68
S5.1	Summary of the simulations in set S: $\tilde{\gamma} = 1.0$	113
S5.2	Summary of the simulations in set S: $\tilde{\gamma} = 0.8$	115
S5.3	Summary of the simulations in set S: $\tilde{\gamma} = 0.6$	117
S5.4	Summary of the simulations in set S that display Scenario 1.	118
S5.5	Summary of the simulations in set L.	119
6.1	Nomenclature of the main symbols – Part 1 of 3.	125
6.2	Nomenclature of the main symbols – Part 2 of 3.	126
6.3	Nomenclature of the main symbols – Part 3 of 3.	127
6.4	Parameters adopted for the numerical simulations	152

Chapter 1

Introduction

Physical phenomena emerging at the interface of two surfaces that slide against one another have been known and studied for centuries, yet the idea of grouping such studies under one unique field of science and engineering is remarkably recent. The word “tribology” – with its definition of “the science and technology of interacting surfaces in relative motion - and of associated subjects and practices” [1, 2] – is in fact the only word in my vocabulary for which I can point to the exact year when it was invented: 1966. The word was indeed coined by the Committee of the British Department of Education and Science led by Jost, in a report that addressed the huge economical consequences of the phenomena associated with friction and wear [2]. Since then, several investigations have been carried out by national committees in several industrialized countries worldwide with the scope of assessing and reducing the impact of tribological phenomena on their economies [3, 4]. Friction and wear are in fact responsible for a large share of energy losses in industrial processes, and energy inefficiencies mean economical inefficiencies – over the years it has been estimated that developments in tribology would lead to savings worth 1.0 to 1.4% of a country’s gross domestic product [3, 5].

Energy inefficiencies have not only an economical cost, but also a remarkable environmental cost. Following the need to reduce the consequences of anthropogenic pollution on the environment, in particular on global warming, attempts to quantify the CO₂ emissions due to tribological phenomena have been made in recent years. A group of researchers led by Holmberg and Erdemir conducted several analyses both on individual industry sectors [6–9] and on a global scale [4], and concluded that CO₂ emissions could be reduced in total by 1 460 MtCO₂ globally within the next 8

Chapter 1. Introduction

years by means of advances in tribology (as a reference, CO₂ emissions produced in the EU amounted to roughly 4000 MtCO₂ in 2010 [10]).

Furthermore, while tribological phenomena are responsible for CO₂ emissions indirectly via energy inefficiencies, they are also directly responsible for health concerns. This happens, for instance, in all industrial applications where frictional processes produce wear debris of small sizes. In the transportation industry, when breaking pads are pulled together to slow down a moving vehicle, they release particles in the atmosphere. Such particles are so small that they can deposit in our lungs, and fine particle air pollution is indeed correlated to a higher death risk [11–13]. Health wise, friction and wear also lead to damage of prostheses and implants and to the presence of wear debris in the organism, with consequences for the patient. The interest in the medical field is such that the word “biotribology” is often used to refer to this subset of tribological investigations.

Recently, Boneh and Reches [14] named “geotribology”^a the tribological approach that they recommended to adopt in the investigations of friction, wear, and lubrication in geology. Systems such as earthquake faults display in fact a wide range of situations that are commonly investigated also in engineering settings, like frictional weakening [16–19], stick-slip [20, 21], and powder lubrication [22, 23] to name a few. Synergy between researchers investigating tribological phenomena at different scales, on different materials, for different purposes is thus desirable to shed light on the fundamental physics that underlies all frictional systems.

My research, too, benefited a lot from the extensive investigations of geophysicists and geologists on the topic of surface roughness [16, 24–35], and many inspiring discussions and some collaborations were prompted by the differences and the common points in our studies. At the beginning of my PhD studies I was in fact surprised by the lack of physical insights in the evolution of the surface morphology during frictional processes, at least within the engineering community. Although the surface roughness is well known to affect the tribological performances of a frictional system, more effort has been put traditionally into quantifying the evolution of the wear volume and other parameters. The work of Rabinowicz [36] gathered much of the knowledge in tribology that was developed mostly in the Western countries until the end of the last century, and he dedicates only a couple of pages to the topic

^aBoneh and Reches [14] report that the term “geotribology” was first used by Blok in 1963 [15]. This of course would at once strip Jost of his most popular contribution to the field and me of my happiness of knowing when one word of my vocabulary was invented. Good news for both Jost and I: I could not actually find any use of “geotribology” in Blok’s paper [15].

of surface roughness evolution. More investigations appear to have been carried out in the former Soviet Union, and, in their comprehensive book on friction and wear, Kragelsky et al [37] have a whole chapter on the topic. The fundamental point engineers seem to agree upon is that, after a transient stage, the surface roughness stabilizes around a so-called steady-state value [36, 37]. A similar behaviour is observed also in the roughness of geological faults [27, 38–40] and of fractured surfaces [41–45] – fracture mechanics being another source of inspiration for my work.

Concerning the methodologies of investigations, tribology has been understandably mainly an experimental field until recently. The first documented observations in the field were conducted by Da Vinci in the Renaissance period [46, 47], and later in the XVII and XVIII centuries Amonton and Coulomb formulated the fundamental laws that still carry their names [48]. The number of empirical studies then grew exponentially in the past century with the increasing importance of manufacturing processes, culminating in the notable works of Bowden and Tabor [49], Archard [50], and Holm [51]. The observations of Holm and Archard led to the formulation of what is commonly known as the Archard wear law. It is considered the fundamental law in wear, and it predicts that the wear volume grows linearly with the distance traveled by the sliding surface, the normal force that keeps the two surfaces in contact, and the reciprocal of the material hardness. While it has been shown to be applicable in a wide range of setups, the proportionality is given by the so-called wear coefficient, which needs a separate experimental fitting for each setting and it includes many other unknown effects which emerge during the process (like those due to the surface roughness). 70 years after this breakthrough in the modeling of wear, we still do not know how different factors contribute to this coefficient and efforts towards a physical explanation are still ongoing.

In Archard's picture, the wear coefficient is explained as the probability that two asperities belonging to opposite surfaces, colliding, form a separate wear fragment. The framework is thus that of a two-body contact – that is, the wear volume grows only by fracture induced mechanisms at the contact interface between the two surfaces. While this is reasonable at first contact, the condition is already altered early in the wear process: once wear fragments are present, they form the third body that is trapped between the surfaces and separates them (at least locally). In such three-body contact configuration, wear volume can potentially grow also by accretion of the third body via removal of material from the surfaces. In general, the presence of wear debris alters significantly the physics of the system and a third-

Chapter 1. Introduction

body approach is thus often desirable when one aims at describing the physical mechanisms in more detail [52].

Complexities in tribology are not limited to changes in the geometry of frictional systems. Several non-linear phenomena arise at the interface of two sliding surfaces, like fracture, plasticity, contact, etc., and they are all intertwined to some degree. Differences in the material properties also play an important role. Such variety of phenomena has led to the observation and definition of different wear types – possibly as many as the authors who have tried to categorize them. Based on a physical rather than a phenomenological description, Rabinowicz [36] classified the mechanisms in four types: adhesive, abrasive, corrosive, and surface fatigue wear. The adhesive and the abrasive type are found to be the primary causes in objects critical deterioration [36]. Both mechanisms are usually linked to the hardness of the materials. When the mating surfaces develops strong adhesion at the interface (adhesive wear), wear fragments are removed from both surfaces, and this is usually encountered when the two materials have comparable hardness values. On the other hand when one material is much harder than the other, it scratches the softer one (abrasive wear).

Because of the aforementioned complexities, a narrower spectrum of tribological problems has been addressed from an analytical perspective. The efforts in such context have been mostly focused on the mechanical behaviour of the first contact between two surfaces, with the fundamental achievements by Hertz [53], Greenwood and Williamson [54], Johnson-Kendall-Roberts [55] and Derjaguin-Muller-Toporov [56].

Similarly, numerical investigations were scarce for a long time – the intricacies of the phenomena demanding complex models and massive computational resources. Such resources have been more and more accessible in recent years though, and numerical modeling has led to new, fundamental observations [57–59]. In Molinari's group, a recent breakthrough about the governing length scale in the wear debris formation process was made possible indeed by the use of a numerical approach [59], and this has been my inspiration for the main methods of investigation adopted throughout the thesis. The advantage of using numerical tools, when compared to an experimental setting, lies in the possibility of having more control over the influence of different parameters and in an easier tracking of such parameters in time and space. Of course there is no free meal, and such advantages come with simplifications of the physics and some departure from reality.

In brief, the lack of a unified picture in the understanding of wear and the surface roughness evolution during wear processes – together with the many implications for our health, the world, and the economy – fueled the motivation for the work of this thesis.

1.1 Objectives

The main objective of this work is to shed light on the roughness evolution of surfaces in adhesive wear processes, by means of both numerical simulations and analytical derivations.

To this end, the questions addressed throughout the dissertation are:

- **Modeling.** Is there a numerical approach suitable to reproduce the same surface roughness that is observed experimentally and, if yes, which one and how? What are its limitations? Can we use an analytical approach instead to gain a zeroth order approximation of what happens at the interface between the surface and the wear debris?
- **Surface roughness.** What are the effects of adhesion, initial geometry, temperature, material composition, and system size on the evolution of the surface roughness? Are the final surfaces self-affine and, if yes, under what conditions? Is there a correlation between roughness evolution and frictional work?
- **Third body.** Is the formation of a third body relevant to the surface roughness evolution? How do adhesion, surface roughness and debris particle formation interplay? Is there a correlation between wear volume and frictional work in the long term? Can we predict if it is more likely for the third body to deposit material on the mating surface or vice versa? Do the different models of friction at the different scales affect such predictions?

1.2 Approach

The work of this thesis relies both on well-established numerical methods and analytical derivations, and on a recently published breakthrough on the physics of wear.

Chapter 1. Introduction

Shortly before the initial investigations presented in this thesis, it was shown that a critical length scale governs wear debris formation [59]. Before, it had been long known that upon contact in a frictional system and under moderate loads, two asperities belonging to opposite surfaces either break or deform plastically. The work of Aghababaei, Warner, and Molinari [59] shows that a material-dependent critical length scale determines which of the two mechanisms takes place^b. If the junction formed by the two asperities in contact is larger than the critical length scale, a debris particle is formed, otherwise the asperities smooth out. The authors also put their finding in the perspective of the possible implications for the roughness of the two surfaces. In particular, they observed that if the critical length scale is large enough with respect to the system size, the surfaces asymptotically smooth each other and no roughness is created. Such findings lay the foundation for the investigations on the long term evolution of the surface roughness presented in this dissertation. The proven existence of such a critical length scale allows to build model systems that are designed to lead to particle formation. The particle is then constrained to roll between the two surfaces, working them and changing their morphology.

This physical insight was possible thanks to the numerical methodology adopted: discrete modeling with molecular dynamics simulations. The mechanics of a system can in fact be investigated numerically in two ways: with a continuum or a discrete approach. In the first case, each body in the system is modeled as a continuum – that is there is no empty spot in it. In discrete modeling approaches, the investigated bodies are modeled by discrete mass points or particles, allowing empty regions of space between them (more details on the two methodologies are provided in Chapter 3). The main advantage of discrete models is the intrinsic capability of capturing non-linear behaviours (like large deformation, contact, creation of new surfaces, dislocations), and many of them are indeed non-negligible in wear processes. The downside is the challenging computational costs needed to simulate systems at scales that are meaningful for engineering applications [60]. The use of simplified constitutive laws helps in this sense and made possible both the discovery of the aforementioned critical length scale [59] and most of the results presented here, although the simulations had to be constrained to two-dimensional systems.

While molecular dynamics and the use of the critical length scale are the core approach for most of the thesis, the last part employs an analytical approach. As briefly

^bIn the following, such concept will be often referred to as “the AWM critical length scale”, from the names of the authors [59]. This choice comes from the fact that using wordings such as “the critical length scale that governs the ductile-to-brittle transition in adhesive wear” is quite heavy and worsens the readability of the dissertation.

mentioned in the previous section, most of the analytical derivations relevant to tribology address the problem of contact between two objects, such as two asperities or a body on a half-plane. The latter is the framework of interest for the analysis of the contact between a rolling debris particle of cylindrical shape and a half-plane. Inspired by Maugis' fracture mechanics approach to analyze the normal adhesive contact of spheres [61], and based on well-established analytical results for the mechanics of rolling bodies [62], the question of which body is more likely to wear – is it the cylinder or the half-plane? – is addressed.

1.3 Outline

The remainder of the dissertation is structured in six chapters and an appendix, that are briefly summarized here. Each chapter is introduced by an abstract that describes the main points discussed.

Chapter 2 – State of the art

From the empirical studies of Da Vinci to the numerical investigations of Molinari's group, the fundamental findings in the field of tribology that are relevant to the present work are introduced. The well-known Archard wear law and other wear equations are presented. The AWM critical length scale is described together with other recent findings that it has led to. Next, the role of surface morphology is discussed, and the main tools to characterize the surface morphology are provided. The concept of self-affinity is explained, and fundamental surface growth concepts are presented.

Chapter 3 – Numerical framework

In this chapter, an overview of the numerical methods adopted in the modeling of wear is given, with a focus on the distinction between continuum and discrete methods. The basic concepts of statistical mechanics and the molecular dynamics approach adopted in Chapters 4 and 5 are described, expanding on the constitutive models. Another suitable approach, the discrete element method, is briefly introduced.

Chapter 1. Introduction

Chapter 4 – Emergence of self-affine surfaces during adhesive wear

The first questions relative to surface roughness evolution are answered here. All modeled surfaces develop full adhesion at the interface. It is shown that the numerical methods adopted can capture the evolution that is experimentally observed, and that the presence of a third body is key for the final self-affine morphology to emerge. The effects of the initial morphology and material composition are addressed. Observations on the wear volume and on the frictional work during these long timescale simulations are reported.

Chapter 5 – The role of interfacial adhesion on minimum wear particle size and roughness evolution

Here, investigations on the surface roughness evolution are extended to the case where reduced adhesion develops at the interface of the two surfaces. The effect of the strength of the interfacial adhesion on the rolling motion of the debris particle and on the wear volume are investigated. The interplay between surface geometry, interfacial adhesion and debris particle formation is also studied.

Chapter 6 – A mechanistic model for the growth of cylindrical debris particles in the presence of adhesion

This chapter addresses the observation first made in Chapter 4 that in the case of full adhesion the third body displays a tendency to grow in terms of volume. The mechanics of the contact between a rolling cylindrical particle and a mating surface are investigated based on known analytical derivations. Crack propagation is then shown to be favoured within the mating surface with a Maugis approach to contact.

Chapter 7 – Conclusions and outlook

The conclusions drawn from the presented work are discussed. Limitations and future perspectives are addressed.

Appendix A – A geometrical model as a tool for surface roughness evolution investigations

Efforts in the development of a simplified geometrical model to study surface roughness evolution are reported here. A model is presented that is based on the AWM critical length scale concept and that is inspired by classical surface growth models. Possible future developments are addressed.

Note that the notation for some variables and parameters change from chapter to chapter, although they are always consistent within each chapter. This is because a large number of variables is needed throughout the thesis, thus the same symbol may not represent only one variable, and Chapters 4 to 6 were first written as standalone work to be submitted to scientific journals. For readability, consistency within each chapter (and previous related work) has been given priority. Chapters 4 and 5 are similar in methodology, thus the notation is essentially the same. The analytical approach of Chapter 6 asked for an unexpected number of parameters, and thus, has a dedicated nomenclature. In all cases, whenever a new parameter or notation is used, the definition of the parameter is re-stated.

Finally, the structure of Chapters 4, 5 and 6 is the same of the relative manuscripts submitted for review. As a consequence, Chapters 4 and 5 present each a 'Supplementary Materials' section, that contains the figures, tables, methods, and discussions that are referred to as 'Supplementary' in the main body of the chapter.

Chapter 2

State of the art

Tribological phenomena have been object of study since the Renaissance period. Systematic investigations specifically on wear started much later – the remarkable contribution of Holm and Archard coming in the middle of the XX century. Later, the advent of experimental setups and numerical simulations that allow investigations at the nanoscale gave new momentum to the field. In this chapter, I recall the milestones in wear modeling at all scales: from the Archard wear law for steady-state processes to the atom-by-atom removal observed at the nanoscale, via the running-in wear model suggested by Queener. The ductile-to-brittle critical length scale governing loose wear particle formation and the third body approach to wear are then addressed. A summary of the knowledge about the surface roughness evolution in tribo-systems is then provided, together with the different and most common methods to characterize the surface morphology. Finally, surface growth models and their role in tribology are discussed.

2.1 Early studies in tribology

As a species, we have had to deal with tribological phenomena in technological applications much earlier than when we invented a word for them. Standing stones sites have been erected since the prehistorical period with stones hauled from hundreds of kilometers, and the Egyptians needed to carry large and heavy blocks to build the pyramids – still nowadays in the tribology community we are debating how that could be possible at the time [63].

Chapter 2. State of the art

The first documented studies in tribology are those of Da Vinci, who conducted investigations on both friction and wear [46, 47, 64]. In his work on friction, he shows that he knew about the physical principles that are known today as Amontons fundamental laws of friction [47]:

1. the frictional force is proportional to the vertical load, and
2. the frictional force is independent of the (apparent) contact area.

On wear, he observed that harder materials wear less^a and that wear increases with the sliding distance^b. Unfortunately, his manuscripts were not available until the 1970s [47], and with them his knowledge. The first available fundamental works were thus those of Amonton and Coulomb on friction. Coulomb in particular found evidence that the kinematic friction is independent of the sliding velocity. The first documented experiments on wear would appear only at the beginning of the XIX century, with the investigations of Hatchett and Cavendish [65] on the wear of golden coins in the United Kingdom. In 1860, Reye [66] was the first to suggest a relation between the wear volume and an applied load, in particular he stated that the wear volume is proportional to the work performed by the frictional forces. Another milestone in the history of tribology is the observation by Bowden and Tabor [49] that the frictional force is proportional to the true contact area, the proportionality given by the interface shear strength.

2.2 Wear across scales

In the broadest sense, one can define *wear* as “the removal of material from solid surfaces”. This includes both natural phenomena like erosion due to weathering and the deterioration of manufactured objects due to their everyday use. Such definition also does not distinguish between the origins of the removal – chemical or mechanical, and indeed in the most general case both can take place, influencing one another [67, 68]. In the following the focus will be on the mechanical wear, as it

^aPerché tenero con tenero, e duro con tenero si consuma l'uno l'altro, è neciessario di fare duro con duro', i.e. 'As soft with soft, and hard with soft wear one the other, it is needed to do hard with hard', in a passage where he recommends to use steel when producing both the axles and the ring of the wheels where the axles sit.' Codex Madrid I, 13r [46].

^bQuella cosa più si consuma, della quale la confregazione fa più lungo cammino', i.e. 'That thing wears most, whose friction walks longest.' Codex Atlanticus, 1043v [64].

is more directly linked to my investigations. One can define as mechanical wear the removal of material due to dynamics effect, and chemical wear the removal due to reactions at the interface between atoms and compounds of (or that form) different species. Clearly, when one investigates the general dynamics of atoms as in this work, there is some overlap.

Independently of the scale, in tribology there are always two surfaces in contact with one another and in relative motion. The so-called tribo-system (Figure 2.1) is thus composed of two bodies in contact, and one can assume that there is a frame of reference in which the bottom body is fixed and the top one slides at velocity v , parallel to the middle planes of the surfaces (it is here reasonably assumed that the middle planes of the two surfaces are parallel, too). At the velocity v correspond a frictional force F_t and a sliding distance s . Finally, the two bodies are pushed together by a normal force F_n acting on the top one and are characterized by their hardness p (which is assumed the same for the two bodies if not otherwise specified). In general, because of the sliding process, wear particles are produced at the interface and form the third-body. A lubricant may be present between the two surfaces, or may develop during the wear production. Note that, although lubricants are of paramount importance in tribology, they will not be discussed in this dissertation, as the investigations focus on dry sliding.

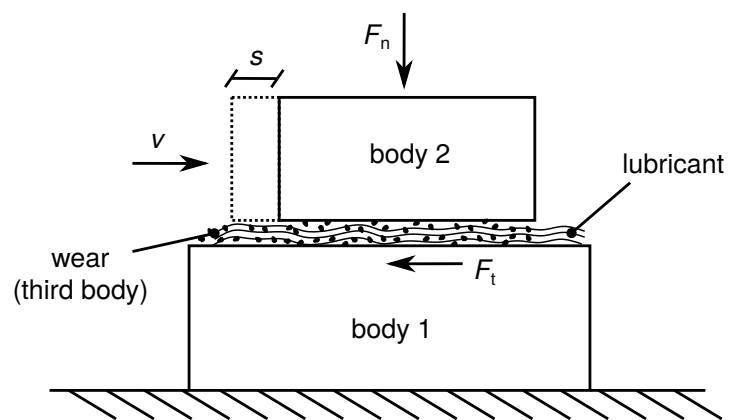


Figure 2.1 – Model of a tribo-system. Two first bodies are in relative motion with respect to one another. A normal force F_n is applied on the top body ('body 2'), which slides over a distance s at velocity v against the bottom body ('body 1', fixed). Upon sliding, the frictional force F_t and wear debris particles develop at the contact interface between the two first bodies. A lubricant may also be present along the interface, separating the two first bodies.

2.2.1 Wear models

The first observations on wear were done at the macroscopic scale, and the models by Archard and Holm and by Barwell and Queener are derived at this scale. Later, the interest in and the accessibility to nano-scale applications have led to investigations of wear at the microscale, and an Eyring-like mechanism has been suggested.

Steady-state wear: Archard wear law

In the 1940s to 1950s, Holm and Archard were interested in the contact between metallic surfaces. Holm interpreted wear as an atomic process (although he did not directly observe such atomic process), and in his theory the wear volume V is given by [50, 51]

$$V = k_H \cdot \frac{F_n s}{p}, \quad (2.1)$$

where s is the sliding distance, F_n is the normal force pressing the two bodies in contact, and p is the hardness of the materials (see Figure 2.1). In Eq. 2.1, k_H is the constant probability that a bond that forms between atoms belonging to opposing surfaces leads to the removal of one of the two atoms from the surface it originally belonged to.

Later, Burwell and Strang [69] and Archard [50] observed in their experiments that the removal of material took the form of distinct wear particles, instead of an atom-by-atom kind of mechanism as in Holm's theory, and suggested to use another formula for the wear volume that is essentially Holm's equation rewritten at the macroscale. Their observation held true after the running-in (or break-in) phase, that is once a steady state of the sliding process was reached. Archard and Hirst [70] would then unite this approach and Holm's under one expression:

$$V = k \cdot \frac{F_n s}{p}, \quad (2.2)$$

where k is called the *wear coefficient*, it is constant for a given tribo-system, and it represents the probability that each contact spot leads to material removal during the frictional process once the steady state is achieved. In Archard's picture, k bridges his observations and Holm's, in that the probability can be defined both for atomic encounters (where $k = k_H$, as in Eq. 2.1) and for contacting asperities

(Archard's experiments [50]). Eq. 2.2 is widely known as the Archard wear law^c, and it has been found to be applicable at the nanoscale in molecular dynamics simulations [71]. To interpret it, at least at the macroscale, one can rewrite it as $V = k \cdot As$, where $A = F_n / p$ is the true contact area, assuming that each contacting asperity plastifies. The volume As is then scaled by the wear coefficient k , which represents the probability of producing a wear fragment for each of the contact spots that contribute to A . One must note that k includes multiple factors, like the morphology of the surface, elastic interactions of close contacting asperities, effects due to the interfacial adhesion and the third body, rate of ejection of the third body from the system, and so on. The wear coefficient k can be determined only experimentally, and each application or setup needs its own tests to quantify its value, which spans several orders of magnitudes depending on the tribo-system [36]. Its physical meaning is thus still unclear, and research efforts are put into shedding some light on it [72, 73].

Furthermore, as Archard observed [70], the formula implies that the wear rate obeys some form of Amontons laws:

1. the wear rate is proportional to the vertical load, and
2. the wear rate is independent of the (apparent) contact area.

This, together with some other experimental observations, has led to conceive the existence of some direct relation between wear and friction, which seems intuitively reasonable. Nevertheless, a conclusive link has never been established. The lack of knowledge that we have on the physical origins of both the friction coefficient and the wear coefficient suggests that more efforts are needed to address the relationship between the two tribological phenomena.

Running-in wear: Queener model

Archard's wear law is derived from observations during the steady state of frictional processes. It is usually observed in fact that in the transition from static to dynamic conditions, the rubbed surfaces undergo a short period of time where the wear rate is high, and then decreases until the steady-state wear rate is reached. In this transition

^cSome authors refer to it as the Archard-Holm wear law, to give credit to Holm's first form of the formula (Eq. 2.1).

time, called *running-in* (or, sometimes, *break-in*), the wear rate is not linear with the sliding distance.

Barwell [74] ascribed such behavior to the initial morphology of the surfaces, that leads to fewer contact spots and higher stresses. When these asperities are broken, contact spreads over a larger area that stays constant, large stresses then decrease, and inelastic phenomena that produce wear are less likely to occur. Building on this, Queener et al. [75] proposed the following empirical relationship for the wear volume:

$$V = V_0 [1 - \exp(-ns)] + k_Q s, \quad (2.3)$$

where V_0 is the total volume that is lost during the running-in stage and is a function of the surface average roughness, n is a parameter that is constant for a given tribo-system, and k_Q is similar to the Archard wear coefficient k and it includes the effect of the true contact area. The model of Eq. 2.3 describes an exponentially decreasing wear rate for the early stages of the sliding process (small values of s) and a constant wear rate for the steady state (large values of s). While the fitted parameter n is ill-defined and its physical origins are even more unclear than Archard's wear coefficient, the model seems to be able to capture the wear volume evolution in grinding processes. Eq. 2.3 somehow corrects Eq. 2.2 for the existence of a finite wear volume V_0 that is produced at the onset of the sliding process, consistently with the results that led to the formulation of Archard's wear law [50, 69, 70]. Recently, molecular dynamics simulations have found the behavior of Eq. 2.3 to best fit wear of the abrasive type at the atomistic scale [76].

Atom-by-atom removal: a transition state approach

While Holm [51] was the first to theorize the atomic nature of wear, the first experimental observations of atomic-scale wear mechanisms came several decades later. In 1996, Parker et al. [77] investigated experimentally the wear behavior of single-crystal calcite in an aqueous solution, and found that the wear rate is best described by an Arrhenius rate law. Similar results were later obtained by other authors in dry conditions [78–80]. Jacobs and Carpick [81] eventually observed directly worn volumes at the nanoscale for silicon and confirmed the previous observations.

Within such regime, where both applied load and adhesion are low, the wear rate k_A

(in units of atoms lost over time) best fits the Arrhenius rate law [81, 82]

$$k_A = k_0 \cdot \exp\left(-\frac{\Delta E_{\text{act}}}{k_B T}\right) = k_0 \cdot \exp\left(-\frac{\Delta U_{\text{act}}}{k_B T}\right) \cdot \exp\left(-\frac{W(F)}{k_B T}\right), \quad (2.4)$$

where k_0 is the attempt frequency, k_B the Boltzmann constant, T the absolute temperature, ΔE_{act} the activation energy, ΔU_{act} is the stress-free internal energy of activation, and $W(F)$ is the work done on the system by the external forces F . According to this mechanism, the activation energy needed to transfer an atom from one surface to another is lowered when a mechanical stress is applied (and thus the rate of transfer is higher). Such variation in the rate of transfer, which is an atomic wear rate, is described by an exponential dependence on the applied load.

2.2.2 AWM critical length scale

A fundamental mechanism that has been recently uncovered with molecular dynamics simulations is the existence of a critical length scale that governs the transition from ductile to brittle behavior in adhesive wear [59]. In the previous section the main wear mechanisms were addressed: atom-by-atom removal takes place in the low interfacial adhesion and low loads limit, while at larger loads plastic deformation or brittle fracture of the contacting asperities is observed. In the latter regime, the transition between the two behaviors is determined by the material-dependent critical length scale [59]

$$d^* = \Lambda \cdot \frac{w}{\tau_j^2 / 2G}, \quad (2.5)$$

where Λ is a geometrical factor that takes into account the shape of the asperities and is of order unity, w is the fracture energy, τ_j is the junction shear strength, and G is the shear modulus of the material. If the size d of the junction formed by the contacting asperities is larger than or equal to d^* , a loose debris particle is formed and the surfaces are roughened, and if $d < d^*$ the two asperities smooth each other (possibly exchanging particles) until they weld or a junction $d \geq d^*$ is formed. Such important implications on the surface roughness were not clear in earlier similar forms of d^* that were put forward by Rabinowicz [36, 83] based on experimental observations.

The derivation of Eq. 2.5 is based on the Griffith approach to fracture, in which a crack propagates when the stored strain elastic energy E_{el} is larger than the energy

Chapter 2. State of the art

E_{ad} required to create two new surfaces. As $E_{\text{el}} \sim d^3$ and $E_{\text{ad}} \sim d^2$, the condition of loose debris particle formation $E_{\text{el}} \geq E_{\text{ad}}$ leads to Eq. 2.5. d^* thus provides a minimum size for loose wear particles in the case of contact between well-defined asperities [59, 73], and its extension to more complex geometries is the object of the investigations reported and discussed in Chapter 5.

Recently, works based on Eq. 2.5 expanded the original observations further [73, 84, 85]. Asperity interactions have been addressed with molecular dynamics simulations, and it has been found that if the two asperities are close enough to one another, they form one debris particle instead of two separate ones [84]. In these cases, the volume of the wear particle is proportional to the apparent contact area given by the two junctions, and wear is more severe. This is in contrast to the single asperity case and to the case where the two couple of contacting asperities are far from one another – the true contact area dictates the particle volume in such circumstances [59, 73, 84]. Further developments have led to a more complete picture of d^* , where the possibility of slip between the surfaces is added to the scenarios of ductile and brittle deformation [85].

2.2.3 Third body

Whenever the size d of the junction formed by two colliding asperities is larger than d^* , a loose wear particle is formed, which constitutes the third body and the tribo-system transitions to a three-body configuration. This is clearly captured by Eq. 2.5 but it is never really taken into account in wear models such as Archard's, where the rationale always assumes that material removal takes place at the contact between the two sliding surfaces (i.e. the two first bodies). Similarly, models that discuss changes in the surface morphology often neglect the existence of any third body [37, 74]. Yet, the role of the third body is relevant, as it changes significantly the dynamics of the system [52, 86, 87]. For example, the loose wear particles themselves can grow by accretion removing material from the opposing surfaces, or can abrade them if they stick to one of the two surfaces and slide against the other. Both examples are wear mechanisms that are not part of the rationales of the models given in Section 2.2, but that are relevant in different setups. In the light of this, Godet [52] suggested to treat wear with a third-body approach, similarly to what is done when lubrication is investigated (the third body can have indeed a lubricating effect). Taking into consideration the rates of third body production and ejection and linking them with a mass balance equation, an analytical model for the wear rate in a three-body

system has been developed based on numerical and experimental investigations [88, 89]. The model predicts a behavior that is similar to that of Queener [75], with the wear rate that decreases exponentially for short tests, and that is constant for long durations (cf. Eq. 2.3). The new approach gives more insights in the physical origins though. Similar trends (i.e. a decreasing wear rate) not only have been observed in classical tribo-systems [90, 91], but have also been theorized for geological faults, where the gouge-production rate is conjectured to decrease over time [26, 92].

2.3 Surface morphology

The surface morphology has long been known to play a non-negligible role in tribological phenomena, yet it has had less attention than other properties of a tribo-system. This is mostly due to the fact that tracking changes in the surface morphology is extremely difficult in experimental settings, and that the non-linearities are too many to address the problem from an analytical perspective.

The effects of and on surface morphology have thus been mostly deduced by observing the surfaces before and/or after slip took place, by assuming some specific morphology of the contacting surfaces, or by the use of rational arguments. For example, it has been shown that larger values of the roughness of a nanoscale surface (in terms of deviation from the mean surface plane) reduce the true contact area and thus the adhesive strength of the overall contact. In turn, adhesive wear decreases. Yet, molecular dynamics investigations has also shown that abrasive wear at the nanoscale increases with the surface roughness, and thus actually the existence of an optimum roughness to minimize wear has been hypothesized [93].

2.3.1 Equilibrium roughness

A feature that has been found to be shared by manufactured surfaces, is that, after running-in, a steady-state roughness is reached. As it will be shown below, different ways of characterizing the roughness of a surface are available and used, thus also the observed steady-state roughness depends on the method adopted. Rabinowicz [36, 83] refers to the peak-to-trough roughness (i.e. the maximum difference in heights along the surface), and argues that such measure of the roughness must have the same size of the typical wear particle that is removed from the surface during the wear process. Kragelsky et al. [37] show measures of the average roughness in wear

Chapter 2. State of the art

experiments where an equilibrium value is reached independently of the initial roughness. They provide an explanation which is similar to the one of Queener [75] (see Section 2.2.1), that is the plastic component of the deformation at the contact interface is reduced during running-in, and the elastic component is increased. During the steady state, the wear rate is thus minimum (additionally they observe that friction and temperature are also lowest during the steady state).

Similarly, in geophysics it has been shown that the scale-dependent roughness (characterized here in terms of the average heights of the surface) of faults scales consistently with the yield strength of the faults themselves [31, 34]. The rationale is that the aspect ratio of the asperities is linked to the maximum strength of the material [31], i.e. the fault profile cannot display asperities that cannot sustain the shear deformation during the sliding process – they must be destroyed in the process as soon as they appear. The well-known scaling of the surface heights for faults gives then a prediction for the scaling of the fault strength. Indentation experiments on rocks at the nanoscale to determine the strength scaling are consistent with the prediction [34]. Furthermore, the roughness scaling has been shown to change at a given length scale, consistently with the fact that different deformation mechanisms (ductile or brittle) prevail at different scales [29]. The strength of the material seems thus a parameter that determines the equilibrium surface profile in the case of geological faults.

2.3.2 Self-affine surfaces

Another feature that is repeatedly observed in surfaces that are subject to wear is that their morphology is *fractal* [27, 38–40]. Fractals are objects that are identical at different observation scales [94]. In the case of surfaces, this means that if one is presented with two different magnifications of the same surface, they cannot tell at which scale each magnification corresponds, nor deduce which scale is larger/smaller (see Figure 2.2). The two magnifications are not identical, i.e. they do not overlap, but they are statistically equivalent and they are called *random* (or *statistical*) *fractals*. The most popular example of such surfaces are geographical lines, such as border and coastlines, which were the first fractal profiles investigated in the notable work of Mandelbrot [95]. More specifically, surfaces are usually found to be *self-affine*, that is they are identical at different observation scales if the magnification is anisotropic, i.e. it is not the same along the axes of the average plane and along the elevation axis.

2.3. Surface morphology

For a one-dimensional profile, such self-affine scaling is expressed as [94, 96]

$$h(\xi x) \sim \xi^H h(x), \quad (2.6)$$

where $h(x)$ is the function describing the heights of the profile, x is the spatial coordinate, ξ is a scaling factor, and H is the Hurst (or roughness) exponent [96, 97], which for physical surfaces is usually found to be in the interval $[0, 1]$. H governs the anisotropy, and if $H = 1$, the scaling is isotropic and the profile is then said to be *self-similar*. H also affects the appearance of the surface (see Figure 2.3), as it relates two consecutive increments $\Delta h(x)$. If $H < 0.5$, the motion that describes the profile is anti-persistent (two increments are more likely to have opposite sign), and the profile appears rougher. If $H > 0.5$, the motion is persistent (two increments are more likely to have the same sign), and the profile appears smoother. If $H = 0.5$ the standard Brownian motion (random walk) is recovered.

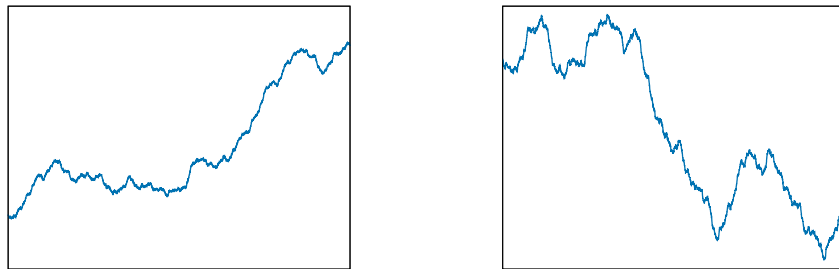


Figure 2.2 – Example of fractal profiles. One of the two pictures is the magnification of the other. Can the reader guess which is which? Solution in the caption of Figure 2.3.

An example of a mathematical function that generates a fractal profile is the Weierstrass-Mandelbrot function [98] (see Figure 2.3)

$$W(x) = \sum_{n=-\infty}^{\infty} \frac{1 - \exp(i\gamma^n x)}{\gamma^{(2-D)n}} \exp(i\phi_n), \quad (2.7)$$

where $1 < D < 2$ is the fractal dimension of the graphs of $\text{Re}W(x)$ and $\text{Im}W(x)$, ϕ_n are arbitrary phases, and $\gamma > 1$ is a parameter that defines the frequencies γ^n of the Weierstrass spectrum. On the other hand, a sinusoidal profile, for instance, is not fractal (see Figure 2.3). The Weierstrass-Mandelbrot function of Eq. 2.7 has the properties of being everywhere continuous, and nowhere derivable. The fractal dimension D in Eq. 2.7 is linked with the Hurst exponent H as $D = 2 - H$.

Real surfaces have a limited range of scales over which they are self-affine: the widest range theoretically possible is identified by the interatomic distance (smallest scale) and by the surface length (largest scale). This is not always the case, as mechanical and chemical properties of the material can alter the scaling, as aforementioned for geological faults [29]. Nonetheless, since Mandelbrot first observations, several surfaces in several conditions have been found to be self-affine [27, 38–41, 44]. In the case of frictional surfaces, such as in geological faults, the scaling is characterized by a persistent Hurst exponent [26, 28, 31, 34], the rationale behind it being the scaling of the material strength [31, 34].

2.3.3 Surface characterization

When it comes to surface characterization, different parameters are available. In the following, the main ones are addressed, considering a one-dimensional profile – extensions to two-dimensional surfaces are possible [99]. First of all, it is usually assumed that a surface is described by a single-valued continuous function $h(x)$, x being the spatial coordinate, over an interval of length L : this implies that no discontinuities or overhangs are present. This of course is a simplification for a real surface, but one that allows to treat it mathematically.

When treating the surface numerically or recording surface data experimentally, one knows a discretized representation of $h(x)$, i.e. the discrete set of N points (x_k, h_k) ($k = 0, 1, \dots, N - 1$) in which the surface is discretized at an interval Δx (here assumed to be constant). $h_k = h(k\Delta x)$ give then the known values of $h(x)$.

In the following, both the continuous and discrete expressions of the most common parameters adopted to characterize a surface are reported (the quantities referring to the discretized surface are distinguished by a tilde accent). It is assumed that the profile $h(x)$ is defined with respect to the center line (mean height) of the surface.

The simplest one is the *peak-to-trough roughness* r_v

$$\begin{aligned} r_v &= \max(h(x)) - \min(h(x)) \\ \tilde{r}_v &= \max(h_k) - \min(h_k) \end{aligned} \quad (2.8)$$

which just provides information on the distance between the highest and lowest points in the profile.

The *central line average roughness* r_a takes into account all the points of the profile:

$$\begin{aligned} r_a &= \frac{1}{L} \int_0^L |h(x)| dx \\ \tilde{r}_a &= \frac{1}{N} \sum_k |h_k| \end{aligned} \quad (2.9)$$

Similar to r_a , but statistically more meaningful, is the *root mean square of the heights* σ

$$\begin{aligned} \sigma &= \sqrt{\frac{1}{L} \int_0^L h(x)^2 dx} \\ \tilde{\sigma} &= \sqrt{\frac{1}{N} \sum_k h_k^2} \end{aligned} \quad (2.10)$$

While both r_a and σ give an indication on the average height of the profile, they do not provide with information about the profile shape or the correlation of the heights along x . For example, two sinusoidal profiles with same amplitude and different frequencies cannot be distinguished with any of the roughness parameters above. The *skewness* r_{sk} and the *Kurtosis* index r_K give instead some insights about the shape of the profile:

$$\begin{aligned} r_{sk} &= \frac{1}{\sigma^3 L} \int_0^L h(x)^3 dx \\ \tilde{r}_{sk} &= \frac{1}{N} \sum_k \left(\frac{h_k}{\tilde{\sigma}} \right)^3 \\ r_K &= \frac{1}{\sigma^4 L} \int_0^L h(x)^4 dx \\ \tilde{r}_K &= \frac{1}{N} \sum_k \left(\frac{h_k}{\tilde{\sigma}} \right)^4 \end{aligned} \quad (2.11)$$

The skewness r_{sk} is an indicator of the asymmetry of the profile, positive values meaning that the profile is characterized by few short valleys and many long peaks (vice versa for negative values). The Kurtosis index provides indication on the sharpness of the peaks, $r_K > 3$ meaning that the asperities are sharp (vice versa for values smaller than 3 the summits are blunt).

All the aforementioned measurements depend on the surface size or on the surface spacing, and they do not provide much information on the statistics of the surface, for instance about its self-affinity. For this, other functions are used, such as the

Chapter 2. State of the art

structure function and the *power spectral density* (PSD) of the surface per unit length.

The structure function $\Delta h(\delta x)$ of order p (where p is a positive integer) has the expression

$$\Delta h(\delta x) = \langle [h(x + \delta x) - h(x)]^p \rangle^{1/p}, \quad (2.12)$$

where δx is the horizontal distance between two points whose change in heights is Δh , and the angled brackets mean that the spatial average is taken. The structure function is thus an indicator of the correlation of the heights along x , and when $p = 2$, one speaks of *height-height correlation function*. For a self-affine surface, the structure function scales as $\Delta h(\delta x) \sim \delta x^H$ and it is thus possible to determine the Hurst exponent H with such mathematical description of the surface.

While the structure function contains information based on the spatial distances, the power spectral density per unit length $\Phi_h(q)$ contains information in terms of wavelengths (or frequencies) that characterize the surface:

$$\Phi_h(q) = \frac{1}{L} \left| \int_L h(x) e^{-iqx} dx \right|^2, \quad (2.13)$$

where q is the wavevector and the integral is the continuous Fourier transform of the profile $h(x)$. More details, such as how to compute it from a discrete data set, are provided in Chapter 4. Here, it suffices to say that the PSD scales as $\Phi_h(q) \sim q^{-(2H+1)}$ and thus the Hurst exponent for a self-affine surface can be derived.

The zeroth, second, and fourth moments of $\Phi_h(q)$ give the squares of respectively the root mean square of heights, slopes, and curvature of the profile:

$$\begin{aligned} \sigma^2 &= \langle h^2(x) \rangle = \int_{q_l}^{q_h} \Phi_h(q) dq \\ (\sigma')^2 &= \left\langle \left(\frac{dh(x)}{dx} \right)^2 \right\rangle = \int_{q_l}^{q_h} q^2 \Phi_h(q) dq, \\ (\sigma'')^2 &= \left\langle \left(\frac{d^2h(x)}{dx^2} \right)^2 \right\rangle = \int_{q_l}^{q_h} q^4 \Phi_h(q) dq \end{aligned} \quad (2.14)$$

where q_l and q_h are the lowest and highest wavevector, respectively. For a large

enough sample it can be assumed that $q_l \gg q_h$, and that the moments scale as [39]

$$\begin{aligned}\sigma^2 &\sim q_l^{-2H} \\ (\sigma')^2 &\sim q_h^{-2(1-H)} \\ (\sigma'')^2 &\sim q_h^{2(2-H)}\end{aligned}\tag{2.15}$$

Eqs. 2.15 show how the minimum and maximum length scales represented in the sample surface affect these parameters. Taking as example the root mean square of heights σ , it mostly contains information at the largest scale – and if a longer profile is sampled from the same experimental surface, the value of σ will increase rapidly. Vice versa, σ' and σ'' will change rapidly if another sample from the same surface is recorded with an instrument providing a different resolution. This shows how such kind of parameters are insufficient to unambiguously characterize a surface from a statistical perspective. The measurement of a parameter such as the Hurst exponent H is thus more relevant when comparing surfaces at different scales or from different processes, e.g. numerically investigated surfaces and geological faults.

2.3.4 Surface growth concepts

Investigations of random rough surfaces go beyond the realm of tribology, and experiments and models have been developed to study the dynamics and the morphology of phenomena such as crack fronts, bacteria colonies growth, atom deposition, and many others [44, 94].

In particular, discrete numerical models and analytical methods have been useful in the quest to reduce the problem at hand to its most meaningful components. The simplest growth model one can think of is the *random deposition* (RD) model. In it, a particle is dropped at a randomly chosen site i of an interface of length L , whose sites are empty at the beginning of the simulation. By applying such move multiple times, the interface grows, i.e. the heights of the sites overall increases. If one indicates the surface heights as $h(i, t)$, where $i = 1, \dots, L$ are the discrete sites and $t = N/L$ is the current time (with N the number of dropped particles until that moment), the algorithm is pretty simple. The only move corresponds to $h(i, t + 1/L) = h(i, t) + 1$ (i being randomly chosen from a uniform distribution), and $h(j, t + 1/L) = h(j, t)$ for all the sites $j \neq i$. It is intuitive to see that the height of each site is independent of the height of the other sites, no matter how close they are and the timestep t . The interface is thus uncorrelated.

One can measure the width of the interface, in terms of its root mean square of heights σ , and find that it scales as $\sigma(L, t) \sim t^\beta$, where $\beta = 1/2$ is the *growth exponent*. This exponent defines how the interface roughens as a function of the simulation time, i.e. of the number of deposited particles. It thus characterizes the dynamics of the roughening.

Yet, the heights of a surface are usually spatially correlated, as in the case of a profile defined by the Weierstrass-Mandelbrot function (Eq. 2.7) and of self-affine surfaces in general, for instance. One can then introduce a second move in the RD model. Once the particle is deposited at the site i , the algorithm checks for all the heights of the sites in the range $i \pm \Delta l$ and moves the particle to the lowest site among the $\Delta l + 1$ ones (if more than one site have the same lowest height, the final site is chosen randomly). Family [100] showed that the scaling of the interface width is independent from Δl , and $\Delta l = 1$ is usually chosen. The additional move diffuses the particle and, equivalently, relaxes the surfaces, so the model is called *random deposition with surface relaxation*.

The diffusion introduces the spatial correlation along the sites, as at each timestep the height of one site depends on all the heights of the neighbouring Δl sites. The interface then grows as $\sigma(L, t) \sim t^{1/4}$, but not indefinitely: the spatial correlation in fact limits the value of σ to the *saturation width* σ_{sat} . This parameter follows another well-defined scaling: $\sigma_{\text{sat}}(L) \sim L^H$, where H is the Hurst exponent introduced in Section 2.3.2, and $H = 1/2$ for the random deposition model with surface relaxation. Note that the scaling of σ_{sat} is consistent with the scaling of σ in Eqs. 2.15, noticing that $q_l \sim 1/L$, and the interface $h(L, t)$ is indeed self-affine at saturation.

The fact that the growth $\sigma(L, t) \sim t^{1/4}$ is capped by the saturation width $\sigma_{\text{sat}}(L)$ implies that a transition takes place from the roughening regime governed by the growth exponent to the steady-state saturated conditions. The time at which the transition occurs is called *crossover time* t_\times and it scales with the surface length as $t_\times \sim L^z$, z being the *dynamic exponent*. The growth regime thus holds for $t \ll t_\times$ and the steady-state regime for $t \gg t_\times$. The three exponents β , H , and z are not independent, and it is $z = H/\beta$. For the random deposition model with surface relaxation is thus $z = 2$. Furthermore, each set of exponents (β, H, z) identifies a *universality class*, that completely defines the statistics of the interface growth, without the need of investigating the details of the process. This means that interfaces that emerge because of different mechanisms (e.g. a crack profile and a directed polymer in a random medium) share the same statistical properties, and one problem can be used to gain insights on the other and vice versa [94].

2.3. Surface morphology

The aforementioned models, and most models available in the literature, are characterized by being symmetric, that is the surface grows only along the direction normal to the mean plane. In the case of frictional systems, the sliding direction breaks down such symmetry, and the surface may grow at an angle with the mean plane. A theoretical model based on a diffusion model of the RD type has been developed to investigate wear processes [101], and the Hurst exponent $H = 0.5$ is recovered. This is not the experimentally observed value of H , which is typically larger than 0.5. The lack of effects due to the aforementioned asymmetry in the growth model might be a reason why a persistent exponent is not recovered. Nevertheless, efforts like this will hopefully lead to the development of simplified geometrical models that reproduce the evolution of an interface into the self-affine morphology commonly observed in tribo-systems. As in the case of crack propagation, molecular beam epitaxy, and other processes, the simplified nature of these models would eventually lead to a better understanding of the underlying mechanisms in wear. Within this scope, a model is developed and tested in the Appendix of this dissertation.

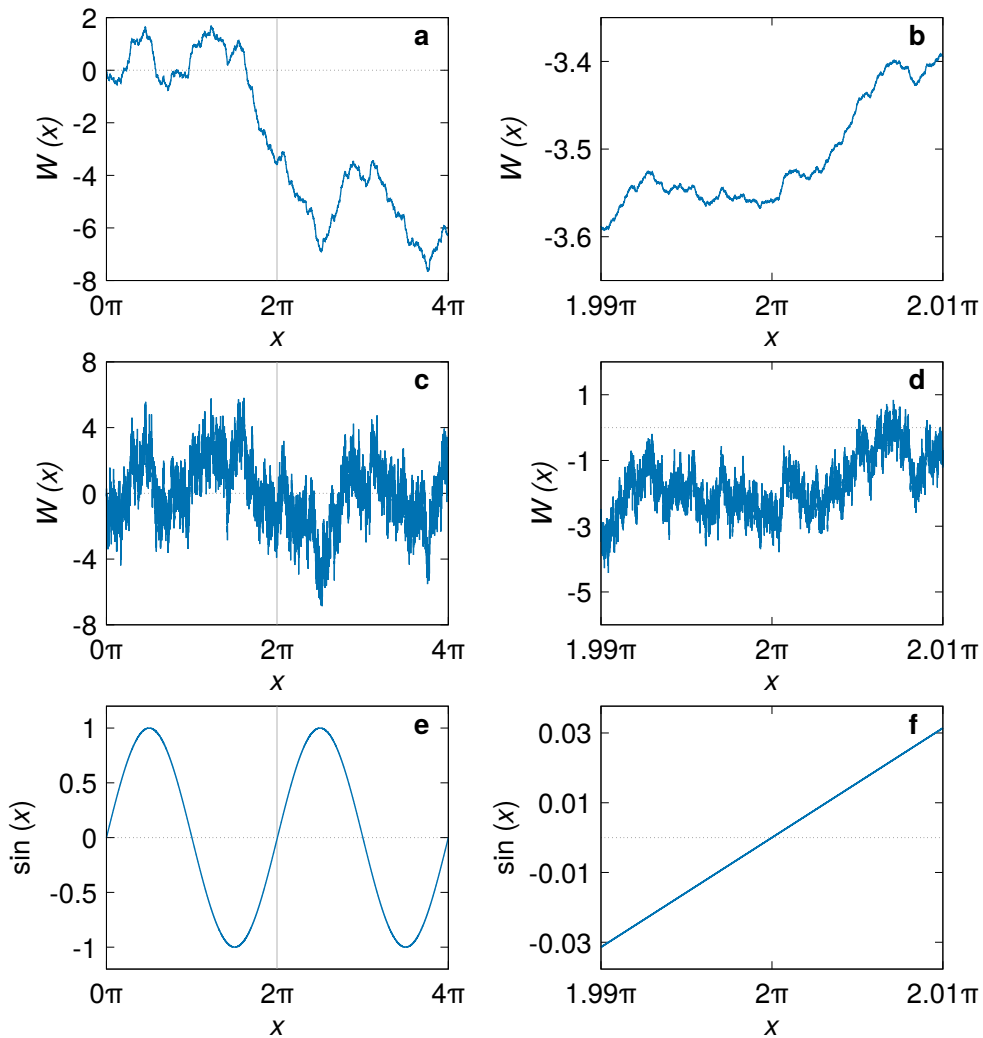


Figure 2.3 – Comparison between fractal profiles and a non-fractal one. $\text{Re}W(x)$ with $D = 1.2$ (see Eq. 2.7) in the intervals $0 \leq x \leq 4\pi$ (a) and $1.99\pi \leq x \leq 2.01\pi$ (b). $\text{Re}W(x)$ with $D = 1.8$ (see Eq. 2.7) in the intervals $0 \leq x \leq 4\pi$ (c) and $1.99\pi \leq x \leq 2.01\pi$ (d). The sinus function in the intervals $0 \leq x \leq 4\pi$ (e) and $1.99\pi \leq x \leq 2.01\pi$ (f). A magnification of $\text{Re}W(x)$ (b, d) leads to a surface that is statistically equivalent to the one at the upper scale (a, c), which is not the case for a sinusoidal wave (e, f). The real part of the Weierstrass-Mandelbrot function has been obtained from Eq. 2.7, with parameters $\gamma = 1.5$, and random phases $0 \leq \Phi_n < 2\pi$ drawn from a uniform distribution. The values for D corresponds to $H = 0.8$ (a, b) and $H = 0.2$ (c,d), that is persistent and anti-persistent motion, respectively. 10 000 sample points are chosen for all panels. Grey shaded area in panels (a, b) show the magnified portion reported in panels (c, d) respectively. Dotted lines in panels (a, c, e, f) represent the zero heights coordinate.

Chapter 3

Numerical framework

Many problems in solid mechanics have exact analytical solutions: all engineers should be familiar with the theories of Love and Timoshenko to name some of the most brilliant minds that influence the field still today. Most of the approaches of this kind rely on the assumption of linear elastic behaviour of the material, which is often key to derive an analytical solution. Non-linearities in the material response though make mechanical fields history-dependent and/or the solution not unique. Complexities in the geometrical configuration (e.g. due to contact, fracture, system size), irreversible processes (e.g. wear, corrosion), and the additional presence of liquid or gaseous phases are other examples of challenging problems that are often encountered in engineering applications. Hence, the need for numerical modelling in engineering. Numerical methods can be divided into two main categories according to their approach in modelling the material: continuum and discrete methods. Both are extensively used in tribology and here I provide an overview of the two approaches and of their main applications to the investigations of wear. Discrete methods are shown to be best suitable for the aim of modelling third-body dynamics, and the molecular dynamics approach is then presented. The constitutive laws later used in the dissertation are also introduced. A brief introduction to the discrete element method and its differences with molecular dynamics is also provided. Finally, the choice of the methodology used in this dissertation is explained.

3.1 Numerical methods in wear modelling

The approaches to numerical modelling are often split in two main categories: continuum and discrete models. The terminology reflects the assumption made about the geometry of the bodies that are analyzed. In continuum approaches, the assumptions are usually the same of the theory of elasticity: the geometry of the body is continuous, and no interpenetration or tearing of the material is possible.^a As a consequence, the mechanical quantities (e.g. displacements, deformations, and stresses) are continuous fields. The most popular continuum approaches are the finite element method [102, 103] and the boundary element method [104]. In discrete modelling instead, the material is represented with a set of discrete entities (points, spheres, etc.) and empty regions of space are present between them. Mechanical quantities as velocities and forces are then known only at each particle center of mass. The main discrete modeling techniques in mechanics are molecular dynamics [105] and the discrete element method [106]. Note that “discrete” and “continuum” refers to the geometry of the body and its consequences on the modeling of the physics of the system – continuum approaches still need to discretize the continuous fields for numerical reasons, and techniques are available to extrapolate continuous fields in discrete approaches. In terms of application, continuum modelling is often preferred at large scales, where the continuum approximation is reasonable, while discrete approaches are often the choice at the microscale, where modelling individual atoms or molecules is relevant. At the mesoscale, both methods have their application, depending on the problem.

In tribology, a wide range of numerical techniques are adopted and a full recount of them can be found in the review paper authored by the participants to the Lorentz workshop *Micro/ Nanoscale Models for Tribology* in Leiden, the Netherlands, in 2017 [107]. In brief, continuum approaches such as the finite element method and the boundary element methods have been extensively applied to the study of normal contact, including the case of rough surfaces [108–110], while molecular dynamics has been widely used to investigate both chemical and mechanical phenomena at the contact interface during sliding [57, 58, 111, 112].

When it comes to the numerical modeling of wear, continuum methods are tradi-

^aSome of these assumptions may seem to be relaxed in some cases, e.g. when crack propagation or contact are investigated. Some degree of interpenetration between two bodies is allowed in contact problems, but it is a numerical need. When fracture is modelled, new separate surfaces can be created with some methods – this is only local though and the region of space where this can occur is somehow forced before hand. In brief, such behaviours are not intrinsic to the modelling approach.

3.1. Numerical methods in wear modelling

tionally used from an engineering perspective, i.e. the objective of the investigations is to study the deterioration of the components of a frictional system. To this end, the macroscale contact between two bodies (e.g. pin on disc, wheel on a railroad) is modelled and the geometry of the components is updated assuming some wear law that relates the wear rate with some mechanical quantity available from the contact analysis. Often the assumed relation is Archard's wear law (see Eq. 2.2), where the wear rate depends on the normal load, and the profile of the components is thus updated on the basis of the local values of the pressures along the interface [113–115]. Other empirical laws can be assumed, e.g. based on the dissipated energy [116, 117]. Such approaches thus do not investigate the nature of the wear phenomenon in the system at hand, rather the implications of a specific, already existing, wear model. This has some rather non-negligible drawbacks from a physics perspective – mainly a macroscale empirical wear model is being applied outside its original scope, i.e. locally at the micro- or mesoscale – yet, at the moment it is still the only possible way to have ballpark estimations for engineering purposes. Different applications of continuum numerical methods can nevertheless lead to meaningful insights, e.g. when information available at a given scale is applied at an upper scale. For instance, in the quest for a mechanical interpretation of Archard's wear coefficient, the AWM critical length scale normally observed at the single asperity level [59] has been applied at the upper scale to the case of contact between rough surfaces by means of a boundary element approach [72]. Continuum modeling is useful also when investigating the onset of wear, that is the cracks that propagate in the asperities of opposing surfaces upon collision. For instance, crack nucleation for contacting asperities has been studied for both elastic and elasto-plastic contact of rough surfaces [110]. Crack propagation from geometrical singularities in the proximity of the contact junction has also been investigated. In this case, the damage process is modelled within the continuum method: numerous techniques are available for this, and a phase-field description of fracture in a finite element approach has been proven effective [118]. Such methodology is applied in Chapter 6, where more details are provided.

Discrete approaches have the advantage of naturally modelling detachment of material, and they are therefore often preferred when investigating the physics of wear. The most widely used methodology in this sense is molecular dynamics [105, 119], which allows to simulate the interaction between atoms, molecules, or small discrete aggregates of any of them. Thanks to this approach it is thus possible to observe, at small scales, phenomena such as the transfer of material from one body to the mating one [57, 120], or the formation of a third body from the collision of the two

surfaces [59, 73, 84, 85]. Similarly, the discrete element method [106, 121] models the interaction between particles at larger scales, and it has allowed for instance to capture the decohesion of particles in materials at the macro-scale (e.g. in rock mechanics) [122] and to investigate the wear rate when a third body develops [88, 89].

3.2 Atomistic simulations

By *atomistic simulations* is commonly meant a group of numerical techniques developed to model the behaviour of materials at the scale of the atoms. The atoms are thus individually modelled, as opposed to the continuum models mentioned in the introduction of this chapter and to other discrete methods.

3.2.1 Sampling

In the development of the atomistic approaches presented here^b, two main assumptions are made:

- for each atom, the motion of the nucleus and of the electrons can be treated separately, and the motion of the electrons can be averaged out (called Born-Oppenheimer approximation);
- following the Born-Oppenheimer approximation, and assuming that the nuclei are heavy enough, a classical description of the nuclei and their motion is valid.

Given their small dimension, the N nuclei of the system are then treated as separate mass points described by the set of their positions \mathbf{q} and momenta \mathbf{p} ,

$$\mathbf{q} = (\mathbf{q}_1, \mathbf{q}_2, \dots, \mathbf{q}_N) \quad (3.1)$$

$$\mathbf{p} = (\mathbf{p}_1, \mathbf{p}_2, \dots, \mathbf{p}_N), \quad (3.2)$$

where the vectors $\mathbf{q}_i = q_{i\alpha}$ and $\mathbf{p}_i = p_{i\alpha}$ contains the Cartesian components ($\alpha = x, y, z$ in 3D) of the momenta and of the positions (or *configurations*) of the i -th

^bThis section presents atomistic simulations in the fashion that I found easiest to digest, notably with a mixed approach between those of the textbook by Allen and Tildesley [119] and of the class by Ceriotti [123]. For the interested reader, another classical textbook in the field is the one by Frenkel and Smit [105].

particle. The particles are subject to the Hamiltonian

$$\mathcal{H}(\mathbf{p}, \mathbf{q}) = \mathcal{K}(\mathbf{p}) + \mathcal{V}(\mathbf{q}) = \sum_{i=1}^N \sum_{\alpha} \frac{p_{i\alpha}^2}{2m_i} + \mathcal{V}(\mathbf{q}) \quad (3.3)$$

where $\mathcal{K}(\mathbf{p})$ and $\mathcal{V}(\mathbf{q})$ are the kinetic and potential energy of the system, and m_i is the mass of the particle i . $\mathcal{V}(\mathbf{q})$ describes how particles interact with one another, and thus it is often referred to as the *interaction potential*. For the moment, it suffices to assume that $\mathcal{V}(\mathbf{q})$ is well-known and that it does not depend on time – some expressions will be provided in Section 3.2.4.

At any given instant, Equation 3.3 fully describes the mechanical state of the system, and we can define the phase space as the $6N$ -dimensional space with the generalized coordinates $\mathbf{x} = (\mathbf{p}, \mathbf{q})$. A point \mathbf{x} in the phase space then has $6N$ components and contains the information about the instantaneous values of \mathbf{p} and \mathbf{q} . We can now write some property of the system (e.g. the potential and kinetic energy) as a function $\mathcal{A}(\mathbf{x})$. We may then be interested in knowing the average $\langle \mathcal{A} \rangle_{\text{ens}}$ of such property over a set of points \mathbf{x} that have a probability distribution $\rho_{\text{ens}}(\mathbf{x})$. The set of points is called *ensemble*, and thus we speak of ensemble density $\rho_{\text{ens}}(\mathbf{x})$ and of ensemble average $\langle \mathcal{A} \rangle_{\text{ens}} = \sum_{\mathbf{q}_i} \mathcal{A}(\mathbf{x}) \rho_{\text{ens}}(\mathbf{x})$, which can be rewritten as [119]

$$\rho_{\text{ens}}(\mathbf{x}) = \frac{w_{\text{ens}}(\mathbf{x})}{Q_{\text{ens}}} \quad (3.4)$$

$$Q_{\text{ens}} = \sum_{\mathbf{q}_i} w_{\text{ens}}(\mathbf{x}) \quad (3.5)$$

$$\langle \mathcal{A} \rangle_{\text{ens}} = \frac{\sum_{\mathbf{q}_i} w_{\text{ens}}(\mathbf{x}) \mathcal{A}(\mathbf{x})}{\sum_{\mathbf{q}_i} w_{\text{ens}}(\mathbf{x})} \quad (3.6)$$

where $w_{\text{ens}}(\mathbf{x})$ is a non-normalized density and the partition function Q_{ens} ensures that the ensemble is thermodynamically consistent, as it is linked to some specific thermodynamic potential Ψ_{ens} by

$$\Psi_{\text{ens}} = -\ln Q_{\text{ens}}. \quad (3.7)$$

Ensembles are defined by the macroscopic thermodynamic properties chosen to be fixed. When such properties are the number of particles N , the volume V and the temperature T , the ensemble is called *canonical* (or *NVT*) ensemble; if the energy E is constant instead of the temperature, one has the *microcanonical* (or *NVE*) ensemble. While other ensembles are also possible, in the following we will restrain

Chapter 3. Numerical framework

our considerations to the canonical ensemble.

For the canonical ensemble is [119]

$$w_{NVT} = e^{-\beta \mathcal{H}(\mathbf{x})} \quad (3.8)$$

$$Q_{NVT} = \int e^{-\beta \mathcal{H}(\mathbf{x})} d\mathbf{x} \quad (3.9)$$

$$\Psi_{NVT} = \beta A = -\ln Q_{NVT} \quad (3.10)$$

where $A = U - TS$ is the Helmholtz free energy (with U the internal energy, S the entropy, and T the temperature of the system) and $\beta = 1/(k_B T)$ is the inverse temperature (with k_B the Boltzmann constant). In the canonical ensemble the energy can always be split into two contributions: the kinetic energy (function of the momenta \mathbf{p}) and the potential energy (function of the configurations \mathbf{q}). This allows to factor the partition function, and the ensemble density becomes

$$\rho_{NVT}(\mathbf{x}) = \rho_{NVT}(\mathbf{p}) \cdot \rho_{NVT}(\mathbf{q}) = \frac{e^{-\beta \mathcal{K}(\mathbf{p})}}{\int e^{-\beta \mathcal{K}(\mathbf{p})} d\mathbf{p}} \cdot \frac{e^{-\beta \mathcal{V}(\mathbf{q})}}{\int e^{-\beta \mathcal{V}(\mathbf{q})} d\mathbf{p}}. \quad (3.11)$$

As a consequence, ensemble averages can also be split in two contributions: the one dependent on the momenta (usually easy to estimate), and the one depending on the configuration, which is

$$\langle \mathcal{A} \rangle_{NVT} = \frac{\int \mathcal{A}(\mathbf{q}) e^{-\beta \mathcal{V}(\mathbf{q})} d\mathbf{q}}{\int e^{-\beta \mathcal{V}(\mathbf{q})} d\mathbf{q}}. \quad (3.12)$$

We now need a computational technique to compute $\langle \mathcal{A} \rangle_{NVT}$. As the number of evaluations rapidly explodes with any quadrature technique, a Monte Carlo method or a Molecular Dynamics approach are adopted.

3.2.2 Monte Carlo methods

In the basic Monte Carlo (MC) strategy, M random configurations \mathbf{q} are chosen and the ensemble average is approximated as

$$\langle \mathcal{A} \rangle_{NVT} = \frac{\sum_i \mathcal{A}(\mathbf{q}) e^{-\beta \mathcal{V}(\mathbf{q})}}{\sum_i e^{-\beta \mathcal{V}(\mathbf{q})}}. \quad (3.13)$$

While this works in principle, the ensemble density $\rho_{NVT}(\mathbf{q})$ can vary widely in the configuration space, and thus one would mostly sample regions of space that bring a negligible contribution to the estimation of the integral, and would not sample as many regions that bring a meaningful contribution. *Importance sampling* is thus a sampling technique developed to improve the efficiency of the estimation of $\langle \mathcal{A} \rangle_{NVT}$. The idea is to generate M configurations that are distributed as $\rho_{NVT}(\mathbf{q})$: this allows to sample more heavily the regions of space where the contribution to the integral is important, and avoid regions where it is negligible. The estimation of the ensemble average then becomes $\langle \mathcal{A} \rangle_{NVT} = \sum_i \mathcal{A}(\mathbf{q}) / M$ (the Boltzmann factor already included by the uneven sampling).

The M configurations are generated as a succession of transformations from a configuration \mathbf{q} to a configuration \mathbf{q}' . Each configuration thus depends only on the previous one. The transformation from one state to another is not deterministic, rather stochastic, i.e. the probability to move from \mathbf{q} to \mathbf{q}' is characterized by the distribution $p(\mathbf{q} \rightarrow \mathbf{q}')$. (In the general case, the move will involve also the momenta of the particles, and it is expressed thus as $p((\mathbf{p}, \mathbf{q}) \rightarrow (\mathbf{p}', \mathbf{q}'))$ or $p(\mathbf{x} \rightarrow \mathbf{x}')$). A necessary condition is that, at equilibrium, the canonical distribution is conserved when generating \mathbf{q}' (*weak balance*). The *detailed balance* (or *microscopic reversibility*) gives a sufficient condition instead, and it states that, at equilibrium, the acceptance of the trial move from \mathbf{q} to any other possible state \mathbf{q}' is the same of that from any possible \mathbf{q}' to \mathbf{q} .

The transition probability $p(\mathbf{q} \rightarrow \mathbf{q}')$ from a state \mathbf{q} to a state \mathbf{q}' can be split in two steps, such that $p(\mathbf{q} \rightarrow \mathbf{q}') = g(\mathbf{q} \rightarrow \mathbf{q}') \cdot a(\mathbf{q} \rightarrow \mathbf{q}')$, where

1. the generation probability $g(\mathbf{q} \rightarrow \mathbf{q}')$ gives the next trial configuration, and
2. the acceptance probability $a(\mathbf{q} \rightarrow \mathbf{q}')$ accepts/rejects the trial configuration.

A common approach to define $g(\mathbf{q} \rightarrow \mathbf{q}')$ and $a(\mathbf{q} \rightarrow \mathbf{q}')$ is the so-called Metropolis method [124]. In this technique, $g(\mathbf{q} \rightarrow \mathbf{q}')$ is symmetric, i.e. is chosen such that going from \mathbf{q} to \mathbf{q}' is as likely as going back from \mathbf{q}' to \mathbf{q} . The acceptance probability is

$$a(\mathbf{q} \rightarrow \mathbf{q}') = \min \left(1, \frac{\rho_{NVT}(\mathbf{q}')}{\rho_{NVT}(\mathbf{q})} \right) \quad (3.14)$$

where $\rho_{NVT}(\mathbf{q})$ and $\rho_{NVT}(\mathbf{q}')$ are the probabilities of observing the configurations \mathbf{q} and \mathbf{q}' , respectively, and Eq. 3.14 satisfies both the weak and detailed balance

Chapter 3. Numerical framework

conditions [119]. Looking at the expression for $\rho_{NVT}(\mathbf{q})$ in Eq. 3.11, one can notice that

$$\frac{\rho_{NVT}(\mathbf{q}')}{\rho_{NVT}(\mathbf{q})} = e^{-\beta(\mathcal{V}(\mathbf{q}') - \mathcal{V}(\mathbf{q}))} \quad (3.15)$$

and that the acceptance of Eq. 3.14 is based on a minimum energy criterion, where the minimized energy is the free energy. If the potential energy of the new configuration $\mathcal{V}(\mathbf{q}')$ is lower than the energy $\mathcal{V}(\mathbf{q})$ of the starting configuration, the move is always accepted ($e^{-\beta(\mathcal{V}(\mathbf{q}') - \mathcal{V}(\mathbf{q}))} > 1$), otherwise the move is accepted with a probability $e^{-\beta(\mathcal{V}(\mathbf{q}') - \mathcal{V}(\mathbf{q}))} < 1$. This inhibits the system to go to regions of space that have higher potential energy. The equilibrium might be a local one though, and the generation step $g(\mathbf{q} \rightarrow \mathbf{q}')$ is important in exploring a large region of space. For example, if $g(\mathbf{q} \rightarrow \mathbf{q}')$ favours new configurations \mathbf{q}' that are close to the starting one and the system is at a local minimum, then the acceptance of Eq. 3.14 will prevent the system to jump over some energy barrier and find any other minima unless a rare trial move is generated such that the trial configuration is far enough from the starting one. To avoid this, one may be tempted to create a generation step $g(\mathbf{q} \rightarrow \mathbf{q}')$ that has a high probability of generating trial moves that are far from the starting configuration. Yet, this increases the likelihood of atoms getting too close to one another or in any other higher energy configuration that would be always rejected by $a(\mathbf{q} \rightarrow \mathbf{q}')$. Some balance between the two approaches is thus needed. Another approach to explore regions of space that are far from the starting one is to set a high temperature. For large values of T , $\beta \rightarrow 0$, and $e^{-\beta(\mathcal{V}(\mathbf{q}') - \mathcal{V}(\mathbf{q}))} \rightarrow 1$: increases in the system potential energy are then much more likely to be accepted, as long as the difference $\mathcal{V}(\mathbf{q}') - \mathcal{V}(\mathbf{q})$ is finite.

3.2.3 Molecular dynamics

Molecular dynamics (MD) is another technique used to evolve the state of a system in a thermodynamically consistent ensemble. The rule to generate a new configuration is to satisfy the Hamiltonian form of the equations of motions:

$$\begin{aligned} \dot{\mathbf{q}} &= \frac{\partial \mathcal{H}}{\partial \mathbf{p}} = \frac{\partial \mathcal{K}}{\partial \mathbf{p}} = \frac{\mathbf{p}}{m} \\ \dot{\mathbf{p}} &= -\frac{\partial \mathcal{H}}{\partial \mathbf{q}} = -\frac{\partial \mathcal{V}}{\partial \mathbf{q}} = \mathbf{f} \end{aligned} \quad (3.16)$$

where $(\dot{\cdot})$ is the time derivative, the Hamiltonian $\mathcal{H}(\mathbf{p}, \mathbf{q})$ is given by Eq. 3.3, and the partial derivative of the potential energy $\mathcal{V}(\mathbf{q})$ results in the forces $f_{i\alpha}$ acting on the atom i and having the usual Cartesian components $\alpha = x, y, z$. One can see that Eqs. 3.16 are just a particular choice of $p((\mathbf{p}, \mathbf{q}) \rightarrow (\mathbf{p}', \mathbf{q}'))$, where the generation step is deterministic and the acceptance probability equals one. It can be shown that, while such choice of $p((\mathbf{p}, \mathbf{q}) \rightarrow (\mathbf{p}', \mathbf{q}'))$ does not satisfy the detailed balance, it does verify the necessary weak balance condition. Note that the map of Eqs. 3.16 introduces a time dependency in the evolution of the system. In the Monte Carlo approach previously described there is no concept of time: at each step the map draws a new configuration from all the possible configurations.

From Eqs. 3.16 one can derive that, under the assumption that \mathcal{V} and \mathcal{K} are not time-dependent, it is $\dot{\mathcal{H}} = 0$, that is the Hamiltonian is constant over time and the energy is conserved. Furthermore, Eqs. 3.16 are time reversible, i.e. if we are given the state $(\mathbf{p}', \mathbf{q}')$, we can go (back) to the state (\mathbf{p}, \mathbf{q}) just by reversing the sign of the momenta \mathbf{p}' .

We now need an algorithm to solve numerically the Hamiltonian equations 3.16, as they cannot be integrated analytically (except in some simple cases). Many methods have been developed, but one of the most common (and simple) ones is the velocity Verlet algorithm, which updates the momenta and the positions in three steps:

$$\begin{aligned}
 \mathbf{p}^{(t_0+\delta t/2)} &= \mathbf{p}^{(t_0)} - \left(\frac{\partial \mathcal{V}}{\partial \mathbf{q}}\right)^{(t_0)} \cdot \frac{\delta t}{2} \\
 \mathbf{q}^{(t_0+\delta t)} &= \mathbf{q}^{(t_0)} + \frac{\mathbf{p}^{(t_0+\delta t/2)}}{m} \cdot \delta t \\
 \mathbf{p}^{(t_0+\delta t)} &= \mathbf{p}^{(t_0+\delta t/2)} - \left(\frac{\partial \mathcal{V}}{\partial \mathbf{q}}\right)^{(t_0+\delta t)} \cdot \frac{\delta t}{2}
 \end{aligned} \tag{3.17}$$

where δt is the integration time step, $(\cdot)^{(t)}$ are quantities estimated at time t , and the starting configuration is given at time t_0 . Splitting the computation of \mathbf{p} in two allows to store only one value of the forces per time step. If the value of the forces computed at the previous time step was also stored, \mathbf{p} could be updated in one step. In practice, the algorithm is implemented in terms of positions \mathbf{q} , velocities \mathbf{v} , and

Chapter 3. Numerical framework

forces \mathbf{f} (or accelerations $\mathbf{a} = \mathbf{f}/m$, in alternative to forces):

$$\begin{aligned}
 \mathbf{v}^{(t_0+\delta t/2)} &= \mathbf{v}^{(t_0)} + \frac{\delta t}{2} \frac{\mathbf{f}^{(t_0)}}{m} \\
 \mathbf{q}^{(t_0+\delta t)} &= \mathbf{q}^{(t_0)} + \delta t \mathbf{v}^{(t_0+\delta t/2)} + \frac{\delta t^2}{2} \frac{\mathbf{f}^{(t_0)}}{m} \\
 \mathbf{f}^{(t_0+\delta t)} &= -\left(\frac{\partial \mathcal{V}}{\partial \mathbf{q}}\right)^{(t_0+\delta t)} \\
 \mathbf{v}^{(t_0+\delta t)} &= \mathbf{v}^{(t_0+\delta t/2)} + \frac{\delta t}{2} \frac{\mathbf{f}^{(t_0+\delta t)}}{m}
 \end{aligned} \tag{3.18}$$

Like the map of Eqs. 3.16, the algorithm is time-reversible, but it does not conserve the energy and the Hamiltonian \mathcal{H} actually drifts away from the initial value with δt^2 . This is due to the use of a finite integration step δt . If δt is sufficiently small, the drift is slowed down and it can be assumed that \mathcal{H} is on average constant during the simulation. Note that local oscillations are anyway present and the assumption is that they cancel out. The velocity Verlet algorithm is the one implemented in LAMMPS [125], the MD simulator used for the simulations of Chapters 4 and 5.

The molecular dynamics technique of Eqs. 3.16 (and in a first approximation the velocity Verlet integrator if δt is small enough) conserves the energy and satisfies the weak balance condition – that is, it samples the microcanonical (NVE) ensemble. If we want to sample the canonical (NVT) ensemble (as in the description of the Monte Carlo methods), the Hamiltonian equations need to be modified. This is possible by applying *thermostats* to the system. Several thermostats have been developed over the years, and the most used are probably the Andersen, the Nosé-Hoover, and the Langevin thermostats [119]. In the simulations of Chapters 4 and 5, the latter is adopted. The Langevin thermostat, considering a one-dimensional system for simplicity, modifies the Hamiltonian equations 3.16 into

$$\dot{q}_i = \frac{p_i}{m_i} \tag{3.19}$$

$$\dot{p}_i = -\frac{\partial \mathcal{V}}{\partial q_i} - \eta p_i + \sqrt{\frac{2m_i \eta}{\beta}} \cdot \xi \tag{3.20}$$

where η is a friction term (if it vanishes, Eqs. 3.16 are recovered) and ξ is some noise term that is uncorrelated in time. Looking at the second equation one can see that the thermostat draws energy from the system in a quantity that is proportional to the momenta (second term at the RHS) and at the same time injects energy into the system (third term at the RHS). If we suppose the system to be at zero temperature

locally ($p_i = 0 \forall i$) and the target temperature to be larger than zero, then the third term prevails over the second term: momenta (and energy) grow and the system is heated up. Vice versa if the system is at a much larger temperature than the target one, the second term prevails: energy is mostly drawn from the system, which cools down. It can be shown that at equilibrium the configurations (\mathbf{p}, \mathbf{q}) are canonically distributed, and indeed a thermostat must modify the Hamiltonian Eqs. 3.16 without altering the ensemble distribution (or we end up sampling something else).

3.2.4 Potential energy

So far we have left the expression of the potential energy $\mathcal{V}(\mathbf{q})$ implicit. In our system with N particles, a general expression for $\mathcal{V}(\mathbf{q})$ is given by

$$\mathcal{V}(\mathbf{q}) = \sum_{i=1}^N v_1(\mathbf{q}_i) + \sum_{i=1}^N \sum_{j>i}^N v_2(\mathbf{q}_i, \mathbf{q}_j) + \sum_{i=1}^N \sum_{j>i}^N \sum_{k>j}^N v_3(\mathbf{q}_i, \mathbf{q}_j, \mathbf{q}_k) + \dots \quad (3.21)$$

In Eq. 3.21 each term $v_1, v_2, v_3, \dots, v_N$ depends on the interactions within all the possible sets of one, two, three, \dots, N particles, and the conditions such as $j > i$ on the sums avoid counting twice the interaction between the same pair (or triplet, \dots) of particles. The term $\sum_{i=1}^N v_1(\mathbf{q})$ is representative of any external force acting on the particle i (for example, due to the repulsion when a rigid body moves against it). The other terms represent the atomistic interactions instead, each term taking into account for an increasing number of atoms involved in the interaction. $v_2(\mathbf{q}_i, \mathbf{q}_j)$ thus represents the contribution due to the interaction of all possible couples of atoms i and j , $v_3(\mathbf{q}_i, \mathbf{q}_j, \mathbf{q}_k)$ of all the triplets i, j, k , and so on. The most important of these terms is the pair potential $v_2(\mathbf{q}_i, \mathbf{q}_j)$. Indeed computing n -body potentials with $n \geq 3$ becomes rapidly resource consuming, and when acceptable some equivalent pair potential is adopted instead. We then leave out these contributions, and rewrite Eq. 3.21 as

$$\mathcal{V}(\mathbf{q}) = \sum_{i=1}^N v_1(\mathbf{q}) + \sum_{i=1}^N \sum_{j>i}^N v_2(q_{ij}) \quad (3.22)$$

where q_{ij} is the Euclidean distance between the particles i and j . As one wants Eq. 3.22 to be representative of the interaction between two atoms (or molecules, or small aggregates of them), $\mathcal{V}(\mathbf{q})$ needs to have an expression such that the particles i and j are repulsed when they are brought in close proximity and attract each other when they are pulled apart. $\mathcal{V}(\mathbf{q})$ will also have a global minimum of the energy

Chapter 3. Numerical framework

at the equilibrium distance and equilibrium coordination, and a reference energy (which equals zero in the present formalism) for when the particles are so far apart that their interaction is negligible.

The Lennard-Jones 12-6 $\mathcal{V}_{\text{LJ}}(\mathbf{q})$ [126] and the Morse $\mathcal{V}_{\text{M}}(\mathbf{q})$ [127] potentials both satisfy these conditions and are among the simplest and most used pair potentials. They are shown in Figure 3.1, and their expressions are

$$\begin{aligned}\mathcal{V}_{\text{LJ}}(q_{ij}) &= 4\varepsilon \left[\left(\frac{\sigma}{q_{ij}} \right)^{12} - \left(\frac{\sigma}{q_{ij}} \right)^6 \right] \\ \mathcal{V}_{\text{M}}(q_{ij}) &= \varepsilon \left[\left(1 - e^{-a(q_{ij}-q_0)} \right)^2 - 1 \right]\end{aligned}\tag{3.23}$$

where ε is the bond-energy at the equilibrium distance q_0 , $\sigma = q_0/2^{1/6}$ is the distance at which $\mathcal{V}_{\text{LJ}}(q_{ij}) = 0$, and a governs the width of the well and the bond stiffness (the larger a , the narrower the well and the stiffer the bond). The Lennard-Jones potential was proved to capture satisfactorily argon's properties [126], while the Morse potential in its original derivation addressed diatomic molecules [127]. Simple potentials like these are computationally efficient and allow to explore material behaviors from a general perspective, by observing the dynamics of the modelled particles [128]. In tribology, for instance, simulations with the Lennard-Jones potential led to a discussion on the validity of continuum theories at the atomistic scale [129].

Other examples of potentials shown in Figure 3.1 are the hard-sphere potential and the harmonic potentials, whose expressions are

$$\begin{aligned}\mathcal{V}_{\text{HS}}(q_{ij}) &= \begin{cases} \infty & \text{if } q_{ij} < q_0 \\ 0 & \text{if } q_{ij} \geq q_0 \end{cases} . \\ \mathcal{V}_{\text{H}}(q_{ij}) &= \frac{1}{2}K(q_{ij} - q_0)^2 - \varepsilon\end{aligned}\tag{3.24}$$

where K , similarly to a , governs the width of the well and the bond stiffness. The hard-sphere potential, as the name suggests, corresponds to the potential energy of two rigid spheres of radius q_0 , which interact only if they come into contact, in which case they bounce back. No attractive part exists. Because of the sharp discontinuity at $q_{ij} = q_0$ and the value of \mathcal{V}_{HS} going to infinity for $q_{ij} < q_0$, this potential is not treatable numerically and soft-sphere potentials are more suitable. The harmonic potential is continuous instead, but the energy diverges for positive values of q_{ij} , that is the attractive part is as strong as the repulsive part. It is therefore clearly not

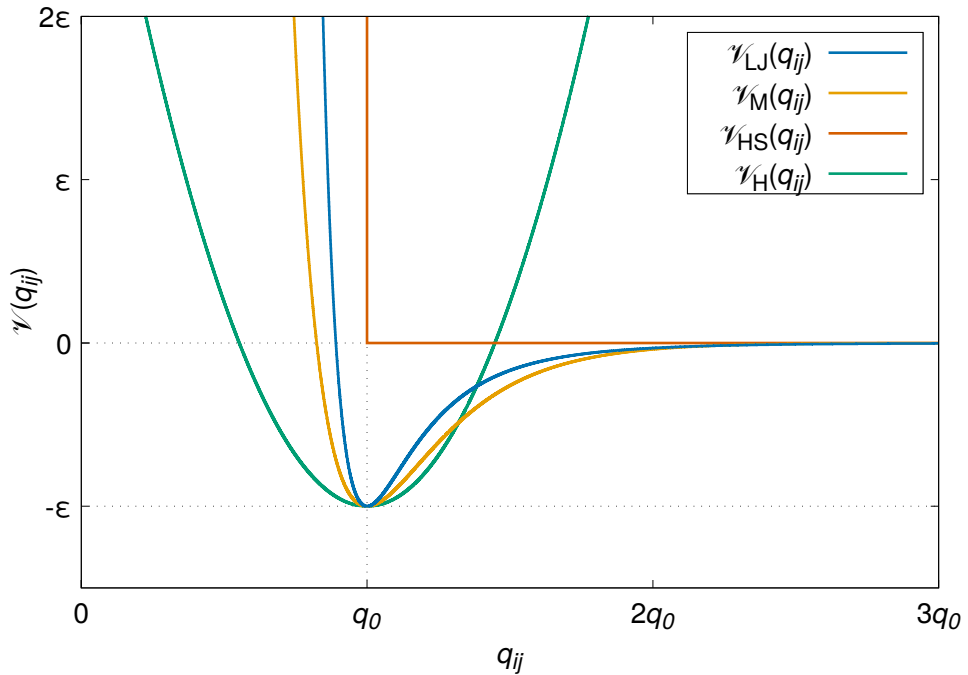


Figure 3.1 – Examples of interaction potentials. Both Lennard-Jones $\mathcal{V}_{LJ}(q_{ij})$ and Morse $\mathcal{V}_M(q_{ij})$ potentials have a strongly repulsive part for $q_{ij} < q_0$ and an attractive tail for $q_{ij} > q_0$ that goes to zero. The hard-sphere potential $\mathcal{V}_{HS}(q_{ij})$ displays diverging repulsive energy and a zero attractive energy part. The harmonic potential $\mathcal{V}_H(q_{ij})$ is symmetric with respect to q_0 and the repulsive and attractive forces have same magnitude. For the purpose of showing the qualitative behaviors of the potentials, parameters have been set to the values $a = 3.93/q_0$ and $K = 10/\epsilon$.

representative of the atomistic interaction that one is usually interested in. On the other hand, one can easily see that it corresponds to the potential energy of a spring of elastic constant K , and it is indeed used to model the normal contact stiffness in the discrete element method.

Considering now the Lennard-Jones and the Morse potentials, they share three features:

1. the energy goes to infinity for $q_{ij} \rightarrow 0$,
2. the energy has one stationary point, which is the minimum $-\epsilon$ at $q_{ij} = q_0$,

Chapter 3. Numerical framework

3. the energy goes to zero for $q_{ij} \rightarrow \infty$.

As the derivative of the potential is the force exerted by one atom on the other (cf. Eq. 3.16), it means that:

1. the force is negative (repulsive) and goes to infinity for $q_{ij} \rightarrow 0$,
2. the force is zero at $q_{ij} = q_0$ (and the particles are at equilibrium),
3. the force is positive (attractive) for $q_{ij} > q_0$ and goes to zero for $q_{ij} \rightarrow \infty$.

In principle, one needs to take into account of all the interactions that each atom i has with all the other atoms j in the system (cf. Eqs. 3.22 and 3.18). This becomes rapidly expensive computationally, as it scales as N^2 , and a wise approach is to introduce a cut-off length $q_{\text{cut}} > q_0$ such that the potential equals zero for all q_{ij} larger than q_{cut} . This allows to reduce significantly the computational time, which can scale as low as N , while discarding contributions that are negligible (it is a reasonable assumption that atoms far apart do not interact in a meaningful fashion).

Figure 3.2 represents another family of pair potentials. These potentials are a modified version of the Morse potential, and their expression is [59]:

$$\mathcal{V}_{\text{AWM}}(q_{ij}) = \begin{cases} \varepsilon \left[\left(1 - e^{-a(q_{ij}-q_0)} \right)^2 - 1 \right] & q_{ij} < 1.1q_0 \\ c_1 \frac{q_{ij}^3}{6} + c_2 \frac{q_{ij}^2}{2} + c_3 q_{ij} + c_4 & 1.1q_0 \leq q_{ij} \leq q_{\text{cut}} \\ 0 & q_{\text{cut}} \leq q_{ij} \end{cases} \quad (3.25)$$

where the c_i coefficients need only to satisfy the condition that both the potential and its first derivative are continuous. These potentials were first presented in the work of Aghababaei, Warner, and Molinari [59], where they played a key role in the possibility of observing the AWM critical length scale (see 2.2.2). They are also the potentials used for the simulations of Chapters 4 and 5. For these pair potentials, different values of the cut-off distance q_{cut} allow to tune the inelastic behaviour, making the model material more or less ductile/brittle. The potentials share the same properties up to 10 % of the bond stretch ($1.1q_0$), that is they share the same elastic properties and surface energy γ_{srf} , as they depend on the equilibrium distance q_0 . Changes in the cut-off distance q_{cut} affect the unstable stacking fault energy γ_{usf} , which gives an estimate of the energy required for two parallel planes of atoms to slip over one another. In Figure 3.2, the potential P1 has the largest cut-off and the

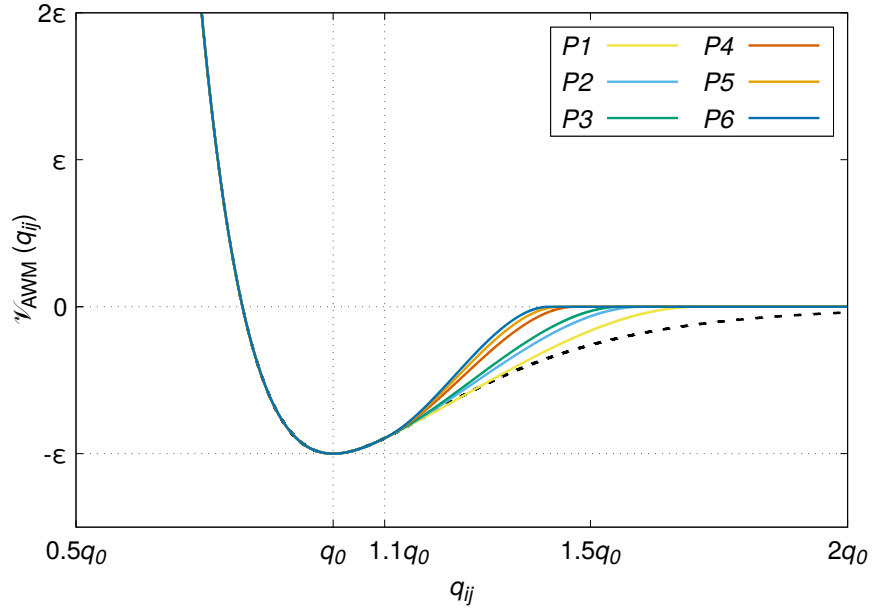


Figure 3.2 – Family of interaction potentials adopted in the simulations of Chapters 4 and 5 [59]. The potentials share the same repulsive behavior and the same elastic behavior up to 10% of bond stretch (cf. Eq. 3.25). Each potential of the family is characterized by a different cut-off distance q_{cut} . This alters the ductility of the potential: the larger q_{cut} , the more ductile the behavior (dislocations are favored over brittle separation of surfaces). The black dotted line represents the Morse potential $\mathcal{V}_M(q_{ij})$, from which $\mathcal{V}_{\text{AWM}}(q_{ij})$ is derived: the potentials differ for their tail, which is smoother for the Morse potential – $\mathcal{V}_M(q_{ij})$ is more ductile and does not allow to observe the AWM critical length scale within the system sizes explored in that work [59].

lowest unstable stacking fault energy, and vice versa P6 has the smallest cut-off and the highest γ_{usf} . Lower values of γ_{usf} are representative of higher ductility (for a given γ_{srf}), as it is easier for dislocations to propagate. The family of potentials $\mathcal{V}_{\text{AWM}}(q_{ij})$ then allow to model materials that are more or less ductile, and eventually observe the ductile-to-brittle transition in adhesive wear [59]. The differences in ductility are also reflected by the values of the hardness of systems with different potentials, P1 being the softest potential and P6 the hardest [59].

3.3 Discrete element method

Another method that models materials as a set of discrete particles is the discrete element method (originally called distinct element method, in any case: DEM), and it is here briefly presented following mostly the original formulation by Cundall [106].

3.3.1 Formulation

The assumptions of this method are that

- the particles can have any size and shape (in practice, discs in 2D and spheres in 3D are often adopted),
- the particles have six degrees of freedom (four in 2D), i.e. they are allowed to both translate and rotate,
- the deformation of each particle is finite but negligible when compared to the deformation of the assembly,
- only pair-wise interactions take place, and such interactions are known,
- the particles obey Newton's second law (i.e. Hamilton's second equation of motion, cf. Eq. 3.16).

The first two assumptions come from the original scale of application of the method – the meso-scale. The method was in fact first developed in the 1970s to investigate granular assemblies in rock mechanics [106].

The system then evolves following Newton's second law applied to the translational and rotational degrees of freedom,

$$\begin{aligned} m_i \ddot{\mathbf{q}}_i &= \mathbf{f}_i \\ I_i \dot{\boldsymbol{\omega}}_i &= \mathbf{t}_i \end{aligned} \quad (3.26)$$

where $\ddot{(\cdot)}$ is the second time derivative, I_i , $\boldsymbol{\omega}$, and \mathbf{t}_i are the particle moment of inertia, angular velocity and torque, respectively. Several constitutive laws can be applied to derive the forces \mathbf{f}_i and torques \mathbf{t}_i that arise from contact between two particles. Both the normal and tangential components of \mathbf{f}_i depend on the direction and magnitude of the velocity of the pair of particles that are interacting. Torques arise

from the tangential forces, whose laws need to take into account friction, rolling resistance, and torsion resistance [121]. Both normal and tangential forces laws include dissipative terms, and additional global (background) dissipative terms are added to the interaction forces and torques acting on each particle. Numerically, Verlet algorithms are traditionally used to evolve the system. One can then see that if the particles interact elastically, in the limit of frictionless particles and no damping, the method is equivalent to a molecular dynamics approach with the repulsive part of an harmonic potential.

3.3.2 Comparison between DEM and MD

Both methods simulate the material in a discrete fashion, and one may argue that the core idea is the same: having a set of particles that evolve following the equations of motion. While this is true, differences between the two methods exist and are significant.

MD, in its theoretical formulation, has strong thermodynamics basis that allow to sample specific ensembles ensuring a thermodynamic equilibrium. The whole MD derivation reported above lies on the assumption that the force fields acting on the particles depend only on the position of the particles themselves, which leads to the conservation of the Hamiltonian. In contrast, in DEM a static equilibrium is looked for, i.e. the aim is to model a system where its components are at rest for a sufficiently long experiment (e.g. sand grains dropped to form a pile). To this end, damping terms need to be introduced to dissipate kinetic energy [106] (they can be justified with physical bases [121]), and the Hamiltonian is not conserved. This has also important implications in the formulation of the method, as DEM potentials are velocity-dependent.

Numerically, while the two approaches have similar implementations (both use algorithms of the Verlet family), more data need to be stored in DEM because of the larger number of degrees of freedom and of the dependence on the velocity of the interactions.

Furthermore, DEM constitutive laws for forces and torques easily involve a large number of parameters (elastic/ friction/ rolling/ torsion stiffness, elastic/ friction/ rolling/ viscosity, etc. [121]), which are poorly understood physically and which need to be somehow fitted. Nonetheless, it should be possible to capture fundamental phenomena such as the ductile-to-brittle transition observed in adhesive wear with

Chapter 3. Numerical framework

a DEM approach, too, as the adhesive behaviour of particles can be modelled [130]. MD potentials can also be complicated and computationally expensive, yet the simplest ones (e.g. the Lennard-Jones and Morse potentials) already allow to investigate relevant fundamental physical phenomena [59, 128]. DEM is then expected to be a precious resource in the extension of the investigations of such phenomena to a larger scale and to constitutive behaviours representative of particular materials (such as rocks).

DEM indeed allows to model macro-scale assemblies, which is just not feasible for MD. Germann and Kai in 2008 [60] performed one of the largest MD simulations, modelling 12 trillion particles (with a simple Lennard-Jones potential), and they corresponded to a cube of edge $2.5 \mu m$. Computational resources are still not available to perform MD simulations at the engineering scale, and the authors estimated that it would take 100 years for it to be possible.

Finally, one must not forget that each method has its own history and its own domain of application. MD was developed in the theoretical physics community, while DEM in the geotechnical engineering community, and the needs of the two groups are clearly different. My need is to be able to capture both brittle and ductile mechanisms during adhesive wear, with cheap and simple potentials that allow me to investigate long timescales. A molecular dynamics approach with the interaction potentials described by the modified Morse potentials presented above (Eq. 3.25) is thus the method that suits best my investigations.

Chapter 4

Emergence of self-affine surfaces during adhesive wear

Friction and wear depend critically on surface roughness and its evolution with time. An accurate control of roughness is essential to the performance and durability of virtually all engineering applications. At geological scales, roughness along tectonic faults is intimately linked to stick-slip behaviour as experienced during earthquakes. While numerous experiments on natural, fractured, and frictional sliding surfaces have shown that roughness has self-affine fractal properties, much less is known about the mechanisms controlling the origins and the evolution of roughness. Here, by performing long-timescale molecular dynamics simulations and tracking the roughness evolution in time, we reveal that the emergence of self-affine surfaces is governed by the interplay between the ductile and brittle mechanisms of adhesive wear in three-body contact, and is independent of the initial state.

Disclaimer This chapter is reproduced from the postprint version of the article Milanese, E., Brink, T., Aghababaei, R. & Molinari, J.-F. Emergence of self-affine surfaces during adhesive wear. *Nature Communications* **10** (2019) [131], and it is freely accessible at <https://doi.org/10.1038/s41467-019-09127-8>. I personally conducted the design and running of the simulations, the analysis of the results, the discussions, and the writing of the article (figures included).

4.1 Introduction

The roughness of surfaces is a key parameter for all tribology-related phenomena, namely friction, wear, and lubrication. This was already clear to the pioneers of tribology, from Da Vinci [47] to Coulomb [48], who linked friction and surface morphology. Their findings were generalized in the past century by Bowden and Tabor [49], who studied the effects of adhesion and introduced the concept of real contact area. More recently, experimental evidence has shown that both natural and manufactured surfaces are self-affine over many scales [27, 38–41, 44]. In geophysics, the fault roughness decreases with slip [26, 28] and is related to the fault's strength [31, 34] and deformation mechanisms [29]. Also, for various engineering surfaces, the roughness is found to converge upon rubbing to a steady-state value [36, 37]. New surfaces generated by tensile fracture are well known to be self-affine, too [41, 44], and different universal Hurst exponents have been linked to different damage mechanisms [44, 45]. However, the physical origins of these observations are still unclear [30].

Several theoretical surface growth models have been developed to explain roughness evolution [94, 132]. Nonetheless, the generalization of simple diffusion models to the complex case of rubbing surfaces [101] still misses significant mechanisms, like the concurrence of ductile and brittle mechanisms when working the surface. Continuum numerical models are also limited, as they struggle to capture all the several intertwined non-linearities, such as contact, adhesion, plasticity, and fracture. Molecular dynamics simulations can capture the aforementioned non-linearities and atomic-scale mechanisms, but the computational cost is high [60, 133] and mechanisms that take place at long time and length scales cannot be modelled.

To overcome the scale limitations in atomistic simulations, simple model potentials have recently been developed [59], which have proved to be able to capture the ductile-to-brittle transition taking place upon collision of surface asperities in adhesive wear processes [59]. When two asperities come into contact, three possible mechanisms can take place [81]: atom by atom removal in the light load and low adhesion limit [80, 81, 111], and alternatively ductile deformation [51, 59, 134] or brittle fracture [50, 59, 135, 136] of the asperities at larger loads and moderate to high adhesion. Our investigations are conducted in the latter conditions, where the mechanism depends on the size of the junction formed by the two contacting asperities [59, 72, 73, 84].

Here, we perform long-time molecular dynamics simulations of rubbing surfaces,

investigating different initial conditions. Thanks to the adopted method, the ductile-to-brittle transition occurs spontaneously (that is, it is not enforced), permitting us to explicitly capture the debris particle formation [59, 73, 84] and the subsequent transition to a three-body configuration. We thus have a competition between the brittle fracture mechanism that roughens the surfaces and the ductile one that flattens them. Once the debris particle is formed, these mechanisms take place at the contact interface between the particle and the surfaces. We find that the resulting worn surfaces are self-affine and characterized by the same statistics independently of the initial state, within the investigated range. Our results also show that the debris particle wear rate is lower in the three-body configuration, i.e. after running-in.

4.2 Results

4.2.1 Simulation set-up

The investigation consists of a large set of 2D molecular dynamics simulations over a long duration to maximize the chances of observing a steady state for some surface feature, as observed experimentally [36, 37]. The analysed condition is dry sliding of one surface on top of the other, both described by the same model interaction potentials, at constant temperature and constant sliding velocity (see Figure 4.1b and methodology in Section 4.4 for details). The simulations differ from one another in bulk material properties, surface topography, temperature, and system size (see Table 4.1 and methodology in Section 4.4 for the full details). Throughout the article quantities are measured in reduced units, the fundamental quantities being the equilibrium bond length r_0 , the bond energy ε at 0 K, and the particle mass m . Recently, a critical length scale d^* was found to govern the ductile-to-brittle transition in adhesive wear [59]: when two asperities collide, if the junction size d formed by the asperities is larger than d^* , the asperities break and a debris particle is formed, otherwise the asperities deform plastically (Figure 4.1a). The critical length scale is expressed as $d^* = \lambda \cdot \Delta w G / \tau_j^2$, where τ_j is the junction shear strength, G is the shear modulus of the material, Δw is the fracture energy and λ is a geometrical factor. In our simulations, the materials are described by interaction potentials, which we characterize by the maximum stress τ_{sf} on the generalized stacking fault curve at zero temperature [137, 138]: the lower τ_{sf} , the more ductile the material is and the larger its critical length scale d^* . We adopt two different initial surface morphologies: single asperity against single asperity (Figure 4.1b) and self-

Chapter 4. Emergence of self-affine surfaces during adhesive wear

affine surface against self-affine surface (Figure 4.1e, 4.1i and 4.1m). In all cases, the initial contact takes place in a two-body configuration, that is the two surfaces come directly into contact with one another. In the single-asperity setup, (Figure 4.1b-d, simulations S1 to S7, where S stands for single asperity, cf. Table 4.1) each surface is atomistically flat, except for one semicircular asperity. By sliding the top surface, its asperity collides with the asperity of the opposing surface and forms a junction. The size of the initial asperities is chosen large enough for the junction size d to be greater than the critical size d^* and to create a debris particle (Figure 4.1c), which is then constrained to roll between the two surfaces. In the case of initially self-affine surfaces rubbing against one another (Figure 4.1e-h, 4.1i-l and 4.1m-p, simulations R1 to R3, H1, G1 and G2, where R stands for rough, H for heterogeneous material and G for grain boundaries, cf. Table 4.1), we construct the two surfaces with the same Hurst exponent and same root mean square roughness, but we do not control the position of the first contact, nor its size. The first contact involves several small asperities in both surfaces, which deform plastically (Figure 4.1f) until they form a junction of size $d > d^*$ and the surfaces break (Figure 4.1g). In this case, several asperities come into contact with the newly formed debris particle and interact with it in a brittle or ductile fashion, according to the size of the contact that is developed each time. The initial stage is even more complex when the material is heterogeneous (Figure 4.1i-l and 4.1m-p, simulations H1, G1, and G2, cf. Table 4.1). We prepared such a case by geometrically dividing the material into irregularly shaped sub-regions (randomly distributed both in size and in position), and randomly assigning one of two potentials within each sub-region. The two potentials differ in their critical size d^* , so that two different critical length scales coexist in the system. As a result of this mixture, the overall surfaces are heterogeneous in terms of inelastic behaviour (with half of the tiles being relatively more brittle than the other half). Upon asperity collision the critical length scale for the ductile-to-brittle transition in the case of the mixture is then no longer well defined. In this case the surfaces favour cracks within the least tough material (or at weak, heterogeneous interfaces), and plastic deformation within the toughest one (cf. Supplementary Movie 1).

After this initial stage, and independently of the original geometrical setup and of the heterogeneity of the material, the surfaces reach a state where the debris particle continuously rolls between them and works them (Figure 4.1d, 4.1h, 4.1l and 4.1p). The contact now takes place in a three-body configuration, the third body being the debris particle that separates the two surfaces (i.e. the first bodies). The surfaces undergo both brittle and ductile deformation and material transfer takes place both ways: from the debris particle to the surfaces and vice versa. This interplay with

the third body allows for a continuous reworking of the surfaces, which appear to be self-affine whenever a steady-state roughness is reached. Remarkably, as we explain below, this self-affine morphology is independent of the initial conditions investigated. The case of heterogeneous materials is particular: each of the two materials is characterized by a different critical length scale and the effect of this on the critical length scale of the mixture is still unknown. From our results, no trace of this heterogeneity is found in the scaling of the self-affine morphology of the worn surfaces. In all cases, the inclusion of the ductile-to-brittle transition within the modelled length scales is fundamental to capture the self-affine nature of the surfaces. When it is not included, asperity collision never leads to the formation of loose debris particles and surfaces always smoothen [57, 71, 139–143].

4.2.2 Self-affine description

For a complete description of the surfaces, we investigate their power spectral density (PSD) Φ per unit length, as it contains information about the contribution of all the length scales involved. Self-affine surfaces are in fact characterized by an anisotropic scale transformation [94]. This means that their heights $h(x)$ scale differently than the horizontal position x , and the scaling relation is [94, 96] $h(\lambda x) \sim \lambda^H h(x)$, where λ is the scaling factor, and $0 < H < 1$ is the Hurst exponent [96, 97] (see Section 4.4 for a more detailed discussion about H). In other words, magnifying the x axis by a factor λ will produce a magnification of the heights $h(x)$ by a factor λ^H . An important consequence of this relation is that if the statistics of a self-affine surface are known at a given scale, they can be extended to all the other scales by means of the Hurst exponent H . The PSD of self-affine surfaces displays a power-law behaviour $\Phi(q) \sim q^{-\alpha}$ (where q is the wavevector) and the Hurst exponent can be expressed in terms of the power-law exponent α [97, 98, 144]: in the case of 1D surfaces $H = (\alpha - 1) / 2$ (see methodology in Section 4.4 for more details).

The results of the analysis are displayed in Figure 4.2 and Supplementary Fig. S4.4, which show the normalized power spectral density and the height–height correlation function averaged over several time steps for the worn top and bottom surfaces of different simulations, respectively. The surfaces are sampled during the steady state, where their roughness (expressed as the root mean square of heights) fluctuates around a stabilized value and their profile can be assumed to be stationary. This is the first time, to the best of our knowledge, that such a trend in the roughness evolution is numerically reproduced. It is in fact known from experimental evidence that

surfaces undergo large roughness variations in the early stage of the wear process, before settling around a steady-state value [37, 75], as reproduced by our simulations (cf. Figure 4.3a). The PSDs in Figure 4.2a and Supplementary Fig. S4.4a collapse around an average value of the Hurst exponent $H = 0.7$, the lowest value being $H = 0.6$ and the highest $H = 0.8$, irrespective of the initial geometry, the material, the heterogeneity of the material or the system size, within the range of conditions investigated. The scaling of the roughness in terms of root mean square of heights σ with the system size is also consistent with a self-affine morphology (cf. Supplementary Fig. S4.5, which shows σ for two surfaces of different size). The estimation obtained for H is in good agreement with the values found for natural faults over a broad range of length scales [27, 34] ($H = 0.77 \pm 0.23$), shear experiments in limestone blocks [33] ($H = 0.65 - 0.8$), and worn asphalt roads [145] ($H = 0.8$). Furthermore, the height-height correlation function $\Delta h(\delta x) = \langle [h(x + \delta x) - h(x)]^2 \rangle^{1/2}$ plotted in Figure 4.2b and in Supplementary Fig. S4.4b allows us to observe if any crossover for H is exhibited around the critical length scale d^* . No pronounced change of behaviour is displayed in the range of d^* values investigated, and the self-affine morphology is thus the same at smaller and larger scales. The upper cutoff exhibited in Figure 4.2b and in Supplementary Fig. S4.4b is due to the box size. The possibility of a change in the Hurst exponent at the largest investigated scales cannot be ruled out.

The fact that no change in the statistics is observed in correspondence to d^* and that the surfaces are rough at all scales is possibly due to the change in the contact configuration. After the debris particle is formed, the system transitions in fact to a three-body contact configuration. The loading conditions are then changed and the critical length scale d^* might thus assume a different value upon rolling contact. Furthermore, atoms can be removed at the interface by attrition, and plastic deformation also contributes to the change of the surface morphology. Another important mechanism, first put forward to explain fault roughness [26, 32], is the smoothing and re-roughening of the surface by the removal of fragments from it. According to this mechanism, a fragment removed from the surface roughens it at the scale of the fragment and smooths it at larger wavelengths. In our simulations, the strong interfacial adhesion allows for this mechanism to happen ideally at all the modelled length scales. An upper length scale for the fragments is set by the current contact size between the debris particle and the surfaces. According to the described picture, larger wavelengths should be smoothed more than shorter ones, which we observe in the initial stage of the process (see Supplementary Discussion, Section 4.5.2). We also remark that, beside the ductile and brittle mechanisms, surface diffusion

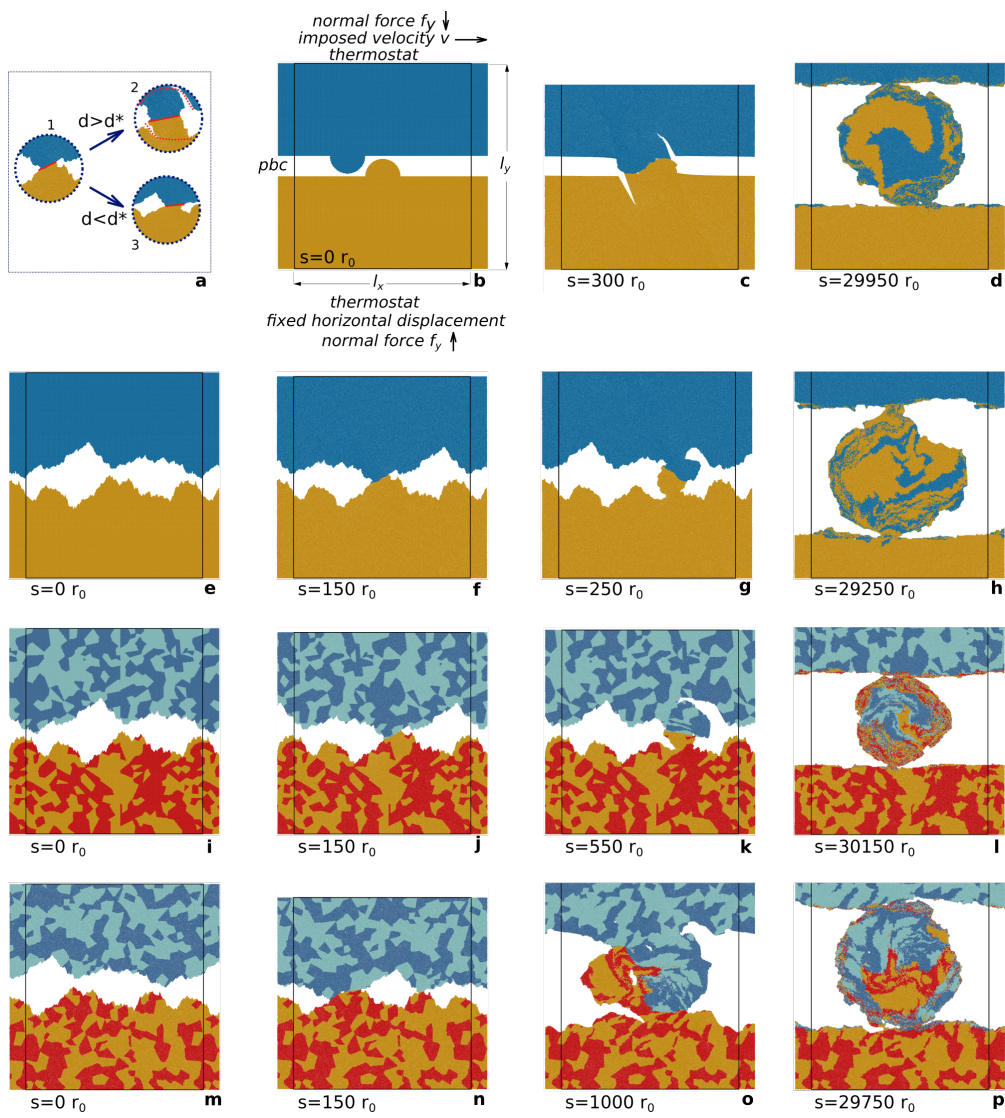
takes place in our simulations and, without sliding, at infinite time the equilibrium surfaces would be close to atomistically flat. The deformation mechanisms, though, are fast enough to counteract diffusion, and contribute to a rich distribution of the surfaces heights. The lattice planes are in fact not aligned across the sample (cf. Supplementary Fig. S4.6). When grain boundaries are modelled, each grain is initially assigned a random rotation and can rotate during the sliding process, providing an additional mechanism for the surface roughening and leading to a larger spread in the height distribution (cf. Supplementary Fig. S4.7).

A theoretical value of $H = 0.5$ (i.e. random correlation) for wear processes was proposed by means of a diffusion model with random deposition [101]. On the other hand, both experimental and numerical results suggest that adhesive wear is not a random Gaussian process, and that $H > 0.5$. Thus, more ingredients are needed in theoretical models that aim at describing the surface evolution during adhesive wear processes, including plastic deformation and brittle fracture. The debris particle is in contact with only a small part of the surface at every instant, localizing the deformation and the material transfer, and the sliding direction breaks down the symmetry in the evolution. This provides some similarities with the gradient percolation models used in fracture front propagation: in this class of models, the self-affine fractal front propagates towards a preferred direction (providing asymmetry) and the predicted Hurst exponent $H = 2/3$ (when small scale effects prevail over large scale elasticity) is consistent with our findings [132]. Models for directed polymers in a random medium also exhibit $H = 2/3$ and may provide further insights [94]. The problem of crack width has indeed been suggested to be connected with that of random directed polymers [146], and the detachment of the particle from the mating surface during the rolling motion may display a similar crack-like behaviour that would contribute to the self-affine morphology. Finally, the inclusion of a scale-dependent material strength is likely another fundamental ingredient needed in theoretical models to capture a persistent Hurst exponent (i.e. $H > 0.5$) [34]. There is in fact evidence [34] that mechanical behaviour underlies a Hurst exponent $H = 0.75 \pm 0.05$ in rocks at the nanoscale.

Chapter 4. Emergence of self-affine surfaces during adhesive wear

Figure 4.1 – Ductile-to-brittle transition, simulation setup, and evolution. a) Upon collision between two asperities (1), two possible mechanisms can take place depending on the junction size d : if it is larger than the critical, material-dependent value d^* , surfaces break and a debris particle is formed (2), else the asperities deform plastically (3). Solid red lines represent the junction of size d and dotted red lines represent the crack path. b) Setup: The two bodies are pressed together by a normal force f_y , while the sliding velocity is imposed on the top layer of atoms of the upper body. The bottom layer of atoms is fixed horizontally. A thermostat is applied on the layers next to the fixed boundaries. The box width l_x is fixed and periodic boundary conditions are applied along x ; the simulation cell, with initial vertical size l_y , is allowed to expand/shrink vertically. b-d) Single asperity setup, example frames from simulation S1. The point of first contact in the two-body configuration is well defined and a debris particle is formed upon asperity collision (c); in the three-body configuration, the debris particle wears away the surfaces while increasing in volume (d). e-h) Setup with self-affine homogeneous surfaces, example frames from simulation R2. The asperities are present at all modelled scales and deform plastically upon contact in the two-body configuration (f) until a junction size is large enough to favour debris particle formation (g) and the transition to the three-body configuration (h). i-l) Setup with heterogeneous self-affine surfaces: harder material is depicted in red and dark blue, softer material in yellow and light blue, example frames from simulation H1. m-p) Setup with heterogeneous self-affine surfaces with grain boundaries, example frames from simulation G1. The steady-state surface appears rougher (p). In all figures colours distinguish particles originally belonging to the top (dark and light blue) and bottom (yellow and red) surfaces; in figures b-p) black lines represent simulation box boundaries and s is the sliding distance expressed in units of r_0 .

4.2. Results



4.2.3 Evolution of a debris particle

A particular feature of our simulations is that the two surfaces are worn mostly during three-body contact, which is relevant for the overall wear formation in both natural and industrial sliding processes [26, 52]. The presence of third bodies clearly plays a key role in the emergence of the self-affine morphology and therefore we now analyse the life of a debris particle once it is formed. Details on how the debris particle is born have already been addressed elsewhere [73].

Two different geometrical setups are adopted for the simulations shown in Figure 4.3: single asperity on single asperity at three different temperatures (S1-S3) and self-affine surface on self-affine surface at two different temperatures (R1 and R2). The evolution of the wear volume in Figure 4.3c shows that in all cases our simulations capture both the severe wear running-in phase (formation of the debris particle, i.e. the non-zero initial wear volume) and the mild wear steady-state phase that follows. This matches experimental observations [75, 99, 147], as suggested by the evolution of the equivalent roughness σ_{eq} (Figure 4.3a and Supplementary Discussion, Section 4.5.2).

It can be observed that the evolution of the three parameters (surface roughness σ_{eq} , tangential work W_t , and wear-particle volume V) exhibits common features among the simulations. In each simulation, a sharp increase in σ_{eq} is observed upon formation of the debris particle, which corresponds to a sudden increase in the frictional work (inset of Figure 4.3b). In this initial stage, the wear volume has been found to be proportional to the work done by the frictional force [73]: $V = W_t/\tau_j$, with τ_j being the junction shear strength and W_t being the integral of the frictional force over the sliding distance. This relation applies during the particle formation, where the frictional force reaches its maximum and then slowly decreases towards small values. Over long time scales, the integral of these small values leads to a significant amount of work, which partly contributes to the particle growth. The inset of Figure 4.3b and the Figure 4.3c indeed show that the initial volume of the debris particle is larger when the frictional work is larger, and for the single asperity setup the frictional work appears to reach a plateau. When the original surfaces are self-affine and more collisions take place at running-in, the plateau is not clearly defined. Looking at the evolution of W_t in Figure 4.3b, it is clear that the frictional work is not constant over the investigated timescale, but that it keeps increasing at an approximately constant rate (consistently with a constant tangential force F_t , cf. Supplementary Fig. S4.8). The rate is nevertheless lower than the average rate

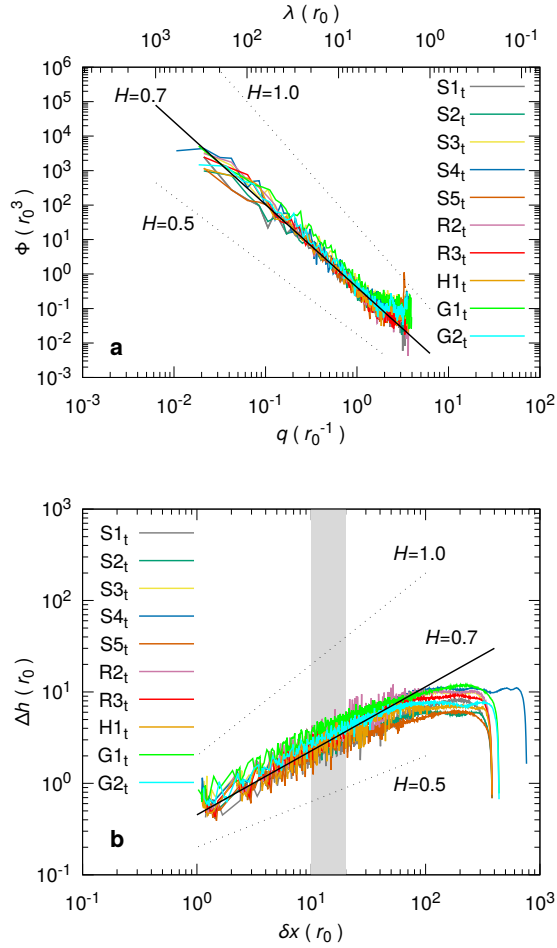


Figure 4.2 – Steady-state surface morphology analysis. a) PSD per unit length Φ as a function of the wavevector q and the wavelength λ , the relation between the two being $q = 2\pi/\lambda$. b) Height-height correlation function $\Delta h(\delta x) = \langle [h(x + \delta x) - h(x)]^2 \rangle^{1/2}$. The surfaces are taken from ten different simulations (see Table 4.1 for details), the subscript indicates the top surface for each simulation. Bottom surfaces for the same simulations are reported in Supplementary Fig. S4.4. In both a) and b) the solid black straight guide-line corresponds to a Hurst exponent $H = 0.7$. Dotted black straight guide-lines show the hypothetical slope for distributions of $H = 0.5$ and $H = 1.0$. In b) the shaded area displays the interval of distances corresponding to the range of critical length scale values d^* exhibited by the adopted potentials. No pronounced crossover is observed in the slope of $\Delta h(\delta x)$ over the range of values for d^* . As a consequence of the assumption of periodic surfaces, the function is roughly symmetric with respect to half the horizontal box size (hence the plateau and the following drop for large values of δx).

Chapter 4. Emergence of self-affine surfaces during adhesive wear

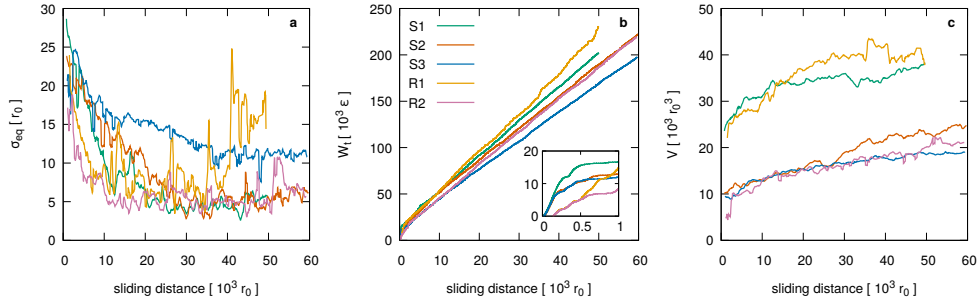


Figure 4.3 – Evolution of equivalent roughness σ_{eq} , frictional work W_t , and wear volume V . See Supplementary Figs. S4.11 and S4.12 for further simulations. a) Evolution of σ_{eq} . While for most simulations the value of σ_{eq} stabilizes, cold temperatures (S3) and debris particle shape (R1) can inhibit this stabilization. b) Evolution of the tangential work W_t with the sliding distance. The work W_t exhibits a sharp increase upon formation of the debris particle [73] (inset: W_t for sliding distances up to $1000 r_0$), after which it grows at smaller rates. c) Evolution of the wear volume of the rolling debris particle, as defined only after its formation. In all simulated conditions the wear rate after the debris particle formation is small compared to the ratio of the initial particle size over the sliding distance necessary to form the particle (cf. Supplementary Fig. S4.9), consistent with the transition from severe to mild wear [75].

displayed in the running-in stage, which governs the initial debris particle size (cf. Supplementary Fig. S4.9). This suggests a change in the mechanism of wear, as supported by the loss of the proportionality of the wear volume to $1/\tau_j$ after running-in (Supplementary Fig. S4.10) and by the change in the wear rate (Supplementary Fig. S4.9).

We can then split the debris particle life into two distinct phases: particle formation and particle evolution. The two situations are characterized by different wear rates (cf. Supplementary Fig. S4.9), the one corresponding to particle formation being much larger. This result is consistent with decreasing gouge-formation rates observed for natural faults [26]. The reduction in the friction coefficient with the sliding distance in fault lubrication processes [16] provides another consistent observation, under the reasonable assumption that wear rate and friction variations are similar under those conditions [22, 92]. Likewise, shear experiments on rocks have shown vanishing wear rates in a three-body steady-state configuration [92], and wear experiments have displayed a reduction in the wear rate if the wear debris is not evacuated [52, 90, 91]. We ascribe the change in the wear rate, i.e. high to low, to

the different contact configurations. In the initial phase, asperities belonging to both surfaces collide continuously upon sliding in a two-body configuration, and wear debris particles are repeatedly formed at a constant rate, as in Archard's picture [50]. As wear experiments are usually performed in open systems, where the wear debris particles are regularly evacuated, the formation of a full three-body contact configuration is avoided and the rate of wear particle creation is constant (due to local collisions of asperities between the two surfaces). If a three-body contact configuration develops instead (for example in faults), the third body behaves similarly to a lubricant [52], separating the first bodies. As a consequence, the two surfaces are not directly in contact with one another, but with the third body only. Wear can then take place exclusively at the interface between the third body and the surfaces. Both our simulations and the cited observations include three-body contact conditions and predict a decrease in the wear rate compatible with the introduction of a lubricating effect in the tribosystem. The rate of evacuation of debris particles from the system is thus fundamental in the evolution of surface roughness. A low evacuation rate is expected to reduce asperity collisions, which are responsible for creating roughness at scales larger than the critical junction size [59]. The mechanical behaviour of the wear debris is also expected to affect the wear rate [52]. While in our case the debris particle has the same mechanical behaviour as the first bodies, the presence of chemical processes that harden the wear debris might actually increase the wear rate. If the debris particles favour rigid rolling over frictional sliding, though, this increase might not occur [52].

4.2.4 Influence of heterogeneity and limitations

The case of heterogeneous materials with grain boundaries (simulations G1 and G2) yields further observations. The inclusion of two different species and the presence of grains, instead of a perfect lattice, provide favourable crack propagation directions that are not present in the homogeneous cases. Cracks propagate more easily along the grain boundaries—where the mismatch of the lattices reduces the overall bond strength between the atoms at the interface—and within the bulk of the least tough species. Additionally, cracks are more likely to stop propagating when the tip meets the tougher material (cf. Supplementary Movie 1). Furthermore, the heterogeneous grains modelled in simulations G1 and G2 can be seen as inclusions of one of the two species in a matrix made of the other one, in the extreme case where the two species have the same phase fraction. The same mechanisms affecting the crack path (because of the lattice mismatch and/or different material properties) are thus

Chapter 4. Emergence of self-affine surfaces during adhesive wear

expected to occur—although more localized—when the inclusions' phase fraction is smaller than the matrix phase fraction. As the latter is a case in between the homogeneous and heterogeneous bulk cases investigated here (i.e. simulations R and G respectively), the findings of this work suggest that a similar self-affine surface morphology should be recovered. Real materials might also contain pre-existing dislocations or point defects, which are not considered in the present set of simulations. In these cases, we would expect the defects to affect the plastic response of the bulk and, thus, its critical length scale and the debris formation process. Moreover, while we restricted ourselves to one possible crystal structure, materials can also be amorphous. Assuming homogeneous materials, we would then expect the crack path to have no favourable direction because of the isotropic structure, contrary to the hexagonal lattice modelled here. Finally, surfaces undergoing continuous reworking are also known to exhibit hardening, which most likely leads to a change of the critical length scale over time, affecting in turn the wear rate.

It should be also noted that our simulations are restricted to 2D systems by the large computational demands of long-timescale simulations in 3D. One relevant difference between 2D and 3D systems is that in the first case, the lattices of the two bodies are more likely to locally match, allowing full, bulk-like adhesion to develop. Furthermore, in 3D the debris particle could roll at some angle with respect to the sliding direction of the top body, as a consequence of local peaks and valleys due to the roughness along the additional dimension. It is also known that the steady-state roughness normal to the sliding direction is different than that parallel to the sliding direction [25], which cannot be captured by 2D simulations. Also, in 3D the debris particles are not forced to pass over the same track again and again. Despite these differences, which might result in a slowdown of the roughness evolution process, we believe that the same mechanisms should be recovered in 3D systems too, as the aforementioned evidence from experiments and field observation of faults suggests. Short timescale 3D simulations have also confirmed 2D observations for the early stages of the sliding process [73]. Further investigations are necessary in any case to address the effects of 3D geometry and of the more complex micro-structures.

With respect to the boundary conditions, a normal force and a sliding velocity are applied at the same time since the beginning of the simulations. This differs from situations where a normal load is first applied, and then the top body is pushed and slides against the bottom one. If the latter conditions were to be applied in the present setup, the initial contact geometry would likely differ. Nonetheless, as long as the formed junction is larger than the critical length scale d^* , a debris particle forms,

is constrained between the two surfaces, and works them – the final morphology is expected to be statistically the same than the one observed for the simulations reported here. Furthermore, for larger system sizes with random initial morphology, the initial contact area is expected to be distributed among multiple spots. This can lead to more complicated settings, like the formation of multiple debris particles and the interaction between asperity contacts [84]. These may in turn alter also the surface morphology evolution (for example because of collisions between rolling debris particles). While such setup is out of the scope of this specific study because of the extensive computational resources that it would require, it would undoubtedly be beneficial to explore it in future investigations.

4.3 Discussion

Our molecular dynamics simulations of rubbing surfaces highlight the importance of including both ductile and brittle deformation mechanisms in the modelling of adhesive wear processes. This allows to explicitly capture the transition to the three-body configuration [59, 73], where the surfaces are worn away by the debris particle.

The approach leads us to two major results. The first is the ability to track the evolution of rubbed surfaces into self-affine fractals characterized by a persistent Hurst exponent. We argue that the development of the self-affine morphology is due to smoothing and re-roughening mechanisms and that these mechanisms take place mostly in a three-body configuration, as in natural faults [26, 32]. The second result is that the wear rate is lower once the system has transitioned to a three-body configuration. We ascribe this to the different contact configuration: two-body contact at running-in and three-body contact later, the latter having a lubricating effect. This unveils the role of the debris evacuation-rate in wear experiments. We conclude that accounting for the ductile-to-brittle transition in wear mechanisms is fundamental when investigating the physics of adhesive wear, from the nano- to the geological-scale.

4.4 Methods

4.4.1 Interaction potentials

The model pair potentials used for this study belong to the family of potentials first introduced in Ref. [59] and also discussed in Ref. [73]. This class of model potentials allows for a critical junction size small enough to observe the ductile-to-brittle transition in adhesive wear with molecular dynamics simulations. Their main feature is to share the same elastic properties up to a bond stretch of 10% and to have a controllable yield strength by modifying the potential tail. This is made possible by modification of the Morse potential [127], leading to the expression:

$$\frac{V(r)}{\varepsilon} = \begin{cases} (1 - e^{-\alpha(r-r_0)})^2 - 1 & r < 1.1r_0 \\ c_1 \frac{r^3}{6} + c_2 \frac{r^2}{2} + c_3 r + c_4 & 1.1r_0 \leq r \leq r_{\text{cut}} \\ 0 & r_{\text{cut}} \leq r \end{cases} \quad (4.1)$$

where r is the interparticle distance, ε is the bond energy at 0 K, r_0 is the equilibrium bond length, and $\alpha = 3.93 r_0^{-1}$ governs the bond stiffness. The value of r_{cut} controls the cut-off distance, governing the inelastic behaviour, and the c_i coefficients are chosen to ensure the potential continuity in energy and force. With respect to the values in Table 4.1, the potential with $\tau_{\text{sf}} = 3.96 \varepsilon r_0^{-2}$ corresponds to the potential named P6 in Ref. [59], the potential with $\tau_{\text{sf}} = 3.52 \varepsilon r_0^{-2}$ corresponds to the potential named P4 in Ref. [59], and the potential with $\tau_{\text{sf}} = 3.42 \varepsilon r_0^{-2}$ is more ductile than potential P4 but more brittle than potential P3.

4.4.2 Simulation geometry and boundary conditions

All simulations were performed in 2D using the molecular dynamics simulator LAMMPS [125]. A simple scheme of the simulation setup is shown in Figure 4.1b. Two different horizontal box sizes have been adopted, i.e. $l_x = 336 r_0$ and $l_x = 673 r_0$, and periodic boundary conditions are applied in the horizontal direction. The initial vertical box size is constant ($l_y = 392 r_0$) and the box is allowed to expand vertically, e.g. upon debris particle formation. A constant force ($f_y = 0.02 \varepsilon r_0^{-1}$) is applied on both horizontal boundaries of the material to press the surfaces together. A constant horizontal velocity $v = 0.01 \sqrt{\varepsilon m^{-1}}$ is imposed on the first layer of atoms of the top surface. The bottom layer of atoms of the bottom surface is fixed. Tempera-

tures are enforced by means of Langevin thermostats with a damping parameter of $0.05 r_0 / \sqrt{\epsilon m^{-1}}$. On each body, the thermostats are applied to the three layers of atoms next to the external layer where the fixed displacement or velocity is imposed. Temperature values provided in Table 4.1 are expressed in terms of equivalent kinetic energy per atom. The integration is performed with a time step of $0.005 r_0 / \sqrt{\epsilon m^{-1}}$ for a large number of steps, i.e. 1 billion for the shortest simulations and 2.6 billion for the longest. Table 4.1 summarizes the main features of the simulations. Simulation names reflect the initial geometry or material heterogeneity: S stands for single asperity, R for rough self-affine surface, H for heterogeneous materials (without grain boundaries), and G for heterogeneous materials with grain boundaries. In the single-asperity setups S1 to S7, we chose to model semicircular asperities, but different shapes (e.g. square or sinusoidal) are not expected to alter our findings [59]. In simulations H1, G1 and G2 both bodies are modelled by two phases (using two different potentials), present in equal shares and randomly distributed in 500 tiles generated from 500 points randomly distributed in the simulation cell by means of Voronoi tessellation. No grain boundaries between the tiles are modelled in simulation H1. Grain boundaries are modelled in simulations G1 and G2: each of the 500 tiles is a grain, whose orientation is determined by a random rotation, leading to lattice mismatch. In simulations G1 and G2, one of the two potentials is the same used for simulations S1, S2, S3, S4, R1, R2 and H1, and it is characterized by $\tau_{sf} = 3.52 \epsilon r_0^{-2}$ (cf. Table 4.1). The other adopted potential has the same equilibrium energy ϵ , but its equilibrium and cutoff distances are scaled by a factor 0.90 in simulation G1 (resulting in $\tau_{sf} = 4.35 \epsilon r_0^{-2}$) and 0.95 in simulation G2 ($\tau_{sf} = 3.90 \epsilon r_0^{-2}$). The potential well of the cross-terms between the two species is 0.9ϵ ; its equilibrium and cut off lengths are given by the average of the respective lengths of the two species. The starting system is obtained by constructing a bulk micro-structure, heating it up and then annealing it at the target temperature, allowing the grains to reach an equilibrium configuration. Atoms are then removed from the system based on a purely geometric criterion to obtain two distinct rough surfaces.

4.4.3 Self-affine surfaces

Fractal surfaces whose heights $h(x)$ scale differently than the horizontal distance x are self-affine fractals, and they obey the scaling relation [94, 96] $h(\lambda x) \sim \lambda^H h(x)$, where λ is the scaling factor and H is the Hurst exponent, which is $0 < H < 1$ for fractional Brownian motion (fBm) [97]. The Hurst exponent describes the correlation between two consecutive increments in the surface. Assuming $x_1 < x_2 < x_3 < x_4$, let

Chapter 4. Emergence of self-affine surfaces during adhesive wear

us consider the two height increments $\Delta h_1 = h(x_2) - h(x_1)$ and $\Delta h_2 = h(x_4) - h(x_3)$. For $H = 0.5$, Δh_1 and Δh_2 are randomly correlated (i.e. standard Brownian motion), which means that Δh_2 has a 50% probability of having the same sign of Δh_1 . For $0 < H < 0.5$, the increments Δh_1 and Δh_2 are negatively correlated, that is Δh_2 is more likely to have the opposite sign of Δh_1 (the motion is anti-persistent: a positive increment is more likely to be followed by a negative one). Finally, for $0.5 < H < 1$ the increments are positively correlated, that is Δh_2 is more likely to have the same sign of Δh_1 (the motion is persistent: a positive increment is more likely to be followed by another positive one). The generation of engineering surfaces, that is surfaces that are manufactured, is known to be non-stationary and random [38], and it can be described as a non stationary process with stationary increments, which allows to relate the fractal dimension D of the surface with its Hurst exponent H through its Euclidean dimension n [97]: $D + H = n + 1$. Moreover, the statistics of this class of surfaces have been investigated studying the Weierstrass-Mandelbrot function [144], allowing to relate the fractal dimension D and the power law exponent α of the power spectral density of a one-dimensional surface profile [98, 144] as $\alpha = 5 - 2D$. Under these assumptions, $H = (\alpha - 1) / 2$ for a 1D surface ($n = 1$).

The latter allows to estimate the Hurst exponent H from a linear fit of the data in the log-log plane, discarding the tail ($\lambda < 4 r_0$), where the definition of surface for a discrete system breaks down and data is inevitably polluted by the numerical surface reconstruction. This method has been shown [148] to be accurate but also to be affected by a systematic error that can possibly lead to an underestimation of H . This underestimation decreases by increasing the system size, and for system sizes of the order of magnitude investigated in this study it is at most 0.1. The range of values of H in our study would then be $H = 0.7 - 0.9$. We refer throughout the text to the values found with the fit, without correcting for the underestimation, for consistency with the methods adopted in the literature [27, 34, 39], where no correction is applied.

4.4.4 Spectral analysis

Let us consider a surface of length L , whose heights are defined by the continuous function $h(x)$, where x is a spatial coordinate. We refer to the power spectral density (PSD) of such surface in terms of PSD per unit length $\Phi_h(q)$, q being the wavevector, defined as [149]

$$\Phi_h(q) \equiv \frac{1}{L} \left| \int_L h(x) e^{-iqx} dx \right|^2, \quad (4.2)$$

where the integral is the continuous Fourier transform of $h(x)$. The PSD defined in Equation (4.2) is equivalent to the PSD of a continuous function $h(x)$ that is zero everywhere except over a distance L , normalized by L . (Note that the specification ‘per unit length’ is often dropped in surface roughness analyses[99, 150]). In particular, we estimate Φ_h as

$$\Phi_h(q_n) \approx \Delta x \cdot P_h(q_n), \quad (4.3)$$

where $P_h(q_n)$ is the classical periodogram [149, 151]:

$$P_h(q_n) = \frac{1}{N} \left| \sum_{k=0}^{N-1} h_k e^{-iq_n x_k} \right|^2, \quad (4.4)$$

the summation being the discrete Fourier transform of the surface. In fact, $h(x)$ is known only at a discrete set of N points x_k ($k = 0, 1, \dots, N - 1$), regularly sampled at an interval Δx , such that $h_k = h(k\Delta x)$ are the known values of $h(x)$. In our case, $\Delta x = L/N$, N being the number of atoms belonging to surface of length L , and is approximately $1 r_0$.

It can be shown that both the PSD Φ_h per unit length and the periodogram P_h are normalized such that $\int_q \Phi_h(q) dq$ and $\sum_n P_h(q_n)$ are equal to the mean squared amplitude σ^2 of $h(x)$ and h_k respectively.

Note that the derivative of both P_h and Φ_h is the same in the log–log plane, as their estimation differs only by a multiplicative factor Δx (see Equation (4.3)): the estimated self-affine exponent would not change if one or the other is considered.

4.4.5 Height–height correlation analysis

Another suitable method to estimate the Hurst exponent H is to investigate the height–height correlation function [94], which describes the change of heights Δh between two points at distance δx horizontally:

$$\Delta h(\delta x) = \langle [h(x + \delta x) - h(x)]^2 \rangle^{1/2}, \quad (4.5)$$

where the angle brackets indicate spatial average. The height–height correlation function scales as $\Delta h(\delta x) \sim \delta x^H$: it is therefore possible to determine the Hurst exponent H from its log–log plot. It is also possible to observe potential upper and lower cutoff values of δx limiting the scaling regime.

4.4.6 Average roughness quantification

The surface roughness is defined as the variations in height of the surface profile with respect to an arbitrary plane of reference [99], which in our case is always taken to be the mid-plane of the surface heights. To quantify the surface roughness, several parameters are used—in particular in engineering practice—but we limit our discussion to the root mean square of heights σ , which in the case of a surface discretized in a set of N points is given by

$$\sigma = \sqrt{\frac{1}{N} \sum_{k=1}^N h_k^2}, \quad (4.6)$$

where h_k is the distance of the point k from the plane of reference. When the system as a whole is investigated, the equivalent σ of the composite surface (given by the two surfaces of the top and bottom materials) becomes[99]

$$\sigma_{\text{eq}} = \sqrt{\sigma_{\text{top}}^2 + \sigma_{\text{bottom}}^2}. \quad (4.7)$$

The root mean square of heights σ can also be expressed as a function of the zeroth moment of the power spectral density per unit length Φ_h , assuming that the surface profile is continuous [39, 149]:

$$\sigma^2 = \int_{q_l}^{q_h} \Phi_h(q) dq, \quad (4.8)$$

where q_l and q_h are the lowest and highest wavevectors modelled in the system. If $q_h \gg q_l$, it has been shown [39] that $\sigma^2 \propto q_l^{-(4-2D)}$.

4.4.7 Data analysis

All frames are visualized with OVITO [152]. Due to the long duration of the simulations, frames are stored every 1 000 000 steps. At first, a surface is reconstructed by identifying atoms with low coordination number. This preliminary surface includes i) the top and bottom surface portions that are not in contact with the debris particle and ii) the debris particle surface portion that is not in contact with any surface. The two top and bottom surfaces are then reconstructed, their portion in contact with the debris particles being approximated by the closest group of atoms belonging

to a straight segment. This approximation to a straight segment gives no loss of information for the spectral analysis by means of the Fast Fourier Transform up to high wavevectors [153]. The atoms contained between the two segments and the previously identified debris particle surface identify the debris particle and are thus discarded in any top and bottom surface analysis. Each reconstructed surface now consists of irregularly spaced atoms and is processed independently. The atom positions are linearly interpolated to recreate a bijective profile that is then discretized in N points, evenly spaced along the horizontal x -axis, where N is the number of unevenly spaced atoms belonging to the surface prior to the linear interpolation. This step allows to proceed with an analysis of the surface by means of the classical periodogram through a Fast-Fourier Transform algorithm, as the Lomb-Scargle periodogram for unevenly spaced data is known to provide poorer results in the spectral analyses of surface morphology [153, 154]. The horizontal spacing of the re-sampled surface is approximately $1/r_0$. Forcing a bijective profile results in a noisy geometry where overhangs are present, affecting the large wavevector amplitudes, but does not alter the data at lower wavevectors, where the self-affine morphology is observed. The interval between two consecutive time steps used for averaging the PSD is large enough for the particle to have rolled over the whole surface at least one time.

The data for σ and σ_{eq} are averaged over 10 consecutive data points. The tangential work W_t is computed as the integral of the tangential force F_t over the sliding distance s : $\int F_t ds$; the tangential force values are stored every 5000 steps and are averaged over 2000 data points. The debris particle volume V is computed by multiplying the number of atoms belonging to the debris particle and the atomic volume. The latter is computed as the lattice unit cell volume at the temperature T , divided by the number of atoms in the unit cell. As the detection code is designed for the most common situation of the particle being in contact with both surfaces at the same time, due to the particular geometry at some time steps, e.g., when the particle is only in contact with one of the two surfaces and is not rolling, the data for the surface roughness σ and σ_{eq} , the wear volume V , and the linear fit exponent α may be unevenly spaced locally around some time steps.

Chapter 4. Emergence of self-affine surfaces during adhesive wear

Name	$\tau_{sf} (\epsilon r_0^{-2})$	$l_x (r_0)$	$T (\epsilon)$	initial $H (-)$	micro-structure
S1	3.52	336	0.075	n/a	single crystal
S2	3.52	336	0.050	n/a	single crystal
S3	3.52	336	0.025	n/a	single crystal
S4	3.52	673	0.075	n/a	single crystal
S5	3.42	336	0.075	n/a	single crystal
S6	3.42	336	0.050	n/a	single crystal
S7	3.42	336	0.025	n/a	single crystal
R1	3.52	336	0.075	0.7	single crystal
R2	3.52	336	0.050	0.7	single crystal
R3	3.52	336	0.075	0.5	single crystal
H1	3.52 ; 3.96	336	0.075	0.7	two phases
G1	3.52 ; 4.35	336	0.075	0.7	two phases with grain boundaries
G2	3.52 ; 3.90	336	0.075	0.7	two phases with grain boundaries

Table 4.1 – Summary of the simulations. S indicates simulations with initial geometry described by a single asperity on each surface. R indicates simulations with surfaces that are initially self-affine. H indicates simulations with surfaces that are initially self-affine and with heterogeneous materials without grain boundaries, modelled by even shares of the potential characterized by the two values of τ_{sf} reported. G indicates simulations with surfaces that are initially self-affine and with heterogeneous materials with grain boundaries, modelled by even shares of the potentials characterized by the values of τ_{sf} reported (see also methodology in Section 4.4). l_x and T indicate the horizontal resolution and the temperature respectively. H is the initial surface Hurst exponent for initially self-affine surfaces. Temperatures are expressed in terms of equivalent kinetic energy per atom. n/a: field not applicable to that simulation.

4.5 Supplementary materials

4.5.1 Supplementary figures

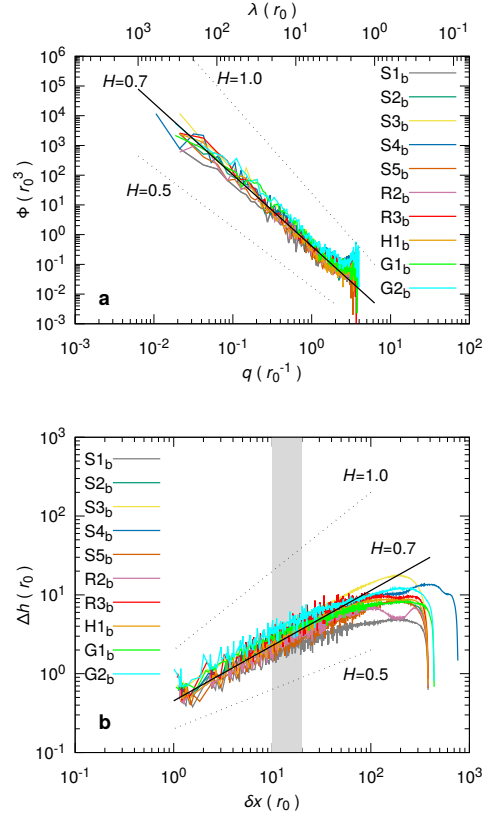


Figure S4.4 – Steady-state surface morphology analysis. a) PSD per unit length Φ as a function of the wavevector q and the wavelength λ , the relation between the two being $q = 2\pi/\lambda$. b) Height-height correlation function $\Delta h(\delta x) = \langle [h(x + \delta x) - h(x)]^2 \rangle^{1/2}$. The surfaces are taken from ten different simulations (see Table 4.1 for details), the subscript indicates the bottom surface for each simulation. Top surfaces for the same simulations are reported in Figure 4.2. In both a) and b) the solid black straight guide-line corresponds to a Hurst exponent $H = 0.7$. Dotted black straight guide-lines show the hypothetical slope for distributions of $H = 0.5$ and $H = 1.0$. In b) the shaded area displays the interval of distances corresponding to the range of critical length scale values d^* exhibited by the adopted potentials. No pronounced crossover is exhibited in the slope of $\Delta h(\delta x)$ over the range of values for d^* . As a consequence of the assumption of periodic surfaces, the function is roughly symmetric with respect to half the horizontal box size (hence the plateau and the following drop for large values of δx).

Chapter 4. Emergence of self-affine surfaces during adhesive wear

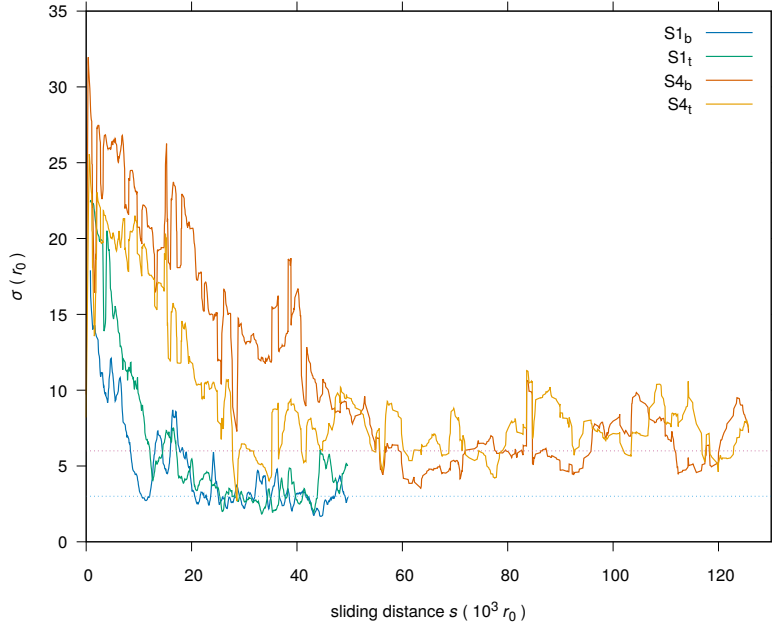


Figure S4.5 – Scaling of the root mean square of heights σ with system size. See Section 4.4 for the definition of σ . Surfaces are taken from the large simulation S4 and from simulation S1, which is run under the same conditions but has half the horizontal box size than simulation S4 (cf. Table 4.1). The different steady-state values are consistent with the size dependency of σ . In a first approximation, assuming the same Hurst exponent, the ratio between the values of σ of two surfaces is $\frac{\sigma_{\text{new}}}{\sigma_{\text{ref}}} \approx \left(\frac{\lambda_{\text{new}}}{\lambda_{\text{ref}}}\right)^H$, where λ_{new} is the largest wavelength represented by the surface for which we do not know σ and λ_{ref} is the largest wavelength of the reference surface for which σ is known. It is reasonable to assume that the largest wavelength is proportional to the system size in our case. Assuming $H = 0.7$, the expected ratio for our simulations is approximately 1.5. In the figure the straight horizontal dotted lines corresponds to $\sigma = 3 r_0$ and $\sigma = 6 r_0$ respectively, which gives a ratio of 2. While the latter is larger than expected, the order of magnitude is comparable and acceptable, given the noise in the data and the assumption that the Hurst exponent is the same for the two surfaces.

4.5. Supplementary materials

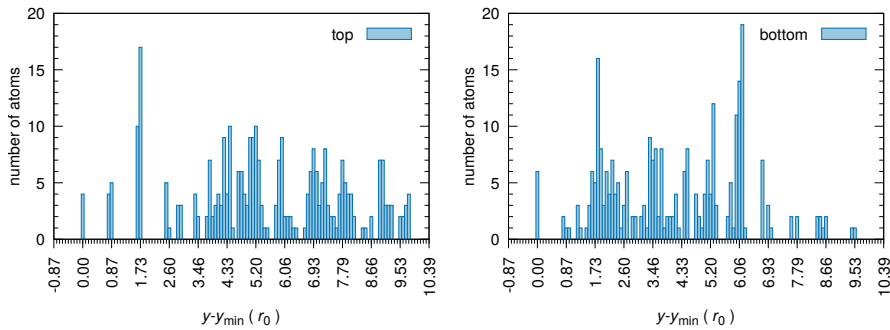


Figure S4.6 – Height distribution for top (left) and bottom (right) surfaces of simulation S1 at sliding distance $29950 r_0$, as in Figure 4.1d, after minimization to avoid effects due to temperature fluctuations. The minimum height y_{\min} in the data set is subtracted from each point's y coordinate. Heights are distributed in bins of size $0.1 \cdot \sqrt{3}/2 r_0$, corresponding to one tenth of the lattice spacing in the y direction. Values in labels along the x axis are in multiples of $\sqrt{3}/2 r_0$; subtics are $0.1 \cdot \sqrt{3}/2 r_0$ apart. The spread of the heights shows that the lattice planes are not aligned across the sample and confirms that deformation mechanisms (such as dislocations) play a role in the roughening of the surface.

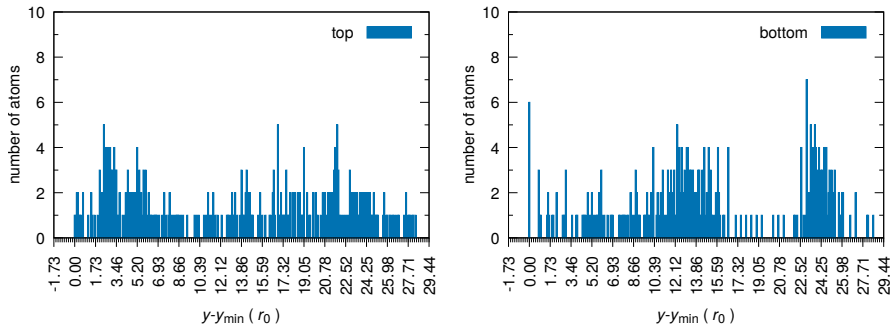


Figure S4.7 – Height distribution for top (left) and bottom (right) surfaces of simulation G1 at sliding distance $29750 r_0$, as in Figure 4.1p, after minimization to avoid effects due to temperature fluctuations. The minimum height y_{\min} in the data set is subtracted from each point's y coordinate. Heights are distributed in bins of size $0.1 \cdot \sqrt{3}/2 r_0$, corresponding to one tenth of the lattice spacing in the y direction. Values in labels along the x axis are in multiples of $2 \cdot \sqrt{3}/2 r_0$; subtics are $0.2 \cdot \sqrt{3}/2 r_0$ apart. The spread of the heights shows that the lattice planes are not aligned across the sample. In this case, where grain boundaries are modelled, the effect is even more pronounced (cf. height distribution for single crystal simulation in Supplementary Fig. S4.6). Grain rotation, in fact, provides an additional mechanism for the surface roughening, besides those already present in the single crystal case (such as dislocations).

Chapter 4. Emergence of self-affine surfaces during adhesive wear

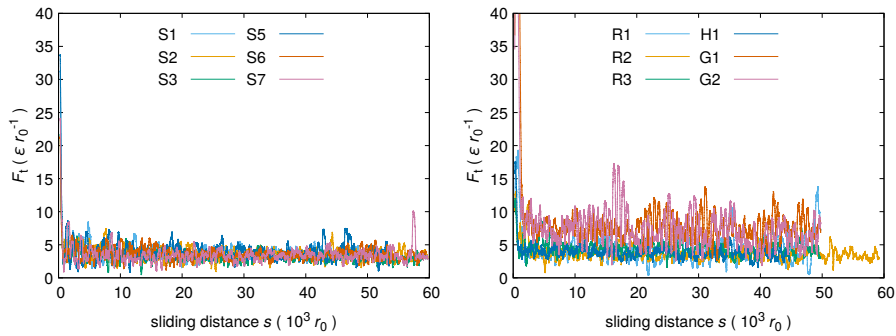


Figure S4.8 – Evolution of tangential force F_t with the sliding distance s . Left: the single-asperity simulations, right: all other simulations. After initial peaks due to the debris particle formation [73], F_t oscillates around a steady-state value. Simulation R1 displays large local oscillations due to re-roughening of the surface (cf. Figure 4.3). Simulations G1 and G2 globally display larger oscillations as a consequence of the presence of grain boundaries (cf. Figure S4.12).

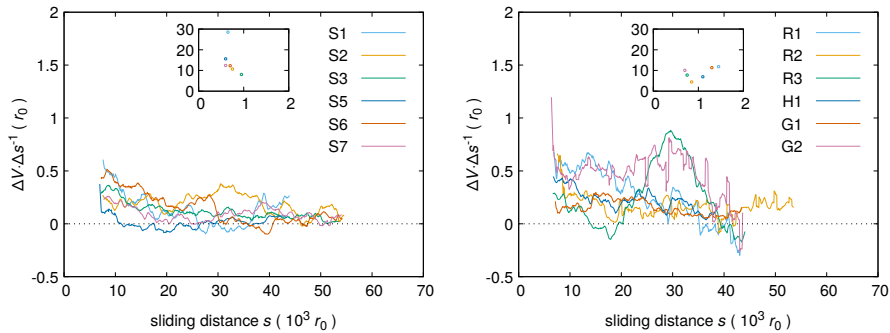


Figure S4.9 – Evolution of the wear rate with the sliding distance s . The wear rate is expressed as the ratio between the change of volume ΔV and the change of sliding distance Δs for the single-asperity simulations (left) and all others (right). The insets show the value of $\Delta V/\Delta s$ upon debris particle formation. In all cases the wear rate decreases from a high initial value due to particle formation (inset) to lower values (main plot), indicating two distinct regimes corresponding respectively to two- and three-body sliding configurations. The dotted, black, straight guide-lines show the null wear rate, i.e. the debris particle would neither accumulate nor lose volume.

4.5. Supplementary materials

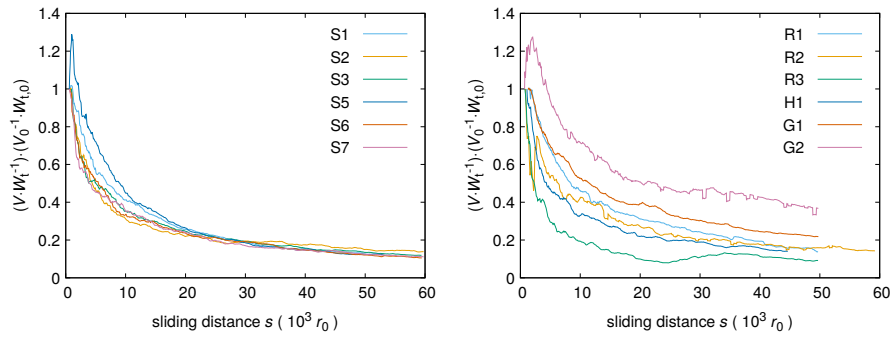


Figure S4.10 – Evolution of the ratio V/W_t between the wear volume V and the tangential work W_t with the sliding distance s . Left: single-asperity simulations, right: all other simulations. The ratio is normalized by the tangential work $W_{t,0}$ and volume V_0 produced during the formation of the wear particle. The ratio is not constant, hinting at a change in the behaviour of the wear volume evolution after running-in.

Chapter 4. Emergence of self-affine surfaces during adhesive wear

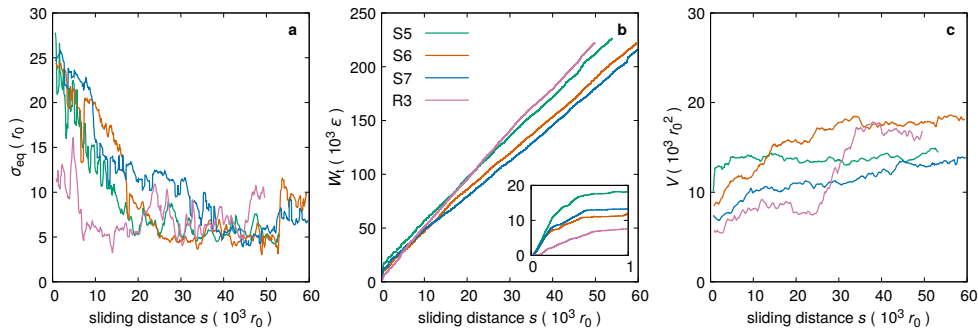


Figure S4.11 – Evolution of equivalent roughness σ_{eq} , frictional work W_t , and wear volume V . See Section 4.4 for the details on the definition of these quantities. See Figure 4.3 and Supplementary Fig. S4.12 for further simulations. a) Evolution of σ_{eq} for the composite surface for simulations S5, S6, S7, and R3 (see Table 4.1 for details). While for most simulations the value of σ_{eq} stabilizes, cold temperatures (S7) can slow down this stabilization (see Supplementary Discussion, Section 4.5.2). b) Evolution of the tangential work W_t with the sliding distance. The work exhibits a sharp increase upon formation of the debris particle (inset) [73], after which the rate decreases and stabilizes. c) Evolution of the wear volume of the rolling debris particle, as defined only after its formation. In all simulated conditions the wear rate after the debris particle formation is small compared to the ratio of the initial particle size over the sliding distance necessary to form the particle (cf. Supplementary Fig. S4.9), consistent with the transition from severe to mild wear. In simulation R3, a significant temporary increase in the wear rate appears in the range of sliding distance $[25 \cdot 10^3; 35 \cdot 10^3] r_0$. No significant change in σ_{eq} , W_t or F_t (cf. Supplementary Fig. S4.8) is linked to this change in volume, thus further investigation on its origin is needed.

4.5. Supplementary materials

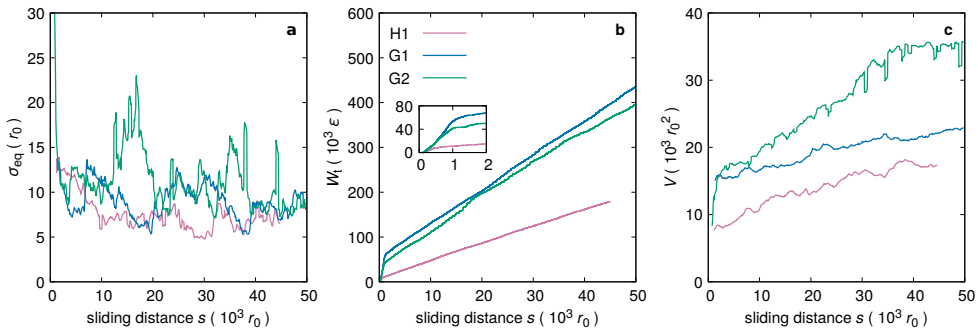


Figure S4.12 – Evolution of equivalent roughness σ_{eq} , frictional work W_t , and wear volume V . See Section 4.4 for the details on the definition of these quantities. See Figure 4.3 and Supplementary Fig. S4.11 for further simulations. a) Evolution of σ_{eq} for the composite surface for simulations H1, G1, and G2 (see Table 4.1 for details). For simulation H1 the value of σ_{eq} stabilizes, and also for simulation G1 it appears to reach a steady-state, but with larger oscillations. A similar behaviour, with even larger oscillations, is observed for G2. The larger oscillations are a consequence of the presence of grain boundaries, which force the bulk to break along the boundaries or within the least tough potential, thus favouring the removal of chunks of material (cf. Supplementary Movie 1). This also leads to larger tangential work (b) input into the system. b) Evolution of the tangential work W_t with the sliding distance. The work exhibits a sharp increase upon formation of the debris particle (inset) [73], after which the rate decreases and stabilizes. c) Evolution of the wear volume of the rolling debris particle, as defined only after its formation. In all simulated conditions the wear rate after the debris particle formation is small compared to the ratio of the initial particle size over the sliding distance necessary to form the particle (cf. Supplementary Fig. S4.9), consistent with the transition from severe to mild wear [75].

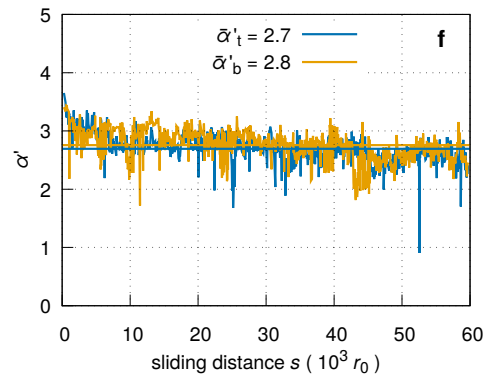
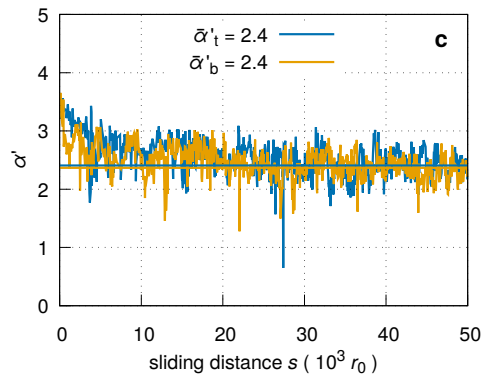
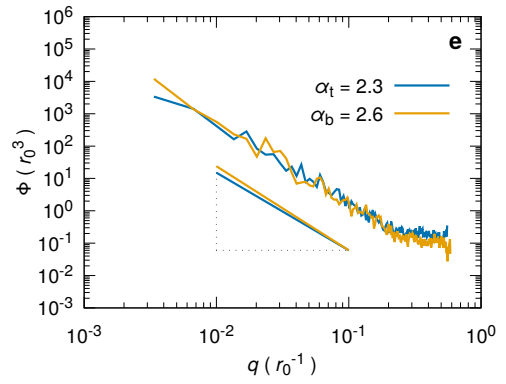
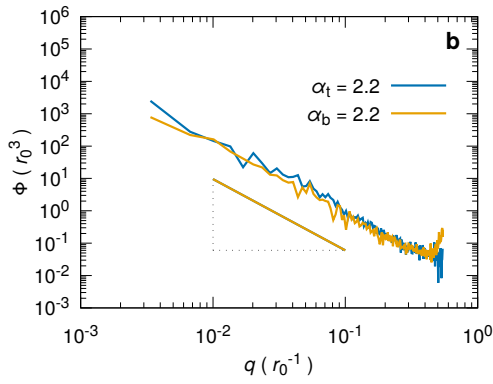
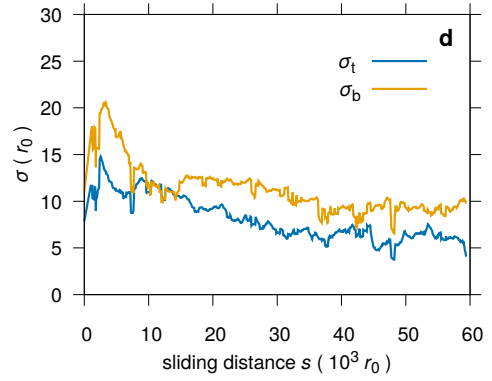
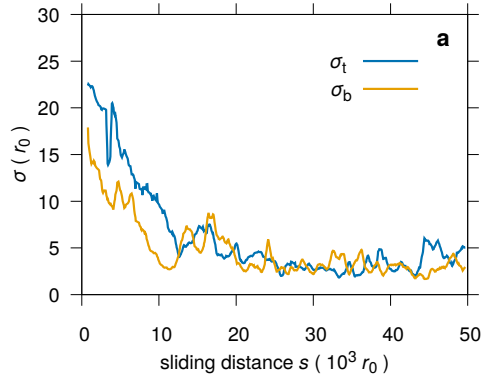
Chapter 4. Emergence of self-affine surfaces during adhesive wear

Figure S4.13 – Comparison between simulations run at different temperatures. Power spectrum analyses for top and bottom surfaces of simulations S1 (a–c) and S3 (d–f) are shown, where the main difference between the two is the temperature T (see Table 4.1). a) Evolution of σ shows that running-in takes place, but that is over within the first half of the simulation. b) PSD per unit length Φ of top and bottom surfaces averaged over ten different time steps in the stabilized state ($r_0 > 30\,000$). The straight segment represents a linear fit with exponents α_t and α_b . c) Linear fit exponent α' for the PSD during the whole simulation. The displayed means are averaged during the stabilized state only ($r_0 > 40\,000$) and have standard deviations 0.24 (top) and 0.20 (bottom). The values for the whole simulation are $\alpha'_t = 2.41 \pm 0.24$ and $\alpha'_b = 2.37 \pm 0.20$. d) No clear distinction between a transient phase and a more stable one appears for the colder case (see also Figure 4.3). e) PSD per unit length Φ of top and bottom surfaces averaged over ten different time steps ($50\,000 < r_0 < 60\,000$). The straight segments represent a linear fit with exponents α_t and α_b . f) Linear fit exponent α' for the PSD during the whole simulation. The displayed means are average values over the whole simulation with a standard deviation equal to 0.23 (top) and 0.26 (bottom).

4.5. Supplementary materials

Simulation S1 ($T = 0.075 \epsilon$)

Simulation S3 ($T = 0.025 \epsilon$)



4.5.2 Supplementary discussion

Surface roughness evolution More insights are gathered by analysing the evolution of the surface roughness throughout the whole simulated sliding distances. Indeed, it has been observed experimentally that the adhesive wear process is characterized by two regimes, both in metals [75] and rocks [147]: a transient phase (or running-in) and a steady-state phase. The transient phase takes place at the beginning of the wear process and it is characterized by a decreasing wear rate, which at some point stabilizes, transitioning to the steady-state phase [75]. The change in the wear process is ascribed to the change in the morphology of the surfaces in contact [37, 75, 147]: the roughness of the surfaces (expressed in terms of centred line average roughness or root mean square of heights) is reduced or increased during the transient phase, until it reaches a stabilized value and a constant contact area, leading to a constant wear rate as described by Archard [50].

Figure 4.3 displays the evolution of the equivalent roughness σ_{eq} , of the work W_t performed by the tangential force, and of the volume V of the debris particle for some representative simulations (cf. Supplementary Fig. S4.11 and S4.12 for further simulations). Focussing first on the evolution of the roughness (see Figure 4.3a) it can be seen that the value of σ_{eq} undergoes a sharp increase upon debris particle formation, and then decreases, settling around the value $\sigma_{\text{eq}} \approx 5 r_0$ for most simulations. This is consistent with the abovementioned picture of a two-regime wear process. The value of σ_{eq} depends of the size of the system, and it is larger for larger systems (see Supplementary Fig. S4.5), as more wavelengths are involved in the description of the surface in the PSD.

The different behaviour observed in the simulation S3 is attributed to the lower temperature of the simulation, which is responsible for inhibiting plastic deformations and diffusion along the surfaces: this results in a more brittle behaviour and a longer running-in phase, which does not appear to finish within the investigated timescale. We thus take this simulation as a reference to investigate the transient phase of the adhesive wear process. We perform a linear fit of $\log(\text{PSD})$ over the whole simulation and monitor the fitting parameter α' (Supplementary Fig. S4.13f). α' does not stabilize, consistent with the fact that no steady-state has been reached yet, and its average value is 2.7, which is larger than the value of 2.5 found during the steady-state (Supplementary Fig. S4.13c). Assuming that the surfaces are also fractal in the transient phase stage, the linear fitting parameter α' provides an estimate of the PSD scaling exponent, and the surfaces during running-in are thus expected to

be rougher than at steady-state ($H \approx 0.85$).

The decreasing value for the linear fit coefficient α' and the steady-state value discussed above suggest a decrease of the Hurst exponent during the running-in, which in turn indicates an uneven decrease in the powers with the wavevectors, i.e. the different wavelengths forming the surface are smoothed in a different fashion. While further investigations are needed to accurately determine the origins of this behaviour, a possible explanation is that large wavelengths are smoothed proportionally more than short wavelengths. This is consistent with experimental findings in wear-polished cobblestone surfaces [40], where powers at long wavelengths undergo larger reduction than short ones, and may explain the large roughness reduction found at larger scales in experiments of rock against rock sliding contact [28]. Recalling the smoothing and re-roughening mechanism put forward in Section 4.2.2, when a fragment is removed from a surface, it smooths the wavelengths larger than the fragment (and roughens those that are smaller). In the three-body configuration, the size of the contact between the debris particle and the opposing surface sets an upper limit for the dimension of newly formed fragments: wavelengths larger than the contact size are therefore expected to always smooth. Shorter wavelengths are smoothed and re-roughened continuously instead, hence the different smoothing rate (and the change in α'). We also observe that the large σ values in the early stage are due to the localization of the material removal in the surface upon the formation of debris particle; as the removed volume has a non-negligible size at the scale of our simulations, it is expected to affect the powers of the large wavelengths more. During the process that reduces σ , then, the power at large wavelengths decreases proportionally more than at short wavelengths, thus reducing the α' values.

Chapter 5

The role of interfacial adhesion on minimum wear particle size and roughness evolution

Adhesion between two bodies is a key parameter in wear processes. At the macroscale, strong adhesive bonds are known to lead to high wear rates, as observed in clean metal-on-metal contact. Reducing the strength of the interfacial adhesion is then desirable, and techniques such as lubrication and surface passivation are employed to this end. Still, little is known about the influence of adhesion on the microscopic processes of wear. In particular, the effects of interfacial adhesion on the wear particle size and on the surface roughness evolution are not clear, and are therefore addressed here by means of molecular dynamics simulations. We show that, at short timescales, the surface morphology and not the interfacial adhesion strength dictates the minimum size of wear particles. However, at longer timescales, adhesion alters the particle motion and thus the wear rate and the surface morphology.

Disclaimer This chapter is reproduced from the preprint version of the article Milanese, E., Brink, T., Aghababaei, R. & Molinari, J.-F. The role of interfacial adhesion on minimum wear particle size and roughness evolution [155]. At the time of writing of this dissertation, the manuscript is under consideration at a peer-reviewed journal covering topics in traditional and interdisciplinary physics, and it is freely accessible at <https://arxiv.org/abs/2003.10192>. I personally conducted the design and running

Chapter 5. The role of interfacial adhesion on minimum wear particle size and roughness evolution

of the simulations, the analysis of the results, the discussions, and the writing of the article (figures included).

5.1 Introduction

Wear, the removal of material from interacting surfaces, not only influences the durability of mechanical systems, but is also a source of health concerns. Frictional processes that normally take place when a vehicle is in motion (e.g. a car's brakes being pulled together, tyre on pavement) release wear particles in the air. Such airborne particles are known to be a health hazard, as they are associated with an overall increase of death risk [11, 12]. In particular, the size of the airborne particles has a fundamental role in this, as particles at the nanoscale can deposit in lungs and other organs [11, 13], and several countries prescribe limits to the concentration of fine particles in the air. We thus here explore the role of adhesion on the size of wear particles, and the subsequent effects on the surface morphology, in a simplified two-dimensional setup. Adhesion is in fact known to affect significantly wear debris formation – most often its effects prevail over those due to other phenomena (e.g. corrosion, fatigue) [36]. In this case, strong bonds develop at the interface between the two surfaces, and, during sliding, bond breaking below one of the two surfaces is favoured. Material is then removed from the solid and it is either transferred to the other surface, or it comes off as a loose wear particle. Loose particles form then the third-body, which alters the system configuration and dynamics [52], before being eventually evacuated from the contact and released into the atmosphere.

Early pioneering work already put forward the concept of a critical contact size for adhesive wear particles to form upon contact [36]. More recent advances in the understanding of wear led us to a more complete picture, and we now know that different mechanisms of material transfer are observed within the adhesive wear regime. For low adhesion and light loads, wear follows an Eyring-like atom-by-atom removal mechanism [80, 81, 111, 156–158]. More relevant for particle formation are higher loads and adhesion. In this regime, we now understand that the particle formation criterion [59] is defined by the competition between plastic deformation [51, 59, 111, 134] and brittle fracture [50, 59, 131, 135, 136] of the contacting asperities. This transition from ductile to brittle behavior is governed by a material-dependent critical length scale d^* [59]. If the junction d formed upon contact by the colliding asperities is smaller than d^* , then the asperities deform plastically (Supplementary Figure S5.7a). Vice versa, if $d \geq d^*$, the asperities break, form a debris

particle, and the system transitions to a three-body configuration (Supplementary Figure S5.7a). The critical length scale d^* has the form

$$d^* = \Lambda \frac{w}{\tau_j^2/2G}, \quad (5.1)$$

where τ_j is the junction shear strength (affected by the adhesion strength and bulk properties), G is the shear modulus of the material, w is the fracture energy and Λ is a geometrical factor (which is of order unity and takes into account the shape of the colliding asperities). This critical length scale d^* explains the resulting transition to a three-body system by a brittle mechanism, which is needed to evolve the initial surface topography into a self-affine morphology [131], and provides further insights into the process of wear debris formation [72, 73, 84, 85, 159]. Furthermore, consistent with the definition of Eq. 5.1, it has recently been shown that lower values of interfacial adhesion (i.e. lower τ_j) leads to larger debris volumes upon formation (larger d^*), if the initial surfaces are both atomistically flat except for a well-defined asperity [160].

Yet it is not clear how reductions in the interfacial adhesion strength affect the debris particle formation process for different initial surface morphologies. Frictional surfaces indeed often appear self-affine [27, 38–40], that is they are rough over many length scales. Investigating self-affine surfaces is thus the next natural step following the understanding of the simplified case of well-defined asperities [160]. Moreover, at longer timescales the reduced interfacial adhesion also influences the motion of the debris particles, possibly altering the mechanisms that govern the roughness evolution observed in the full adhesion case [131]. Therefore, the present study is concerned with investigations of self-affine surfaces and of the interplay between their geometry, the interfacial adhesion, and the particle formation and evolution.

5.2 Materials and methods

The study consists of two sets of molecular dynamics simulations and each set is characterized by a different simulated timescale. In both sets, dry sliding of two opposing two-dimensional (2D) surfaces is investigated, at constant temperature, normal pressure, and sliding velocity. The initial surfaces are self-affine (with Hurst exponent H between 0.3 and 1.0) and both consist of the same bulk material. Three different values of interfacial adhesion $\tilde{\gamma}$ are investigated: $\tilde{\gamma} \in \{1.0, 0.8, 0.6\}$. The interfacial adhesion is expressed in dimensionless terms as $\tilde{\gamma} = \gamma_{\text{int}}/\gamma_{\text{bulk}}$, where γ_{int}

Chapter 5. The role of interfacial adhesion on minimum wear particle size and roughness evolution

is the surface energy of passivated atoms on the surfaces and γ_{bulk} is the surface energy without any passivation. For $\tilde{\gamma} = 1.0$, the full adhesion case is recovered. For $\tilde{\gamma} < 1.0$ we speak of reduced interfacial adhesion. During the simulations, atoms belonging to a free surface are detected on the fly and the interaction potential between such atoms is re-assigned to the interfacial adhesion potential characterized by $\tilde{\gamma}$ in order to model passivation of the surfaces [160]. Atom interactions, both in the bulk and between the two different surfaces, are described by the same class of model pair potentials [59, 131]. These potentials allow to explicitly capture at acceptable computational costs the ductile-to-brittle transition in adhesive wear that takes place in the moderate to large adhesion limit [59]. To include such transition within our simulation box, the chosen potential is characterized by d^* smaller than the horizontal box size l_x . The short-timescale set of simulations provides insights into the effect on adhesion and random surface topography upon debris particle formation, while the long-timescale simulations allow us to study the effects of adhesion on the long-term surface roughness evolution and on the wear rate.

Throughout the article, quantities are measured in reduced units, the fundamental quantities being the equilibrium bond length r_0 , the bond energy ε at zero temperature, and the atom mass m .

5.2.1 Interaction potentials

All simulations belonging to this study are run with scaled versions of the same potential, which belongs to the same class of model pair potentials introduced in Ref. [59] and also used in Ref. [131]. This family of model potentials is a modified version of the Morse potential [127]:

$$\frac{V(r)}{\varepsilon} = \zeta \begin{cases} (1 - e^{-\alpha(r-r_0)})^2 - 1 & r < 1.1r_0 \\ c_1 \frac{r^3}{6} + c_2 \frac{r^2}{2} + c_3 r + c_4 & 1.1r_0 \leq r \leq r_{\text{cut}} \\ 0 & r_{\text{cut}} \leq r \end{cases}, \quad (5.2)$$

where ζ is a scaling factor that equals 1 for bulk atoms and can be smaller than 1 for surface atoms, r is the distance between two atoms, ε is the bond energy at zero temperature, r_0 is the equilibrium bond length, and $\alpha = 3.93 r_0^{-1}$ governs the bond stiffness. The c_i coefficients are chosen such that the potential $V(r)/\varepsilon$ is continuous both in energy and force. The cut-off distance is set by r_{cut} and determines the inelastic behavior. This allows for changes in the potential tail (and, thus, in the

material yield strength), while keeping the same elastic properties up to a 10% bond stretch. The potential adopted in this study to model the bulk is characterized by $r_{\text{cut}} = 1.48 r_0$. In Refs. [59] and [131] this potential is called P4. The interfacial potentials, i.e. the potentials used to represent the adhesion between passivated atoms, are scaled versions of the bulk potential. Three scaling factors ζ are used, which corresponds to the three different $\tilde{\gamma}$ investigated: 1.0 (full adhesion), 0.8, and 0.6. The on-the-fly algorithm to assign surface atoms to the interfacial adhesion potential is the same adopted in Ref. [160] and works as follows. At time $t = 0$ all the atoms belong to the bulk potential. All atoms in the simulation box (except those where a thermostat or displacements are prescribed) are then checked every 1000 time steps: if their coordination number is less or equal to n_c , they are considered to belong to a free surface and thus passivated and are re-assigned to the interfacial potential chosen for that simulation. We used $n_c = 15$ (within a radius of $2.23 r_0$) as in Ref. [160].

5.2.2 Simulation geometry and boundary conditions

All simulations were performed in 2D using the molecular dynamics simulator LAMMPS [125]. A simple scheme of the simulation setup is shown in Supplementary Figure S5.7. Two different horizontal box sizes have been adopted, i.e. $l_x = 339.314 r_0$ (sets S and L) and $l_x = 678.627 r_0$ (set L, see below). Periodic boundary conditions are enforced along the horizontal direction. The initial vertical box size is the same for all simulations of all sets and is $l_y = 394.823 r_0$, the box is then allowed to expand vertically, e.g. upon debris particle formation. A constant pressure ($f_y = 0.02 \epsilon r_0^{-2}$) is applied on the top and bottom boundaries to press the surfaces together and avoid that the surfaces are driven away by inertia at the first collision. A constant horizontal velocity $v_{\text{ref}} = 0.01 \sqrt{\epsilon m^{-1}}$ is imposed on the first layer of atoms of the top surface. The bottom layer of atoms of the bottom surface is fixed. A temperature of 0.075ϵ (expressed in terms of equivalent kinetic energy per atom) is enforced by means of Langevin thermostats with a damping parameter of $0.05 r_0 / \sqrt{\epsilon m^{-1}}$. On each body, the thermostats are applied to the three layers of atoms next to the layer where the fixed displacement or velocity is imposed. The time integration is performed with a time step of $0.005 r_0 / \sqrt{\epsilon m^{-1}}$. The two sets differ in the duration of the simulated timescale: set L contains long-timescale simulations, for a total of minimum 1.200 billion and maximum 3.113 billion time steps, while all simulations in set S are run for 40 million time steps. The main features of the two sets are summarized in Supplementary Tables S5.1, S5.2, S5.3, and S5.5. The starting

Chapter 5. The role of interfacial adhesion on minimum wear particle size and roughness evolution

geometry of the system is obtained by filling the whole simulation box with atoms relaxed at the target temperature, and then removing a subset of them based on a purely geometric criterion to obtain two distinct rough surfaces. The self-affine morphology is generated with a random phase filter [150].

5.2.3 Self-affine surfaces

The same definitions and conventions of Ref. [131] are adopted throughout the manuscript and are briefly summarized here. For more details on fractal concepts, see Refs. [94] and [96].

Fractal surfaces whose heights $h(x)$ scale differently than the horizontal distance x are self-affine fractals, and they obey the scaling relation $h(\xi x) \sim \xi^H h(x)$ [94], where ξ is the scaling factor and H is the Hurst (or roughness) exponent, with $0 < H < 1$ for fractional Brownian motion (fBm) [97]. The Hurst exponent describes the correlation between two consecutive increments in the surface: if $H = 0.5$, the increments are randomly correlated (i.e. standard Brownian motion), if $0 < H < 0.5$, the increments are negatively correlated, and if $0.5 < H < 1$ the increments are positively correlated.

The generation of engineering surfaces is non-stationary and random [38], and it can be described as a non-stationary process with stationary increments. This allows to relate the fractal dimension D of the surface with its Hurst exponent H through its Euclidean dimension n [97]: $D + H = n + 1$. For this class of surfaces, assuming a 1D surface profile, the fractal dimension D and the power law exponent α of the power spectral density are related as $\alpha = 5 - 2D$ [98, 144]. Under these assumptions, a direct relation between H and α is found: $H = (\alpha - 1) / 2$.

5.2.4 Surface analysis

The power spectral density (PSD) of a 1D surface $h(x)$ in terms of PSD per unit length $\Phi_h(q)$, q being the wavevector, is defined as [149]

$$\Phi_h(q) \equiv \frac{1}{L} \left| \int_L h(x) e^{-iqx} dx \right|^2, \quad (5.3)$$

where the integral is the continuous Fourier transform of $h(x)$ and L is the surface length projected on the horizontal axis x . The surface profile $h(x)$ is a continuous function and it contains the value of the surface height at each value of the spatial

coordinate x . In particular, we estimate Φ_h as

$$\Phi_h(q_n) \approx \Delta x P_h(q_n), \quad (5.4)$$

where $P_h(q_n)$ is the classical periodogram [149, 151]:

$$P_h(q_n) = \frac{1}{N} \left| \sum_{k=0}^{N-1} h_k e^{-iq_n x_k} \right|^2, \quad (5.5)$$

the summation being the discrete Fourier transform of the surface. In fact, $h(x)$ is known only at a discrete set of N points x_k ($k = 0, 1, \dots, N-1$), regularly sampled at an interval Δx , such that $h_k = h(k\Delta x)$ are the known values of $h(x)$. In our case, $\Delta x = L/N$, N being the number of atoms belonging to the surface of length L ($\Delta x \approx 1 r_0$).

The Hurst exponent H can also be estimated with the height–height correlation function [94], which describes the average change of heights Δh between two points at a horizontal distance δx :

$$\Delta h(\delta x) = \langle [h(x + \delta x) - h(x)]^2 \rangle^{1/2}, \quad (5.6)$$

where the angle brackets indicate spatial average. H can be derived by the log–log plot of $\Delta h(\delta x)$, as the height–height correlation function scales as $\Delta h(\delta x) \sim \delta x^H$.

The surface roughness, that is the variations in height of the surface profile with respect to an arbitrary plane of reference [99], is measured here in terms of the equivalent root mean square of heights

$$\sigma_{\text{eq}} = \sqrt{\sigma_{\text{top}}^2 + \sigma_{\text{bottom}}^2}, \quad (5.7)$$

where σ_{top} and σ_{bottom} are the root mean square of heights of the top and bottom surface respectively. The root mean square of heights σ of a surface profile $h(x)$ is defined as:

$$\sigma = \sqrt{\frac{1}{N} \sum_{k=1}^N h_k^2}, \quad (5.8)$$

where N is the number of discretization points of the surface and h_k is the distance of the point k from the plane of reference (the surface mid-plane, in our case).

5.2.5 Data analysis

All the simulations were visualized with OVITO [152]. Due to the large amount of data, frames were saved every 10^6 steps for both the simulations in set L and set S.

In order to obtain the surface morphology and the debris particle volume, we need to define a way to differentiate the particle from the surfaces, since the particle is usually in contact with at least one surface. We start from the assumption that the interface between particle and surface should probably have a minimal length. As such, we chose a simulated annealing approach [161] using a semi-grand-canonical lattice Metropolis-Monte Carlo [124] algorithm to find this minimal interface by penalizing the interface as described below. We found that to reliably detect the particle without manual intervention, some heuristics for the initial state are needed. As a preparation step, we therefore split the system into horizontal bins of height $7.5 r_0$ and define those with a number density of atoms below 70% of the bulk value as likely regions for the gap between surfaces (which should contain the rolling particle). The atoms above this gap are assigned type “1” and below the gap type “2”. The very bottom and top bins are fixed to never change their type. Now two simulated annealing runs are started, each with pseudo-temperatures of $k_B T = 2.1, 0.9, 0.3$, down to 0.0. The difference between these two runs is that we switched all atoms in the gap to either type 1 or type 2 initially. We found that this works better than to use three types, one of which represents the debris particle. The Monte Carlo trial moves were performed as follows:

1. Choose a random atom i that has at least one unlike neighbor and switch its type ($1 \rightarrow 2$ or $2 \rightarrow 1$).
2. Calculate the pseudo-energy difference $\Delta E = E_{\text{after}} - E_{\text{before}}$, with

$$E = \sum_{i=1}^{N_{\text{tot}}} \sum_{j \in \text{NN}_i} \begin{cases} 0.0 & T_i = T_j \\ 0.8 & T_i \neq T_j \text{ and } j \in P, \\ 1.0 & T_i \neq T_j \text{ and } j \notin P \end{cases} \quad (5.9)$$

where N_{tot} is the number of atoms, NN_i is the set of atoms in the first nearest neighbor shell of i , T_i is the type of atom i , and P is the set of passivated atoms. Note that this pseudo-energy is a purely numerical parameter for the optimization algorithm. The reduced bond energy for passivated atoms favors interfaces along previously passivated regions, which we regard as the most sensible demarcations of the debris particle.

3. If $\Delta E \leq 0$ accept the trial move, else accept the trial move with probability $\exp(-\Delta E/k_B T)$.

For one Monte Carlo step, N_{tot} of these trial moves are performed. For the two high temperatures, 50 Monte Carlo steps are performed and for the two low temperatures 200. For each simulated annealing run, the lowest energy configuration is saved. These two configurations are compared, and the atoms that differ in type between the two are marked as belonging to the debris particle. This works because the two sub-surface bulk regions (top and bottom) keep their respective type 1 or 2 in both runs, while the atom types in the debris particle will depend on the initial state and thus be different in both runs. We verified by visual inspection of all simulations that the algorithm performs adequately.

Once the debris particle is identified, the surfaces are reconstructed by identifying atoms with a coordination number smaller than 15. For each surface of each analyzed time step, a bijective profile is reconstructed by linear interpolation of the N surface atoms. The surface profile is then discretized in N equally spaced points [131]. The surface analysis is performed on these discretized reconstructions of the surfaces. The PSD and structure functions are averaged over 15 samples, spaced such that the debris particle rolls over the whole surface at least one time between two consecutive samples. Data for σ and σ_{eq} is averaged over 10 consecutive data points.

The tangential force values for simulations in set S are stored every 5000 steps and are averaged over windows of 10^6 steps to have the same discretization of the volume detection algorithm (see Figure 5.2d).

The debris particle volume V and its initial volume V_0 are computed by multiplying the number of atoms belonging to the debris particle and the atomic volume [73, 131], which is $\sqrt{3}/2 r_0^2$.

5.3 Results

In the following sections we discuss the results of our investigations. In section 5.3.1, we find that the initial random morphology governs the initial debris particle volume, and deviations in the adhesion strength from the full adhesion regime do not have a significant influence. The minimum wear particle size in the general situation of rough surfaces is then predicted by the critical length scale of Eq. 5.1, with the

Chapter 5. The role of interfacial adhesion on minimum wear particle size and roughness evolution

junction shear strength given by the full adhesion case (i.e. $\tau_j = \tau_{\text{bulk}}$). At long timescales, we find that the surface morphology is self-affine with a persistent Hurst exponent, provided that the adhesion is strong enough to ensure the continuous re-working of the surfaces due to the third body (section 5.3.2), and that the reduced interfacial adhesion affects the wear particle growth (section 5.3.3).

5.3.1 Particle formation

We first focus on the effect of surface morphology and reduced interfacial adhesion in the early stage of the adhesive wear process, when the wear debris particle is formed. We thus ran 135 short-timescale simulations (set S) with a sliding distance of $2000 r_0$. Within this set, we explored different values of the interfacial adhesion ($\tilde{\gamma} \in \{1.0, 0.8, 0.6\}$), the initial Hurst exponent ($H \in \{0.5, 0.7, 1.0\}$) and the root mean square of heights ($\sigma \in \{5, 10, 20\} r_0$) of the surfaces. For each value of (H, σ) , five different random seeds are used to generate five different initial fractal surfaces. The simulations of this set are identified with the first letter 'S' (where 'S' stands for 'short timescale'), followed by three digits that are representative of the value of the interfacial adhesion $\tilde{\gamma}$, and a progressive two-digit number 01 to 45 that is linked to a set of values (H, σ, seed) : simulation S-080-01 thus indicates a short timescale simulation, with $\gamma = 0.8$ and $(H, \sigma, \text{seed}) = (0.5, 5 r_0, 19)$. Details are reported in Supplementary Tables S5.1, S5.2, and S5.3. The simulated timescale is large enough to fully reproduce the debris particle formation (see Figure 5.1) and obtain the initial debris particle volume V_0 .

We observe that at the beginning of the sliding process, when two rough surfaces come into contact, the formation of a wear particle is complex and not well defined: contact can develop at multiple spots along the surface, different contact junctions interact elastically [84, 159], and they can coalesce into fewer, larger junctions. The process of debris particle formation is then markedly affected by the surface topography and hard to predict. This situation is more complex than the simplified case of a system with two non-random surfaces, e.g. two atomistically flat surfaces exhibiting each a well-defined semicircular asperity. In such case, a contact junction is clearly formed only along the contact interface of the two asperities and Eq. 5.1 fully describes the loose particle formation. When the two asperities come into contact, they either form a junction of size $d \geq d^*$ and create a wear particle immediately, or they form a junction $d < d^*$, which, upon continuous sliding, increases until $d = d^*$ and a debris particle is formed [59]. (If the asperities are not large enough, d remains

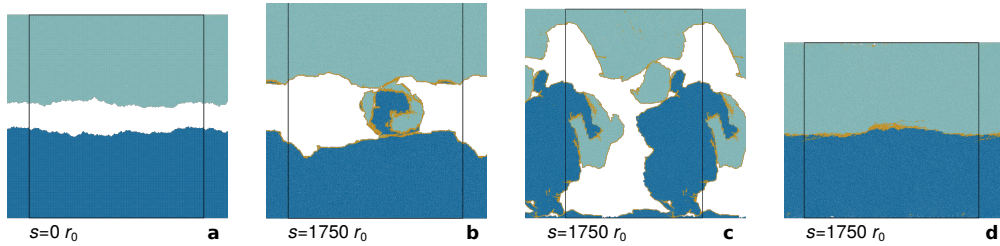


Figure 5.1 – Short timescale evolution. Starting from the same geometry (a), two different scenarios can develop. Either a well-defined debris particle is formed (Scenario 1, (b), frame from simulation S-100-01, see Supplementary Table S5.1), or the effective contact spreads throughout the interface. In the latter case (Scenario 2), the system attempts to create a debris particle comparable in size with l_x (c) (frame from simulation S-080-01, see Supplementary Table S5.2), or even larger, which results in welding of the interface within the simulated box size and damage initiating near the boundaries (d) (frame from simulation S-060-01, see Supplementary Table S5.3). In all panels colors distinguish atoms originally belonging to the top (light blue) and bottom (dark blue) surfaces. Atoms that at some previous instant were detected as surface atoms and re-assigned to the interfacial adhesion potential are depicted in yellow. Black lines represent simulation box boundaries and s is the sliding distance.

smaller than d^* and the two asperities mutually deform plastically, until the surfaces are smooth enough and welding of the interface takes place [59]).

Within the 135 simulations, two different scenarios are observed. Scenario 1: the initial collisions lead to the formation of a distinct wear debris particle – this is observed in 55.6% of the cases (75 simulations). Scenario 2: multiple interacting contact junctions form or the contact spreads throughout the whole system, and a debris particle of characteristic size $d \sim l_x$ or larger would be formed. In such cases, cracks propagate from the surface until they reach the boundaries of the system (Figure 5.1c) or the surfaces weld at the interface (Figure 5.1d). In the latter case, the periodic boundary conditions suppress any stress concentration required for crack propagation, and a larger system size would be needed to observe cracks that lead to debris particle formation. Because in Scenario 2 cracks either reach the boundaries of the simulation cell (Figure 5.1c) or are inhibited (Figure 5.1d), simulations that display such scenario are discarded from the analysis. Scenario 2 is observed in the remaining 44.4% (65 simulations).

The likelihood of one scenario or the other correlates with the root mean square of heights σ of the initial surfaces (see Supplementary Table S5.4). This is due to the fact that, for a given value of $\tilde{\gamma}$, the rougher the surface, the more pronounced the

Chapter 5. The role of interfacial adhesion on minimum wear particle size and roughness evolution

asperities and valleys, and the system is more likely to form a junction size smaller than the system size l_x (Scenario 1). When surfaces are smooth, the probability of having multiple contact spots that interact and/or coalesce is larger, and the system is more likely to attempt to create a particle of characteristic size $d \sim l_x$ or larger (i.e. Scenario 2).

Scenario 1 is also observed more often when adhesion is larger (see Supplementary Table S5.4). A reduction in $\tilde{\gamma}$ is expected to reduce the junction shear strength τ_j and thus to increase the critical length scale d^* (see Eq. 5.1). As the system needs a larger junction size to create a debris particle, contact can develop at other places at the same time, increasing the likelihood of Scenario 2.

Note that when the surface roughness and the interfacial adhesion are minimum, i.e. $\tilde{\gamma} = 0.6$ and $\sigma = 5 r_0$, no simulation displayed Scenario 1, consistent with the two effects that were just described.

For the subset of simulations that exhibit Scenario 1, i.e. a debris particle smaller than the system size is formed, the initial volume V_0 is investigated. For this, an unambiguous definition of V_0 is needed, and we use the tangential force F_t as a reference. When the two surfaces first come into contact, the tangential force F_t starts increasing. After a peak is reached, the force decreases, signaling debris particle formation and the onset of rolling (Figure 5.2). We thus define V_0 as the volume of the debris particle measured at the first local minimum exhibited by F_t , after the initial peak, as it corresponds to the work needed to form the debris particle [73]. Identified volumes are then checked for erroneous measures, which are discarded. Erroneous measures are due to false positives of the particle detection algorithm and to the tangential force exhibiting a peak and a following local minimum when the particle is not formed yet (e.g. because of an initial ductile event). This procedure allows us to compare consistent values of V_0 from the different simulations.

The data for V_0 is reported in Figure 5.3 and Supplementary Tables S5.1, S5.2, S5.3, and S5.4. We observe (Supplementary Table S5.4) that the average value of the initial volume \bar{V}_0 increases with $\tilde{\gamma}$, contrary to Eq. 5.1. While at first this seems surprising, as lower values of $\tilde{\gamma}$ imply larger d^* , we argue that this is an artifact of the system size for low values of $\tilde{\gamma}$. When reducing $\tilde{\gamma}$, more simulations display in fact Scenario 2, i.e. the system attempts to form a debris particle that is too large with respect to the simulation cell. These cases are then not captured by the values of \bar{V}_0 that we measured.

When identical initial geometries are compared (i.e. for the same values of (H, σ, seed)),

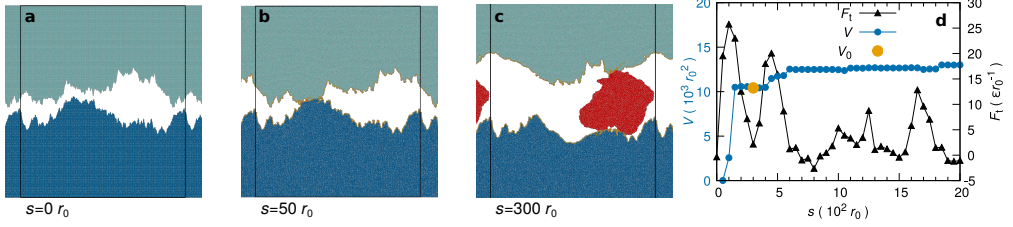


Figure 5.2 – Scenario 1: debris particle formation and initial volume V_0 . a-c) The surfaces, initially self-affine (a), come into contact at multiple points (b) and a peak in the tangential force F_t is recorded (d). Upon further sliding, the contact junction is large enough to generate a debris particle, whose formation is over (c) when the first local minimum of the tangential force F_t is reached (d). At this moment the initial debris particle volume V_0 is measured (d). d) Recorded tangential force F_t (black triangles), measured debris particle volume V (blue circles) and measured initial debris particle volume V_0 (large orange circle) during a simulation that exhibits Scenario 1. In panels (a-c) colors distinguish atoms originally belonging to the top (light blue) and bottom (dark blue) bodies; in panels (b-c) colors further identify atoms that at some previous instant were detected as surface atoms and re-assigned to the interfacial adhesion potential (yellow) and atoms detected as belonging to the debris particle (red); in panels (a-c) black lines represent simulation box boundaries. In all panels s is the sliding distance expressed in units of r_0 . Snapshots in panels (a-c) and data in panel (d) are from simulation S-060-32 (see Supplementary Table S5.3).

no correlation between the strength of adhesion and the initial volume V_0 arises. This leads to the observation that the randomness of the initial surface morphology governs the debris particle formation, in contrast to what is observed at long timescales, where the effect of adhesion is significant (see Section 5.3.3).

We now investigate the effects of the interfacial adhesion and the morphology on the minimum size of the generated debris particle. We know that the critical length scale d^* governs the particle formation process, and that the strength of the interface enters the definition of d^* by affecting τ_j : Once a junction of size $d < d^*$ is formed, if the interface is weak the asperities slide against one another, otherwise they deform plastically [85]. We thus rewrite Eq. 5.1 to make explicit the effect of the interfacial adhesion,

$$d^*(\Lambda, \tilde{\gamma}) = \Lambda \frac{2Gw}{\left(\tilde{\gamma}\tau_{j,\text{full}}\right)^2}, \quad (5.10)$$

Chapter 5. The role of interfacial adhesion on minimum wear particle size and roughness evolution

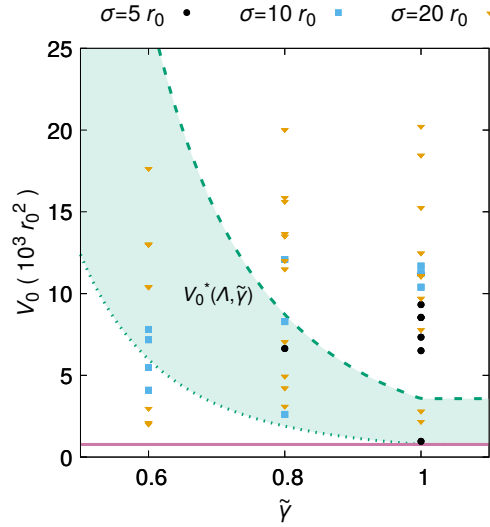


Figure 5.3 – Effect of interfacial adhesion $\tilde{\gamma}$ and surface morphology on the initial debris particle volume V_0 . In all cases V_0 is larger than the minimum size $V_{0,\min}^*$ determined by the material critical length scale (solid purple line). The actual value $V_0 \geq V_{0,\min}^*$ is controlled by the random morphology. No statistically significant increase in the minimum V_0 is observed when the interfacial adhesion decreases, as would be expected by a corresponding reduction in the junction shear strength (green shaded area). The green dotted line corresponds to $V_0^*(\Lambda_{\min}, \tilde{\gamma})$ and the green dashed line to $V_0^*(\Lambda_{\max}, \tilde{\gamma})$. Each symbol identifies a unique initial surface roughness in terms of root mean square of heights σ : $\sigma = 5 r_0$ (black circles), $\sigma = 10 r_0$ (light blue squares), and $\sigma = 20 r_0$ (orange triangles). One data point ($\tilde{\gamma} = 1.0$, $V_0 = 40339 r_0^2$, $\sigma = 5 r_0$) is not represented for readability.

where at the denominator the junction shear strength in the case of reduced interfacial adhesion is expressed as a reduction of the junction shear strength $\tau_{j,\text{full}}$ of the full adhesion case ($\tilde{\gamma} = 1.0$), with the proportionality given by $\tilde{\gamma}$ for the potentials adopted in this work [59]. In the limiting case of atomistically flat surfaces with semicircular asperities, this correctly predicts wear particle volumes that are larger when the interface is weaker [160]. To verify such prediction in the case of random rough surfaces, we assume that the minimum initial volume V_0^* is given by a circular particle (in two dimensions), i.e.

$$V_0^*(\Lambda, \tilde{\gamma}) = \frac{\pi}{4} d^*(\Lambda, \tilde{\gamma})^2. \quad (5.11)$$

V_0^* is then minimum when Λ is minimum and $\tilde{\gamma}$ is maximum, and vice versa. In

our work, the extreme values of $\tilde{\gamma}$ are the minimum and maximum input values, i.e. $\tilde{\gamma}_{\min} = 0.6$ and $\tilde{\gamma}_{\max} = 1.0$. The geometrical factor Λ is instead determined by the geometry of contact, which is non-trivial to obtain in our case of self-affine surfaces. The two limiting cases that we assume for our simulations are flat contact ($\Lambda_{\min} = 0.70$, see Section 5.5.1) [159] and contact between well-defined semicircular asperities ($\Lambda_{\max} = 1.50$) [59, 85]. If the reduced interfacial adhesion would play a key role in the initial debris particle volume V_0 , we would thus expect that

$$V_0 \geq V_0^*(\Lambda, \tilde{\gamma}), \quad (5.12)$$

where V_0 is the initial volume observed in our simulations and which is reported in Figure 5.3. The green shaded area in Figure 5.3 depicts the values of $V_0^*(\Lambda, \tilde{\gamma})$, where the limiting cases of $\Lambda = \Lambda_{\min}$ and $\Lambda = \Lambda_{\max}$ are given by the lower green dotted line and the upper green dashed line, respectively. Our results show that the initial debris particle volume V_0 does not obey the trend of Eq. 5.12, as we observe volumes V_0 measured for $\tilde{\gamma} = 0.6$ that are smaller than the expected lower bound $V_0^*(\Lambda = \Lambda_{\min}, \tilde{\gamma} = \tilde{\gamma}_{\min})$.

This shows that changes in the interfacial adhesion do not affect significantly the initial volume V_0 of the debris particle. Instead, we observe that all the recorded values of V_0 are larger than $V_{0,\min}^* = V_0^*(\Lambda_{\min}, \tilde{\gamma}_{\max})$ (solid purple line in Figure 5.3), which is the minimum d^* given in the full adhesion case. We ascribe such behavior to the morphology of the surfaces, which in the current work is random. Recently, a refined version of Eq. 5.1 was derived [85], where the junction shear strength depends on the angle of contact between the two ideal asperities. It was shown that if the angle of contact is larger than a critical value, the junction shear strength τ_j is given by $\tau_{j,\text{full}}$ and independent of $\tilde{\gamma}$. In the case of contact between self-affine surfaces, the contact junction is rough and the concept of angle of contact is ill-defined. Interlocking is thus expected in at least some cases. Furthermore, we argue that the ratio between the contact size and the thickness of the passivated layer also plays a significant role in the value of τ_j and, thus, of V_0^* . In our simulations, the junction size is much larger than the passivated layer, which is thin when the surfaces come into contact. The bulk strength thus markedly affects the junction strength τ_j , which can be approximated by $\tau_{j,\text{full}}$. If the thickness of the passivated layer were larger than the contact size, then we would expect τ_j to be influenced by $\tilde{\gamma}$ and thus d^* to be close to the reduced adhesion value $d^*(\Lambda, \tilde{\gamma}) > d_{\text{full}}^*$. (Note that in such case a proportional reduction in the fracture energy w is also expected, but the effect on τ_j is squared and thus $d^*(\Lambda, \tilde{\gamma}) > d_{\text{full}}^*$.)

Chapter 5. The role of interfacial adhesion on minimum wear particle size and roughness evolution

We also recall that for the smoothest cases ($\sigma = 5 r_0$), the likelihood of Scenario 1 correlates with the strength of the interfacial adhesion (Supplementary Table S5.4). This is consistent with the aforementioned argument that when the contact interface is thin enough (compared with the passivated layer), $\tilde{\gamma}$ affects the minimum debris particle volume (Eq. 5.10 and 5.11), as interlocking is less likely to occur.

We thus find that for the general case of rough surfaces, and for the conditions here investigated, the surface morphology dominates the minimum size of the wear debris particles. This appears independent of reductions in the interfacial adhesion strength (within the explored range of values of reduced adhesion), and is determined by the junction shear strength in the full adhesion case (i.e. by the bulk shear strength). We do not expect the surface morphology to necessarily dominate the average size of the wear particles, where effects of interfacial adhesion are expected to emerge – larger system sizes than those used in this set of simulations are needed to explore this question.

5.3.2 Long timescale self-affine morphology

Self-affine objects differ from self-similar ones by displaying anisotropic instead of isotropic scaling [94]. For a one-dimensional surface, the scaling relation is expressed as $h(\xi x) \sim \xi^H h(x)$ [94, 96], where $h(x)$ is a function describing the surface heights as a function of the spatial coordinate x , ξ is the scaling factor, and H is the Hurst (or roughness) exponent [96, 97]. This relation shows how the heights scale differently than the horizontal distances, with H the scaling exponent. For physical surfaces, the Hurst exponent is constrained between 0 and 1. In the limit $H \rightarrow 1$ isotropic scaling and, thus, self-similarity are recovered. The interest in the self-affine description of surfaces lies in the fact that, for such objects, the statistics of the surface are known at any scale once the Hurst exponent is also known. This allows to gather meaningful insights at the scale that is most convenient to investigate.

To investigate the effects of the reduced interfacial adhesion on the long term evolution of the surface morphology, the set of simulations L was prepared. It is characterized by 14 long-timescale simulations – the shortest simulated sliding distance being $60000 r_0$ and the longest $155650 r_0$. Within this set, simulations differ in the interfacial adhesion ($\tilde{\gamma} \in \{1.0, 0.8, 0.6\}$), the initial Hurst exponent of the surfaces ($H \in \{0.3, 1.0\}$), and the random seed used to generate the initial fractal surfaces. We selected such values of H to avoid that the initial surfaces are already characterized by the same roughness observed at long timescales [27, 31, 131]. The simulations

of this group are identified by a code where the first letter is 'L' for 'long timescale', the following three digits represents the value of the interfacial adhesion $\tilde{\gamma}$, and the last letter identifies a set of values (H , seed, l_x). The simulation L-100-B, for instance, indicates a long timescale simulation, with full adhesion at the interface, and $(H, \text{seed}, l_x) = (0.3, 29, 339.314 r_0)$. The length of the investigated timescales ensures that the whole running-in phase is over and a steady-state for the roughness in terms of equivalent root mean square of heights σ_{eq} is reached, allowing to analyze the surface morphology in the steady-state [131]. The initial geometry is then forgotten by the system and the measured morphology is a consequence of the frictional process. During each simulation, four stages are observed. Initially, the surfaces come into contact, possibly at multiple locations as the surfaces are randomly rough. The contacting spots then deform plastically, until the junction size d is larger than d^* and a debris particle is formed (Figures 5.4a and 5.4c). The wear particle is then constrained to roll between the surfaces, if the interfacial adhesion is large enough (Figure 5.4b). Otherwise, if the adhesion is low, the particle alternates between rolling and sticking to one surface (while sliding against the other one, Figures 5.4d-f). When the particle rolls between the two surfaces, these are continuously worn as material is transferred back and forth between the particle and each surface.

To determine if the resulting surfaces are self-affine, we investigate both their power spectral density per unit length $\Phi(q)$ and their height-height correlation function $\Delta h(\delta x)$, where q and δx are respectively the wavevector and the horizontal distance between two given points on the surface. It is known in fact that, for self-affine 1D profiles, they scale as $\Phi(q) \sim q^{-2H-1}$ [97, 98, 144] and $\Delta h(\delta x) \sim \delta x^H$ [94], respectively (see methodology in Section 5.2 for more details). Figure 5.5 and Supplementary Figure S5.8 report the results of the surface analysis for the simulations in set L. The data are averaged over different independent surfaces extracted during the steady-state roughness (in terms of equivalent root mean square of heights σ_{eq}) that follows the running-in phase [36, 37, 131]. While it is known that in the full adhesion case ($\tilde{\gamma} = 1.0$) surfaces display a self-affine morphology characterized by a persistent Hurst exponent [131], it is observed here that the self-affine description holds also in the case of reduced interfacial adhesion ($\tilde{\gamma} < 1.0$), but under some conditions.

We thus investigated the distance travelled by the debris particle in each simulation (see Figure 5.4 and Supplementary Figure S5.10). We observe that, in simulations for which $\tilde{\gamma} = 1.0$ or $\tilde{\gamma} = 0.8$, the particle travelled a comparable distance s_t (between 30000 and 35000 r_0) among the different simulations, and in all cases the surfaces exhibit self-affine behavior (see Figure 5.5 and Supplementary Figure S5.8). The

Chapter 5. The role of interfacial adhesion on minimum wear particle size and roughness evolution

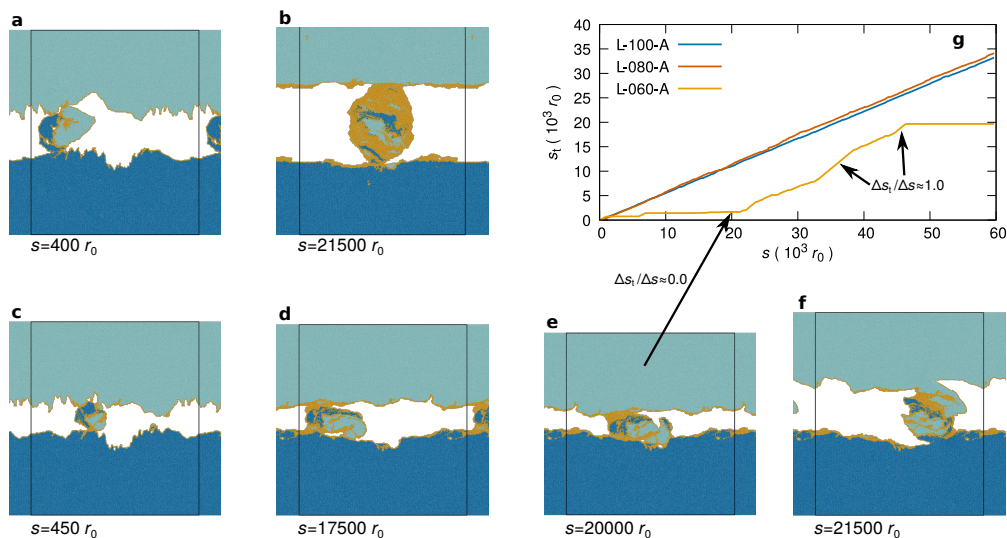


Figure 5.4 – Long timescale evolution and effect of adhesion on debris particle motion. a-b) Full adhesion, $\tilde{\gamma} = 1.0$ (frames from full adhesion simulation L-100-A, see Supplementary Table S5.5). Upon sliding, contacts develop at multiple spots and grow, until cracks develop and a debris particle is formed (a). The particle then rolls between the two surfaces, wearing them and growing significantly in size (b). c-f) Low adhesion, $\tilde{\gamma} = 0.6$ (frames from reduced adhesion simulation L-060-A, see Supplementary Table S5.5). Starting from the same geometry of the full adhesion simulation L-100-A, upon sliding a debris particle is formed (c). This is constrained between the two surfaces and, because of the reduced interfacial adhesion and perhaps counterintuitively, it can stick for long times to one of the surfaces (e.g. the bottom one in (d)), the opposing surface sliding against the particle. The particle is gradually pushed into a valley (e) and, after a sticking time (where $\Delta s_t / \Delta s \approx 0.0$, see arrow and (g)), it detaches again with a fracture event in a two-body like configuration (f). g) Distance s_t travelled by the debris particle as a function of the sliding distance. For full and intermediate adhesion simulations (i.e. $\tilde{\gamma} = 1.0$ and $\tilde{\gamma} = 0.8$), the particle rolls most of the time. For low adhesion cases ($\tilde{\gamma} = 0.6$), the particle undergoes long times of sticking to one surface (and sliding against the other). These periods are characterized by $\Delta s_t / \Delta s \approx 0.0$ and $\Delta s_t / \Delta s \approx 1.0$ (see arrows). In panels (a-f) colors distinguish atoms originally belonging to the top (light blue) and bottom (dark blue) surfaces. Atoms that at some previous instant were detected as surface atoms and re-assigned to the interfacial adhesion potential are depicted in yellow. In panels (a-f), black lines represent simulation box boundaries and s is the sliding distance. See Supplementary Figure S5.10 for data of s_t for further simulations.

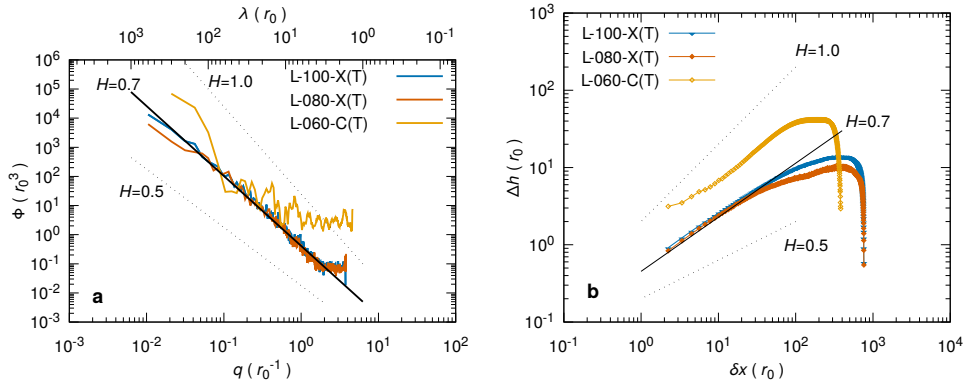


Figure 5.5 – Surface morphology analysis. a) PSD per unit length Φ as a function of the wavevector q and the wavelength λ , where $q = 2\pi/\lambda$. b) Height-height correlation function $\Delta h(\delta x) = \langle [h(x + \delta x) - h(x)]^2 \rangle^{1/2}$. The surfaces are taken from the top ('T') bodies of different simulations with different values of interfacial adhesion $\tilde{\gamma}$ and system sizes (see Supplementary Table S5.5 for details). While top surfaces of full adhesion simulation L-100-X and low adhesion L-080-X display a self-affine morphology, this is not observed for the top surface of reduced adhesion simulation L-060-C. In this case the particle travelled a longer distance s_t but did not roll for most of the simulation (see Supplementary Fig. S5.10b). In both panels the solid black straight guide-line corresponds to a Hurst exponent $H = 0.7$. Dotted black straight guide-lines show the hypothetical slope for distributions of $H = 0.5$ and $H = 1.0$. Data for all the other surfaces are reported in Supplementary Figure S5.8.

travelled distance is consistent with the estimation of $s_t = s/2$ that is expected for a particle in perfect rolling conditions. To explain this expected value of $s_t = s/2$, let us assume that both the particle and the surfaces are rigid, with the top surface sliding at constant velocity v and the bottom one fixed. The highest point of the particle is then in contact with the top surface and must be sliding at velocity v . Similarly, the lowest point is in contact with the bottom surface and its velocity is zero. The center of the particle (which coincides with the center of mass) then rolls at velocity $v/2$, and the travelled distance is half the one of the top surface, within a given time period. When $\tilde{\gamma} = 0.6$, the travelled distance s_t is markedly different, the value at the end of the simulations being between 20 000 and 26 000 r_0 (see Figure 5.4 and Supplementary Figure S5.10) or over 40 000 (see Supplementary Figure S5.10). These Figures show that the particle undergoes long periods where it continuously slides against one of the surfaces (sticking to the other one), as significant portions at constant slope $\Delta s_t/\Delta s = 0.0$ (sticking to bottom fixed surface) and $\Delta s_t/\Delta s = 1.0$ (sticking to top

Chapter 5. The role of interfacial adhesion on minimum wear particle size and roughness evolution

sliding surface) confirm. During these periods, the particle does not roll and only works the surface against which it slides, with mechanisms that differ from the ones that take place during rolling. This is reflected by larger values of σ_{eq} (see Figure 5.6) and the surfaces not always being characterized by a self-affine morphology (see Figure 5.5). We believe that longer sliding distances would compensate for this effect, i.e. the travelled distance s_t and the rolled distance would increase, allowing for the working of the surfaces that leads to the fractal morphology observed for larger values of the interfacial adhesion. This observation strengthens the hypothesis [131] that a frictional system needs to develop third bodies that work the surfaces for them to evolve into a self-affine topography. Finally, long sliding distances may also level local differences in the surface roughness evolution due, for instance, to changes over time in the interfacial adhesion. In more complex setups, environmental conditions (such as humidity and oxidation) can change during the experiment and thus their effect on the interfacial adhesion would not be constant. Such behaviour is not modelled here and may generally give a more intricate evolution of the morphology, with alternating periods of sticking/slipping and rolling. Based on our observations, long sliding distances are expected to average out such intricacies – although proper investigations are needed to draw any conclusion.

5.3.3 Wear rate

The length of simulations in set L allows us to investigate also the wear rate over long distances for different values of the interfacial adhesion. Figure 5.6b and Supplementary Figure S5.9b show the evolution of the wear volume V with the sliding distance s . Simulations with the lowest interfacial adhesion ($\tilde{\gamma} = 0.6$) display a markedly different behavior than the persistent increase in volume commonly expected, and observed for the full adhesion case [131]. For reduced interfacial adhesion cases, the wear volume V is characterized mostly by an almost zero wear rate, the particle volume being determined upon formation. This is due to the long sticking time. The low interfacial adhesion reduces or inhibits material transfer between the particle and the surface it slides against. And evidently no material is transferred between the particle and the surface it sticks to. Therefore the sliding motion involves only mutual deformation of the two bodies, without significant transfer of atoms (if anything, the wear particle seems to lose mass in some cases). After long periods of sticking, the deformation that takes place in the two bodies is such that the debris particle is again detached from the surface it sticks to. For example, during such a period of sticking, the particle can be pushed into a valley, then forced out of it

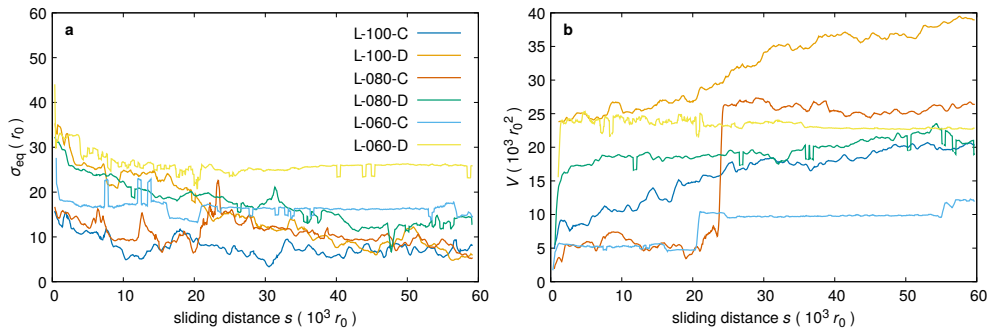


Figure 5.6 – Evolution of the equivalent roughness σ_{eq} and of the wear volume V . a) Evolution of σ_{eq} for the simulations in set L (see Supplementary Table S5.1). For simulations with $\tilde{\gamma} = 1.0$ and $\tilde{\gamma} = 0.8$, σ_{eq} decreases until a steady-state is reached, where possible fluctuations due to local events can take place. For simulations with $\tilde{\gamma} = 0.6$, the steady-state is not always reached (e.g. reduced adhesion simulation L-060-D), because of the long sticking times (see also Figure 5.4). b) Evolution of the wear volume V of the rolling debris particle, as defined only after its formation. The simulations with $\tilde{\gamma} = 1.0$ display steady growth of the particle volume, while simulations with $\tilde{\gamma} = 0.6$ are characterized by a negligible wear rate for most of the sliding distance, and the wear volume significantly increases only through fracture-like brittle events (see Figure 5.4). Simulations with $\tilde{\gamma} = 0.8$ show an intermediate behavior. Further simulations are shown in Supplementary Figure S5.9.

by a fracture-like event and finally it rolls for a while, until it sticks again (Figures 5.4c-f). These rare events can lead to significant local increases in the particle volume, as the detachment is fracture induced in a two-body configuration (Figure 5.6 and Supplementary Figure S5.9). The growth of the debris particle volume in the low interfacial adhesion case is then not continuous and is controlled by rare fracture events.

The case for $\tilde{\gamma} = 0.8$ falls between the full and low adhesion cases. While the debris particle does not display extended sticking times, the growth rate is significantly lower than in full adhesion conditions. Rare fracture events can happen and significantly affect the wear debris volume, but they are not the predominant mechanism for mass transfer between the surfaces and the debris particle.

In the most general situation, multiple debris particles form and at any time each would roll or stick/slide between the two surfaces, a part of them would be ejected from the system and new particles would be created upon further asperity collisions. This gives a more complex picture than the one investigated here, yet our observa-

Chapter 5. The role of interfacial adhesion on minimum wear particle size and roughness evolution

tions lead us to think that such effects may compensate over long timescales (as put forward in the previous paragraph when discussing the effects on the interfacial adhesion due to changes in the environment). The final surface morphology would then be statistically equivalent to the one observed here. Further investigations of more complex systems are nonetheless necessary to gain more insights and a more sound understanding.

5.4 Discussion

In this study, we performed 2D molecular dynamics simulations of frictional systems to investigate the effect of reductions in the interfacial adhesion strength and initial surface morphology on three aspects of the adhesive wear process: the minimum size of loose wear particles, the long-term evolution of the surface roughness, and the wear rate. Our results show that, within the high adhesion regime that we explored, reducing the interfacial adhesion does not fundamentally change the nature of the processes occurring when two rough surfaces slide against one another and transition into a three-body configuration.

When the initial surfaces are self-affine, as is commonly expected in real applications, reducing the interfacial adhesion does not significantly affect the minimum initial volume of the debris particle that forms in the early stages of the sliding process. The random surface morphology thus governs the minimum size of the debris particles, which is then predicted by the critical length scale d^* estimated with the values of the bulk properties (full adhesion situation). This is potentially relevant to the many engineering applications where the minimum size of wear fragments is of particular interest – for instance in the transport industry, where particle emissions play an important role in health hazards that are linked to airborne particles.

Reduced interfacial adhesion nevertheless slows down some of the processes taking place during adhesive wear, namely the evolution of the surfaces into a self-affine morphology and the debris particle growth. Over long timescales, low values of interfacial adhesion increase the possibility of the debris particle to continuously slide against one of the surfaces (and stick to the other one), almost in a temporary two-body configuration, altering the wear mechanisms. If such periods are not too long with respect to the sliding distance, the particle still has time to roll against the surfaces and work them, and the surfaces finally exhibit a self-affine morphology, otherwise no fractal scaling is observed. Furthermore, during these periods where

the particle sticks to one surface, the wear rate decreases significantly and it can become negligible.

Finally, we note that these conclusions are drawn on the basis of two-dimensional simulations, as the investigated long timescales are computationally challenging for three-dimensional systems. While analogous observations have been previously extended from 2D to 3D [59, 73, 85], further work is needed to extend our conclusions to three-dimensional systems and to engineering applications.

5.5 Supplementary materials

5.5.1 Supplementary methods

Geometrical factor Λ for flat contacts

In the original formulation of Ref. [59], the critical length scale d^* for the ductile-to-brittle transition stems from a Griffith-like criterion applied to asperities of a generic shape. According to the criterion, if the elastic energy E_{el} is larger or equal than the adhesive energy E_{ad} , crack propagation is favoured over plastic deformation, and a debris particle is formed. As the two energies scale as $E_{el} \sim d^3$ and $E_{ad} \sim d^2$, the minimum contact junction size at which crack propagation takes place is found for $E_{el} = E_{ad}$ and it has the form

$$d^* = \Lambda \frac{\Delta w G}{\tau_j^2}, \quad (5.13)$$

where τ_j is the junction shear strength (and in the general case depends on $\tilde{\gamma}$), G is the shear modulus of the material, Δw is twice the fracture energy and Λ is a geometrical factor. In the derivation of Eq. 5.13, it is assumed that the elastic energy is fully contained in the asperity volume, which is uniformly loaded at the shear junction strength τ_j . E_{el} thus depends on both the characteristic size d and the shape of the asperity. E_{ad} also depends on both, as the shape of the asperity defines the crack path and, consequently, the free surfaces that needs to be created in the fracture process. The geometrical factor Λ takes into account the shape of the asperities and the actual stress distribution (due to this shape). The meaning of Λ is clear in the

Chapter 5. The role of interfacial adhesion on minimum wear particle size and roughness evolution

expression of d^* if Eq. 5.13 is rewritten in the form used in Eq. 5.1

$$d^* = \Lambda \frac{w}{\tau_j^2/2G}, \quad (5.14)$$

where Λ regulates the ratio between the fracture energy $w = \Delta w/2$ and the stored elastic energy density $\tau_j^2/2G$. In Ref. [59], data from molecular dynamics simulations shows that $\Lambda = 1.50$ for well-defined semicircular asperities in 2D.

More recently, another formulation for d^* in two dimensions was derived based on an analytical approach in Ref. [159]. Here, the asperity is replaced by a distributed constant shear load of magnitude τ_j applied along a length d on the flat surface of a semi-infinite body. An analytical expression for E_{el} in the whole body is then provided. The value of E_{el} then depends on the length of contact d (i.e. the characteristic size of the debris particle to be detached), but not on the shape of the debris particle that is detached. The expression of the elastic energy is then

$$E_{el} = \frac{Bd^2\tau_j^2\mathcal{M}}{\pi E'}, \quad (5.15)$$

where $E' = E$ for plane stress and $E' = E/(1 - \nu^2)$ for plane strain (E and ν being the elastic modulus and the Poisson ratio of the material), B is the thickness of the semi-infinite body along the z direction, and \mathcal{M} is an infinite integral term in 2D,

$$\mathcal{M} = \int_0^\infty \frac{dy}{y}. \quad (5.16)$$

The shape of the detached particle still defines the crack path, and in Ref. [159] it assumed to be semi-circular. This leads to the adhesive energy

$$E_{ad} = \pi\gamma Bd, \quad (5.17)$$

where γ is the surface energy of the material, and two semi-circular surfaces of circumference $\pi d/2$ are created. The critical length scale is found again by imposing the condition $E_{el} = E_{ad}$, and it is (for plane stress, as in our simulations)

$$d_{\text{flat}}^* = \frac{\pi^2\gamma E}{\tau_j^2\mathcal{M}}. \quad (5.18)$$

As $\Delta w = 4\gamma$ and, for the model potentials adopted in Ref. [59] and in this work,

$E/G = 8/3$, we can express d_{flat}^* in terms of d^* :

$$d_{\text{flat}}^* = \frac{2 \pi^2}{3 \mathcal{M}} \frac{w}{\tau_j^2 / 2G} = \frac{2 \pi^2}{3 \mathcal{M}} \frac{d^*}{\Lambda}. \quad (5.19)$$

The integral \mathcal{M} is finite in our case, as it is bounded by the plastic zone ($\approx 1 r_0$), where the integral is capped ($\int_0^{r_0} dy/r_0 = 1$) and the height of the body along the y direction ($\approx 150 r_0$). It is then $\mathcal{M} \approx 6$, and

$$d_{\text{flat}}^* = \frac{\pi^2}{9} \frac{d^*}{\Lambda}. \quad (5.20)$$

which is true if $\Lambda = \pi^2/9 \approx 1.10$. In the flat contact case, Λ is then smaller than the empirical value of $\Lambda_{\text{max}} = 1.50$ found in Ref. [59] for the asperity case.

In the simulations of this current work, the first contact takes place between two rough self-affine surfaces, for which the concept of asperity is ill-defined. Furthermore, when the root mean square of heights σ of the surfaces is small, the collision between the two bodies is close to the flat contact situation. This is shown in Supplementary Figure S5.11, where it is also observed that the areas that contribute to the detached particle are not semicircular (red atoms in Supplementary Figure S5.11d). We thus derive d_{flat}^* for the general case of a semi-elliptical detached particle. Note that, as previously explained, the elastic energy E_{el} contained in the body is independent of the shape of the detached particle, and we need to generalize only the expression for E_{ad} .

As no exact formula for the perimeter of an ellipse exists, we rely on the second Ramanujan approximation, which provides an accurate estimation also in the limiting case $a/b \rightarrow 0$ (two overlapping segments), $2a$ and $2b$ being the axes of the ellipse. The formula gives the perimeter $P(a, b)$ as

$$P(a, b) = \pi(a + b) \left(1 + \frac{3h(a, b)}{10 + \sqrt{4 - 3h(a, b)}} \right), \quad (5.21)$$

where

$$h(a, b) = \frac{(a - b)^2}{(a + b)^2}. \quad (5.22)$$

We substitute for $a = d/2$ and $b = \kappa d/2$, where we assume that the major axis is the

Chapter 5. The role of interfacial adhesion on minimum wear particle size and roughness evolution

contact junction d and that the proportionality of the minor axis to the major axis is given by the scalar $0 < \kappa \leq 1$. Expressions 5.21 and 5.22 become

$$P(\kappa, d) = \pi \frac{d}{2} (1 + \kappa) \left(1 + \frac{3h(\kappa, d)}{10 + \sqrt{4 - 3h(\kappa, d)}} \right) = dp(\kappa) \quad (5.23)$$

$$h(\kappa, d) = \frac{\left(\frac{1}{2} - \frac{\kappa}{2}\right)^2}{\left(\frac{1}{2} + \frac{\kappa}{2}\right)^2}, \quad (5.24)$$

where

$$p(\kappa) = \frac{\pi}{2} (1 + \kappa) \left(1 + \frac{3h(\kappa, d)}{10 + \sqrt{4 - 3h(\kappa, d)}} \right). \quad (5.25)$$

The adhesive energy (Eq. 5.17) is now expressed as

$$E_{\text{ad}} = \gamma B d p(\kappa), \quad (5.26)$$

and the critical length scale d_{flat}^* (Eq. 5.18) becomes

$$d_{\text{flat}}^*(\kappa) = \frac{\pi p(\kappa) \gamma E}{\tau_j^2 \mathcal{M}} = \frac{\pi p(\kappa)}{9} \frac{d^*}{\Lambda}. \quad (5.27)$$

The two limit cases are $\kappa = 1$ (circular particle), for which $p(\kappa) = \pi$ and Equations 5.18 and 5.20 are recovered, and $\kappa \rightarrow 0$ (two overlapping segments), for which $p(\kappa) = 2$, and is

$$d_{\text{flat}}^*(\kappa \rightarrow 0) = \frac{2\pi\gamma E}{\tau_j^2 \mathcal{M}} = \frac{2\pi}{9} \frac{d^*}{\Lambda}, \quad (5.28)$$

and $\Lambda = 0.70 = \Lambda_{\text{min}}$.

Supplementary Figure S5.11e shows the variation of Λ as a function of the factor κ , and it grows sub-linearly for small values of κ , i.e. a high eccentricity of the ellipse gives values of Λ close to Λ_{min} .

In the case of the simulations of Supplementary Figure S5.11a-d, we can derive the minor and major axes $2a$ and $2b$ from the position at the first contact of the atoms that will later form the debris particle (Supplementary Figure S5.11d). The atoms describe two distinct portions, one on each surfaces, whose maximum and minimum lengths are estimated. The average of the two minimum (maximum)

lengths gives us an approximation of the axis $2a$ ($2b$), and, thus, $\kappa = 0.23$. We can then compute Λ from Eq. 5.27, which gives $\Lambda = 0.74$.

5.5.2 Supplementary figures

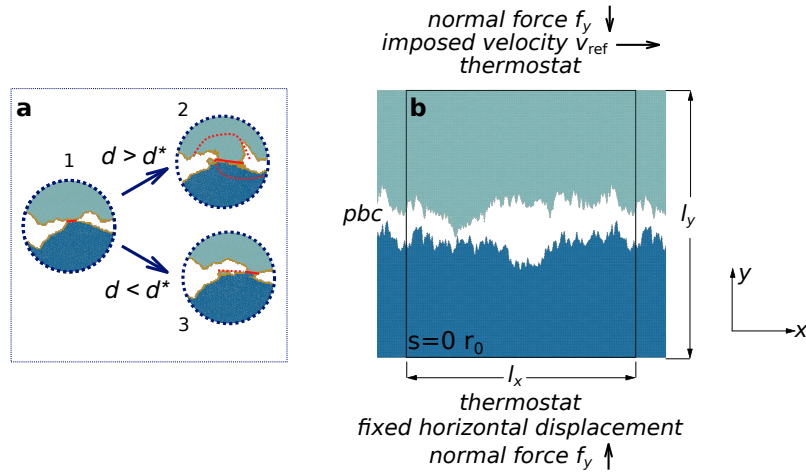


Figure S5.7 – Ductile-to-brittle transition and simulation setup. a) When two asperities collide, (1), a junction of size d is formed - if it is larger than the critical, material-dependent value d^* , cracks appear at both surfaces and a wear debris particle is formed (2), otherwise asperities smooth each other (3). Solid red lines represent the junction of size d and dotted red lines represent the crack path in (2) and the sliding distance in (3). b) Setup for both sets S and L. The bottom body has zero horizontal velocity, its first layer of atoms being fixed horizontally. The top body slides against the bottom one with velocity v_{ref} , which is imposed on the top layer of atoms. The normal force f_y pushes the two bodies against one another to ensure contact. Periodic boundary conditions are enforced along x , and the simulation box can expand and shrink along y . A thermostat in each body is applied on the layers next to the fixed boundaries. In all panels colors distinguish atoms originally belonging to the top (light blue) and bottom (dark blue) bodies. Atoms that at some previous instant were detected as surface atoms and re-assigned to the interfacial adhesion potential are depicted in yellow. In panel (b), black lines represent simulation box boundaries and s is the sliding distance (which is zero).

Chapter 5. The role of interfacial adhesion on minimum wear particle size and roughness evolution

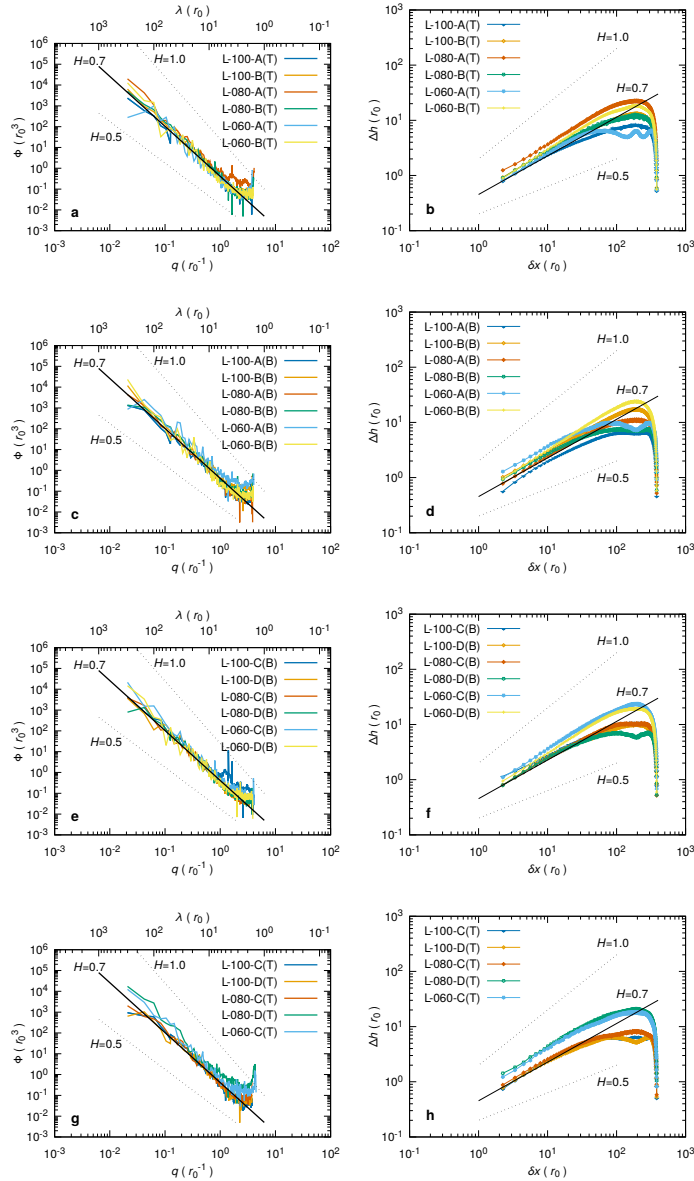


Figure S5.8 – Steady-state surface morphology analysis. Left panels: PSD per unit length Φ as a function of the wavevector q and the wavelength λ , the relation between the two being $q = 2\pi/\lambda$. Right panels: height-height correlation function $\Delta h(\delta x) = \langle [h(x + \delta x) - h(x)]^2 \rangle^{1/2}$. The surfaces are taken from the bottom ('B') and top ('T') bodies of different simulations with different values of interfacial adhesion $\tilde{\gamma}$ and system sizes (see Supplementary Table S5.5 for details). Further surfaces are reported in Figure 5.5. In all panels the solid black straight guide-line corresponds to a Hurst exponent $H = 0.7$. Dotted black straight guide-lines show the hypothetical slope for distributions of $H = 0.5$ and $H = 1.0$.

5.5. Supplementary materials

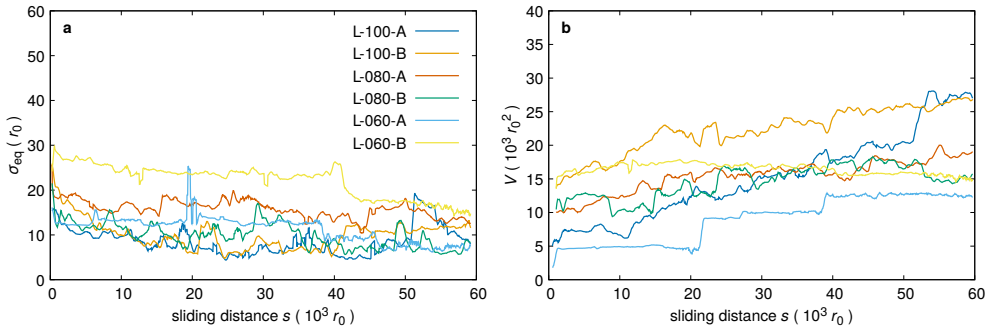


Figure S5.9 – Evolution of the equivalent roughness σ_{eq} and of the wear volume V . a) Evolution of σ_{eq} for the simulations in set L (see Supplementary Table S5.1). For simulations with $\tilde{\gamma} = 1.0$ and $\tilde{\gamma} = 0.8$, σ_{eq} decreases until a steady-state is reached, where possible fluctuations due to local events can take place. For simulations with $\tilde{\gamma} = 0.6$, the steady-state is not always reached, because of the long sticking times (see also Figure 5.4). b) Evolution of the wear volume V of the rolling debris particle, as defined only after its formation. The simulations with $\tilde{\gamma} = 1.0$ display steady growth of the particle volume, while simulations with $\tilde{\gamma} = 0.6$ are characterized by a negligible wear rate for most of the sliding distance, and the wear volume significantly increases only through fracture-like brittle events (see Figure 5.4). Simulations with $\tilde{\gamma} = 0.8$ show an intermediate behavior.

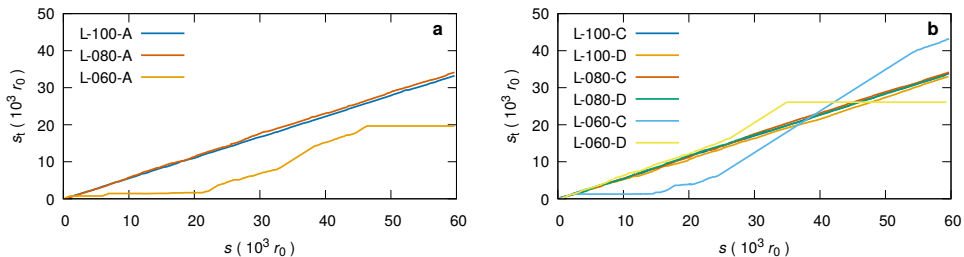
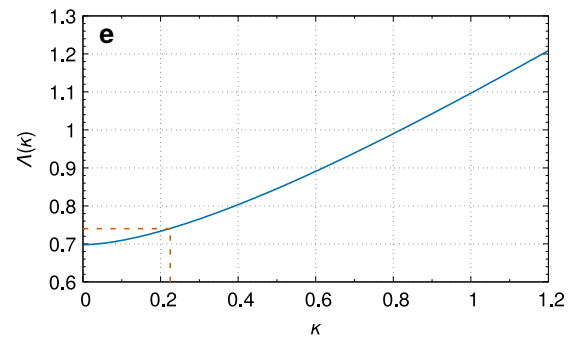
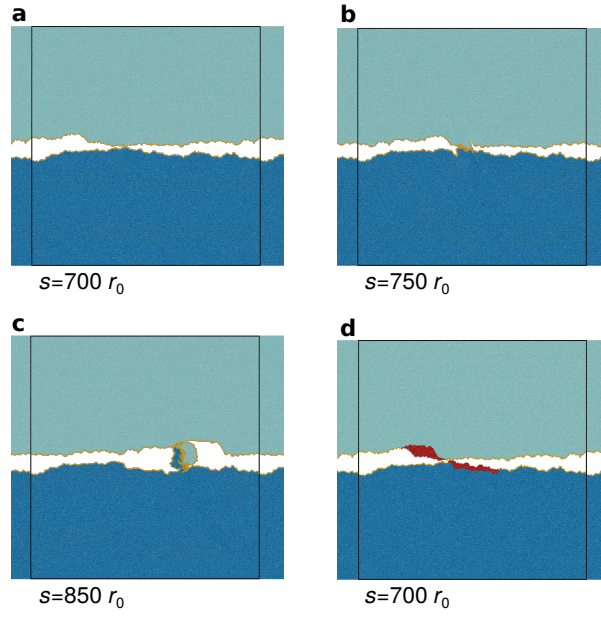


Figure S5.10 – Distance s_t travelled by the debris particle as a function of the sliding distance. For full and intermediate adhesion simulations (i.e. $\tilde{\gamma} = 1.0$ and $\tilde{\gamma} = 0.8$), the particle rolls most of the time. For low adhesion cases ($\tilde{\gamma} = 0.6$), the particle undergoes long times of sticking to one surface (and sliding against the other). These periods are characterized by $\Delta s_t / \Delta s \approx 0.0$ and $\Delta s_t / \Delta s \approx 1.0$. See Figure 5.4 for data from further simulations.

Chapter 5. The role of interfacial adhesion on minimum wear particle size and roughness evolution

Figure S5.11 – Effect of roughness on debris particle formation and d^* . a-d) The top surface slides and comes into contact with the bottom surface over a few atoms (a). Upon further sliding, the junction grows until cracks on both surfaces appear (b), and a debris particle is finally formed (c). The positions at $s = 700 r_0$ of the atoms belonging to the debris particle are highlighted in (d). In the case of rough surfaces, the initial geometry affect the stress distribution and the crack path differently than in the well-defined asperities case. This is highlighted by the distribution in the original surface of the atoms that later belong to the debris particle (d). The detached debris particle involves atoms close to the surface, and the process resembles the flat contact case [159]. This implies a smaller geometrical factor Λ in the expression of d^* than the well-defined asperities case [59] (see Supplementary Methods). e) Values of the geometrical factor Λ as a function of the shape of the detached particle for the simulations of the present work. In the case of the simulation of this Figure, the average ratio between the minor and major sizes of the two red areas (d) is $\kappa = 0.23$, which gives $\Lambda = 0.74$ (dashed orange lines). In panels (a-d) colors distinguish atoms originally belonging to the top (light blue) and bottom (dark blue) surfaces. Atoms that at some previous instant were detected as surface atoms and re-assigned to the interfacial adhesion potential are depicted in yellow. In panel (d), dark red atoms identify atoms that belong to the debris particle shown in panel (c). Black lines represent simulation box boundaries and s is the sliding distance expressed in units of r_0 . Snapshots in panels (a-d) are from simulation S-100-03 (see Supplementary Table S5.1).



Chapter 5. The role of interfacial adhesion on minimum wear particle size and roughness evolution

5.5.3 Supplementary Tables

ID	$\tilde{\gamma}$	H	$\sigma (r_0)$	seed	scenario	$V_0 (10^3 r_0^2)$
S-100-01	1.00	0.5	5	19	1	6.50
S-100-02	1.00	0.5	5	32	1	7.34
S-100-03	1.00	0.5	5	42	1	0.97
S-100-04	1.00	0.5	5	66	2	n/a
S-100-05	1.00	0.5	5	91	1	disc.
S-100-06	1.00	0.7	5	19	1	9.32
S-100-07	1.00	0.7	5	32	1	11.19
S-100-08	1.00	0.7	5	42	2	n/a
S-100-09	1.00	0.7	5	66	2	n/a
S-100-10	1.00	0.7	5	91	2	n/a
S-100-11	1.00	1.0	5	19	1	8.53
S-100-12	1.00	1.0	5	32	1	8.55
S-100-13	1.00	1.0	5	42	2	n/a
S-100-14	1.00	1.0	5	66	1	40.34
S-100-15	1.00	1.0	5	91	2	n/a
S-100-16	1.00	0.5	10	19	2	n/a
S-100-17	1.00	0.5	10	32	2	n/a
S-100-18	1.00	0.5	10	42	2	n/a
S-100-19	1.00	0.5	10	66	1	disc.
S-100-20	1.00	0.5	10	91	1	11.68
S-100-21	1.00	0.7	10	19	1	disc.
S-100-22	1.00	0.7	10	32	1	disc.
S-100-23	1.00	0.7	10	42	2	n/a
S-100-24	1.00	0.7	10	66	1	disc.
S-100-25	1.00	0.7	10	91	1	10.39
S-100-26	1.00	1.0	10	19	2	n/a
S-100-27	1.00	1.0	10	32	2	n/a
S-100-28	1.00	1.0	10	42	2	n/a
S-100-29	1.00	1.0	10	66	1	disc.
S-100-30	1.00	1.0	10	91	1	11.24
S-100-31	1.00	0.5	20	19	1	11.13
S-100-32	1.00	0.5	20	32	1	disc.
S-100-33	1.00	0.5	20	42	2	n/a
S-100-34	1.00	0.5	20	66	1	11.08

5.5. Supplementary materials

S-100-35	1.00	0.5	20	91	1	2.20
S-100-36	1.00	0.7	20	19	1	20.25
S-100-37	1.00	0.7	20	32	1	18.49
S-100-38	1.00	0.7	20	42	1	7.82
S-100-39	1.00	0.7	20	66	1	disc.
S-100-40	1.00	0.7	20	91	1	disc.
S-100-41	1.00	1.0	20	19	1	15.28
S-100-42	1.00	1.0	20	32	1	12.50
S-100-43	1.00	1.0	20	42	1	2.83
S-100-44	1.00	1.0	20	66	1	9.74
S-100-45	1.00	1.0	20	91	1	disc.

Table S5.1 – Summary of the simulations in set S: $\tilde{\gamma} = 1.0$. H , σ and 'seed' are respectively the Hurst exponent, root mean square of heights and random seed used to create the initial self-affine surface. 'scenario' indicates which of the two situations were observed in the simulations: 1 - a debris particle is formed, or 2 - no debris particle is generated because a junction comparable to the system size is formed and the surfaces weld or a debris particle of the order of the system size would form. V_0 is the initial volume of the debris particle. disc.: detected value discarded because of erroneous measures (see Section 5.3.1 for details). n/a: not applicable to simulations that displayed Scenario 2.

Chapter 5. The role of interfacial adhesion on minimum wear particle size and roughness evolution

ID	$\tilde{\gamma}$	H	$\sigma (r_0)$	seed	scenario	$V_0 (10^3 r_0^2)$
S-080-01	0.80	0.5	5	19	2	n/a
S-080-02	0.80	0.5	5	32	1	disc.
S-080-03	0.80	0.5	5	42	2	n/a
S-080-04	0.80	0.5	5	66	2	n/a
S-080-05	0.80	0.5	5	91	2	n/a
S-080-06	0.80	0.7	5	19	2	n/a
S-080-07	0.80	0.7	5	32	1	6.63
S-080-08	0.80	0.7	5	42	2	n/a
S-080-09	0.80	0.7	5	66	2	n/a
S-080-10	0.80	0.7	5	91	2	n/a
S-080-11	0.80	1.0	5	19	1	disc.
S-080-12	0.80	1.0	5	32	2	n/a
S-080-13	0.80	1.0	5	42	2	n/a
S-080-14	0.80	1.0	5	66	2	n/a
S-080-15	0.80	1.0	5	91	2	n/a
S-080-16	0.80	0.5	10	19	2	n/a
S-080-17	0.80	0.5	10	32	2	n/a
S-080-18	0.80	0.5	10	42	2	n/a
S-080-19	0.80	0.5	10	66	2	n/a
S-080-20	0.80	0.5	10	91	1	disc.
S-080-21	0.80	0.7	10	19	2	n/a
S-080-22	0.80	0.7	10	32	1	disc.
S-080-23	0.80	0.7	10	42	2	n/a
S-080-24	0.80	0.7	10	66	1	2.61
S-080-25	0.80	0.7	10	91	1	12.09
S-080-26	0.80	1.0	10	19	1	disc.
S-080-27	0.80	1.0	10	32	2	n/a
S-080-28	0.80	1.0	10	42	2	n/a
S-080-29	0.80	1.0	10	66	2	n/a
S-080-30	0.80	1.0	10	91	1	8.28
S-080-31	0.80	0.5	20	19	1	disc.
S-080-32	0.80	0.5	20	32	1	7.08
S-080-33	0.80	0.5	20	42	1	disc.
S-080-34	0.80	0.5	20	66	1	4.97
S-080-35	0.80	0.5	20	91	1	3.13

5.5. Supplementary materials

S-080-36	0.80	0.7	20	19	1	13.70
S-080-37	0.80	0.7	20	32	1	15.90
S-080-38	0.80	0.7	20	42	1	0.34
S-080-39	0.80	0.7	20	66	1	11.53
S-080-40	0.80	0.7	20	91	1	disc.
S-080-41	0.80	1.0	20	19	1	13.53
S-080-42	0.80	1.0	20	32	1	15.65
S-080-43	0.80	1.0	20	42	1	4.25
S-080-44	0.80	1.0	20	66	1	12.04
S-080-45	0.80	1.0	20	91	1	20.05

Table S5.2 – Summary of the simulations in set S: $\tilde{\gamma} = 0.8$. H , σ and 'seed' are respectively the Hurst exponent, root mean square of heights and random seed used to create the initial self-affine surface. 'scenario' indicates which of the two situations were observed in the simulations: 1 - a debris particle is formed, or 2 - no debris particle is generated because a junction comparable to the system size is formed and the surfaces weld or a debris particle of the order of the system size would form. V_0 is the initial volume of the debris particle. disc.: detected value discarded because of erroneous measures (see Section 5.3.1 for details). n/a: not applicable to simulations that displayed Scenario 2.

Chapter 5. The role of interfacial adhesion on minimum wear particle size and roughness evolution

ID	$\tilde{\gamma}$	H	$\sigma (r_0)$	seed	scenario	$V_0 (10^3 r_0^2)$
S-060-01	0.60	0.5	5	19	2	n/a
S-060-02	0.60	0.5	5	32	2	n/a
S-060-03	0.60	0.5	5	42	2	n/a
S-060-04	0.60	0.5	5	66	2	n/a
S-060-05	0.60	0.5	5	91	2	n/a
S-060-06	0.60	0.7	5	19	2	n/a
S-060-07	0.60	0.7	5	32	2	n/a
S-060-08	0.60	0.7	5	42	2	n/a
S-060-09	0.60	0.7	5	66	2	n/a
S-060-10	0.60	0.7	5	91	2	n/a
S-060-11	0.60	1.0	5	19	2	n/a
S-060-12	0.60	1.0	5	32	2	n/a
S-060-13	0.60	1.0	5	42	2	n/a
S-060-14	0.60	1.0	5	66	2	n/a
S-060-15	0.60	1.0	5	91	2	n/a
S-060-16	0.60	0.5	10	19	2	n/a
S-060-17	0.60	0.5	10	32	2	n/a
S-060-18	0.60	0.5	10	42	2	n/a
S-060-19	0.60	0.5	10	66	2	n/a
S-060-20	0.60	0.5	10	91	1	5.47
S-060-21	0.60	0.7	10	19	1	7.81
S-060-22	0.60	0.7	10	32	2	n/a
S-060-23	0.60	0.7	10	42	2	n/a
S-060-24	0.60	0.7	10	66	2	n/a
S-060-25	0.60	0.7	10	91	1	7.18
S-060-26	0.60	1.0	10	19	1	disc.
S-060-27	0.60	1.0	10	32	2	n/a
S-060-28	0.60	1.0	10	42	2	n/a
S-060-29	0.60	1.0	10	66	2	n/a
S-060-30	0.60	1.0	10	91	1	4.08
S-060-31	0.60	0.5	20	19	1	10.45
S-060-32	0.60	0.5	20	32	1	10.42
S-060-33	0.60	0.5	20	42	1	2.14
S-060-34	0.60	0.5	20	66	1	disc.
S-060-35	0.60	0.5	20	91	1	0.85

5.5. Supplementary materials

S-060-36	0.60	0.7	20	19	1	disc.
S-060-37	0.60	0.7	20	32	1	13.05
S-060-38	0.60	0.7	20	42	1	2.04
S-060-39	0.60	0.7	20	66	1	3.01
S-060-40	0.60	0.7	20	91	1	disc.
S-060-41	0.60	1.0	20	19	1	disc.
S-060-42	0.60	1.0	20	32	1	13.02
S-060-43	0.60	1.0	20	42	1	disc.
S-060-44	0.60	1.0	20	66	1	disc.
S-060-45	0.60	1.0	20	91	1	17.67

Table S5.3 – Summary of the simulations in set S: $\tilde{\gamma} = 0.6$. H , σ and 'seed' are respectively the Hurst exponent, root mean square of heights and random seed used to create the initial self-affine surface. 'scenario' indicates which of the two situations were observed in the simulations: 1 - a debris particle is formed, or 2 - no debris particle is generated because a junction comparable to the system size is formed and the surfaces weld or a debris particle of the order of the system size would form. V_0 is the initial volume of the debris particle. disc.: detected value discarded because of erroneous measures (see Section 5.3.1 for details). n/a: not applicable to simulations that displayed Scenario 2.

Chapter 5. The role of interfacial adhesion on minimum wear particle size and roughness evolution

$\tilde{\gamma}$	Scenario 1 $\sigma = 5 r_0$	Scenario 1 $\sigma = 10 r_0$	Scenario 1 $\sigma = 20 r_0$	Scenario 1 Total	\bar{V}_0 ($10^3 r_0^2$)
1.0	60.0 % (53.3 %)	53.3 % (20.0 %)	93.3 % (66.6 %)	68.9 % (46.7 %)	13.1
0.8	20.0 % (6.7 %)	40.0 % (20.0 %)	100 % (80.0 %)	53.3 % (35.6 %)	11.0
0.6	0.0 % (0.0 %)	33.3 % (26.7 %)	100 % (60.0 %)	44.4 % (28.9 %)	8.6
all	26.7 % (20.0 %)	42.2 % (22.2 %)	97.8 % (68.9 %)	55.6 % (37.0 %)	10.9

Table S5.4 – Summary of the simulations in set S that display Scenario 1. In each cell, the first percentage shows the relative amount of simulations that exhibit Scenario 1, the second percentage, in brackets, indicates the relative amount of simulations that exhibit Scenario 1 and for which the initial volume V_0 was not discarded. E.g. for $\tilde{\gamma} = 1.0$, 9 simulations out of the 15 with $\sigma = 5 r_0$ displayed Scenario 1 (i.e. 60.0 %), and for 8 out of 15 the initial volume V_0 was correctly estimated and taken into account in the analysis (i.e. 53.3 %). 'all' refers to estimation across all the values of $\tilde{\gamma}$. 'Scenario 1 Total' refers to estimation across all the values of σ . \bar{V}_0 is the average initial volume. It emerges that the likelihood of displaying Scenario 1 positively correlates with both $\tilde{\gamma}$ and σ .

5.5. Supplementary materials

ID	$\tilde{\gamma}$	H	seed	l_x
L-100-A	1.0	0.3	29	339.314
L-100-B	1.0	0.3	42	339.314
L-100-C	1.0	1.0	29	339.314
L-100-D	1.0	1.0	42	339.314
L-080-A	0.8	0.3	29	339.314
L-080-B	0.8	0.3	42	339.314
L-080-C	0.8	1.0	29	339.314
L-080-D	0.8	1.0	42	339.314
L-060-A	0.6	0.3	29	339.314
L-060-B	0.6	0.3	42	339.314
L-060-C	0.6	1.0	29	339.314
L-060-D	0.6	1.0	42	339.314
L-100-X	1.0	0.3	42	678.627
L-080-X	0.8	0.3	42	678.627

Table S5.5 – Summary of the simulations in set L. H and 'seed' are respectively the Hurst exponent and random seed used to create the initial self-affine surface. $\tilde{\gamma}$ is the reduced interfacial adhesion adopted and the value is referred to in the ID by the two digits. In the ID, 'A' and 'B' distinguish two different random realizations of the initial surface for $H = 0.3$. Similarly, 'C' and 'D' distinguish two different random realizations of the initial surface for $H = 1.0$. 'X' indicates simulations with the largest box size l_x .

Chapter 6

A mechanistic model for the growth of cylindrical debris particles in the presence of adhesion

The wear volume is known to keep increasing during frictional processes, and Archard notably proposed a model to describe the probability of wear particle formation upon asperity collision in a two-body contact configuration. While this model is largely adopted in the investigations of wear, the presence of wear debris trapped between the surfaces changes the system into a three-body contact configuration already since the early stages of the process. In such a configuration, a significant amount of wear is produced at the interface between the trapped debris and the sliding bodies. Here, relying on analytical models, we develop a framework that describes crack growth in a three-body configuration at the particle-surface interface. We then show that crack growth is favoured within the sliding surfaces, instead of within the debris particle, and test such result by means of numerical simulations with a phase-field approach to fracture. This leads to an increase in the wear volume and to debris particle accretion, rather than its breakdown. The effects of adhesion, coefficient of friction, and ratio of the applied global tangential and normal forces are also investigated.

Chapter 6. A mechanistic model for the growth of cylindrical debris particles in the presence of adhesion

Disclaimer This chapter is reproduced from the preprint version of the article Milanese, E., & Molinari, J.-F. A mechanistic model for the growth of cylindrical debris particles in the presence of adhesion [162]. At the time of writing of this dissertation, the manuscript is under consideration at a peer-reviewed scientific journal publishing research on the topic of mechanics of solids, and it is freely accessible at <https://arxiv.org/abs/2003.05812>. I personally conducted the development of the concept and its analytical derivation, the design and analysis of the numerical validation, the discussions, and the writing of the article (figures included).

6.1 Introduction

The importance of wear for the performance and durability of mechanical components has been known for centuries, as the first documented studies of the topic date back to Da Vinci's work [46]. While his contributions saw the light only recently and are still to be clearly assessed [47], he observed that the amount of wear was larger when the sliding motion was longer [46], and that harder materials would wear less [64]. The link between these quantities was made much clearer by Holm [51] and Archard [50] in the past century, at least for the case of adhesive wear. Archard formulated the wear law that still carries his name and that states that the wear volume is linearly proportional to the sliding distance, the normal load, and the inverse of the hardness of the materials. The proportionality is governed by the wear coefficient, which is generally constant and is determined experimentally. According to Archard's picture, the wear volume steadily increases during adhesive wear processes, and the wear coefficient describes the probability of two asperities belonging to opposite rough surfaces to form a debris particle upon collision.

In recent years, extensive experimental [80, 81, 111, 134–136] and numerical [57, 59, 73, 84] investigations have been carried out to shed light on what happens during such asperity contacts or collisions, and three possible mechanisms have been identified. When both the normal load and the adhesion forces are low, atom-by-atom removal takes place [80, 81, 111], while for larger loads and larger adhesion forces, asperities mutually deform plastically [59, 134], or break in a brittle fashion [59, 135, 136]. The transition from the ductile to the brittle behaviour is determined by a material-dependent critical length scale [59]. In the brittle scenario, the asperities form a debris particle with a well-defined initial volume, which is proportional to the tangential load [73]. It has been hypothesized that Archard's wear coefficient includes the probability of each asperity junction being smaller or

larger than the aforementioned critical length scale, and efforts are made towards a mechanical description of the wear coefficient [72].

This body of work focuses though on two-body contacts, that is two surfaces (the first bodies) come directly into contact at the asperity level. As soon as a loose debris particle forms, this constitutes the third body in the system and it is trapped between the two first bodies. Three-body contact then takes place locally: the debris particle separates the two surfaces, which are each in contact with the particle, and not directly with one another. Such transition to a three-body contact has been recently found to be key, for instance, in the evolution of the sliding surfaces into rough self-affine morphology [131]. It is arguable that loose debris particles form since the early stages, and that in the study of wear a third-body approach is more suitable [52, 89, 163, 164]. According to this approach, a load-bearing film of rolling third bodies is responsible for the changes in the rheology of the system, and behaves as a lubricant. This approach is supported by experimental [90, 91, 165] and numerical [88, 131, 166, 167] evidence: the transition to three-body contact is linked, for instance, to a reduction of the wear rate [88, 90, 91, 131, 166]. Similarly, a decrease in gouge-formation rates has been observed in natural faults [26] and rock experiments [92]. According to some characteristics of the system (e.g. surface roughness, system size, wear evacuation rate, wear production rate, debris particle size), the portion of the system where contact happens in a three-body configuration can be more or less spread.

Finally, recent numerical simulations [131] have shown that the volume of a debris particle trapped between two surfaces overall increases with time (or, equivalently, the sliding distance), and particle accretion is generally favoured over deposition of fragments from the particle onto the surfaces. Inspired by such observations (see Figure 6.1), we focus here on the wear production during three-body contact, within a solid mechanics framework. In particular, we show that the stress field in a three-body contact configuration favours an increase in the wear volume. To this end, the framework of our approach is presented in Section 6.2, and in Section 6.3 the existing contact solutions relevant to our problem are briefly presented, and they are used to determine the stress field in rolling contact with and without adhesion. In Section 6.4, the results of such approach are discussed, and tested with a numerical method. The conclusions are finally reported in Section 6.5.

Chapter 6. A mechanistic model for the growth of cylindrical debris particles in the presence of adhesion

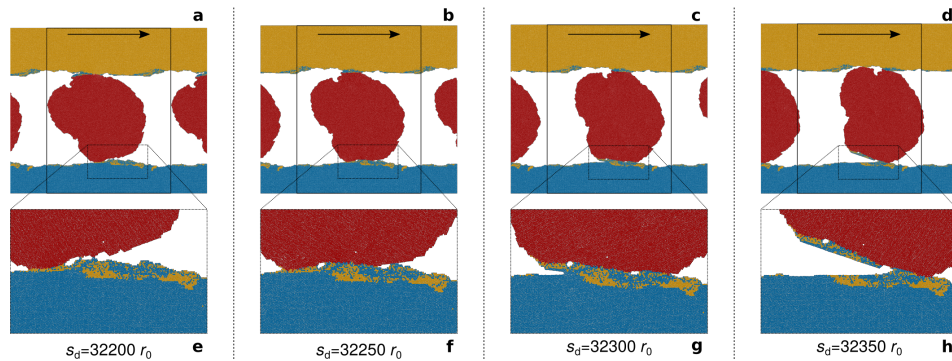


Figure 6.1 – Example of particle accretion observed in 2D molecular dynamics simulations. a-d) The debris particle (identified by red atoms) is rolling between the two first bodies (a) and adheres to the bottom surface (b); upon continuous rolling, the trailing edge is being pulled away (c) and material is transferred from the surface to the debris particle (d). e-h) Magnification of the areas within the dotted black rectangles in panels (a-d). In all panels, colours distinguish atoms originally belonging to the top (yellow) and bottom (blue) bodies. In panels (a-d), solid black lines represent simulation box boundaries (periodic boundary conditions are applied), and the arrow indicates the sliding direction of the top body (the bottom body is fixed). Snapshots are taken at the sliding distance s_d expressed in multiples of the atoms equilibrium distance r_0 . Atom interactions are all described by the same pair potential (i.e. full adhesion conditions are recovered upon contact). Snapshots are taken from simulation R1 of [131], the reader is referred to such work for more details.

Symbol	Expression	Description	Physical dimension
ξ, η, ζ	$x/l, y/l, z/l$	non-dimensional $x, y,$ and z coordinate	—
a, b, c	—	half-width of contact, ad- hesion, and interaction	length
α, β, χ	$a/l, b/l, c/l$	non-dimensional half- width of contact, adhe- sion, and interaction	—
m	χ/α	scaled non-dimensional interaction half-width	—
λ	σ_0/s	non-dimensional lim- iting adhesive stresses (Maugis parameter)	—
l	$\left(\frac{R^2 w}{E^*}\right)^{1/3}$	non-dimensionalizing length	length
s	$\left(\frac{w E^{*2}}{R}\right)^{1/3}$	non-dimensionalizing pressure	force/area
P_0	$\left(R w^2 E^*\right)^{1/3}$	non-dimensionalizing load	force/length
R	—	cylindrical particle radius	length
w	—	fracture energy	energy/area
E^*	—	effective elastic modulus	force/area
P, T	—	normal and tangential component of the trans- mitted force per unit length	force/length
$Z(x), X(x)$	—	transmitted normal and tangential tractions	force/area
$X'(x), X''(x)$	—	components of the trans- mitted tangential trac- tions	force/area
μ	—	Coulomb coefficient of friction	—

Table 6.1 – Nomenclature of the main symbols – Part 1 of 3.

Chapter 6. A mechanistic model for the growth of cylindrical debris particles in the presence of adhesion

Symbol	Expression	Description	Physical dimension
σ_{ij}	—	Cauchy stress	force/area
σ_{ij}^n	—	Cauchy stresses due to $Z(x)$	force/area
σ_{ij}^t	—	Cauchy stresses due to $X(x)$	force/area
$\sigma_{1,2}$	—	maximum (1) and minimum (2) principal Cauchy stresses on the $\langle \xi, \zeta \rangle$ plane	force/area
σ_0	—	limiting adhesive stresses	force/area
$\tilde{\sigma}_c$	—	limiting non-dimensional tensile stresses	—
$(\tilde{\cdot})$	—	non-dimensional loads and pressures	—
$(\bar{\cdot})$	—	quantities computed at $\zeta = 0$	—
θ_p	—	angle between the ξ axis and the direction of the maximum principal stress	—
θ_c	$\theta_p - \pi/2$	angle between the ξ axis and the direction of crack propagation	—

Table 6.2 – Nomenclature of the main symbols – Part 2 of 3.

Symbol	Expression	Description	Physical dimension
ρ	—	non-dimensional half-width over which X'' is applied	—
ψ	—	non-dimensional coordinate of the midpoint of 2ρ	—
\tilde{p}_0	$2\tilde{P}/\pi\alpha$	maximum value of $\tilde{Z}(\xi)$ at the center of the contact width	—
\tilde{X}_{adh}	—	tangential tractions due to adhesive friction	—
$\tilde{\tau}_0$	$\tilde{X}_{\text{adh}}/2\chi$	non-dimensional adhesive friction tangential stress	—
$\tilde{\tau}_c$	—	non-dimensional shear strength of the contact interface	—

Table 6.3 – Nomenclature of the main symbols – Part 3 of 3.

6.2 Theory

6.2.1 Approach

In the simplest three-body contact, one wear debris particle is rolling between two surfaces, while in contact with both of them. The core idea of our approach is to view the rolling motion of the particle as the opening and closure of two cracks. At the leading edge of the contact, the rolling motion is closing the crack, while at the trailing edge the crack opens. This approach is inspired by the work of Maugis [61, 168], who used a fracture mechanics approach to investigate the adhesive contact of spheres.

In the remaining of the manuscript we focus on the contact between the particle and one of the surfaces, as the behaviour at the contact with the other surface is quickly derivable with symmetry arguments. Our approach then implies that the direction of propagation of the opening crack at the trailing edge of contact determines which of the bodies wears out: the particle or the surface.

In the following Sections, we derive the stress fields due to the rolling contact with adhesion, the principal stresses and the crack propagation angle at the trailing edge based on the maximum hoop stress criterion [169].

6.2.2 Framework

We consider the case of two-dimensional contact between two cylinders with their longitudinal axis y aligned (see Figure 6.2). In our case we assume that one of the two cylinders has infinite radius of curvature and represents the surface against which the debris particle is rolling.

Three different types of rolling motion can take place in such conditions [62, 170]:

- free rolling: if the transmitted resultant force is normal to the contact width;
- tractive rolling: if the transmitted resultant force is not normal to the contact width (i.e. tangential forces are transmitted, too);
- rolling with spin: if a relative angular velocity along the axis normal to the contact width (ζ -axis in Figure 6.2) exists between the cylinder and the surface;

we will consider here the first two types of rolling.

Frame of reference and formalism Following the common conventions of contact mechanics [62], we adopt a frame of reference with the axes centered at the midpoint of the width of the contact area and orientated as shown in Figure 6.2. Forces are taken as positive when pointed towards positive values of the axes direction, the consequent convention for positive values of the stresses being shown in Figure 6.2.

We then introduce:

- the effective elastic modulus $E^* = \left(\frac{1-\nu_c^2}{E_c} + \frac{1-\nu_s^2}{E_s} \right)^{-1}$, where E_c , ν_c and E_s , ν_s are the elastic modulus and Poisson's ratio of the cylindrical particle and the opposing surface respectively;
- the equivalent curvature $\frac{1}{R} = \frac{1}{R_c} + \frac{1}{R_s}$, where R_c and R_s are the radius of curvature of the cylindrical particle and the opposing surface respectively; note that $\frac{1}{R} \rightarrow \frac{1}{R_c}$ in our case ($R_s \rightarrow \infty$).

Throughout the manuscript, the following non-dimensionalization is then adopted^a:

$$\alpha := \frac{a}{l} \tag{6.1a}$$

$$\beta := \frac{b}{l} \tag{6.1b}$$

$$\chi := \frac{c}{l} \tag{6.1c}$$

$$\xi := \frac{x}{l} \tag{6.1d}$$

$$l := \left(\frac{R^2 w}{E^*} \right)^{1/3} \tag{6.1e}$$

$$\lambda := \frac{\sigma_0}{s} \tag{6.1f}$$

$$s := \left(\frac{w E^{*2}}{R} \right)^{1/3} \tag{6.1g}$$

^aNote that the normalization adopted here differs from that of Maugis [61] and Baney and Hui [171]. There, some lengths are non-dimensionalized by l and some others by a , which can be confusing – hence our choice. Here the non-dimensional parameters are those used by Johnson [172]. The equations of this section and of Section 6.3 are presented in the Maugis formalism in Section 6.7 for the reader who is more familiar with that approach.

Chapter 6. A mechanistic model for the growth of cylindrical debris particles in the presence of adhesion

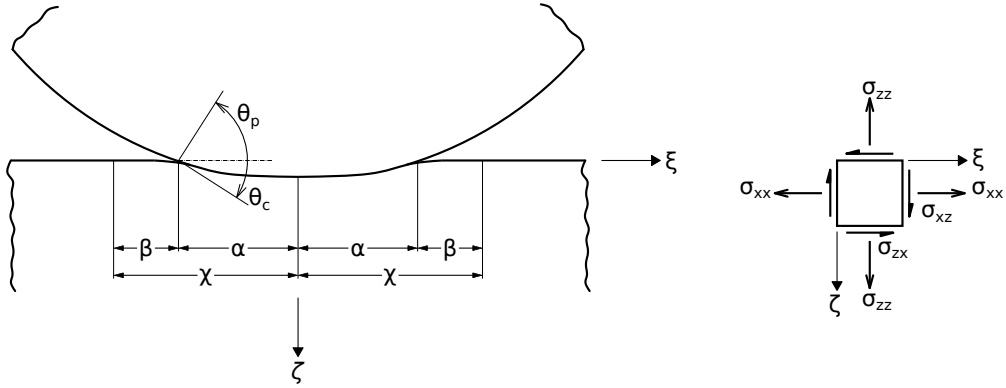


Figure 6.2 – Frame of reference for a body in contact with a half-space (left) and stress directions taken as positive for a small representative square element at a random point within the bodies (right). Lengths are non-dimensionalized by l (see Equations 6.1a to 6.1e): $\xi = x/l$, $\zeta = z/l$. Note that the signs of the shear stresses are the opposite than in the traditional continuum solid mechanics frame of reference. Normal stresses are positive when tensile. The η -axis, with $\eta = y/l$, is not displayed and is orthogonal to the $\langle \xi, \zeta \rangle$ plane and pointed toward the reader. θ_p is the angle between the direction of the largest principal stress and the axis ξ , $\theta_c = \theta_p - \pi/2$ is the angle between the axis ξ and the crack path (see Section 6.2.6). Angles are positive if measured counter-clockwise.

$$\tilde{P} := \frac{P}{P_0} \quad (6.1h)$$

$$\tilde{T} := \frac{T}{P_0} \quad (6.1i)$$

$$P_0 := \left(R w^2 E^* \right)^{1/3} \quad (6.1j)$$

with a and c the half-width of contact and interaction respectively, σ_0 the limiting adhesive stress that the material can sustain, w the surface energy, P and T the normal and tangential force (per unit length) transmitted at the contact interface (the main symbols with their meaning and dimensions are summarized in Tables 6.1, 6.2, and 6.3).

The particle is assumed to roll towards positive values of ξ , and interacts with the opposite surface over the width $2\chi = 2(\alpha + \beta)$, where α is the non-dimensionalized half-width of contact and β is the non-dimensionalized half-width of adhesion, i.e. the region where the bodies interact through the adhesive forces even if not directly in contact. When no adhesion is considered, $\beta \rightarrow 0$ and $\chi \rightarrow \alpha$.

In the derivation of the stress fields, it is assumed that the contact width is small compared to the dimensions of the bodies and their radius of curvature. These hypotheses imply [62] that strains are small, both bodies can be regarded as half-spaces, both surfaces are continuous, and contact is non-conforming (i.e. the geometries of the surfaces are dissimilar and contact takes place only at a point or line prior any deformation, like for a sphere on a plane).

Transmitted forces The normal and tangential components of the non-dimensionalized transmitted force (per unit length) \tilde{P} and \tilde{T} are related to the non-dimensionalized normal and tangential tractions $\tilde{Z}(\xi)$ and $\tilde{X}(\xi)$ by satisfying equilibrium at the interface:

$$\tilde{P} = \int_{-\chi}^{\chi} \tilde{Z}(\xi) d\xi \quad (6.2a)$$

$$\tilde{T} = \int_{-\alpha}^{\alpha} \tilde{X}(\xi) d\xi \quad (6.2b)$$

where $\tilde{Z}(\xi)$ and $\tilde{X}(\xi)$ are the transmitted normal and tangential stress distributions respectively. $\tilde{Z}(\xi)$ and $\tilde{X}(\xi)$ have same magnitude and opposite sign on the cylinder and on the half-space surfaces. Note that as we consider two-dimensional contact, \tilde{T} and $\tilde{X}(\xi)$ are aligned with the ξ -axis. Furthermore, it is assumed that the tangential forces can be transmitted only where the two bodies are in direct contact (i.e. $|\xi| \leq \alpha$), and that the normal forces can be transmitted across the whole interaction width (i.e. $|\xi| \leq \chi$).

Under the assumption of Coulomb friction, the following conditions need be satisfied:

$$|\tilde{T}| \leq \mu \tilde{P} \quad (6.3a)$$

$$|\tilde{X}(\xi)| \leq \mu \tilde{Z}(\xi), \forall \xi \in [-\alpha, \alpha] \quad (6.3b)$$

where μ is the coefficient of friction. Equations 6.3a and 6.3b require the Coulomb law to be satisfied globally and locally, respectively. When the equal sign holds in Equation 6.3a, slip takes place, while when the equal sign holds in Equation 6.3b, sliding takes place^b.

^bWe define slip the relative motion at a point on the contact interface where the two surfaces have different velocities. If slip takes place at all the points on the contact interface, then we refer to it as sliding or complete slip [170].

6.2.3 Adhesive forces: Maugis model

When adhesion is present, tensile stresses normal to the contact interface can be sustained. The two extreme cases are those of the JKR [55] and the DMT [56] theories, better suitable respectively for the cases of soft materials with high adhesion, and hard materials with low adhesion. Later, Maugis [61] developed a comprehensive theory of the adhesion of spheres, which is able to capture the continuous transition from the JKR to the DMT limit. In his 3D contact model, Maugis assumes that the part of adhesive forces acting outside the contact area between the sphere and the half-plane are constant and analogue to the cohesive forces between the lips of a crack, as in Dugdale's work [173]. These adhesive forces act within an adhesive ring of length $\beta = \chi - \alpha$ (cf. Figure 6.2). To study the conditions under which the crack propagates (or closes), i.e. the contact radius decreases (or increases), the Griffith criterion for equilibrium $G = w$ is investigated, where G is the energy release rate and $w = 2\gamma$ is the fracture energy (i.e. the work necessary to separate two surfaces characterized by the same surface energy γ). By imposing the equilibrium condition, the Maugis parameter^c λ allows to investigate the problem as a function of the material parameters. When $\lambda \rightarrow \infty$ (soft materials, high adhesion), the adhesive ring vanishes ($\beta \rightarrow 0$), the inner pressure distribution coincides with the well known JKR limit [55], the adhesive forces act only within the contact area and go to infinity at the edges of the contact. If $\lambda \rightarrow 0$ (hard materials, low adhesion), the adhesive ring is infinitely large ($\beta \rightarrow \infty$), and the DMT limit [56] is recovered instead.

Maugis' approach was later adopted in two dimensions, i.e. for cylinders [171, 174], and the distribution of non-dimensionalized normal tractions in such case is (see Figure 6.3a)

$$\tilde{Z}(\xi) = \begin{cases} -\frac{1}{2}\sqrt{\alpha^2 - \xi^2} + \frac{2\lambda}{\pi} \arctan \sqrt{\frac{\chi^2 - \alpha^2}{\alpha^2 - \xi^2}} & |\xi| \leq \alpha \\ -\lambda & \alpha < |\xi| \leq \chi \\ 0 & |\xi| > \chi \end{cases} \quad (6.4)$$

The non-dimensionalized contact half-width α is determined by solving the load

^cThe work of [61] being in 3D, λ has actually a different expression than the one derived from Eqs. 6.1e and 6.1f: $\lambda_{3D} = 2\sigma_0 \cdot (\pi w K^2 / R)^{-1/3}$, where $K = 4/3 \cdot E / (1 - \nu^2)$. One can see that λ and λ_{3D} behave the same (cf. Eqs. 6.1e and 6.1f), thus for readability the general notation λ is kept throughout the text also when referring to the 3D case.

equation ([172])

$$\tilde{P} = \frac{\pi}{4} \alpha^2 - 2\lambda\alpha\sqrt{m^2 - 1} \quad (6.5)$$

where

$$m := \frac{\chi}{\alpha} = \frac{\chi}{\alpha} \cdot \frac{l}{l} = \frac{c}{a} \quad (6.6a)$$

Once α is known as a function of m , m is determined by solving the equation for the cut-off distance at which the adhesive stresses fall to zero:

$$\lambda\alpha^2 g_1(m) + \lambda^2 \alpha g_2(m) = 1 \quad (6.7)$$

where

$$g_1(m) := \frac{1}{2} \left[m\sqrt{m^2 - 1} - \cosh^{-1}(m) \right] \quad (6.8)$$

$$g_2(m) := \frac{4}{\pi} \left[\cosh^{-1}(m) \sqrt{m^2 - 1} - m \ln(m) \right] \quad (6.9)$$

and the values of α and χ are eventually found. Following the aforementioned steps, it is possible to fully determine the non-dimensionalized tractions $\tilde{Z}(\xi)$ at the interface. For the details of the derivation we refer the reader to Ref. [61, 171, 172, 175].

6.2.4 Tractive rolling forces: Carter model

To the best of our knowledge, no analytical solution for tractive rolling contact in the presence of adhesive forces have been found yet. Here, we assume that it can be obtained by superposition of the analytical solutions for the normal adhesive contact (described above) and the classical solution for the case of a cylinder rolling on an elastic half-space (described in the following). Contact then takes place along a frictional interface (characterized by the friction coefficient μ) and the tangential forces due to the rolling motion are transmitted between the two bodies along the contact area ($|\xi| \leq a$). The problem was first solved by Carter [176], with an approach that is conceptually similar to that of Cattaneo [177] for the contact of cylinders with partial slip – two tangential distributions of the Hertzian type are superimposed, so that Coulomb law (Equation 6.3b) is satisfied everywhere along the contact area.

Chapter 6. A mechanistic model for the growth of cylindrical debris particles in the presence of adhesion

The two distributions, non-dimensionalized, are

$$\tilde{X}'(\xi) = \begin{cases} \mu \frac{2\tilde{P}}{\pi\alpha^2} \sqrt{\alpha^2 - \xi^2} & |\xi| \leq \alpha \\ 0 & |\xi| > \alpha \end{cases} \quad (6.10a)$$

$$\tilde{X}''(\xi) = \begin{cases} -\mu \frac{2\tilde{P}}{\pi\alpha^2} \sqrt{\rho^2 - (\xi - \psi)^2} & |\xi - \psi| \leq \rho \\ 0 & |\xi - \psi| > \rho \end{cases} \quad (6.10b)$$

where $\rho := \alpha - \psi = (1 - \frac{T}{\mu P})^{1/2} \leq 1$ is the non-dimensionalized half-width over which $\tilde{X}''(\xi)$ is applied. Note that $\tilde{X}'(\xi) = \mu \tilde{Z}(\xi)$ corresponds to the tangential distribution in the case of sliding, and the superposition of $\tilde{X}''(\xi)$ allows to take into account the stick region [170]. The total tangential tractions at the interface are then (see Figure 6.4a) [170]

$$\tilde{X}(\xi) = \tilde{X}'(\xi) + \tilde{X}''(\xi) \quad (6.11)$$

and are positive when transmitted from the particle to the surface, to oppose the direction of motion. The Coulomb law (Equations 6.3) is satisfied both globally and locally.

6.2.5 Stress field

We now assume that the total Cauchy stress $\sigma_{ij}(x, y, z)$, with $i, j = x, y, z$, is made up of the linear superposition of two different contributions: σ_{ij}^n due to the normal component of the transmitted force, and σ_{ij}^t due to the tangential component of the transmitted force. We define then the total non-dimensionalized stress $\bar{\sigma}_{ij}(\xi)$ anywhere along the surface as

$$\bar{\sigma}_{ij}(\xi) = \bar{\sigma}_{ij}^n(\xi) + \bar{\sigma}_{ij}^t(\xi) \quad (6.12)$$

where the overbar indicates that the stresses are considered at $\zeta = 0$. The assumption of plain strains reduces the number of independent components of stress, and in Eq. 6.12 is $\bar{\sigma}_{yy}(\xi) = \nu (\bar{\sigma}_{xx}(\xi) + \bar{\sigma}_{zz}(\xi))$. We will then not consider explicitly $\bar{\sigma}_{yy}(\xi)$ in the rest of the manuscript.

Furthermore, to satisfy equilibrium and assuming that the tractions $\tilde{Z}(\xi)$ and $\tilde{X}(\xi)$

are specified independently, it is

$$\begin{aligned}\bar{\bar{\sigma}}_{zz}(\xi) &= \bar{\bar{\sigma}}_{zz}^n(\xi) = -\bar{Z}(\xi) \\ \bar{\bar{\sigma}}_{xz}(\xi) &= \bar{\bar{\sigma}}_{xz}^t(\xi) = -\bar{X}(\xi) \quad .\end{aligned}\tag{6.13}$$

and thus the stress state of Equation 6.12 reduces to

$$\begin{aligned}\bar{\bar{\sigma}}_{xx}(\xi) &= \bar{\bar{\sigma}}_{xx}^n(\xi) + \bar{\bar{\sigma}}_{xx}^t(\xi) \\ \bar{\bar{\sigma}}_{zz}(\xi) &= \bar{\bar{\sigma}}_{zz}^n(\xi) \\ \bar{\bar{\sigma}}_{xz}(\xi) &= \bar{\bar{\sigma}}_{xz}^t(\xi) \quad .\end{aligned}\tag{6.14}$$

In the absence of tangential tractions at the interface, the plain strain assumption in elasticity also implies that [62]

$$\bar{\bar{\sigma}}_{xx}(\xi) = \bar{\bar{\sigma}}_{zz}(\xi) = -\bar{Z}(\xi) \quad .\tag{6.15}$$

Stresses due to normal load From Equations 6.4, 6.14 and 6.15, it follows that the surface stresses due to the normal component of the force transmitted at the interface are (see Figure 6.3a)

$$\begin{aligned}\bar{\bar{\sigma}}_{xx}^n(\xi) = \bar{\bar{\sigma}}_{zz}^n(\xi) &= \begin{cases} \frac{1}{2}\sqrt{\alpha^2 - \xi^2} - \frac{2\lambda}{\pi} \arctan \sqrt{\frac{\chi^2 - \alpha^2}{\alpha^2 - \xi^2}} & |\xi| \leq \alpha \\ \lambda & \alpha < |\xi| \leq \chi \\ 0 & |\xi| > \chi \end{cases} \quad .\tag{6.16} \\ \bar{\bar{\sigma}}_{xz}^n(\xi) &= 0\end{aligned}$$

To fully determine $\bar{\bar{\sigma}}_{ij}^n(\xi)$ is thus necessary and sufficient to know the non-dimensionalized normal component \bar{P} of the transmitted force and the Maugis parameter λ .

In Equations 6.4 and 6.16, no discontinuity is present between the constant value λ of the non-dimensionalized adhesive forces and the pressure distribution within the contact width, i.e. $\lim_{|\xi| \rightarrow \alpha^\pm} \bar{\bar{\sigma}}_{zz} = \lambda$, and compressive pressures are described at the center and tensile pressures at the edge of the contact. A discontinuity in the normal stresses is present instead at the edges of the interaction area, where $\lim_{\xi \rightarrow -\chi^+} \bar{\bar{\sigma}}_{zz} = \lambda \neq \lim_{\xi \rightarrow -\chi^-} \bar{\bar{\sigma}}_{zz} = 0$ (and similarly for $\xi \rightarrow \chi^-$).

Chapter 6. A mechanistic model for the growth of cylindrical debris particles in the presence of adhesion

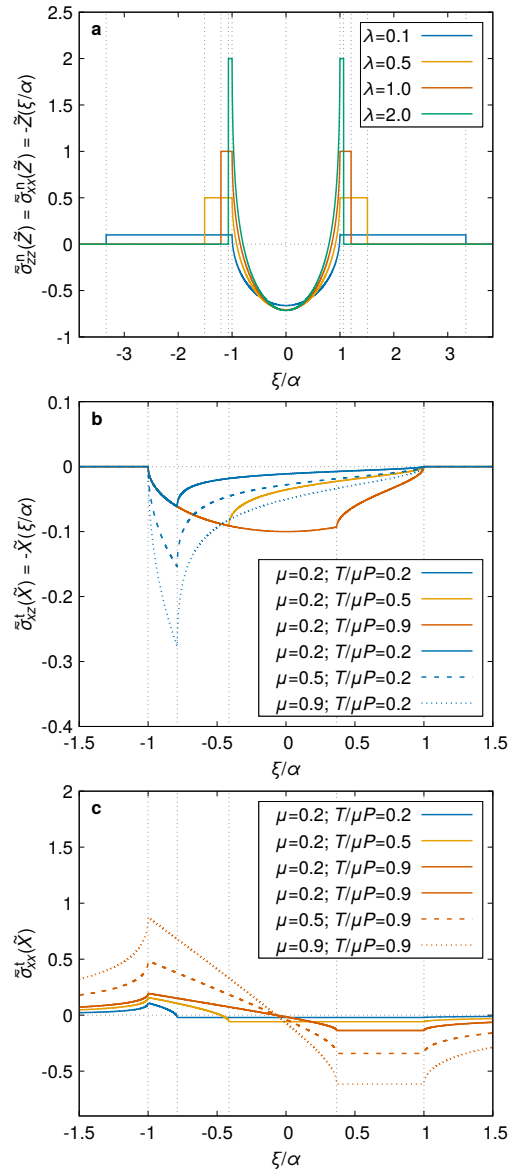


Figure 6.3 – Tractions and stress distributions. The horizontal axis is scaled by α . a) Stresses $\bar{\sigma}_{ij}^n(\xi)$ due to normal load of the Maugis type (Equations 6.16); larger λ values give larger tensile stresses at the edge of contact and smaller adhesive width. b) Tangential stress $\bar{\sigma}_{xz}^t(\xi)$ due to tangential load (Equation 6.17b); $T/\mu P$ affects the shape of the distribution (the larger the ratio, the larger the slip zone), μ scales it. c) Normal stress $\bar{\sigma}_{xx}^t(\xi)$ due to tangential load (Equation 6.17c); $T/\mu P$ affects the shape of the distribution, μ scales it. In all the figures $\tilde{P} = \pi/2$.

Stresses due to tangential load The stresses due to the transmitted tangential tractions $\tilde{X}(\xi)$ are determined from the superposition of the stresses due to $\tilde{X}'(\xi)$ and $\tilde{X}''(\xi)$, which have the same shape but different magnitude and opposite sign.

The surface stresses due to the tangential component of force transmitted at the interface are then (see Figure 6.4b)

$$\bar{\sigma}_{zz}^t(\xi) = 0 \quad (6.17a)$$

$$\begin{aligned} \bar{\sigma}_{xz}^t(\xi) &= -\tilde{X}(\xi) = -\tilde{X}'(\xi) - \tilde{X}''(\xi) = \\ &= \begin{cases} -\mu \frac{2\tilde{P}}{\pi\alpha^2} \sqrt{\alpha^2 - \xi^2} & |\xi| \leq \alpha \\ 0 & |\xi| > \alpha \end{cases} + \begin{cases} \mu \frac{2\tilde{P}}{\pi\alpha^2} \sqrt{\rho^2 - (\xi - \psi)^2} & |\xi - \psi| \leq \rho \\ 0 & |\xi - \psi| > \rho \end{cases} \end{aligned} \quad (6.17b)$$

$$\begin{aligned} \bar{\sigma}_{xx}^t(\xi) &= \bar{\sigma}_{xx}^{\tilde{X}'}(\xi) + \bar{\sigma}_{xx}^{\tilde{X}''}(\xi) = \\ &= \begin{cases} -2\mu \frac{2\tilde{P}}{\pi\alpha^2} \xi & |\xi| \leq \alpha \\ -2\mu \frac{2\tilde{P}}{\pi\alpha^2} \left(\xi - \text{sgn}(\xi) \sqrt{\xi^2 - \alpha^2} \right) & |\xi| > \alpha \end{cases} + \\ &+ \begin{cases} 2\mu \frac{2\tilde{P}}{\pi\alpha^2} (\xi - \psi) & |\xi - \psi| \leq \rho \\ 2\mu \frac{2\tilde{P}}{\pi\alpha^2} \left[\xi - \psi - \text{sgn}(\xi - \psi) \sqrt{(\xi - \psi)^2 - \rho^2} \right] & |\xi - \psi| > \rho \end{cases} \end{aligned} \quad (6.17c)$$

and the effects of μ and $T/\mu P$ are depicted in Figures 6.3b and 6.3c. For the derivation of Equation 6.17c we refer the reader to Ref. [62].

6.2.6 Crack propagation angle

Once the stress field is determined, the principal stresses are then computed as:

$$\bar{\sigma}_1(\xi) = \frac{\bar{\sigma}_{xx}(\xi) + \bar{\sigma}_{zz}(\xi)}{2} + \sqrt{\left(\frac{\bar{\sigma}_{xx}(\xi) - \bar{\sigma}_{zz}(\xi)}{2} \right)^2 + \bar{\sigma}_{xz}^2(\xi)} \quad (6.18)$$

$$\bar{\sigma}_2(\xi) = \frac{\bar{\sigma}_{xx}(\xi) + \bar{\sigma}_{zz}(\xi)}{2} - \sqrt{\left(\frac{\bar{\sigma}_{xx}(\xi) - \bar{\sigma}_{zz}(\xi)}{2} \right)^2 + \bar{\sigma}_{xz}^2(\xi)} \quad (6.19)$$

such that $\bar{\sigma}_1(\xi) \geq \bar{\sigma}_2(\xi)$ for all ξ .

The stress field $\bar{\sigma}_{ij}(\xi, \eta, \zeta)$ at a given point can be visualized in the Mohr plane

Chapter 6. A mechanistic model for the growth of cylindrical debris particles in the presence of adhesion

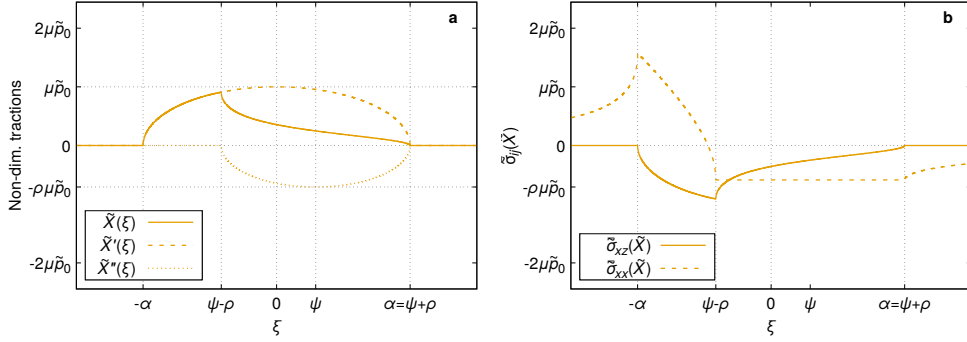


Figure 6.4 – Construction of the tangential tractions and relative stresses. a) Transmitted tangential tractions $\tilde{X}(\xi) = \tilde{X}'(\xi) + \tilde{X}''(\xi)$ (Equations 6.17); slip takes place over the strip $-\alpha \leq \xi \leq \psi - \rho$, whose size increases with $T/\mu P$ (cf. Figure 6.3) and where is $|\tilde{X}(\xi)| = \mu|\tilde{Z}(\xi)|$. b) Stresses $\tilde{\sigma}_{ij}^t(\xi)$ due to the tractions $\tilde{X}(\xi)$. $\pm 2\mu\tilde{p}_0$ are the limiting values for $\tilde{\sigma}_{xx}^t(\xi \rightarrow \mp\alpha)$ and they are reached when $T/\mu P \rightarrow 1$. In both figures $\tilde{P} = \pi/4$ and thus $\alpha = 1$ (cf. Equation 6.5).

(Figure 6.5), following the convention that shear stresses are positive when rotating the representative square clockwise. This implies that $\tilde{\sigma}_{xz}$ has opposite sign in the Mohr plane with respect to the contact mechanics convention (cf. Section 6.2.2 and Figure 6.2). Note that for the problem at hand $\tilde{\sigma}_{xy} = \tilde{\sigma}_{yz} = 0$ (because of symmetry) and η is the principal direction of the principal stress $\tilde{\sigma}_3 \equiv \tilde{\sigma}_{yy} \forall \xi$. The other two principal directions lie then on the $\langle \xi, \zeta \rangle$ plane and they can be determined by analysing only the stresses $\tilde{\sigma}_{xx}$, $\tilde{\sigma}_{zz}$, and $\tilde{\sigma}_{xz}$ ^d.

The angle θ_p between the direction of the largest principal stress $\tilde{\sigma}_1(\xi)$ and the ξ -axis (cf. Figure 6.2) is then

$$\theta_p(\xi) = \begin{cases} -\frac{\text{sgn}(\tilde{\sigma}_{xz}(\xi))}{2} \cdot \arctan\left(\frac{2|\tilde{\sigma}_{xz}(\xi)|}{\tilde{\sigma}_{xx}(\xi) - \tilde{\sigma}_{zz}(\xi)}\right) & \tilde{\sigma}_{xx}(\xi) \geq \tilde{\sigma}_{zz}(\xi) \\ -\frac{\text{sgn}(\tilde{\sigma}_{xz}(\xi))}{2} \cdot \left[\pi + \arctan\left(\frac{2|\tilde{\sigma}_{xz}(\xi)|}{\tilde{\sigma}_{xx}(\xi) - \tilde{\sigma}_{zz}(\xi)}\right)\right] & \tilde{\sigma}_{xx}(\xi) < \tilde{\sigma}_{zz}(\xi) \end{cases} \quad (6.20)$$

Hence the angle θ_c between the direction of crack propagation and the ξ -axis (cf. Figure 6.2) is

$$\theta_c(\xi) = \theta_p(\xi) - \frac{\pi}{2} \quad (6.21)$$

^dWhile we focus here only on the surface stress $\tilde{\sigma}_{ij}(\xi)$, these arguments hold for the general stress state $\tilde{\sigma}_{ij}(\xi, \eta, \zeta)$ in the problem at hand, i.e. $\tilde{\sigma}_{xy} = \tilde{\sigma}_{yz} = 0$ always and $\tilde{\sigma}_3 \equiv \tilde{\sigma}_{yy} \forall (\xi, \eta, \zeta)$, η is principal direction, and the other two directions always lie on the $\langle \xi, \zeta \rangle$ plane.

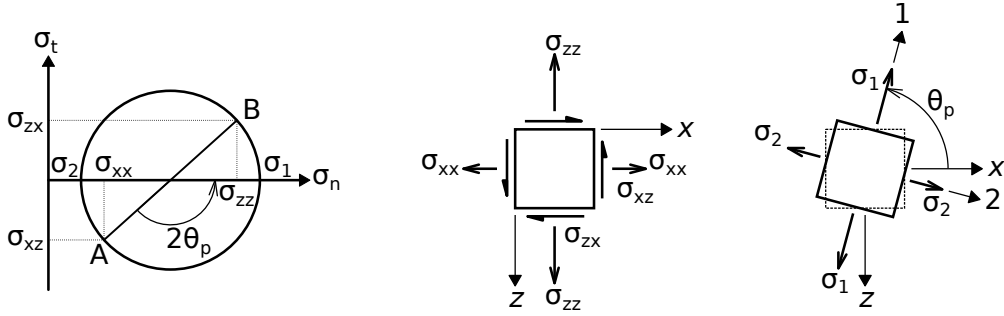


Figure 6.5 – Mohr diagram (left) for a generic stress state (centre) and principal stresses directions (right). According to Mohr’s convention, shear stresses are positive when rotating the representative square clockwise.

In the next sections we will see how it is always the case that $\bar{\sigma}_{xy}(\xi \rightarrow -\chi^+) \leq 0$, and thus $-\frac{\pi}{2} \leq \theta_c \leq 0$: crack propagation within the half-space is favoured over crack propagation inside the particle.

Finally, we assume that the rolling motion is equivalent to applying the following infinitesimal stresses ($\delta\bar{\sigma}$ being positive):

$$\begin{cases} \delta\bar{\sigma} > 0 & \text{if } -\chi \leq \xi \leq -\alpha \\ -\delta\bar{\sigma} < 0 & \text{if } \alpha \leq \xi \leq \chi \end{cases} \quad (6.22)$$

According to the fracture mechanics picture of contact introduced by Maugis [61], this leads to closing the crack at the leading edge and opening it at the trailing edge — the particle now rolls towards positive values of ξ .

6.3 Calculation

In the present section we present the surface stresses from Section 6.2 for the most general case only: tractive rolling with adhesion. A detailed discussion on the crack propagation angle and on the influence of the various parameters is reported in Section 6.4. Three more cases, that is free rolling with and without adhesion and tractive rolling without adhesion, are reported and discussed in Section 6.6.

When adhesion is present and the transmitted force has a tangential component, the stress state is given by Equations 6.14, with $\bar{\sigma}_{ij}^n(\xi)$ given by Equations 6.16 and with

Chapter 6. A mechanistic model for the growth of cylindrical debris particles in the presence of adhesion

$\bar{\sigma}_{ij}^t(\xi)$ given by Equations 6.17:

$$\begin{aligned}
 \bar{\sigma}_{zz}(\xi) &= \begin{cases} \frac{\bar{p}_0}{\alpha} \sqrt{\alpha^2 - \xi^2} - \frac{2\lambda}{\pi} \arctan \sqrt{\frac{\chi^2 - \alpha^2}{\alpha^2 - \xi^2}} & |\xi| \leq \alpha \\ \lambda & \alpha < |\xi| \leq \chi \\ 0 & |\xi| > \chi \end{cases} \\
 \bar{\sigma}_{xx}(\xi) &= \begin{cases} -\frac{\bar{p}_0}{\alpha} \left(\sqrt{\alpha^2 - \xi^2} - 2\mu\xi \right) - \frac{2\lambda}{\pi} \arctan \sqrt{\frac{\chi^2 - \alpha^2}{\alpha^2 - \xi^2}} & |\xi| \leq \alpha \\ -2\mu \frac{\bar{p}_0}{\alpha} \left(\xi - \text{sgn}(\xi) \sqrt{\xi^2 - \alpha^2} \right) + \lambda & \alpha < |\xi| \leq \chi + \\ -2\mu \frac{\bar{p}_0}{\alpha} \left(\xi - \text{sgn}(\xi) \sqrt{\xi^2 - \alpha^2} \right) & |\xi| > \chi \end{cases} \quad (6.23) \\
 &+ \begin{cases} 2\mu \frac{\bar{p}_0}{\alpha} (\xi - \psi) & |\xi - \psi| \leq \rho \\ 2\mu \frac{\bar{p}_0}{\alpha} \left[\xi - \psi - \text{sgn}(\xi - \psi) \sqrt{(\xi - \psi)^2 - \rho^2} \right] & |\xi - \psi| > \rho \end{cases} \\
 \bar{\sigma}_{xz}(\xi) &= \begin{cases} -\mu \frac{\bar{p}_0}{\alpha} \sqrt{\alpha^2 - \xi^2} & |\xi| \leq \alpha \\ 0 & |\xi| > \alpha \end{cases} + \begin{cases} \mu \frac{\bar{p}_0}{\alpha} \sqrt{\rho^2 - (\xi - \psi)^2} & |\xi - \psi| \leq \rho \\ 0 & |\xi - \psi| > \rho \end{cases}
 \end{aligned}$$

where $\bar{p}_0 := \frac{2\bar{P}}{\pi\alpha} = \frac{\alpha}{2}$ is the pre-factor written in the classical Hertz convention (cf. Equation 6.5, with $m \rightarrow 0$) and represents the maximum value of the tractions at the center of the contact width. The distributions of $\bar{\sigma}_{zz}(\xi)$ and $\bar{\sigma}_{xz}(\xi)$ are depicted in Figures 6.3a and 6.3b, $\bar{\sigma}_{xx}(\xi)$ in Figure 6.6. Note that the non-dimensionalized load \bar{P} , the friction coefficient μ and the ratio $T/\mu P$ need to be known to fully determine the stress field $\bar{\sigma}_{ij}^t(\xi)$.

6.4 Results and discussion

In this section we examine the principal stresses that arise from the stress field derived in Section 6.3 and their principal direction. From that, we can determine the direction of crack propagation (cf. Equations 6.20 and 6.21). We will finally discuss the effects of different geometries and material parameters on the crack propagation angle.

Figures 6.7a and 6.7b show the maximum principal stress $\bar{\sigma}_1(\xi)$ due to the stress field derived in section 6.3 (Eqs. 6.23). The stress is tensile in a region around both the leading and trailing edge, its maximum being at the trailing edge ($\xi = -\alpha$). If $\bar{\sigma}_1(-\alpha) \geq \bar{\sigma}_c$, where $\bar{\sigma}_c$ is the limiting tensile resistance of the material, the crack can

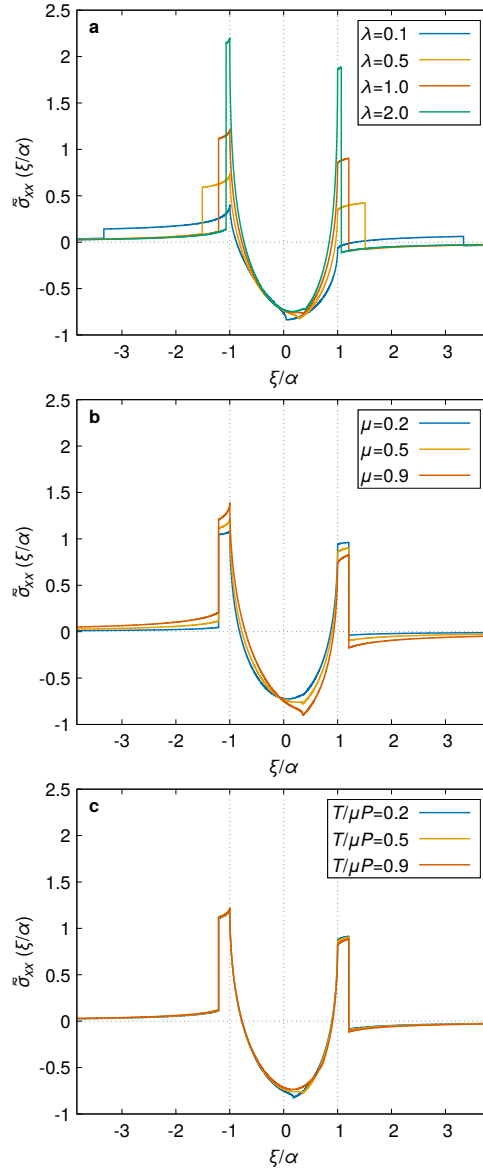


Figure 6.6 – Stress $\bar{\sigma}_{xx}(\xi)$ in the case of tractive rolling with adhesion. The horizontal axis is scaled by α . a) Effect of the Maugis parameter λ for constant values of the friction coefficient and of the ratio between the transmitted tangential force and the limiting frictional force (here: $\mu = 0.5$ and $T/\mu P = 0.5$). b) Effect of the friction coefficient μ for constant values of the Maugis parameter and of the ratio between the transmitted tangential force and the limiting frictional force (here: $\lambda = 1$ and $T/\mu P = 0.5$). c) Effect of the ratio $T/\mu P$ between the transmitted tangential force and the limiting frictional force for constant values of the Maugis parameter and of the coefficient of friction (here: $\lambda = 1$ and $\mu = 0.5$). In all the figures $\tilde{P} = \pi/4$.

Chapter 6. A mechanistic model for the growth of cylindrical debris particles in the presence of adhesion

propagate with an angle θ_c , where θ_c is fully determined by the stress state and, ahead of the crack tip, is always $-\pi/2 < \theta_c \leq 0$ (see Figures 6.7c and 6.7d). Alternatively, the crack can propagate also along the contact interface, if $\bar{\sigma}_{zz}(-\alpha) = \lambda$, i.e. if the tensile stress along the direction normal to the surface is equal to the interface strength λ . We now investigate when one or the other scenario prevails.

In the process zone ahead of the crack tip, it is always $\bar{\sigma}_{zz}(\xi) < \lambda$ (cf. Eq. 6.23): this implies that whenever in this region the principal stress $\bar{\sigma}_1$ is larger than or equal to the material strength $\bar{\sigma}_c$, the crack propagates within the bulk with an angle $\theta_c > -\pi/2$.

When this is not the case, the stress state at $\xi = -\alpha$ determines if the crack propagates along the interface or within the bulk. Here, if the principal stress $\bar{\sigma}_1(-\alpha)$ is smaller than the material strength $\bar{\sigma}_c$, the crack propagates along the interface. If instead is $\bar{\sigma}_1(-\alpha) > \bar{\sigma}_c$, the crack propagates within the bulk if

$$\frac{\bar{\sigma}_1(-\alpha)}{\bar{\sigma}_c} > \frac{\bar{\sigma}_{zz}(-\alpha)}{\lambda}. \quad (6.24)$$

The effects of friction on the criterion of Eq. 6.24 is then of particular interest. Larger values of μ imply in fact larger values of $\bar{\sigma}_1(\xi)$ (see Eq. 6.23 and Figure 6.7a), thus enhancing crack propagation within the bulk. A similar trend is also expected for increasing values of $T/\mu P$, although the effects of a variation of such parameter appear negligible compared to those of μ (cf. Figure 6.7b).

Note that, if the crack propagates along the interface, neither the rolling particle nor the surface are worn. If the crack propagates within the bulk, detachment of material from the surface takes place, and the particle grows in size.

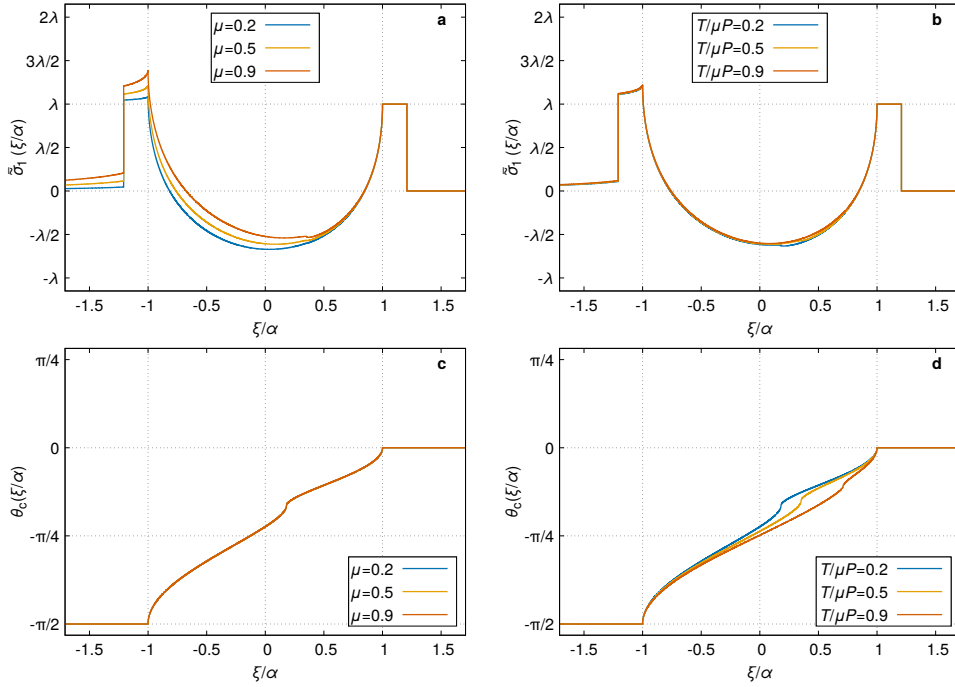


Figure 6.7 – Maximum principal stress $\bar{\sigma}_1(\xi)$ and crack propagation angle θ_c along the interface in the case of tractive rolling with adhesion. The horizontal axis is scaled by α . a) Effect of the friction coefficient μ on $\bar{\sigma}_1(\xi)$ for constant values of the Maugis parameter and of the ratio between the transmitted tangential force and the limiting frictional force (here: $\lambda = 1$ and $T/\mu P = 0.5$). b) Effect of the ratio $T/\mu P$ on $\bar{\sigma}_1(\xi)$ for constant values of the Maugis parameter and of the coefficient of friction (here: $\lambda = 1$ and $\mu = 0.5$). c) The friction coefficient μ has no effect on θ_c (all the curves superpose), for constant values of the Maugis parameter and of the ratio between the transmitted tangential force and the limiting frictional force (here: $\lambda = 1$ and $T/\mu P = 0.5$). d) Effect of the ratio $T/\mu P$ on θ_c for constant values of the Maugis parameter and of the coefficient of friction (here: $\lambda = 1$ and $\mu = 0.5$).

Chapter 6. A mechanistic model for the growth of cylindrical debris particles in the presence of adhesion

6.4.1 Effect of cylinder radius

The value of the radius of the cylinder affects the value of the contact width, through the load equation (Eq. 6.5) and the non-dimensionalization of Equations 6.1. The positive solution for α of Equation 6.5 is

$$\alpha = \frac{2}{\pi} \left[2\lambda \sqrt{m^2 - 1} + \sqrt{\pi \tilde{P} + 4\lambda^2 (m^2 - 1)} \right] \quad (6.25)$$

which scales with R as (cf. non-dimensionalizations 6.1e to 6.1h, and 6.1j)

$$\alpha \sim \sigma_0 R^{1/3} + \sqrt{PR^{-1/3} + \sigma_0 R^{2/3}} \quad (6.26)$$

The contact width a thus scales as (cf. non-dimensionalizations 6.1a)

$$a \sim R^{2/3} \left(\sigma_0 R^{1/3} + \sqrt{PR^{-1/3} + \sigma_0 R^{2/3}} \right) \quad (6.27)$$

and it always increases for increasing values of R (holding the other parameters unchanged). Simple examples are the cases of zero applied load ($P = 0$), for which $a \sim R$, and the Hertzian limit ($\sigma_0 = 0$), for which $a \sim R^{1/2}$.

For a given set of parameters, an increase in the contact width leads to lower values of the principal stress $\bar{\sigma}_1(\xi)$: following from Equations 6.1g, the true principal stress at the interface is in fact expressed as

$$\bar{\sigma}_1(\xi) = s \cdot \bar{\sigma}_1(\xi) = \left(\frac{wE^{*2}}{R} \right)^{1/3} \cdot \bar{\sigma}_1(\xi) \quad (6.28)$$

and when R increases, the true principal stress $\bar{\sigma}_1(\xi)$ generally decreases. Ahead of the crack tip, a reduction in the true principal stress $\bar{\sigma}_1(\xi)$ implies that there exists a crossover value R_\times such that, for all $R \geq R_\times$, $\bar{\sigma}_1(\xi) < \sigma_c$, and the crack propagation is governed by the stress state for $\xi = -\alpha$.

In this case, the value of the true stress $\bar{\sigma}_{zz}(-\alpha)$ is not affected by a change in R , as it is always given by the limiting adhesive stresses σ_0 :

$$\bar{\sigma}_{zz}(-\alpha) = s \cdot \lambda = s \cdot \frac{\sigma_0}{s} = \sigma_0 \quad (6.29)$$

We can now rewrite the criterion of Eq. 6.24 in terms of true stresses:

$$\frac{\bar{\sigma}_1(-\alpha)}{\sigma_c} > \frac{\bar{\sigma}_{zz}(-\alpha)}{\sigma_0}, \quad (6.30)$$

and the only value that changes in Eq. 6.30 when R increases is $\bar{\sigma}_1(-\alpha)$, which decreases, and it is thus harder to satisfy the criterion for crack propagation within the bulk: the probability of crack propagation along the interface thus increases.

To recap, for small values of R , crack propagation is more likely within the bulk, and for large values of R , crack propagation is more likely along the interface. If a particle then exhibits continuous growth during the rolling motion in the wear process, such growth is expected to decrease over time (as R increases).

6.4.2 Effect of Maugis parameter

The Maugis parameter is (cf. Equations 6.1f and 6.1g)

$$\lambda = \sigma_0 \left(\frac{R}{wE^*2} \right)^{1/3} \quad (6.31)$$

and it affects the magnitude of the tensile stresses at the trailing edge: larger values of λ imply larger values of $\bar{\sigma}_1(\xi = -\alpha)$ and a higher chance of reaching the material resistance $\bar{\sigma}_c$ (cf. criterion of Eq. 6.24). Large, soft bodies with strong adhesion ($\lambda \rightarrow \infty$, JKR limit) favour then crack propagation within the bulk (instead of along the interface) more than small, hard bodies with low adhesion ($\lambda \rightarrow 0$, DMT limit).

6.4.3 Effect of load

An increase in the applied load P alone does not lead to an increase of $\bar{\sigma}_{zz}(\xi)$ (the values being capped by λ which depends on the material and the geometry, not on the loading conditions), but it does allow for larger tensile stresses $\bar{\sigma}_{xx}^t(\xi)$ due to the tangential component of the force transmitted at the interface (see Eq. 6.17c). This is a consequence of the assumption of Coulomb friction, and it leads to larger principal stresses $\bar{\sigma}_1(\xi \rightarrow -\alpha)$ and thus a higher likelihood of damage within the bulk. The trend of $\theta_c(\xi/a)$ does not change.

6.4.4 Effect of friction

Coefficient of friction For a given value of $T/\mu P$, the effect of the coefficient of friction μ is simply to scale the tractions $X(\xi)$ (cf. Equations 6.10) and thus larger values of μ leads to larger stresses $\bar{\sigma}_1(\xi = -\alpha)$ (see Figures 6.7 and 6.11), extending the tensile zone ahead of the trailing edge and favouring crack propagation within the bulk (as the trend of $\theta_c(\xi/a)$ is not affected by the value of μ , see Figure 6.7c).

Transmitted forces ratio For a given value of μ , the ratio $T/\mu P$ between the transmitted tangential force and the maximum frictional force changes the trend in $\theta_c(\xi/a)$. Larger values of the ratio gives a larger tensile zone ahead of the trailing edge and a softer decrease in the values of θ_c with ξ/α (see Figures 6.7 and 6.11). This favours crack propagation within the bulk as large values of $|\theta_c|$ are encountered in the process zone.

In the limiting case of $\mu \rightarrow \infty$, it is $T/\mu P \rightarrow 0$, $\psi \rightarrow 0$, $\lim_{\xi \rightarrow -\chi^-} \theta_c \rightarrow -\pi/2$ and $\lim_{\xi \rightarrow -\chi^+} \theta_c \rightarrow -\pi/4$. The crack propagation angle ahead of the trailing edge is thus the smallest. In the most general case is then $-\pi/2 < \theta_c(\xi \rightarrow \alpha^+) \leq \pi/4$.

Adhesive friction Throughout the manuscript we assumed Coulomb friction. This is not strictly true when adhesion is strong, as is the case at small scales, where the frictional force is proportional to the true contact area instead [49, 58] and the linear proportionality with the normal load is lost [58]. In a first approximation, when such contribution prevails, we can replace the tractions of Equation 6.11 with the distribution

$$\tilde{X}_{\text{adh}}(\xi) = \begin{cases} \bar{\tau}_0 & |\xi| \leq \chi \\ 0 & |\xi| > \chi \end{cases} \quad (6.32)$$

where $\bar{\tau}_0$ is simply the stress due to the applied tangential force if it is equally distributed over the interaction width 2χ . The latter coincides with the true contact area in our case, defined as the area over which the two bodies interact [58]. Note that in this case the tangential distribution is applied over the whole interaction area, as it is assumed that tangential forces are sustained also where the two bodies are not in direct contact, as long as they interact with one another [58]. Equation 6.2b

becomes then

$$\tilde{T} = \int_{-\chi}^{\chi} \tilde{X}_{\text{adh}}(\xi) d\xi \quad . \quad (6.33)$$

and, to prevent sliding and slip, is limited by Equations 6.3 which now read

$$|\tilde{T}| \leq 2\chi\tilde{\tau}_c \quad (6.34)$$

$$|\tilde{X}_{\text{adh}}(\xi)| \leq \tilde{\tau}_c, \forall \xi \in [-\chi, \chi] \quad (6.35)$$

where $\tilde{\tau}_c$ is a non-dimensional effective shear strength of the contact interface.

The stress distribution $\bar{\sigma}_{xx}^t(\xi)$ for a constant tangential load is [62]

$$\begin{aligned} \bar{\sigma}_{zz}^t(\xi) &= 0 \\ \bar{\sigma}_{xx}^t(\xi) &= \frac{2\tilde{\tau}_0}{\pi} \ln\left(\frac{\xi - \chi}{\xi + \chi}\right) \\ \bar{\sigma}_{xz}^t(\xi) &= \begin{cases} -\tilde{\tau}_0 & |\xi| \leq \chi \\ 0 & |\xi| > \chi \end{cases} \end{aligned} \quad (6.36)$$

which leads to a positive infinite value of $\bar{\sigma}_{xx}^t(\xi = -\chi)$ (the singularity is negative for $\xi = \chi$). We argue that such singularity may result in local plastification, but not crack propagation, as the crack tip is further ahead at $\xi = -\alpha$.

The effects of the distribution of Equation 6.36 on the maximum principal stress and on the crack propagation angle are depicted in Figure 6.8. With respect to the Coulomb friction case, $\bar{\sigma}_1(\xi)$ changes significantly, and it shows a positive infinite value at $\xi = -\alpha$ independently of the value of $\tilde{\tau}_0$. The angle θ_c is still in the interval $[-\pi/2, 0]$, but its value is smaller at $\xi = \alpha$ than the Coulomb case. Adhesive friction is thus expected to lead to damage in a region closer to the surface.

Similarly to μ for the Coulomb friction case, $\tilde{\tau}_0$ has the effect of scaling the magnitude of $\bar{\sigma}_1(\xi)$ leaving θ_c unchanged.

In the most general case, the tangential tractions \tilde{X} should include a term \tilde{X}_μ for the Coulomb friction and a second term $\tilde{X}_{\tilde{\tau}_0}$ for the adhesive friction, leading to an expression of the type [178]

$$\tilde{X}(\xi) = \tilde{X}_\mu(\mu, \tilde{P}, \alpha) + \tilde{X}_{\tilde{\tau}_0}(\tilde{\tau}_0, \chi) \quad (6.37)$$

where one term or the other can prevail according to the material properties and the

Chapter 6. A mechanistic model for the growth of cylindrical debris particles in the presence of adhesion

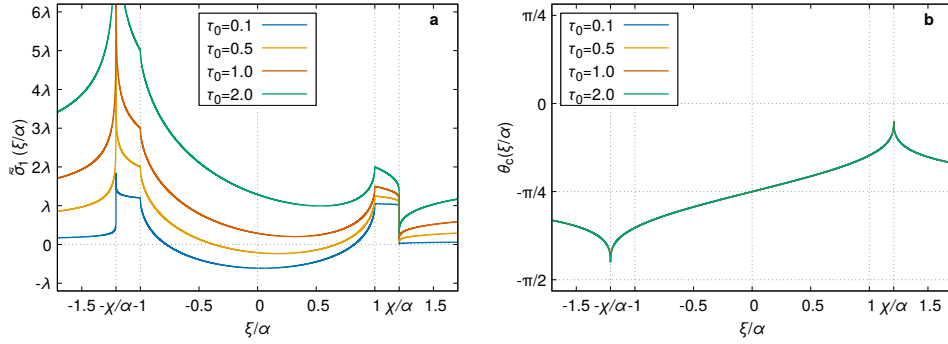


Figure 6.8 – Maximum principal stress $\bar{\sigma}_1(\xi)$ and crack propagation angle θ_c along the interface in the case of tractive rolling with adhesion, with adhesive friction. The horizontal axis is scaled by α . a) Effect of the applied constant tangential stress $\bar{\tau}_0$ on $\bar{\sigma}_1(\xi)$. b) The magnitude of the applied constant tangential stress $\bar{\tau}_0$ has no effect on θ_c (all curves superpose). In all the figures $\tilde{P} = \pi/4$ and $\lambda = 1$.

scale of the problem.

6.4.5 Effect of pre-existing surface flaws

So far we assumed that the contact interface is continuous and homogeneous, the crack tip is located at $\xi = -\alpha$, and the crack propagates with an angle θ_c if $\bar{\sigma}_1(\xi) \geq \bar{\sigma}_c$ in the proximity of the crack tip. If it is always $\bar{\sigma}_1(\xi) < \bar{\sigma}_c$, we can assume that rolling takes place without damaging the particle nor the surface, i.e. $\bar{\sigma}_{zz}(\xi = -\alpha) = \lambda$, the interface adhesive resistance λ is overcome, and the crack propagates along the contact interface. In other words, the tensile resistance λ of the contact interface is reached before the tensile resistance $\bar{\sigma}_c$ of the bulk material.

On the other hand, the frame of reference moves with the contact interface: the surfaces of the cylinder and of the opposing surface flowing through it. This means that a point belonging to the surface goes through different stress states, from right to left in our stress diagrams, and the tensile resistance $\bar{\sigma}_c$ of the material can be reached at such points before they reach $\xi = -\alpha$. This has two consequences: First, if no surface flaw exists, the crack always propagates in the bulk with an angle $\theta_c > -\pi/2$, as soon as the material point reaches a high enough stress within the process zone. Second, if a surface flaw exists at the material point, a secondary crack may propagate before the point reaches $\xi = -\alpha$. The secondary crack still always propagates within the bulk (cf. θ_c trends in previous sections and in 6.6), but at a

lower angle, possibly leading to damage which is closer to the surface.

6.4.6 Further considerations

In order to treat the problem analytically, the proposed approach is simplified in a number of aspects, such as the assumptions of plain strain, continuity at the interface, homogeneity of the material (which is the same for the rolling cylinder and the mating surface). While this seems reasonable in a variety of applications (from molecular dynamics simulations to powder rolling phenomena in faults), it is not necessarily the most frequent scenario in other tribosystems. Tribological phenomena are known to include several intertwined non-linearities, and for instance the debris particle may display different mechanical properties than the surfaces it originated from. This can be due to chemo-physical transformation activated during the debris formation process. Also, high stresses act at the interface and on the portions of the surfaces that will form the debris particle, which may then easily accommodate inelastic behaviour (both brittle or ductile). In such conditions, the particle may favour breakdown or loss of material, the accretion mechanism becoming negligible.

6.4.7 Numerical validation

Methods Several numerical methods to model fracture are available in the literature, and are often divided into local and non-local approaches, depending on the crack propagation criterion. The extended finite element method [179] and cohesive zone models [173, 180] are examples of local models, where the criterion for crack propagation is applied at the tip of an existing crack or notch, and the crack is represented by a strong discontinuity in the material. In non-local methods, the crack is modelled instead as a continuous field: examples of such approaches are thick level sets [181] and phase-field approaches [182]. In the current work we adopted a phase-field approach, as it is based on a global energy minimization that takes into account of the energy needed to create new surfaces. This is possible because of the Γ -convergence of the method [183], that allows to compute the fracture energy with an integral over the volume of the whole system instead of an integral over the crack surface (which is unknown). Another important feature of the approach is that the crack path is mesh independent.

The phase-field approach is based on Griffith's energy criterion for crack propaga-

Chapter 6. A mechanistic model for the growth of cylindrical debris particles in the presence of adhesion

tion [184], which states that, as the free energy of a system remains constant, the creation of new surfaces within a body takes place at the expenses of the potential energy of said body:

$$\mathcal{E}(u_i, d) = \mathcal{E}_{\text{el}}(u_i, d) + \mathcal{E}_{\text{frac}}(d) - \mathcal{W}_{\text{ext}}(u_i, d), \quad (6.38)$$

where u_i and d are the displacements and damage field, \mathcal{E} , \mathcal{E}_{el} and $\mathcal{E}_{\text{frac}}$ indicate the free, elastic strain and fracture energies respectively, and \mathcal{W}_{ext} is the work done by the external forces on u . An increase in $\mathcal{E}_{\text{frac}}$ is then possible only with concurrent reduction of the potential energy $\mathcal{E}_{\text{pot}} = \mathcal{E}_{\text{el}} - \mathcal{W}_{\text{ext}}$. No kinetic energy appears in Eq. 6.38 as we are interested in a quasi-static approach, but extension of the method to include dynamics effects exist [185, 186]. The introduction of a continuous damage field d (with $d \in [0, 1]$) in the phase-field approximation allows to represent the damage in the material, from intact ($d = 0$) to fully damaged material ($d = 1$). The fracture energy is then expressed as

$$\mathcal{E}_{\text{frac}}(d) = \int_{\Omega} w \Gamma(d) d\Omega, \quad (6.39)$$

where w is the fracture energy, Ω is the investigated body, and $\Gamma(d)$ the crack density functional introduced by the phase-field theory. Different expressions of $\Gamma(d)$ have been developed [187, 188] – in our simulations we adopt the second order functional AT2 [188]:

$$\Gamma(d) = \frac{1}{4l_0} \left(d^2 + 4l_0^2 |\nabla d|^2 \right), \quad (6.40)$$

where l_0 is a regularization length scale and ∇ is the gradient operator. To allow the crack to propagate only under tension (and not under compression), the elastic strain energy density in the phase-field approach is expressed as

$$\Psi_{\text{el}}(\varepsilon_{ij}, d) = (1 - d)^2 \Psi_{\text{el}}^+(\varepsilon_{ij}) + \Psi_{\text{el}}^-(\varepsilon_{ij}), \quad (6.41)$$

where [189]

$$\Psi_{\text{el}}^{\pm}(\varepsilon_{ij}) = \frac{\lambda'}{2} \langle \varepsilon_{ii} \rangle_{\pm}^2 + G \varepsilon_{\pm ii}^2, \quad (6.42)$$

with λ' and G the Lamé first parameter and the shear modulus respectively, $\langle \bullet \rangle_{\pm} = (\bullet \pm |\bullet|)/2$. Note that other splits of $\Psi_{\text{el}}(\varepsilon_{ij}, d)$ are possible [185, 186]. By substituting Eq. 6.39 and 6.41 in Eq. 6.38, the variational formulation of the phase-field approach is obtained. Numerically, the finite element method is used to discretize the system,

and the free energy is minimized for (u_i, d) with a staggered scheme [190, 191]. For each load increment, first the linear elastic problem is solved for the given values of the damage d , obtaining the updated values of the displacements u_i . These values of u_i are then used to solve the phase-field problem and update the values of d , that are in turn used in the next solution of the linear elastic problem, and so on, until the values of d and u_i converge. The load is then incremented again. The phase-field and the finite element methods are available in the finite element library Akantu [192].

Simulation The analytical prediction that the crack propagates within the bulk and not within the rolling particle has been tested with a numerical approach. A simplified geometry is then considered, where a cylinder in contact with a half-plane is modelled as one body, with no discontinuity along the contact interface (Figure 6.9a). The half-plane is represented by a large enough rectangular shape. The rolling motion is represented by applying uniform horizontal displacements to the bottom and to the sides of the half-plane, and by fixing the center of mass of the cylinder. This choice allows the cylinder boundary to be stress-free. Details of the input parameters are provided in Table 6.4. The fracture process is modelled by means of the phase-field approach described in the previous paragraph.

The results of the simulation are presented in Figures 6.9b and 6.9c. The crack propagates from the trailing to the leading edge, consistently with the rolling motion of a cylinder that advances towards positive values of the horizontal axis. The crack also propagates within the half-plane, as it is correctly predicted by our analytical model, until it reaches the leading edge. The phase-field model ensures that the crack path does not depend on the mesh.

6.5 Conclusions

We have presented a framework to investigate wear formation and growth in a three-body contact configuration, where all bodies have the same material properties. This framework is inspired by the work of Maugis and sees the rolling motion as the opening of a crack at the trailing edge (and the closure of a crack at the leading edge). The direction of propagation of the opening crack determines from which body the material is removed in the wear process. We derive the full stress state at the surface in the free rolling and tractive rolling cases, with and without adhesion.

Chapter 6. A mechanistic model for the growth of cylindrical debris particles in the presence of adhesion

Parameter	Value
E	1.0
ν	0.25
w	0.1
l_0	0.01
h_{\min}	0.002
R	10
l_x	30
l_y	15
displacement rate	0.01
number of steps	2500

Table 6.4 – Parameters adopted for the numerical simulations. All values are in dimensionless units; lengths are non-dimensionalized by the half-width of contact. h_{\min} is the value of the minimum mesh size, which extends over a stripe of thickness 1.8 along the contact interface. This ensures the ratio $l_0/h_{\min} = 5$ which allows to correctly represent the crack thickness [188]. l_x and l_y are half-plane dimensions along the horizontal and vertical direction respectively.

If no tangential force is transmitted at the contact interface, the crack propagates along the interface and no wear is expected. If the resultant transmitted force has a tangential component, which opposes the direction of motion, the crack always propagates within the opposing surface, and never within the third-body. The effects of the particle size, the Maugis parameter, the frictional parameters, the adhesive friction, and surface flaws are also investigated. The trend of crack propagation within the bulk that we observe in our simplified model helps understanding recent observations revealing the growth of wear particles with time.

6.6 Further cases

In this section, the cases of free rolling with and without adhesion and the case of tractive rolling without adhesion are discussed.

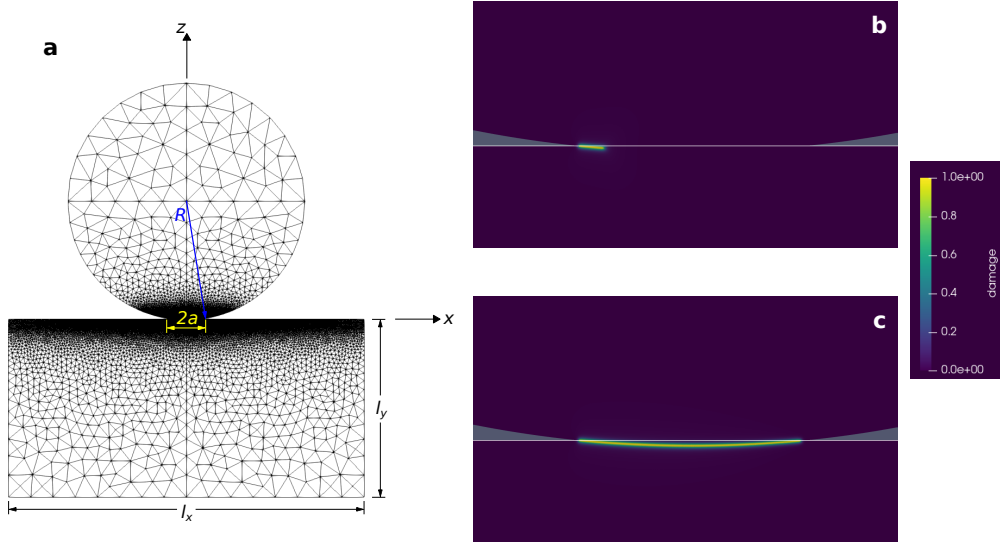


Figure 6.9 – Discretized geometry (a) for the phase-field simulations and damage evolution (b-c). Note that the frame of reference of the finite element library Akantu follows the traditional continuum mechanics one, thus differing from the contact mechanics adopted throughout the manuscript (Figure 6.2). b) Crack develops at the trailing edge of the contact interface and propagates with an angle $\theta_c < 0$. c) At large loads, the crack bends back towards the leading edge. In both picture the white horizontal line refers to $z = 0$.

6.6.1 Calculation

When no adhesion is present ($\beta \rightarrow 0$ and $\lambda \rightarrow 0$)^e, the classical Hertzian case [53] is recovered and Maugis' normal tractions distribution reduces to (cf. Equation 6.4):

$$\tilde{Z}(\xi) = \begin{cases} \frac{\tilde{p}_0}{\alpha} \sqrt{\alpha^2 - \xi^2} & |\xi| \leq \alpha \\ 0 & |\xi| > \alpha \end{cases} \quad (6.43)$$

where \tilde{p}_0 is the pre-factor written in the classical Hertz convention (cf. Equation 6.23).

^eNote that both assumptions on β and λ are needed. If only vanishing adhesive stresses are assumed ($\lambda \rightarrow 0$), then $m \rightarrow \infty$ is admissible and the DMT limit is recovered. If only vanishing adhesive half-width is assumed ($\beta \rightarrow 0$), then $\lambda \rightarrow \infty$ is admissible and the JKR limit is recovered.

Chapter 6. A mechanistic model for the growth of cylindrical debris particles in the presence of adhesion

Free rolling without adhesion

If no tangential load is transmitted, i.e. $X(\xi) = 0$, the rolling motion is free, the tractions at the interface are fully given by Equation 6.43, and the stresses $\bar{\sigma}_{ij}(\xi)$ are those due to pure Hertzian contact (cf. Equations 6.14 and 6.15):

$$\begin{aligned}\bar{\sigma}_{zz}(\xi) = \bar{\sigma}_{zz}^n(\xi) &= \begin{cases} -\frac{\bar{p}_0}{\alpha} \sqrt{\alpha^2 - \xi^2} & |\xi| \leq \alpha \\ 0 & |\xi| > \alpha \end{cases} \\ \bar{\sigma}_{xx}(\xi) = \bar{\sigma}_{xx}^n(\xi) = \bar{\sigma}_{zz}(\xi) \\ \bar{\sigma}_{xz}(\xi) = \bar{\sigma}_{xz}^n(\xi) = 0\end{aligned}\quad (6.44)$$

$\bar{\sigma}_{xx}(\xi)$ and $\bar{\sigma}_{zz}(\xi)$ are then also principal stresses (cf. Equation 6.18), the stress state is hydrostatic, and all directions are principal directions.

Tractive rolling without adhesion

When the transmitted force has a tangential component, the stress state is given by Equations 6.14, with $\bar{\sigma}_{ij}^n(\xi)$ given by Equations 6.44 in absence of adhesion and $\bar{\sigma}_{ij}^t(\xi)$ by Equations 6.17 (see Figure 6.10):

$$\begin{aligned}\bar{\sigma}_{zz}(\xi) &= \begin{cases} -\frac{\bar{p}_0}{\alpha} \sqrt{\alpha^2 - \xi^2} & |\xi| \leq \alpha \\ 0 & |\xi| > \alpha \end{cases} \\ \bar{\sigma}_{xx}(\xi) &= \begin{cases} -\frac{\bar{p}_0}{\alpha} \left(\sqrt{\alpha^2 - \xi^2} - 2\mu\xi \right) & |\xi| \leq \alpha \\ -2\mu\frac{\bar{p}_0}{\alpha} \left(\xi - \text{sgn}(\xi) \sqrt{\xi^2 - \alpha^2} \right) & |\xi| > \alpha \end{cases} + \\ &+ \begin{cases} 2\mu\frac{\bar{p}_0}{\alpha} (\xi - \psi) & |\xi - \psi| \leq \rho \\ 2\mu\frac{\bar{p}_0}{\alpha} \left[\xi - \psi - \text{sgn}(\xi - \psi) \sqrt{(\xi - \psi)^2 - \rho^2} \right] & |\xi - \psi| > \rho \end{cases} \\ \bar{\sigma}_{xz}(\xi) &= \begin{cases} -\mu\frac{\bar{p}_0}{\alpha} \sqrt{\alpha^2 - \xi^2} & |\xi| \leq \alpha \\ 0 & |\xi| > \alpha \end{cases} + \\ &+ \begin{cases} \mu\frac{\bar{p}_0}{\alpha} \sqrt{\rho^2 - (\xi - \psi)^2} & |\xi - \psi| \leq \rho \\ 0 & |\xi - \psi| > \rho \end{cases}\end{aligned}\quad (6.45)$$

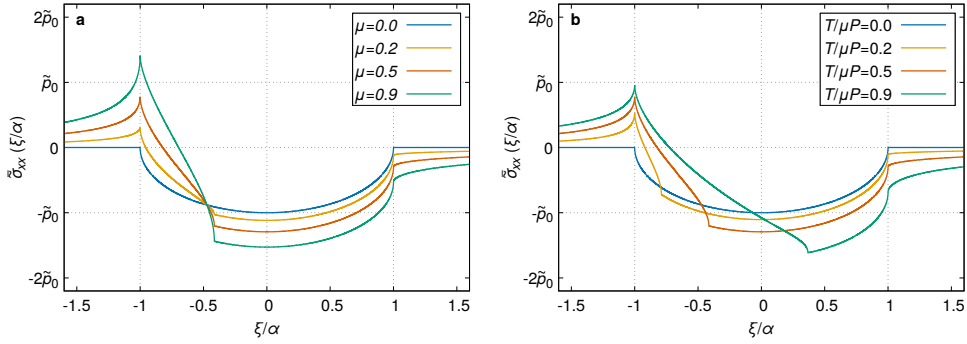


Figure 6.10 – Stress $\bar{\sigma}_{xx}(\xi)$ in the case of tractive rolling without adhesion. The horizontal axis is scaled by α . a) Effect of the friction coefficient μ for constant values of the ratio between the transmitted tangential force and the limiting frictional force (here: $T/\mu P = 0.5$). b) Effect of the ratio $T/\mu P$ between the transmitted tangential force and the limiting frictional force for constant values of the coefficient of friction (here: $\mu = 0.5$). In all the figures $\tilde{P} = \pi/4$ and thus $\alpha = 1$ (cf. Equation 6.5, with $m \rightarrow 1$, $\lambda \rightarrow 0$ without adhesion.). $\mu = 0$ coincides with the Hertzian case, for which also holds $\bar{\sigma}_{zz}(\xi) = \bar{\sigma}_{xx}(\xi)$.

Note that in this case, besides the non-dimensionalized load \tilde{P} , (as for free rolling without adhesion, Section 6.6.1), it is necessary to know μ and $T/\mu P$ to determine the stresses $\bar{\sigma}_{ij}(\xi)$.

Free rolling with adhesion

In the case of adhesion, the general expression of the Maugis tractions of Equations 6.4 is used. As in Section 6.6.1, no tangential traction is transmitted and is $X(\xi) = 0$. The surface stresses are then exactly those of Equations 6.16 and are fully determined once the non-dimensionalized load \tilde{P} and the Maugis parameter λ are known. Also in this case $\bar{\sigma}_{xx}(\xi)$ and $\bar{\sigma}_{zz}(\xi)$ are principal stresses (cf. Equation 6.18), the stress state is hydrostatic, and all directions are principal directions.

Chapter 6. A mechanistic model for the growth of cylindrical debris particles in the presence of adhesion

6.6.2 Results and discussion

Free rolling without adhesion

From the stress state derived in section 6.6.1, at the trailing edge is $\bar{\sigma}_{xx}(-\alpha) = \bar{\sigma}_{zz}(-\alpha) = \bar{\sigma}_{xz}(-\alpha) = 0$. As all directions are principal, the crack will open along the weakest plane – which normally is the contact interface.

Tractive rolling without adhesion

Figures 6.11a and 6.11b show the maximum principal stress $\bar{\sigma}_1(\xi)$ due to the stress fields derived in section 6.6.1. The stress is maximum at the trailing edge ($\xi = -\alpha$), and is positive (tensile stress) over a region around the trailing edge. If $\bar{\sigma}_1(-\alpha) > \bar{\sigma}_c$, $\bar{\sigma}_c$ being the maximum tensile stress that the material can sustain, the crack propagates with an angle θ_c . Such angle is fully determined by the stress state, and is represented in Figures 6.11c and 6.11d, and is always $-\pi/2 < \theta_c(\xi/a) \leq 0$ ahead of the crack tip (i.e. for all $\xi > -\alpha$). The crack thus always propagates within the bottom material or along the contact interface, the actual angle depending on the size of the process zone.

Free rolling with adhesion

From the stress state derived in section 6.6.1, at the trailing edge is $\bar{\sigma}_{xx}(-\alpha) = \bar{\sigma}_{zz}(-\alpha) = \lambda$ and $\bar{\sigma}_{xz}(-\alpha) = 0$. Similarly to the case of free rolling without adhesion (Section 6.6.2), all directions are principal, the crack will open along the weakest plane – which normally is the contact interface.

6.6. Further cases

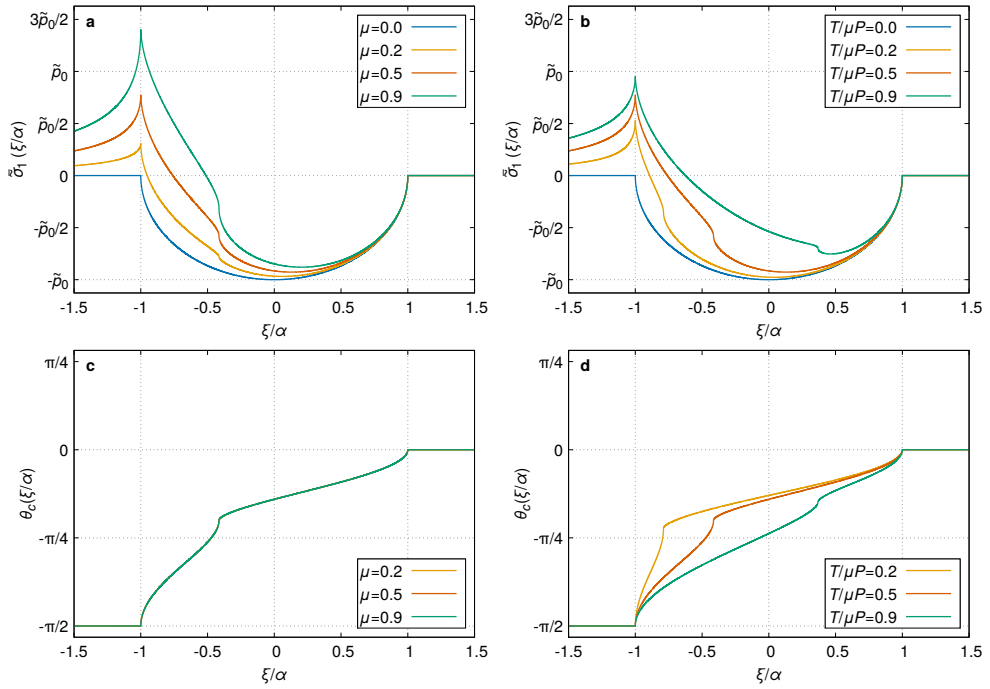


Figure 6.11 – Maximum principal stress $\bar{\sigma}_1(\xi)$ and crack propagation angle θ_c along the interface in the case of tractive rolling without adhesion. The horizontal axis is scaled by α . a) Effect of the friction coefficient μ on $\bar{\sigma}_1(\xi)$ for constant values of the ratio between the transmitted tangential force and the limiting frictional force (here: $T/\mu P = 0.5$). b) Effect of the ratio $T/\mu P$ on $\bar{\sigma}_1(\xi)$ for constant values of the coefficient of friction (here: $\mu = 0.5$). c) The friction coefficient μ has no effect on θ_c (all the curves superpose), for constant values of the ratio between the transmitted tangential force and the limiting frictional force (here: $T/\mu P = 0.5$). d) Effect of the ratio $T/\mu P$ on θ_c for constant values of the coefficient of friction (here: $\mu = 0.5$). In all the figures $\tilde{P} = \pi/4$ and thus $\alpha = 1$ (cf. Equation 6.5).

6.7 Maugis formalism

Here we re-derive the equations presented in Sections 6.2 and 6.3 following Maugis' formalism. In such context, only the contact half-width a is non-dimensionalized by the parameter l (cf. Equations 6.1a and 6.1e), while the other lengths are non-dimensionalized by a itself. Stresses are then plotted as a function of x/a . Note that such scaling for the stresses gives the same plots reported in the previous sections as $\xi/\alpha = x/a$. Also, the procedure in deriving the crack propagation angles θ_c is not affected by the formalism, and all the arguments and the results reported in the previous sections hold unchanged.

In the following, we define $\tilde{x} := x/a$, and all the parameters already introduced keep the same meaning.

6.7.1 Theory

Normal and tangential tractions

Equations 6.2 and 6.3 in the Maugis formalism are:

$$\tilde{P} = \int_{-m}^m \tilde{Z}(\tilde{x}) d\tilde{x} \quad (6.46a)$$

$$\tilde{T} = \int_{-1}^1 \tilde{X}(\tilde{x}) d\tilde{x} \quad (6.46b)$$

$$|\tilde{T}| \leq \mu \tilde{P} \quad (6.46c)$$

$$|\tilde{X}(\tilde{x})| \leq \mu \tilde{Z}(\tilde{x}) \quad (6.46d)$$

Equations 6.4 for the Maugis tractions become

$$\tilde{Z}(\tilde{x}) = \begin{cases} -\frac{\alpha}{2} \sqrt{1 - \tilde{x}^2} + \frac{2\lambda}{\pi} \arctan \sqrt{\frac{m^2 - 1}{1 - \tilde{x}^2}} & |\tilde{x}| \leq 1 \\ -\lambda & 1 < |\tilde{x}| \leq m \\ 0 & |\tilde{x}| > m \end{cases} \quad (6.47a)$$

The distributions for the tangential load (Equations 6.10) are

$$\tilde{X}'(\tilde{x}) = \begin{cases} \mu \frac{2\tilde{P}}{\pi\alpha} \sqrt{1 - \tilde{x}^2} & |\tilde{x}| \leq 1 \\ 0 & |\tilde{x}| > 1 \end{cases} \quad (6.48a)$$

$$\tilde{X}''(\tilde{x}) = \begin{cases} -\mu \frac{2\tilde{P}}{\pi\alpha} \sqrt{\tilde{\rho}^2 - (\tilde{x} - \tilde{\psi})^2} & |\tilde{x} - \tilde{\psi}| \leq \tilde{\rho} \\ 0 & |\tilde{x} - \tilde{\psi}| > \tilde{\rho} \end{cases} \quad (6.48b)$$

where $\tilde{\rho} = \frac{r}{a} = 1 - \tilde{\psi} = (1 - \frac{T}{\mu P})^{1/2} \leq 1$ is the non-dimensionalized half-width over which $\tilde{X}''(\tilde{x})$ is applied. The total tangential tractions at the interface are then [170]

$$\tilde{X}(\tilde{x}) = \tilde{X}'(\tilde{x}) + \tilde{X}''(\tilde{x}) \quad (6.49)$$

Stress field

Equations 6.12 to 6.15 hold just by replacing ξ with \tilde{x} .

Stresses due to normal load The surface stresses due to the normal component of the force transmitted at the interface are then

$$\tilde{\sigma}_{xx}^n(\tilde{x}) = \tilde{\sigma}_{zz}^n(\tilde{x}) = \begin{cases} \frac{\alpha}{2} \sqrt{1 - \tilde{x}^2} - \frac{2\lambda}{\pi} \arctan \sqrt{\frac{m^2 - 1}{1 - \tilde{x}^2}} & |\tilde{x}| \leq 1 \\ \lambda & 1 < |\tilde{x}| \leq m \\ 0 & |\tilde{x}| > m \end{cases} \quad (6.50a)$$

$$\tilde{\sigma}_{xz}^n(\tilde{x}) = 0 \quad (6.50b)$$

To fully determine $\tilde{\sigma}_{ij}^n(\tilde{x})$ is thus necessary and sufficient to know the non-dimensionalized normal component \tilde{P} of the transmitted force and the Maugis parameter λ .

Stresses due to tangential load The surface stresses due to the tangential component of force transmitted at the interface are now (cf. Equations 6.17)

$$\tilde{\sigma}_{zz}^t(\tilde{x}) = 0 \quad (6.51a)$$

Chapter 6. A mechanistic model for the growth of cylindrical debris particles in the presence of adhesion

$$\begin{aligned} \bar{\sigma}_{xz}^t(\tilde{x}) &= -\tilde{X}(\tilde{x}) = -\tilde{X}'(\tilde{x}) - \tilde{X}''(\tilde{x}) = \\ &= \begin{cases} -\mu\tilde{p}_0\sqrt{1-\tilde{x}^2} & |\tilde{x}| \leq 1 \\ 0 & |\tilde{x}| > 1 \end{cases} + \begin{cases} \mu\tilde{p}_0\sqrt{\tilde{\rho}^2 - (\tilde{x} - \tilde{\psi})^2} & |\tilde{x} - \tilde{\psi}| \leq \tilde{\rho} \\ 0 & |\tilde{x} - \tilde{\psi}| > \tilde{\rho} \end{cases} \end{aligned} \quad (6.51b)$$

$$\begin{aligned} \bar{\sigma}_{xx}^t(\tilde{x}) &= \bar{\sigma}_{xx}'(\tilde{x}) + \bar{\sigma}_{xx}''(\tilde{x}) = \\ &= \begin{cases} -2\mu\tilde{p}_0\tilde{x} & |\tilde{x}| \leq 1 \\ -2\mu\tilde{p}_0\left(\tilde{x} - \text{sgn}(\tilde{x})\sqrt{\tilde{x}^2 - 1}\right) & |\tilde{x}| > 1 \end{cases} + \\ &+ \begin{cases} 2\mu\tilde{p}_0(\tilde{x} - \tilde{\psi}) & |\tilde{x} - \tilde{\psi}| \leq \tilde{\rho} \\ 2\mu\tilde{p}_0\left[\tilde{x} - \tilde{\psi} - \text{sgn}(\tilde{x} - \tilde{\psi})\sqrt{(\tilde{x} - \tilde{\psi})^2 - \tilde{\rho}^2}\right] & |\tilde{x} - \tilde{\psi}| > \tilde{\rho} \end{cases} \end{aligned} \quad (6.51c)$$

where the relation $\tilde{p}_0 = \frac{2\tilde{P}}{\pi\alpha}$ has been used. For the derivation of Equations 6.51c we refer the reader to Ref. [62].

6.7.2 Calculation

We report here the general cases of tractive rolling, with and without adhesion, as the cases of free rolling are straightforward once it is assumed $\mu = 0$.

Tractive rolling without adhesion

Equations 6.45 in the Maugis formalism become

$$\begin{aligned}
 \bar{\sigma}_{zz}(\tilde{x}) &= \begin{cases} -\tilde{p}_0 \sqrt{1 - \tilde{x}^2} & |\tilde{x}| \leq 1 \\ 0 & |\tilde{x}| > 1 \end{cases} \\
 \bar{\sigma}_{xx}(\tilde{x}) &= \begin{cases} -\tilde{p}_0 (\sqrt{1 - \tilde{x}^2} - 2\mu\tilde{x}) & |\tilde{x}| \leq 1 \\ -2\mu\tilde{p}_0 (\tilde{x} - \text{sgn}(\tilde{x}) \sqrt{\tilde{x}^2 - 1}) & |\tilde{x}| > 1 \end{cases} + \\
 &+ \begin{cases} 2\mu\tilde{p}_0(\tilde{x} - \tilde{\psi}) & |\tilde{x} - \tilde{\psi}| \leq \tilde{\rho} \\ 2\mu\tilde{p}_0 [\tilde{x} - \tilde{\psi} - \text{sgn}(\tilde{x} - \tilde{\psi}) \sqrt{(\tilde{x} - \tilde{\psi})^2 - \tilde{\rho}^2}] & |\tilde{x} - \tilde{\psi}| > \tilde{\rho} \end{cases} \cdot \quad (6.52) \\
 \bar{\sigma}_{xz}(\tilde{x}) &= \begin{cases} -\mu\tilde{p}_0 \sqrt{1 - \tilde{x}^2} & |\tilde{x}| \leq 1 \\ 0 & |\tilde{x}| > 1 \end{cases} + \\
 &+ \begin{cases} \mu\tilde{p}_0 \sqrt{\tilde{\rho}^2 - (\tilde{x} - \tilde{\psi})^2} & |\tilde{x} - \tilde{\psi}| \leq \tilde{\rho} \\ 0 & |\tilde{x} - \tilde{\psi}| > \tilde{\rho} \end{cases}
 \end{aligned}$$

Chapter 6. A mechanistic model for the growth of cylindrical debris particles in the presence of adhesion

Tractive rolling with adhesion

Finally, Equations 6.23 become

$$\begin{aligned}
 \bar{\sigma}_{zz}(\tilde{x}) &= \begin{cases} \tilde{p}_0 \sqrt{1 - \tilde{x}^2} - \frac{2\lambda}{\pi} \arctan \sqrt{\frac{m^2 - 1}{1 - \tilde{x}^2}} & |\tilde{x}| \leq 1 \\ \lambda & 1 < |\tilde{x}| \leq m \\ 0 & |\tilde{x}| > m \end{cases} \\
 \bar{\sigma}_{xx}(\tilde{x}) &= \begin{cases} -\tilde{p}_0 \left(\sqrt{1 - \tilde{x}^2} - 2\mu\tilde{x} \right) - \frac{2\lambda}{\pi} \arctan \sqrt{\frac{m^2 - 1}{1 - \tilde{x}^2}} & |\tilde{x}| \leq 1 \\ -2\mu\tilde{p}_0 \left(\tilde{x} - \text{sgn}(\tilde{x}) \sqrt{\tilde{x}^2 - 1} \right) + \lambda & 1 < |\tilde{x}| \leq m \\ -2\mu\tilde{p}_0 \left(\tilde{x} - \text{sgn}(\tilde{x}) \sqrt{\tilde{x}^2 - 1} \right) & |\tilde{x}| > m \end{cases} \\
 &+ \begin{cases} 2\mu\tilde{p}_0(\tilde{x} - \tilde{\psi}) & |\tilde{x} - \tilde{\psi}| \leq \tilde{\rho} \\ 2\mu\tilde{p}_0 \left[\tilde{x} - \tilde{\psi} - \text{sgn}(\tilde{x} - \tilde{\psi}) \sqrt{(\tilde{x} - \tilde{\psi})^2 - \tilde{\rho}^2} \right] & |\tilde{x} - \tilde{\psi}| > \tilde{\rho} \end{cases} \\
 \bar{\sigma}_{xz}(\tilde{x}) &= \begin{cases} -\mu\tilde{p}_0 \sqrt{1 - \tilde{x}^2} & |\tilde{x}| \leq 1 \\ 0 & |\tilde{x}| > 1 \end{cases} + \\
 &+ \begin{cases} \mu\tilde{p}_0 \sqrt{\tilde{\rho}^2 - (\tilde{x} - \tilde{\psi})^2} & |\tilde{x} - \tilde{\psi}| \leq \tilde{\rho} \\ 0 & |\tilde{x} - \tilde{\psi}| > \tilde{\rho} \end{cases}
 \end{aligned} \quad (6.53)$$

Chapter 7

Conclusions and outlook

7.1 Summary

This thesis addressed the role of surface roughness in adhesive wear processes, under dry sliding conditions, with molecular dynamics simulations and an analytical framework. The numerical simulations of two-dimensional systems allowed to model long-term effects on the surface roughness evolution due to the wear process, and short-term effects upon wear particle formation. The analytical framework allowed to explain the overall particle growth observed in the numerical simulations.

The numerical method adopted in the first part of the dissertation is molecular dynamics (MD). MD is a discrete method, and as such it allows to naturally take into account the several non-linearities that are present in tribological phenomena (e.g. contact, large deformation, inelastic behaviour, detachment of material, etc.). Continuum methods, in contrast, need ad hoc formulations to address them. Among the discrete methods, another suitable approach could have been the discrete element method (DEM). Yet, MD had already been proven to capture the ductile-to-brittle transition that is observed experimentally in adhesive wear, which was needed in this work to model a system where a debris particle is formed and constrained to roll between the surfaces.

A fundamental choice when using MD simulations are the potentials, which define the constitutive behaviour of the materials. Here, a family of potentials which are a modified version of the Morse potential has been adopted. These potentials are

Chapter 7. Conclusions and outlook

characterized by a common elastic and fracture behaviour, but a different ductile response. In particular, those with a more brittle response were proven to capture crack propagation upon asperity collision, and the consequent debris particle formation. Moreover, the characteristics of these potentials, like having only pairwise interactions over a short distance, make them cheap computationally. To contain the computational cost further, two-dimensional systems are modelled.

The first main result of the thesis is the capability of the method to track the surface morphology evolution into a self-affine fractal with a persistent Hurst exponent. Such statistical description is encountered in several frictional systems at different scales, from the geological- to the nano-scale, and was not reproduced numerically before. A set of long-timescale simulations was performed, so that in each of them the system could go past the running-in phase and reach a steady state for the average surface roughness, as observed experimentally. The surfaces analyzed in this phase are found to be well described by a self-affine morphology, with a Hurst exponent in the range 0.6-0.8. Several initial conditions, specifically in terms of material composition and surface morphology, led to the same final observations. The final self-affine morphology is the same that is found in several experimental conditions at different scales. In particular, as suggested for natural faults, the development of a third body is fundamental to work the surfaces by means of smoothing and re-roughening mechanisms that eventually lead to the final self-affine roughness.

Another important result from the same set of simulations concerns the wear rate. When the debris particle first forms, the wear rate (in terms of wear volume per unit of sliding distance) is much higher than in the remaining of the simulation. This is ascribed to the different system configurations. Upon particle formation, contact takes place in a two-body configuration where two asperities collide and form a debris particle that is proportional to the asperity junction size. After, the particle exchanges materials with the surfaces it rolls in-between (mostly removing it from them), in what is a three-body contact configuration.

A limitation of the simulations of this set is that full adhesion at the contact interface was considered. A second extended investigation regarded then the effects of reduced interfacial adhesion. Here, it is found that a self-affine morphology with a persistent Hurst exponent is still developed even if the interfacial adhesion is low, as long as the debris particle effectively works the surfaces. This is not always the case for the lowest values of interfacial adhesion explored.

Furthermore, the interplay between surface roughness, interfacial adhesion, and the

particle formation was investigated with a set of short timescale simulations. It was shown that reducing adhesion does not affect the minimum size of the debris particle. The size is still predicted by the AWM critical length scale, in which the junction shear strength appears. This property was previously found to be affected by a reduction in the interfacial adhesion for systems with simple geometries (atomistically flat surfaces with semicircular asperities). On the contrary, no effect of interfacial adhesion on the particle size has been found for initially complex rough surfaces. This is ascribed to the complexity of the geometry itself, which affects the junction growth and the debris particle formation in a more convoluted manner than in the case of simple geometries, as shown by different values of the geometrical factor. The bulk shear strength enters then the expression of the AWM critical length scale, and not the reduced interfacial adhesion.

In the long timescales simulations, it was also observed that the wear particle volume steadily increases. This led to the development of the second part of the thesis. An analytical framework is presented here to investigate particle accretion during rolling contact. The approach is inspired by Maugis' view of normal adhesive contact as a fracture process. In my work, the rolling contact of a cylinder against a flat surface is then seen as the closing of a crack at the leading edge, and the contemporary opening of a crack at the trailing edge. The stresses at the contact interface are then investigated, and a maximum hoop stress criterion is applied at the trailing edge to estimate where the crack is more likely to grow: within the surface or the rolling particle. The crack is found to propagate either along the interface or within the bulk, and particle accretion is thus favoured over particle breakdown. The trend is confirmed with numerical simulations.

7.2 Outlook

The results summarized above are a remarkable contribution to the understanding of wear. Through both its strengths and its limitations, the work of this dissertation can inspire further studies in the field.

The main limitation of the molecular dynamics investigations is that the modelled systems are two-dimensional. This was a necessary choice, as three-dimensional simulations are computationally too expensive to investigate surface roughness evolution over long timescales. Furthermore, the AWM critical length scale was also first proven in a two-dimensional setup, and later short timescale simulations proved

Chapter 7. Conclusions and outlook

it in a three-dimensional setup, too [85]. The interesting insights gained from the 2D simulations are then a motivation to extend the analysis to 3D, possibly with some simplifications (e.g. starting already from a three-body configuration) to contain the computational resources required.

The second limitation of the numerical simulations is the constitutive behaviour of the materials. The chosen pair potentials do not in fact directly model the properties of a specific material, nor that is their aim. Their scope of application in fact is in general to explore possible material behaviours. Once again, this approach has led recently to the formulation of the AWM critical length scale, which was later confirmed also by employing potentials that model the behaviour of silicon [85]. Further work should extend such investigations to other classes of materials, such as metals, ceramics, rocks and mixtures.

For some of these materials, notably rocks and granular assemblies in general, the discrete element method (DEM) might be a more suitable numerical method. Although computationally more expensive (for a given number of particles in the system), DEM has been widely used to model such materials at larger scales than the MD scale. Moreover, the method has already been capable of capturing some ductile-to-brittle transition in rock cutting [122].

Wear, as all the tribological phenomena, is known to be sensitive to a wide range of parameters: temperature, sliding velocity, surface morphology, material properties, material structure, contact configuration, applied loads, etc. In the present dissertation, only a subset of these could be investigated. To build a more complete picture of the phenomena, further studies should take into account the effects due to conditions not considered here.

The main limitations of the analytical framework are those that are common to such approaches: the material is linear elastic, materials are homogeneous and continuity along the contact interface is assumed. Of course the purpose of these approaches is not to provide a detailed prediction of such a complex phenomena, rather to give a first order explanation of some specific observation. Nonetheless, the model being two-dimensional, it can be extended to 3D systems.

Furthermore, the dissertation focused on wear of the adhesive type, which takes place when strong bonds are developed at the contact interface between the sliding bodies – which usually have comparable values of hardness. The other most common type of wear, abrasive wear, happens when a hard body scratches a softer one (e.g. rock cutting). The definitions are quite qualitative, and usually one speaks of one or

the other type based on the ratio of the hardness values of the sliding materials. It is known that a transition occurs from one mechanism to the other, e.g. from large values of the ratio to values close to unity. Numerical methods such as MD and DEM are then a suitable approach to explore this transition, in particular if employed with constitutive laws that inhibits adhesive bonding and/or allow for a significant contrast in the hardness of the materials.

Finally, the dissertation clearly did not explore any experimental setup. Experimental works in the contest of the surface roughness evolution in wear processes are limited due to the complexity of tracking the real time evolution. Extending approaches such as the one by Davidesko et al. [28] to other materials and scales would help with building a general picture of the phenomenon, together with numerical simulations of the kind presented here (and suggested above). The results obtained on the minimum size of a debris particle would also need experimental verification, and these might be easier to achieve: indeed the timescale is shorter and no continuous tracking of the surface roughness is needed.

In conclusion, this dissertation provided novel and remarkable insights into the surface roughness evolution in adhesive wear processes. The work also shows how the road towards a global picture of wear is still long ahead. Yet, this implies that there are room and motivation for further investigations that would lead to significant progress in our understanding of tribological phenomena at all scales, and consequently in technological developments.

Appendix A

A geometrical model as a tool for surface roughness evolution investigations

Simple growth models can successfully predict the statistical scaling of surfaces in some manufacturing processes, for example molecular beam epitaxy (MBE). Similar models do not exist for frictional processes, i.e. no growth model can currently capture the statistics of surfaces produced upon sliding as a function of some fundamental parameters of the system (such as material transfer rate or true contact area, for instance). The work reported in this chapter has thus the aim to explore the development of a simple geometrical model that would fulfill this gap. Inspired by classical surface growth models, the development of a new geometrical model is presented. The model considers two one-dimensional profiles and evolves their morphology with three steps. The profiles are first overlapped, then deformed locally, and finally slide. The fundamental ingredient is the deformation rule, which is based on the AWM critical length scale: the size of each junction determines whether it is deformed plastically or in a brittle fashion. Preliminary results are reported and show that the model does not reproduce the profile evolution into a self-affine morphology. A discussion follows on the possible reasons why this is the case, and a different approach to the geometrical modelling of frictional surfaces evolution is suggested.

A.1 Introduction

The source of inspiration for this approach are the surface growth models, such as the random deposition model introduced in Chapter 2. The idea is to reduce to the minimum the number of parameters needed to capture the evolution of the initial surface morphology into a self-affine one. The rules that govern this evolution are geometrical, in the sense that there is no mechanical, chemical, or other physical analysis of interfacial phenomena, although the rules are based on physical observations. This is the case also for the random deposition model with surface relaxation: the move that diffuses the particle does not follow any physical rule and only the heights of the neighbouring sites are in fact needed. A purely geometrical quantity then drives the particle movement. At the same time, this move is meant to mimic the physical diffusion that is known to happen at the surfaces. Ideally, the final model would be able to successfully predict the final surface geometry, given some input geometrical parameters that can be linked to material properties, in particular to the AWM critical length scale. The model would then possibly be useful also to practitioners for a zeroth order estimation of the surface roughness evolution in dry sliding contacts, and to thus orientate design choices.

A.2 Model

In the classical surface growth models, one interface is modelled: a system containing L sites with initial zero height is considered, particles are dropped one at the time, and the height of the interface grows. The morphology of this interface is then investigated. In the model developed here, two profiles are considered instead. The profiles are identified by the two sets of points $h_t(i, t)$ and $h_b(i, t)$, where 't' and 'b' indicate the top and bottom profile respectively, $i = 1, \dots, N$ is the i -th site and N the resolution, t is the time step. Note that in the figures, horizontal distances are non-dimensionalized by the profile length L , and the horizontal positions of the site i is then expressed as $x_i = i/N$. The profiles have the same length L , and they are initially rough, i.e. their average height at $t = 0$ deviates from the mean plane. At time $t = 0$, the top surface is not in contact with the bottom one, i.e. $h_t(i, 0) > h_b(i, 0)$ for all i . The two profiles are then overlapped for a given percentage of their length, and, following a geometrical criterion, their heights are updated along those overlapping portions. The top profile is then displaced horizontally, is overlapped again on the

bottom one, their geometries are updated, and so on. Note that, in contrast with the random deposition model, here the values of the heights are continuous, not discrete.

There are thus three consecutive moves within each time step:

1. from t to $t + 1/3$: overlapping of the profiles;
2. from $t + 1/3$ to $t + 2/3$: local geometry update;
3. from $t + 2/3$ to $t + 1$: horizontal translation of the top profile.

All of these moves are geometrical, although they can be linked to physical aspects of the sliding process. The overlapping of the profiles corresponds to the contact between the two surfaces. The true contact area A is prescribed as a fraction a of the surfaces length L , and the profiles are displaced vertically such that the vertical projection of the overlapping portions amount to $A = aL$, where a can ideally take any value in the continuous interval $(0, 1)$. After this move, m overlapping portions (junctions) are formed, where locally is $h_t(i, t + 1/3) < h_b(i, t + 1/3) = h_b(i, t)$. The geometry of these junctions is updated following a deformation rule that is based on the AWM critical length scale, and that is detailed in the next subsection. Finally, the horizontal translation represents the sliding motion, and it amounts to the value d_{\max} , where d_{\max} is the largest junction formed upon contact. The rationale behind the choice of d_{\max} is that it is assumed that the top surface needs to slide such distance to deform the geometry of the largest contact junction. This last step is equivalent to displacing the top surface horizontally towards increasing values of i , such that $h_t(i + d_{\max}, t + 1) = h_t(i, t + 2/3)$. The algorithm then restarts from the first move: the amount of residual overlap after the last move of the previous step is neglected, and the overlapping is dictated again by the input contact area, which is kept constant. Periodic boundary conditions are applied at all stages of the algorithm.

A.2.1 Local geometry update

After the first move, the two profiles overlap over some regions, which represent the contact junctions. The profiles need then to be deformed locally at these contact junctions. The concept of AWM critical length scale [59] is applied to define the rule

Appendix A. A geometrical model as a tool for surface roughness evolution investigations

to deform the profiles. The AWM critical length scale d^* governs in fact the ductile-to-brittle transition in adhesive wear, and it depends on mechanical properties of the materials (namely the fracture energy, the shear modulus, and the junction shear strength, see Chapter 2). When two asperities come into contact forming a junction of size d , if $d < d^*$ they plastically deform, otherwise if $d \geq d^*$ they fracture and form a loose debris particle. In the geometrical model, d^* is provided as an input parameter (in terms of a fraction of L). Once the profiles are overlapped, the size d_j of each junction j (with $j = 1, \dots, m$) is measured and the two possible mechanisms described by d^* are applied:

- If $d_j < d^*$, the asperities plastify (Figures A.1 and A.2): this is achieved by locally pushing back both profiles to the average heights of the two profiles along the junction j . Assuming that the junction goes from the site k to the site $k + d_j$, then is

$$h_t(i, t + 2/3) = h_b(i, t + 2/3) = \frac{1}{2d_j} \left(\sum_{i=k}^{k+d_j} h_t(i, t + 1/3) + \sum_{i=k}^{k+d_j} h_b(i, t + 1/3) \right) \quad (\text{A.1})$$

for all $i = k, \dots, k + d_j$. To preserve the volume, pile-up is allowed, that is the height of the sites ahead of each junction is increased up to the opposing surface, for as many sites as it is necessary to recover the whole plastified volume (Figure A.2). If another junction is encountered before the whole volume can be compensated, the residual volume is compensated after the next asperity. The pile-up involves the sites $i > k + d_j$ for the bottom surface and $i < k$ for the top surface, consistently with a sliding motion of the top surface towards increasing values of i .

- If $d_j \geq d^*$, the asperities break (Figure A.3): material is removed from both profiles such that the removed volume V_r equals twice the overlapped volume V_o . Considering the bottom surface, it is

$$V_{r,b} = h_b(i, t + 1/3) - h_b(i, t + 2/3) = 2(h_t(i, t + 1/3) - h_b(i, t + 1/3)) = 2V_o. \quad (\text{A.2})$$

The first substep to achieve this is to identify the site r where $h_t(i, t + 1/3)$ is minimum (with $i = k, \dots, k + d_j$). The new height for the site $h_b(r, t + 2/3)$ is then determined such that $V_{r,b} = 2V_o$. This is done under the conditions that the heights of the first and last points of the asperity are not affected

($h_b(k, t + 1/3) = h_b(k, t + 2/3)$ and $h_b(k + d_j, t + 1/3) = h_b(k + d_j, t + 2/3)$) and that a linear interpolation of the heights is performed from $h_b(k, t + 2/3)$ to $h_b(r, t + 2/3)$ and from $h_b(r, t + 2/3)$ to $h_b(k + d_j, t + 2/3)$. The volume is clearly not conserved, and no debris particle is actually modelled.

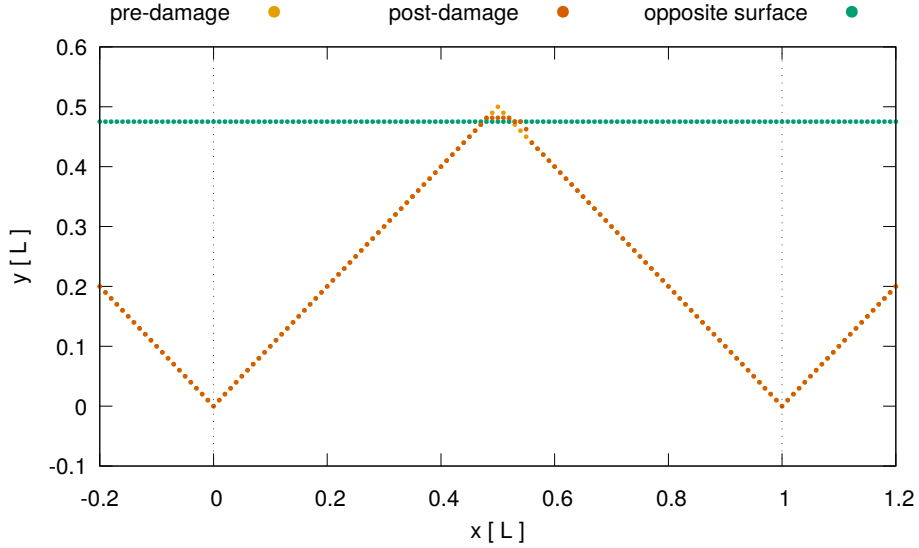


Figure A.1 – Local geometry update: ductile damage. The top profile (horizontal, green dots) overlaps the bottom one (orange dots: before damage at time $t + 1/3$, red dots: after damage at time $t + 2/3$) for 5% of the profile length. Outside the junction, the before and after damage geometries coincide. Both surfaces have length $L = 1$ and are discretized in 100 points, the true contact area is then 5 points. The critical size is $d^* = 6$ points. The top profile slides against the bottom one towards increasing values of x . Only the bottom surface is damaged in this example. Pile-up takes place ahead of the asperity to preserve the volume. Vertical dotted lines at $x = 0$ and $x = L$ represent system periodic boundaries. The horizontal and vertical axes are displayed with different scales.

The two mechanisms are in competition with one another: plastification smooths the surface, which is locally flattened, and fracture roughens it. The competition is present also in the random deposition model with surface relaxation: the particle deposition roughens the surface and the diffusion step smooths it. In that case, this leads to a well defined saturated roughness $\sigma_{\text{sat}}(L) \sim L^{1/2}$ for times t larger than the crossover time t_x . If only the roughening mechanism is present (simple random deposition, without diffusion) such equilibrium roughness is never reached, and σ continues growing with time as $\sigma(L, t) \sim t^{1/2}$.

Appendix A. A geometrical model as a tool for surface roughness evolution investigations

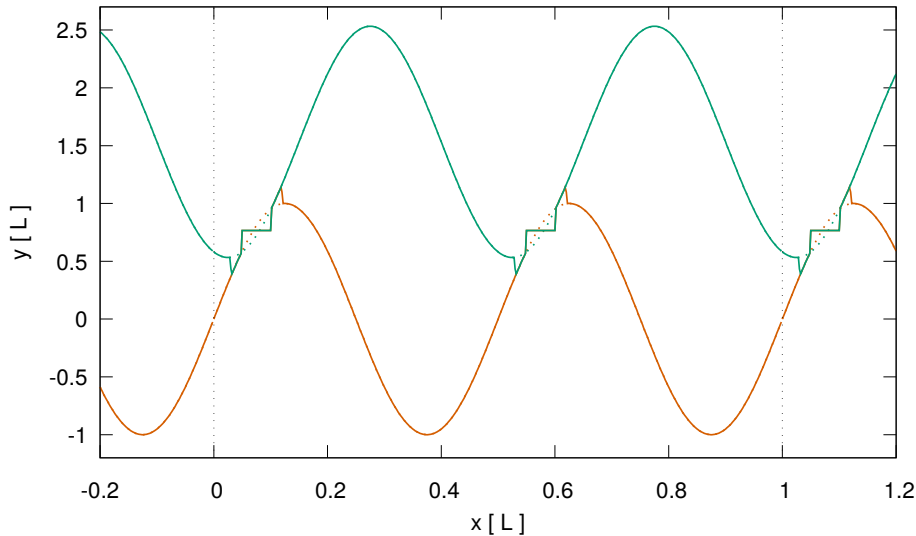


Figure A.2 – Local geometry update: ductile damage and pile-up. Two sinusoidal profiles are overlapped to generate a contact area of 5%. The overlapped profiles at time $t + 1/3$ are plotted with dotted lines (green for the top profile, red for the bottom). The deformed profiles at time $t + 2/3$ are plotted with continuous lines. Outside the junction, the before and after damage geometries coincide. The critical size is $d^* = 6$ points. The top profile slides against the bottom one towards increasing values of x . Pile up is consistent with the sliding direction, and it takes place towards increasing (decreasing) values of x for the bottom (top) profile. Note how the profiles are pushed against each other in the pile-up region to preserve volume. Vertical dotted lines at $x = 0$ and $x = L$ represent system periodic boundaries. The horizontal and vertical axes are displayed with different scales.

A.2.2 Asperity interaction

The geometry update described so far sees the asperities as independent, that is each junction j is plastified or fractured only based on its size d_j , and the proximity with other junctions is not taken into account. Yet, it is known that if two asperities are close to one another, they can create a unique loose debris particle instead of two separate ones [84]. This was found to be the case when the distance between the two asperities is equal to or smaller than the asperity size (assuming both asperities have the same size) [84]. Another step is then introduced in the model, where it is established if two (or more) asperities interact and undergo a unique brittle fracture event. The criterion is a chain rule, i.e. two consecutive junctions j and m undergo

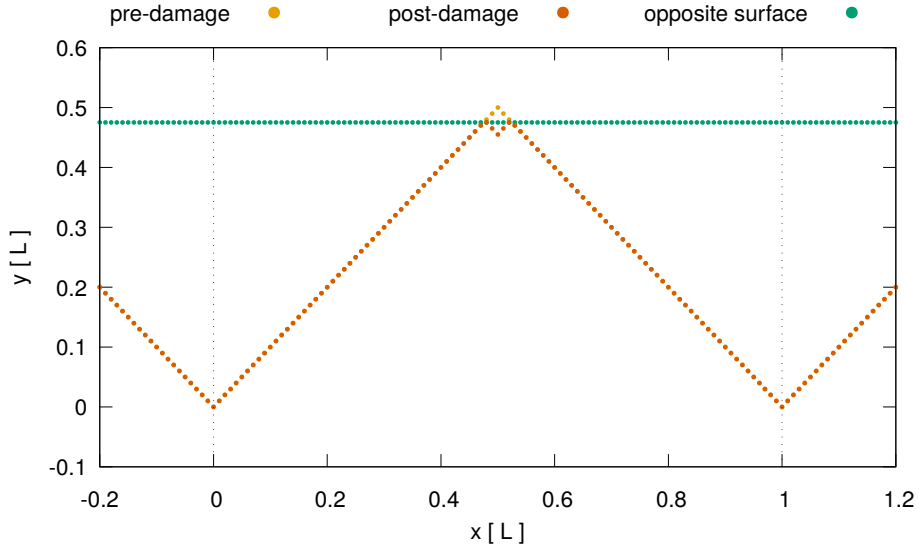


Figure A.3 – Local geometry update: brittle damage. The top profile (horizontal, green dots) overlaps the bottom one (orange dots: before damage at time $t + 1/3$, red dots: after damage at time $t + 2/3$) for 5% of the profile length. Outside the junction, the before and after damage geometries coincide. Both surfaces have length $L = 1$ and are discretized in 100 points, the true contact area is then 5 points. The critical size is $d^* = 5$ points. Only the bottom surface is damaged in this example. Vertical dotted lines at $x = 0$ and $x = L$ represent system periodic boundaries. The horizontal and vertical axes are displayed with different scales.

the same fracture event if

$$d_j > d^* \text{ and } d_m > d^* \text{ and } d_j + d_m > d_{jm} \tag{A.3}$$

where d_j and d_m are the asperity sizes and d_{jm} is the distance between the two asperities. If the asperities j and m satisfy the criterion, then the next two consecutive asperities m and p are checked. If also m and p satisfy it, then the three junctions j , m and p undergo the same brittle event. The chain stops whenever two consecutive asperities do not satisfy the criterion. An example of the application of such criterion is given in Figure A.4.

Appendix A. A geometrical model as a tool for surface roughness evolution investigations

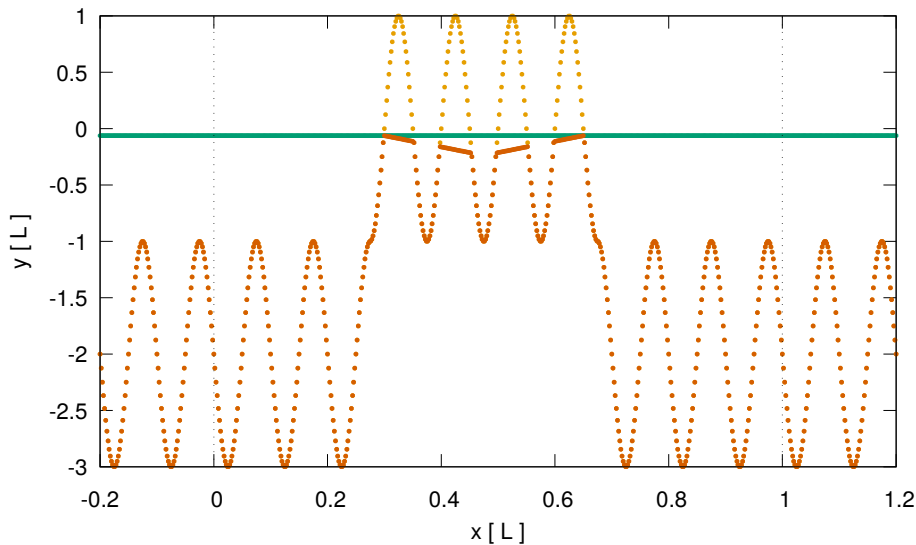


Figure A.4 – Local geometry update: brittle damage with asperity interaction. The top profile (horizontal, green dots) overlaps the bottom one (orange dots: before damage at time $t + 1/3$, red dots: after damage at time $t + 2/3$) for 20% of the profile length. Outside the junction, the before and after damage geometries coincide. Both surfaces have length $L = 1$ and are discretized in 500 points, the true contact area is then 100 points. The critical size is $d^* = 4$ points. Only the bottom surface is damaged in this example. Vertical dotted lines at $x = 0$ and $x = L$ represent system periodic boundaries. The horizontal and vertical axes are displayed with different scales.

A.3 Preliminary results

The scope of the model is to reproduce the evolution of frictional interfaces often observed in natural faults and other worn surfaces [27, 33, 145]. This consists of the initial running-in phase, followed by a steady state where the roughness in terms of deviation from the mid-plane stays constant and the surfaces are self-affine with a persistent Hurst exponent. Preliminary results indicate that the model captures the transition to a steady-state roughness, but that the morphology of the final surfaces is not self-affine. Here, I present the analyses of two different simulations and then discuss possible reasons why the final profiles are not fractal.

The two simulations considered here are GM1 and GM2 (where 'GM' stands for 'geometrical model'). In both simulations, the top and bottom profiles at $t = 0$

are synthetically generated to be self-affine, with a Hurst exponent $H = 0.9$, root mean square of heights $\sigma = 0.05 L$, critical length scale $d^* = 16/2048 L$ and they are discretized in 2048 points. For each simulation the contact area is set to $A = 0.05 L$ and $t = 10^6$ time steps were performed. The difference between GM1 and GM2 is the random seed used in the random phase filter algorithm [150] to generate the initial random profiles. The profiles at $t = 0$ are depicted in Figures A.5a and A.6a. Figures A.5b and A.6b show the deformed profiles at the end of each simulation.

To investigate the self-affinity of the final profiles, the height-height correlation function $\Delta h(\delta x)$ is estimated for the bottom profile at the end of each simulation, and it is reported in Figure A.7a. Reminding that for a self-affine profile is $\Delta h(\delta x) \sim \delta x^H$ (see Chapters 2 and 4 for more details), one can see that a clear and sustained scaling is not shown in any of the reported cases. The guidelines in Figure A.7a also show that the overall correlation of the heights changed during the simulation, as the original scaling ($H = 0.9$) is lost.

Several reasons can be hypothesized for these results. First, both the plastic and brittle damage mechanisms introduce straight segments along the profiles. In particular, the ductile mechanism flattens them, as it is shown by the presence of several horizontal segments in Figures A.5 and A.6. This also introduces a second issue. When several segments of the profile are horizontal and close to one another (in terms of height coordinate $h(i, t)$), it is not possible to enforce the prescribed contact area. This is due to sets of points at the same height. For simplicity, let us consider the case of a bottom profile where the points for $x < L/2$ are at height h_{b1} , and the other half ($x \geq L/2$) are at $h_{b2} \neq h_{b1}$. If the opposing profile is flat, i.e. $h_t(i, t) = h_{t0}$ for all i , then overlapping the two profiles can lead only to $A = 0.5 L$ or $A = 1.0 L$. No other values can be enforced in such case. In the implemented algorithm, a rule is set such that if the input A cannot be enforced, then the smallest possible value larger than the prescribed one is used. This leads nonetheless to large differences from the prescribed contact area (see Figure A.7). The height-height correlation function also seems to be affected by the value of d^* (Figure A.7a), which governs the transition between the two damage mechanisms. It is possible then that the different mechanisms affect differently the heights correlation. The flattening effect of the ductile damage also slows down the wear process. Large segments of the profiles are in fact not worn (see Figure A.5b) and the final profile is a mixture of the original one and worn parts. Nonetheless, this is an interesting feature, as polished surfaces can exhibit asymmetrical wear between the valleys and the peaks, the latter being smoother [145]. The trend in the evolution of the root mean square of heights σ

Appendix A. A geometrical model as a tool for surface roughness evolution investigations

(Figure A.8) also shows how changes in the profiles are large in the early stages of the simulation, and then is much harder to work the surface. This is consistent with the known trend of rubbed surfaces to reach a steady-state roughness.

A.4 Conclusions

Here, a simplified geometrical model for the roughness evolution of rubbed surfaces was introduced and tested. The main feature of the model is to deform the profiles with two different rules according to the size of the overlapping segments. Furthermore, the top profile artificially slides against the bottom one. While the model is purely geometrical, its evolution is based on physical observations of the wear process. The preliminary results show that the model captures the running-in phase and the transition to a steady-state roughness, yet the final profiles are not self-affine. This calls for a reflection on the fundamental ingredient of the model, i.e. the damaging mechanism. Similarly to the random deposition model with surface diffusion, the local evolution of the surface consists of two competing mechanisms – plastic damage smooths the surface, brittle damage roughens it. Still each mechanism is applied at different length scales, and they never coexist at the same scale. This is a possible reason for the lack of a consistent and continuous scaling of the heights correlation of the final profiles.

Furthermore, the model does not take into account the presence of any third body. Third bodies are always present between surfaces during frictional processes, and they affect the wear mechanisms at the interface. In particular, they keep the surfaces separate, reducing the amount of two-body contacts that lead to the ductile or brittle deformation mechanisms that are actually modelled here. Moreover, the third body exchange material with the two first bodies, leading to an erosion of the two mating profiles. A different approach to the geometrical modelling of surface roughness evolution might then be to model the exchange of material between the third body and the profiles. This could be done with a modified random deposition model, where the deposited particles are actually cluster of varying size (simulating the different amount of material that can be removed at the interface). Efforts towards the development of such approach are currently ongoing.

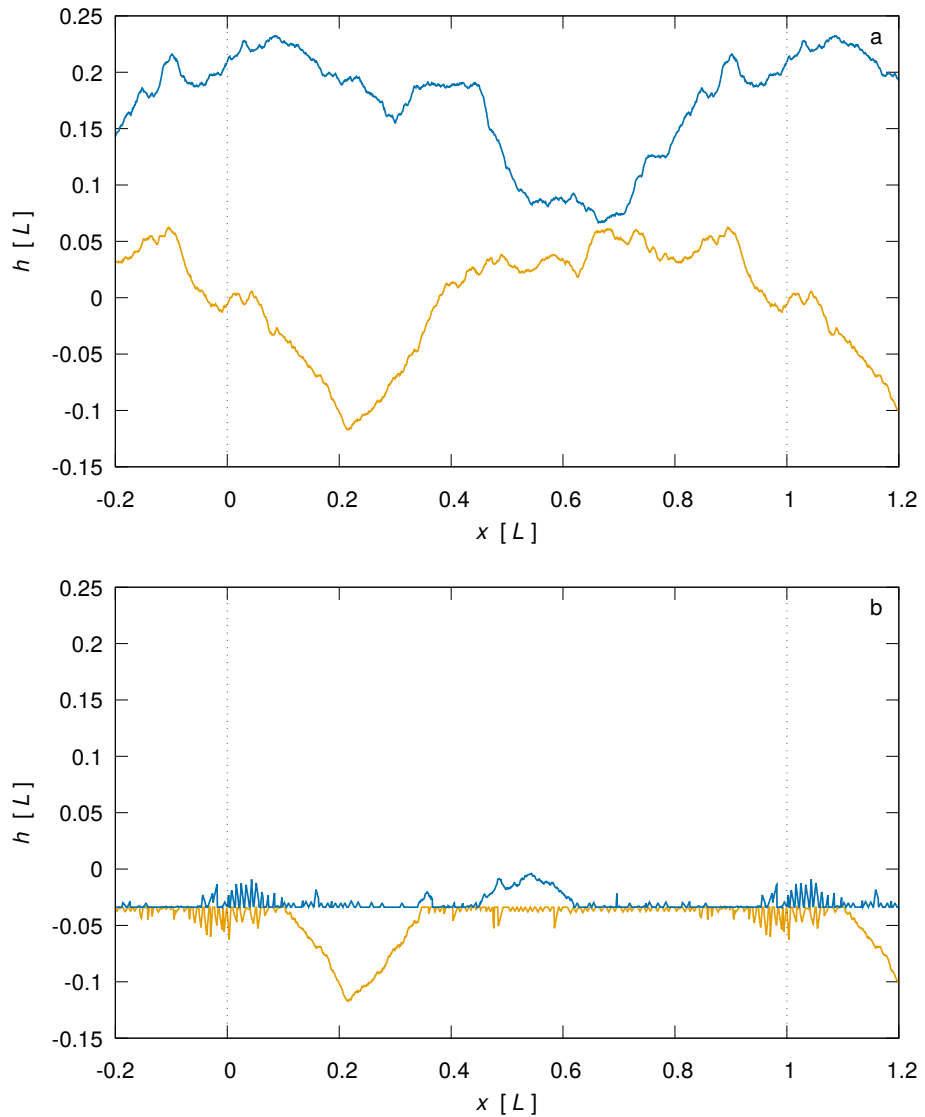


Figure A.5 – Profile evolution for the simulation GM1. a) Two self-affine profiles with $H = 0.9$ are generated at $t = 0$. Both profiles are characterized by $d^* = 16/2048 L$, $\sigma = 0.05 L$, and are discretized in 2048 points. b) The profiles at $t = 10^6$ iterations. Both profiles still show significant sections that did not undergo any damage. Vertical dotted lines at $x = 0$ and $x = L$ represent system periodic boundaries. The horizontal and vertical axes are displayed with different scales.

Appendix A. A geometrical model as a tool for surface roughness evolution investigations

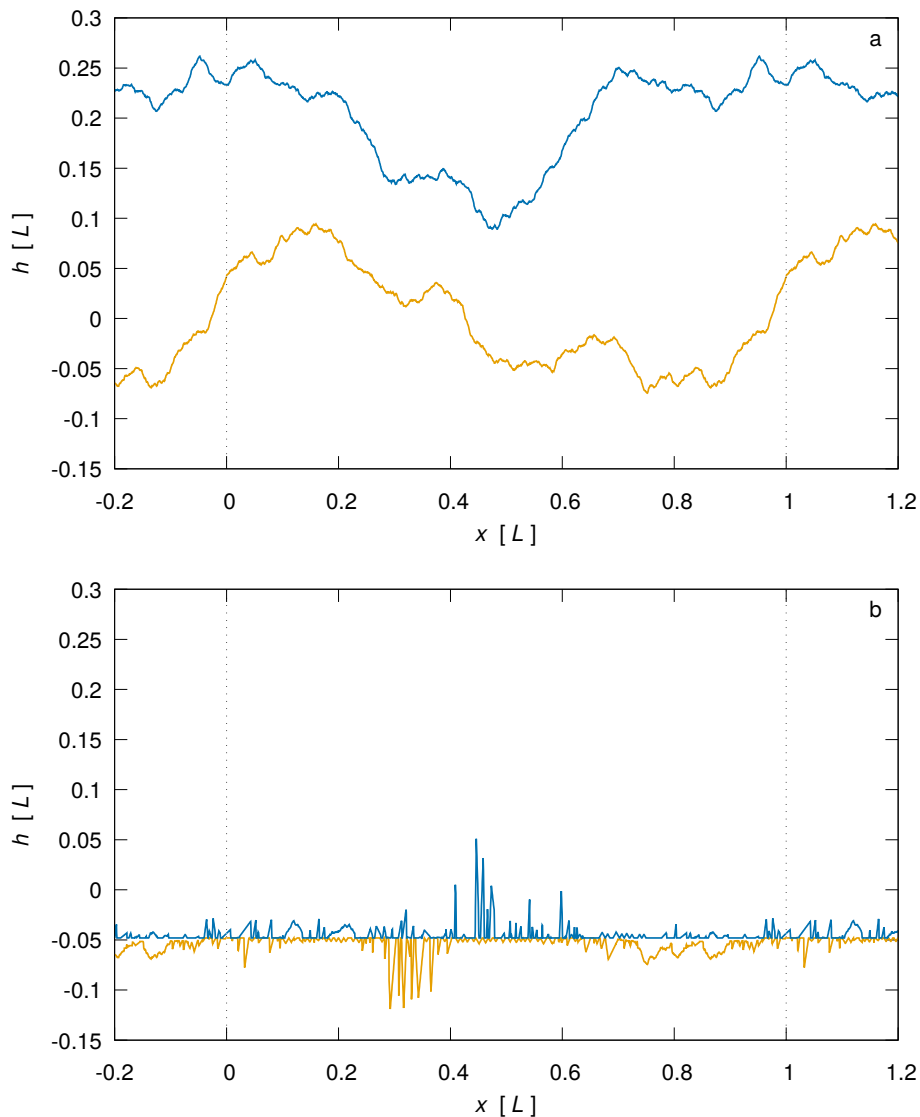


Figure A.6 – Profile evolution for the simulation GM2. a) Two self-affine profiles with Hurst exponent $H = 0.9$ are generated at $t = 0$, with a different random seed than the simulation GM1 (Figure A.5). Both profiles are characterized by $d^* = 16/2048 L$, $\sigma = 0.05 L$, and are discretized in 2048 points. b) The profiles at $t = 10^6$ iterations. Both profiles still show several sections that did not undergo any damage. Vertical dotted lines at $x = 0$ and $x = L$ represents system periodic boundaries. The horizontal and vertical axes are displayed with different scales.

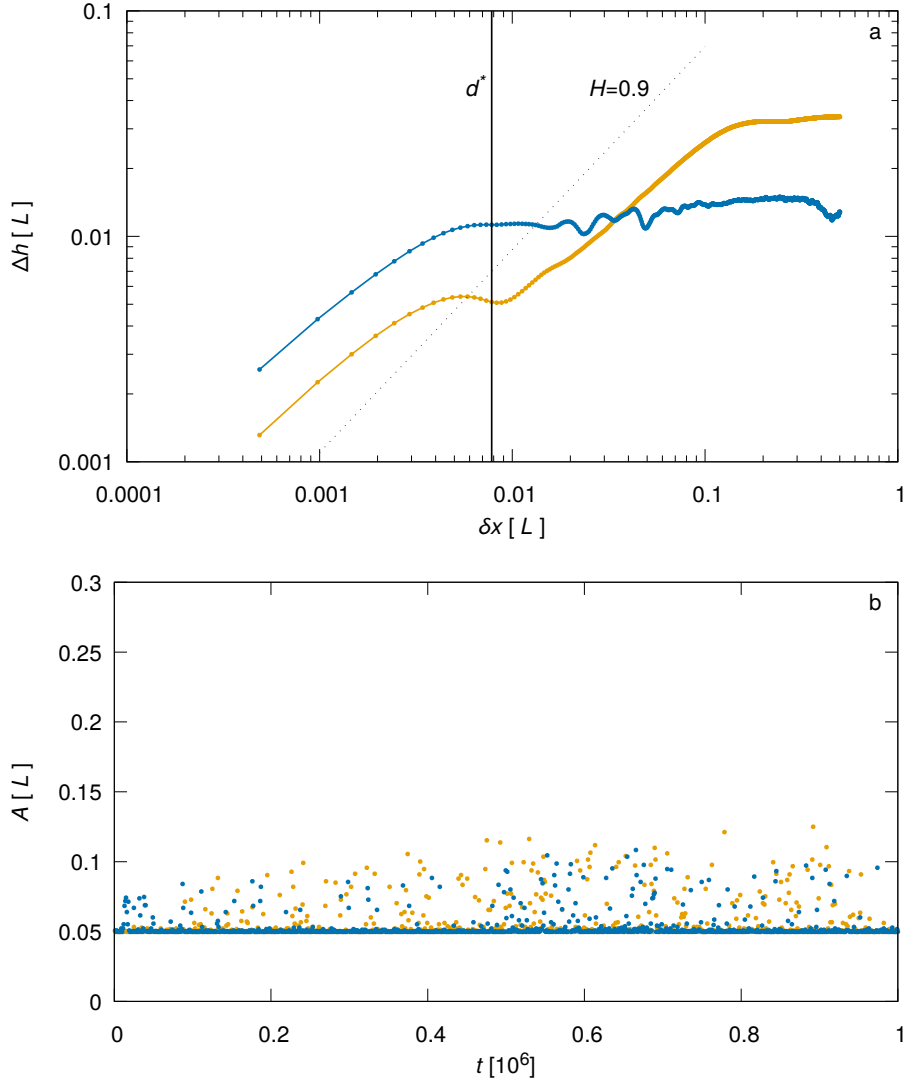


Figure A.7 – Height-height correlation (a) and contact area evolution (b) for the simulations of Figures A.5 and A.6. a) Height-height correlation $\Delta h(\delta x)$ of the bottom surface for the simulations GM1 (orange) and GM2 (blue). None of them shows a clear self-affine scaling over several orders of magnitude. The vertical black solid line indicates the value of d^* of the profiles. The black dotted line represents the scaling expected for $H = 0.9$. b) Evolution of the contact area A with t for the simulations GM1 (orange) and GM2 (blue). While for most timesteps the contact area is at the imposed value of $0.05 L$, in a significant amount of steps the value is markedly above. This artifact is due to the flattening of the heights during plastic deformation mechanisms. Data for A are stored every 1000 time steps.

Appendix A. A geometrical model as a tool for surface roughness evolution investigations

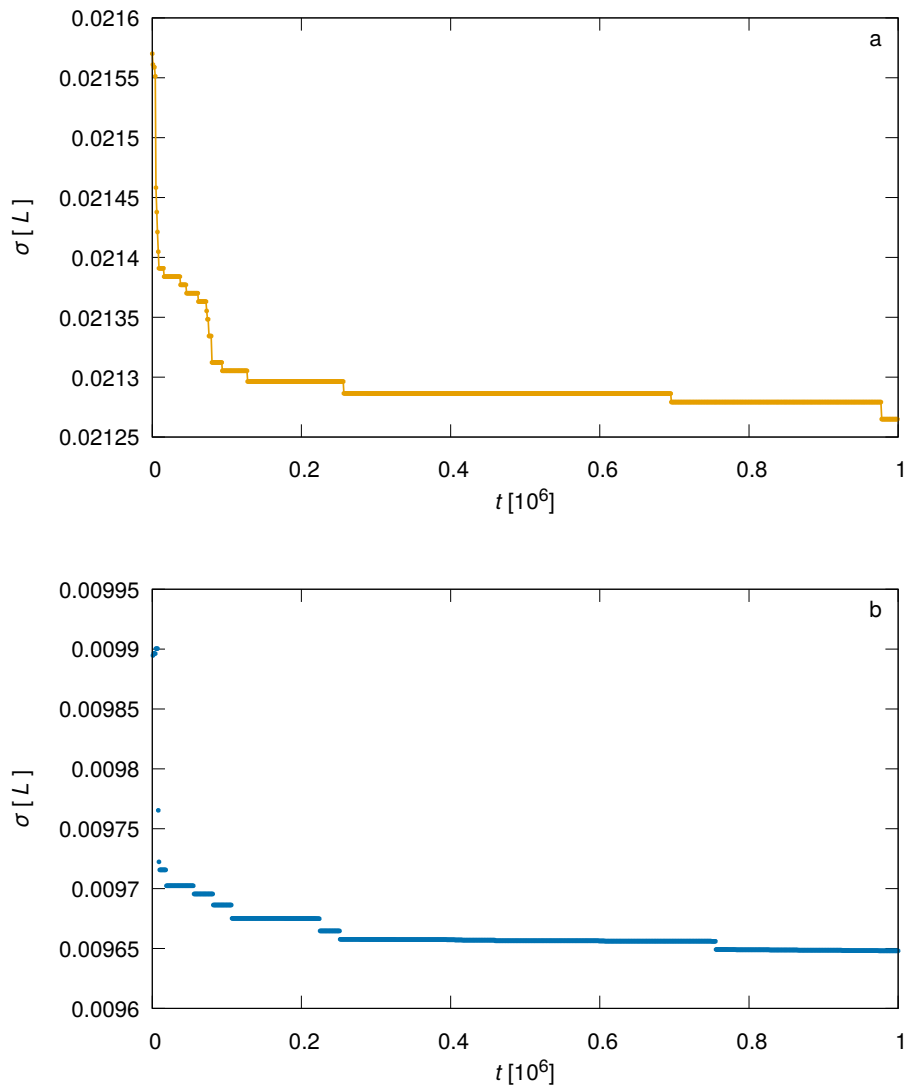


Figure A.8 – Evolution of root mean square of heights σ for simulations GM1 (a) and GM2 (b). In both simulations, σ decreases rapidly at the beginning of the simulation (at $t = 0$ is $\sigma = 0.05 L$, not shown in the plots), and then undergoes long periods where it is apparently constant. Repeated ductile damage between flat segments of the rubbed profiles lead in fact to small decreases in σ , until a large enough overlap takes place to lead to a brittle event. Data for σ are stored every 1 000 time steps.

Bibliography

- [1] Jost, H. P. Tribology — origin and future. *Wear* **136**, 1–17 (1990).
- [2] Jost, H. P. *Lubrication: Tribology; Education and Research; Report on the Present Position and Industry's Needs (submitted to the Department of Education and Science by the Lubrication Engineering and Research) Working Group* (Her Majesty's Stationery Office, London, 1966).
- [3] Carpick, R., Jackson, A., Lee, P., Argibay, N., Garcia, A. P., Sawyer, G. & Bennett, K. Tribology opportunities for enhancing America's energy efficiency: A report to the Advanced Research Projects Agency-Energy at the U.S. Department of Energy 1–116 (2017).
- [4] Holmberg, K. & Erdemir, A. Influence of tribology on global energy consumption, costs and emissions. *Friction* **5**, 263–284 (2017).
- [5] Carpick, R. W., Jackson, A., Sawyer, W. G., Argibay, N., Lee, P., Pachon, A. & Gresham, R. M. The tribology opportunities study: can tribology save a quad? *Tribology & Lubrication Technology* **72**, 44 (2016).
- [6] Holmberg, K., Andersson, P. & Erdemir, A. Global energy consumption due to friction in passenger cars. *Tribology International* **47**, 221–234 (2012).
- [7] Holmberg, K., Siilasto, R., Laitinen, T., Andersson, P. & Jäsberg, A. Global energy consumption due to friction in paper machines. *Tribology International* **62**, 58–77 (2013).
- [8] Holmberg, K., Andersson, P., Nylund, N.-O., Mäkelä, K. & Erdemir, A. Global energy consumption due to friction in trucks and buses. *Tribology International* **78**, 94–114 (2014).

Bibliography

- [9] Holmberg, K., Kivikytö-Reponen, P., Härkisaari, P., Valtonen, K. & Erdemir, A. Global energy consumption due to friction and wear in the mining industry. *Tribology International* **115**, 116–139 (2017).
- [10] European Commission. *In-depth analysis in support of the commission communication COM(2018) 773* (European Commission, Bruxelles, 2018).
- [11] Samet, J. M., Dominici, F., Curriero, F. C., Coursac, I. & Zeger, S. L. Fine particulate air pollution and mortality in 20 US cities, 1987–1994. *New England Journal of Medicine* **343**, 1742–1749 (2000).
- [12] Pope III, C. A., Burnett, R. T., Thun, M. J., Calle, E. E., Krewski, D., Ito, K. & Thurston, G. D. Lung cancer, cardiopulmonary mortality, and long-term exposure to fine particulate air pollution. *JAMA* **287**, 1132–1141 (2002).
- [13] Olofsson, U. A study of airborne wear particles generated from the train traffic—block braking simulation in a pin-on-disc machine. *Wear* **271**, 86–91 (2011).
- [14] Boneh, Y. & Reches, Z. Geotribology — friction, wear, and lubrication of faults. *Tectonophysics* **733**, 171–181 (2018).
- [15] Blok, H. The flash temperature concept. *Wear* **6**, 483–494 (1963).
- [16] Di Toro, G., Han, R., Hirose, T., De Paola, N., Nielsen, S., Mizoguchi, K., Ferri, F., Cocco, M. & Shimamoto, T. Fault lubrication during earthquakes. *Nature* **471**, 494 (2011).
- [17] Acosta, M., Passelègue, F., Schubnel, A. & Violay, M. Dynamic weakening during earthquakes controlled by fluid thermodynamics. *Nature Communications* **9**, 1–9 (2018).
- [18] Cornelio, C., Spagnuolo, E., Di Toro, G., Nielsen, S. & Violay, M. Mechanical behaviour of fluid-lubricated faults. *Nature Communications* **10**, 1–7 (2019).
- [19] Ciardo, F. & Lecampion, B. Effect of dilatancy on the transition from aseismic to seismic slip due to fluid injection in a fault. *Journal of Geophysical Research: Solid Earth* **124**, 3724–3743 (2019).
- [20] Dieterich, J. H. Time-dependent friction in rocks. *Journal of Geophysical Research* **77**, 3690–3697 (1972).

- [21] Spagnuolo, E., Nielsen, S., Violay, M. & Di Toro, G. An empirically based steady state friction law and implications for fault stability. *Geophysical Research Letters* **43**, 3263–3271 (2016).
- [22] Reches, Z. & Lockner, D. A. Fault weakening and earthquake instability by powder lubrication. *Nature* **467**, 452 (2010).
- [23] Chen, X., Madden, A. S. E. & Reches, Z. Friction evolution of granitic faults: Heating controlled transition from powder lubrication to frictional melt. *Journal of Geophysical Research: Solid Earth* **122**, 9275–9289 (2017).
- [24] Renard, F., Voisin, C., Marsan, D. & Schmittbuhl, J. High resolution 3D laser scanner measurements of a strike-slip fault quantify its morphological anisotropy at all scales. *Geophysical Research Letters* **33** (2006).
- [25] Sagy, A., Brodsky, E. E. & Axen, G. J. Evolution of fault-surface roughness with slip. *Geology* **35**, 283–286 (2007).
- [26] Brodsky, E. E., Gilchrist, J. J., Sagy, A. & Collettini, C. Faults smooth gradually as a function of slip. *Earth and Planetary Science Letters* **302**, 185–193 (2011).
- [27] Renard, F., Candela, T. & Bouchaud, E. Constant dimensionality of fault roughness from the scale of micro-fractures to the scale of continents. *Geophysical Research Letters* **40**, 83–87 (2013).
- [28] Davidesko, G., Sagy, A. & Hatzor, Y. H. Evolution of slip surface roughness through shear. *Geophysical Research Letters* **41**, 1492–1498 (2014).
- [29] Candela, T. & Brodsky, E. E. The minimum scale of grooving on faults. *Geology* **44**, 603–606 (2016).
- [30] Marone, C. & Richardson, E. Research focus: Connections between fault roughness, dynamic weakening, and fault zone structure. *Geology* **44**, 79 (2016).
- [31] Brodsky, E. E., Kirkpatrick, J. D. & Candela, T. Constraints from fault roughness on the scale-dependent strength of rocks. *Geology* **44**, 19–22 (2016).
- [32] Shervais, K. A. & Kirkpatrick, J. D. Smoothing and re-roughening processes: the geometric evolution of a single fault zone. *Journal of Structural Geology* **91**, 130–143 (2016).

Bibliography

- [33] Sagy, A., Tesei, T. & Collettini, C. Fault-surface geometry controlled by faulting mechanisms: experimental observations in limestone faults. *Geology* **45**, 851–854 (2017).
- [34] Thom, C., Brodsky, E., Carpick, R., Pharr, G., Oliver, W. & Goldsby, D. Nanoscale roughness of natural fault surfaces controlled by scale-dependent yield strength. *Geophysical Research Letters* **44**, 9299–9307 (2017).
- [35] Orellana, L. F., Scuderi, M. M., Collettini, C. & Violay, M. Do scaly clays control seismicity on faulted shale rocks? *Earth and Planetary Science Letters* **488**, 59–67 (2018).
- [36] Rabinowicz, E. *Friction and wear of materials* (Wiley, New York, 1995).
- [37] Kragelsky, I. V., Dobychin, M. N. & Kambalov, V. S. *Friction and wear: calculation methods* (Pergamon Press, 1981).
- [38] Sayles, R. S. & Thomas, T. R. Surface topography as a nonstationary random process. *Nature* **271**, 431–434 (1978).
- [39] Majumdar, A. & Tien, C. Fractal characterization and simulation of rough surfaces. *Wear* **136**, 313–327 (1990).
- [40] Persson, B., Albohr, O., Tartaglino, U., Volokitin, A. & Tosatti, E. On the nature of surface roughness with application to contact mechanics, sealing, rubber friction and adhesion. *Journal of Physics: Condensed Matter* **17**, R1 (2004).
- [41] Mandelbrot, B. B., Passoja, D. E. & Paullay, A. J. Fractal character of fracture surfaces of metals. *Nature* **308**, 721 (1984).
- [42] Ponson, L., Bonamy, D. & Bouchaud, E. Two-dimensional scaling properties of experimental fracture surfaces. *Physical Review Letters* **96**, 035506 (2006).
- [43] Bonamy, D., Ponson, L., Prades, S., Bouchaud, E. & Guillot, C. Scaling exponents for fracture surfaces in homogeneous glass and glassy ceramics. *Physical Review Letters* **97**, 135504 (2006).
- [44] Bonamy, D. & Bouchaud, E. Failure of heterogeneous materials: a dynamic phase transition? *Physics Reports* **498**, 1–44 (2011).
- [45] Vernède, S., Ponson, L. & Bouchaud, J.-P. Turbulent fracture surfaces: A footprint of damage percolation? *Physical Review Letters* **114**, 215501 (2015).

-
- [46] Da Vinci, L. *Codex Madrid I* (1490-1499). URL <https://www.leonardodigitale.com/en/>. Last visited on 24/02/2020.
- [47] Hutchings, I. M. Leonardo da Vinci's studies of friction. *Wear* **360**, 51–66 (2016).
- [48] Popova, E. & Popov, V. L. The research works of Coulomb and Amontons and generalized laws of friction. *Friction* **3**, 183–190 (2015).
- [49] Bowden, F. P. & Tabor, D. *The friction and lubrication of solids* (Oxford University Press, 2001).
- [50] Archard, J. Contact and rubbing of flat surfaces. *Journal of Applied Physics* **24**, 981–988 (1953).
- [51] Holm, R. *Electric contacts: theory and application* (Springer Science & Business Media, 2013).
- [52] Godet, M. The third-body approach: a mechanical view of wear. *Wear* **100**, 437–452 (1984).
- [53] Hertz, H. Über die Berührung fester elastischer Körper. *Journal für die reine und angewandte Mathematik* **92**, 156–171 (1882).
- [54] Greenwood, J. A. & Williamson, J. P. Contact of nominally flat surfaces. *Proceedings of the Royal Society of London A: Mathematical, Physical and Engineering Sciences* **295**, 300–319 (1966).
- [55] Johnson, K., Kendall, K. & Roberts, A. Surface energy and the contact of elastic solids. *Proceedings of the Royal Society of London A: Mathematical, Physical and Engineering Sciences* **324**, 301–313 (1971).
- [56] Derjaguin, B. V., Muller, V. M. & Toporov, Y. P. Effect of contact deformations on the adhesion of particles. *Journal of Colloid and Interface Science* **53**, 314–326 (1975).
- [57] Sorensen, M., Jacobsen, K. W. & Stoltze, P. Simulations of atomic-scale sliding friction. *Physical Review B* **53**, 2101–2113 (1996).
- [58] Mo, Y., Turner, K. T. & Szlufarska, I. Friction laws at the nanoscale. *Nature* **457**, 1116 (2009).
- [59] Aghababaei, R., Warner, D. H. & Molinari, J.-F. Critical length scale controls adhesive wear mechanisms. *Nature Communications* **7** (2016).

Bibliography

- [60] Germann, T. C. & Kadau, K. Trillion-atom molecular dynamics becomes a reality. *International Journal of Modern Physics C* **19**, 1315–1319 (2008).
- [61] Maugis, D. Adhesion of spheres: the JKR-DMT transition using a Dugdale model. *Journal of Colloid and Interface Science* **150**, 243–269 (1992).
- [62] Johnson, K. L. *Contact mechanics* (Cambridge university press, 1987).
- [63] Liefferink, R., Weber, B. & Bonn, D. Ploughing friction on wet and dry sand. *Physical Review E* **98**, 052903 (2018).
- [64] Da Vinci, L. *Codex Atlanticus* (1478-1519). URL <https://www.leonardodigitale.com/en/>. Last visited on 24/02/2020.
- [65] Hatchett, C. IV. Experiments and observations on the various alloys, on the specific gravity, and on the comparative wear of gold. Being the substance of a report made to the Right Honourable the Lords of the Committee of Privy Council, appointed to take into consideration the state of the coins of this Kingdom, and the present establishment and constitution of his Majesty's Mint. *Philosophical Transactions of the Royal Society of London* **93**, 43–194 (1803).
- [66] Reye, T. Zur Theorie der Zapfenreibung. *Der Civilingenieur* **4**, 235–255 (1860).
- [67] Mischler, S. Triboelectrochemical techniques and interpretation methods in tribocorrosion: a comparative evaluation. *Tribology International* **41**, 573–583 (2008).
- [68] Cao, S. & Mischler, S. Modeling tribocorrosion of passive metals—a review. *Current Opinion in Solid State and Materials Science* **22**, 127–141 (2018).
- [69] Burwell, J. & Strang, C. On the empirical law of adhesive wear. *Journal of Applied Physics* **23**, 18–28 (1952).
- [70] Archard, J. & Hirst, W. The wear of metals under unlubricated conditions. *Proceedings of the Royal Society of London A: Mathematical, Physical and Engineering Sciences* **236**, 397–410 (1956).
- [71] Sha, Z.-D., Sorkin, V., Branicio, P. S., Pei, Q.-X., Zhang, Y.-W. & Srolovitz, D. J. Large-scale molecular dynamics simulations of wear in diamond-like carbon at the nanoscale. *Applied Physics Letters* **103**, 073118 (2013).

- [72] Frérot, L., Aghababaei, R. & Molinari, J.-F. A mechanistic understanding of the wear coefficient: from single to multiple asperities contact. *Journal of the Mechanics and Physics of Solids* **114**, 172–184 (2018).
- [73] Aghababaei, R., Warner, D. H. & Molinari, J.-F. On the debris-level origins of adhesive wear. *Proceedings of the National Academy of Sciences* **114**, 7935–7940 (2017).
- [74] Barwell, F. Wear of metals. *Wear* **1**, 317–332 (1958).
- [75] Queener, C., Smith, T. & Mitchell, W. Transient wear of machine parts. *Wear* **8**, 391–400 (1965).
- [76] Eder, S., Feldbauer, G., Bianchi, D., Cihak-Bayr, U., Betz, G. & Vernes, A. Applicability of macroscopic wear and friction laws on the atomic length scale. *Physical Review Letters* **115**, 025502 (2015).
- [77] Park, N.-S., Kim, M.-W., Langford, S. & Dickinson, J. Atomic layer wear of single-crystal calcite in aqueous solution using scanning force microscopy. *Journal of Applied Physics* **80**, 2680–2686 (1996).
- [78] Sheehan, P. The wear kinetics of nacl under dry nitrogen and at low humidities. *Chemical Physics Letters* **410**, 151–155 (2005).
- [79] Gotsmann, B. & Lantz, M. A. Atomistic wear in a single asperity sliding contact. *Physical Review Letters* **101**, 125501 (2008).
- [80] Bhaskaran, H., Gotsmann, B., Sebastian, A., Drechsler, U., Lantz, M. A., Despont, M., Jaroenapibal, P., Carpick, R. W., Chen, Y. & Sridharan, K. Ultralow nanoscale wear through atom-by-atom attrition in silicon-containing diamond-like carbon. *Nature Nanotechnology* **5**, 181 (2010).
- [81] Jacobs, T. D. & Carpick, R. W. Nanoscale wear as a stress-assisted chemical reaction. *Nature Nanotechnology* **8**, 108 (2013).
- [82] Mate, C. M. & Carpick, R. W. *Tribology on the Small Scale: A Modern Textbook on Friction, Lubrication, and Wear* (Oxford University Press, USA, 2019).
- [83] Rabinowicz, E. Practical uses of the surface energy criterion. *Wear* **7**, 9–22 (1964).
- [84] Aghababaei, R., Brink, T. & Molinari, J.-F. Asperity-level origins of transition from mild to severe wear. *Physical Review Letters* **120**, 186105 (2018).

Bibliography

- [85] Brink, T. & Molinari, J.-F. Adhesive wear mechanisms in the presence of weak interfaces: Insights from an amorphous model system. *Physical Review Materials* **3**, 053604 (2019).
- [86] Deng, F., Tsekenis, G. & Rubinstein, S. M. Simple law for third-body friction. *Physical Review Letters* **122**, 135503 (2019).
- [87] Hsia, F.-C., Elam, F. M., Bonn, D., Weber, B. & Franklin, S. E. Wear particle dynamics drive the difference between repeated and non-repeated reciprocated sliding. *Tribology International* **142**, 105983 (2020).
- [88] Fillot, N., Iordanoff, I. & Berthier, Y. Simulation of wear through mass balance in a dry contact. *Journal of Tribology* **127**, 230–237 (2005).
- [89] Fillot, N., Iordanoff, I. & Berthier, Y. Wear modeling and the third body concept. *Wear* **262**, 949–957 (2007).
- [90] Hintikka, J., Lehtovaara, A. & Mäntylä, A. Third particle ejection effects on wear with quenched and tempered steel fretting contact. *Tribology Transactions* **60**, 70–78 (2017).
- [91] Harris, K. L., Curry, J. E., Pitenis, A. A., Rowe, K. G., Sidebottom, M. A., Sawyer, W. G. & Krick, B. A. Wear debris mobility, aligned surface roughness, and the low wear behavior of filled polytetrafluoroethylene. *Tribology Letters* **60**, 2 (2015).
- [92] Boneh, Y., Sagy, A. & Reches, Z. Frictional strength and wear-rate of carbonate faults during high-velocity, steady-state sliding. *Earth and Planetary Science Letters* **381**, 127–137 (2013).
- [93] Hu, X. & Martini, A. Atomistic simulation of the effect of roughness on nanoscale wear. *Computational Materials Science* **102**, 208–212 (2015).
- [94] Barabási, A.-L. & Stanley, H. E. *Fractal concepts in surface growth* (Cambridge university press, 1995).
- [95] Mandelbrot, B. How long is the coast of Britain? Statistical self-similarity and fractional dimension. *Science* **156**, 636–638 (1967).
- [96] Meakin, P. *Fractals, scaling and growth far from equilibrium*, vol. 5 (Cambridge University Press, 1998).

- [97] Mandelbrot, B. B. Self-affine fractals and fractal dimension. *Physica Scripta* **32**, 257 (1985).
- [98] Berry, M. & Lewis, Z. On the Weierstrass-Mandelbrot fractal function. *Proceedings of the Royal Society of London A: Mathematical, Physical and Engineering Sciences* **370**, 459–484 (1980).
- [99] Bhushan, B. Surface roughness analysis and measurement techniques. In Bhushan, B. (ed.) *Modern tribology handbook, two volume set*, chap. 4, 49–120 (CRC press, 2000).
- [100] Family, F. Scaling of rough surfaces: effects of surface diffusion. *Journal of Physics A: Mathematical and General* **19**, L441 (1986).
- [101] Schargott, M. & Popov, V. Diffusion as a model of formation and development of surface topography. *Tribology International* **39**, 431–436 (2006).
- [102] Bathe, K.-J. *Finite element procedures* (Prentice-Hall, Upper Saddle River, New Jersey, 1996).
- [103] Zienkiewicz, O. C., Taylor, R. L., Nithiarasu, P. & Zhu, J. *The finite element method*, vol. 3 (McGraw-Hill, London, 1977).
- [104] Bonnet, M. *Boundary integral equation methods for solids and fluids* (John Wiley, New York, 1995).
- [105] Frenkel, D. & Smit, B. *Understanding molecular simulation: from algorithms to applications*, vol. 1 (Elsevier, 2001).
- [106] Cundall, P. A. & Strack, O. D. A discrete numerical model for granular assemblies. *Geotechnique* **29**, 47–65 (1979).
- [107] Vakis, A. I., Yastrebov, V. A., Scheibert, J., Nicola, L., Dini, D., Minfray, C., Almqvist, A., Paggi, M., Lee, S., Limbert, G., Molinari, J.-F., Anciaux, G., Aghababaei, R., Echeverri Restrepo, S., Papangelo, A., Cammarata, A., Nicolini, P., Putignano, C., Carbone, G., Stupkiewicz, S., Lengiewicz, J., Costagliola, G., Bosia, F., Guarino, R., Pugno, N. M., Müser, M. H. & Ciavarella, M. Modeling and simulation in tribology across scales: an overview. *Tribology International* **125**, 169–199 (2018).
- [108] Müser, M. H., Dapp, W. B., Bugnicourt, R., Sainsot, P., Lesaffre, N., Lubrecht, T. A., Persson, B. N., Harris, K., Bennett, A., Schulze, K., Rohde, S., Ifju, P., Sawyer, W. G., Angelini, T., Esfahani, H. A., Kadkhodaei, M., Akbarzadeh, S.,

Bibliography

- Wu, J.-J., Vorlaufer, G., Vernes, A., Solhjoo, S., Vakis, A. I., Jackson, R. L., Xu, Y., Streater, J., Rostami, A., Dini, D., Medina, S., Carbone, G., Bottiglione, F., Afferrante, L., Monti, J., Pastewka, L., Robbins, M. O. & Greenwood, J. A. Meeting the contact-mechanics challenge. *Tribology Letters* **65**, 118 (2017).
- [109] Carpick, R. W. The contact sport of rough surfaces. *Science* **359**, 38–38 (2018).
- [110] Frérot, L., Bonnet, M., Molinari, J.-F. & Anciaux, G. A Fourier-accelerated volume integral method for elastoplastic contact. *Computer Methods in Applied Mechanics and Engineering* **351**, 951–976 (2019).
- [111] Yang, Y., Huang, L. & Shi, Y. Adhesion suppresses atomic wear in single-asperity sliding. *Wear* **352**, 31–41 (2016).
- [112] Hu, X., Altoe, M. V. P. & Martini, A. Amorphization-assisted nanoscale wear during the running-in process. *Wear* **370**, 46–50 (2017).
- [113] Chongyi, C., Chengguo, W. & Ying, J. Study on numerical method to predict wheel/rail profile evolution due to wear. *Wear* **269**, 167–173 (2010).
- [114] Mattei, L. & Di Puccio, F. Influence of the wear partition factor on wear evolution modelling of sliding surfaces. *International Journal of Mechanical Sciences* **99**, 72–88 (2015).
- [115] Curreli, C., Di Puccio, F. & Mattei, L. Application of the finite element submodeling technique in a single point contact and wear problem. *International Journal for Numerical Methods in Engineering* **116**, 708–722 (2018).
- [116] Pearce, T. & Sherratt, N. Prediction of wheel profile wear. *Wear* **144**, 343–351 (1991).
- [117] Rovira, A., Roda, A., Marshall, M., Brunskill, H. & Lewis, R. Experimental and numerical modelling of wheel–rail contact and wear. *Wear* **271**, 911–924 (2011).
- [118] Carollo, V., Paggi, M. & Reinoso, J. The steady-state Archard adhesive wear problem revisited based on the phase field approach to fracture. *International Journal of Fracture* **215**, 39–48 (2019).
- [119] Allen, M. P. & Tildesley, D. J. *Computer simulation of liquids* (Oxford University Press, New York, 1991).

- [120] Landman, U., Luedtke, W. & Ringer, E. M. Atomistic mechanisms of adhesive contact formation and interfacial processes. *Wear* **153**, 3–30 (1992).
- [121] Luding, S. Introduction to discrete element methods: basic of contact force models and how to perform the micro-macro transition to continuum theory. *European Journal of Environmental and Civil Engineering* **12**, 785–826 (2008).
- [122] Huang, H., Lecampion, B. & Detournay, E. Discrete element modeling of tool-rock interaction I: rock cutting. *International Journal for Numerical and Analytical Methods in Geomechanics* **37**, 1913–1929 (2013).
- [123] Ceriotti, M. EPFL MSE-639, Lecture notes: Statistical methods in atomistic computer simulations (2018). URL: https://www.epfl.ch/labs/cosmo/wp-content/uploads/2018/11/sampling_atomistic_simulations-lecture_notes.pdf. Last visited on 19/02/2020.
- [124] Metropolis, N., Rosenbluth, A. W., Rosenbluth, M. N., Teller, A. H. & Teller, E. Equation of state calculations by fast computing machines. *The Journal of Chemical Physics* **21**, 1087–1092 (1953).
- [125] Plimpton, S. Fast parallel algorithms for short-range molecular dynamics. *Journal of Computational Physics* **117**, 1–19 (1995).
- [126] Jones, J. E. On the determination of molecular fields.—II. From the equation of state of a gas. *Proceedings of the Royal Society of London A: Mathematical, Physical and Engineering Sciences* **106**, 463–477 (1924).
- [127] Morse, P. M. Diatomic molecules according to the wave mechanics. II. Vibrational levels. *Physical Review* **34**, 57 (1929).
- [128] Dong, Y., Li, Q. & Martini, A. Molecular dynamics simulation of atomic friction: a review and guide. *Journal of Vacuum Science & Technology A: Vacuum, Surfaces, and Films* **31**, 030801 (2013).
- [129] Luan, B. & Robbins, M. O. The breakdown of continuum models for mechanical contacts. *Nature* **435**, 929–932 (2005).
- [130] Zhang, Y., Mollon, G. & Descartes, S. Significance of third body rheology in friction at a dry sliding interface observed by a multibody meshfree model: Influence of cohesion between particles. *Tribology International* **145**, 106188 (2020).

Bibliography

- [131] Milanese, E., Brink, T., Aghababaei, R. & Molinari, J.-F. Emergence of self-affine surfaces during adhesive wear. *Nature Communications* **10**, 1116 (2019).
- [132] Gjerden, K. S., Stormo, A. & Hansen, A. Universality classes in constrained crack growth. *Physical Review Letters* **111**, 135502 (2013).
- [133] Zepeda-Ruiz, L. A., Stukowski, A., Ooppelstrup, T. & Bulatov, V. V. Probing the limits of metal plasticity with molecular dynamics simulations. *Nature* **550**, 492 (2017).
- [134] Merkle, A. P. & Marks, L. D. Liquid-like tribology of gold studied by in situ tem. *Wear* **265**, 1864–1869 (2008).
- [135] Liu, J., Notbohm, J. K., Carpick, R. W. & Turner, K. T. Method for characterizing nanoscale wear of atomic force microscope tips. *ACS Nano* **4**, 3763–3772 (2010).
- [136] Liu, J., Grierson, D. S., Moldovan, N., Notbohm, J., Li, S., Jaroenapibal, P., O'Connor, S. D., Sumant, A. V., Neelakantan, N., Carlisle, J. A., Turner, K. T. & Carpick, R. W. Preventing nanoscale wear of atomic force microscopy tips through the use of monolithic ultrananocrystalline diamond probes. *Small* **6**, 1140–1149 (2010).
- [137] Cai, J., Lu, C., Yap, P. & Wang, Y. How to affect stacking fault energy and structure by atom relaxation. *Applied Physics Letters* **81**, 3543–3545 (2002).
- [138] Van Swygenhoven, H., Derlet, P. & Frøseth, A. Stacking fault energies and slip in nanocrystalline metals. *Nature Materials* **3**, 399 (2004).
- [139] Stoyanov, P., Romero, P. A., Merz, R., Kopnarski, M., Stricker, M., Stemmer, P., Dienwiebel, M. & Moseler, M. Nanoscale sliding friction phenomena at the interface of diamond-like carbon and tungsten. *Acta Materialia* **67**, 395–408 (2014).
- [140] Pastewka, L., Moser, S., Gumbsch, P. & Moseler, M. Anisotropic mechanical amorphization drives wear in diamond. *Nature Materials* **10**, 34–38 (2011).
- [141] Bouchet, M. D. B., Matta, C., Vacher, B., Le-Mogne, T., Martin, J., von Lautz, J., Ma, T., Pastewka, L., Otschik, J., Gumbsch, P. & Moseler, M. Energy filtering transmission electron microscopy and atomistic simulations of tribo-induced hybridization change of nanocrystalline diamond coating. *Carbon* **87**, 317–329 (2015).

- [142] Zhong, J., Shakiba, R. & Adams, J. B. Molecular dynamics simulation of severe adhesive wear on a rough aluminum substrate. *Journal of Physics D: Applied Physics* **46**, 055307 (2013).
- [143] Spijker, P., Anciaux, G. & Molinari, J.-F. Dry sliding contact between rough surfaces at the atomistic scale. *Tribology Letters* **44**, 279 (2011).
- [144] Ganti, S. & Bhushan, B. Generalized fractal analysis and its applications to engineering surfaces. *Wear* **180**, 17–34 (1995).
- [145] Persson, B. On the fractal dimension of rough surfaces. *Tribology Letters* **54**, 99–106 (2014).
- [146] Hansen, A., Hinrichsen, E. L. & Roux, S. Roughness of crack interfaces. *Physical Review Letters* **66**, 2476 (1991).
- [147] Wang, W. & Scholz, C. H. Wear processes during frictional sliding of rock: A theoretical and experimental study. *Journal of Geophysical Research: Solid Earth* **99**, 6789–6799 (1994).
- [148] Schmittbuhl, J., Vilotte, J.-P. & Roux, S. Reliability of self-affine measurements. *Physical Review E* **51**, 131 (1995).
- [149] Press, W. H., Teukolsky, S. A., Vetterling, W. T. & Flannery, B. P. *Numerical recipes 3rd edition: The art of scientific computing* (Cambridge university press, 2007).
- [150] Jacobs, T. D., Junge, T. & Pastewka, L. Quantitative characterization of surface topography using spectral analysis. *Surface Topography: Metrology and Properties* **5**, 013001 (2017).
- [151] VanderPlas, J. T. Understanding the Lomb–Scargle periodogram. *The Astrophysical Journal Supplement Series* **236**, 16 (2018).
- [152] Stukowski, A. Visualization and analysis of atomistic simulation data with OVITO—the Open Visualization Tool. *Modelling and Simulation in Materials Science and Engineering* **18**, 015012 (2009).
- [153] Munteanu, C., Negrea, C., Echim, M. & Mursula, K. Effect of data gaps: comparison of different spectral analysis methods. *Annales Geophysicae* **34**, 437–449 (2016).

Bibliography

- [154] Bistacchi, A., Griffith, W. A., Smith, S. A., Di Toro, G., Jones, R. & Nielsen, S. Fault roughness at seismogenic depths from lidar and photogrammetric analysis. *Pure and Applied Geophysics* **168**, 2345–2363 (2011).
- [155] Milanese, E., Brink, T., Aghababaei, R. & Molinari, J.-F. The role of interfacial adhesion on minimum wear particle size and roughness evolution. *arXiv preprint:2003.10192* (2020).
- [156] Schirmeisen, A. Wear: One atom after the other. *Nature Nanotechnology* **8**, 81 (2013).
- [157] Shao, Y., Jacobs, T. D., Jiang, Y., Turner, K. T., Carpick, R. W. & Falk, M. L. Multibond model of single-asperity tribochemical wear at the nanoscale. *ACS Applied Materials & Interfaces* **9**, 35333–35340 (2017).
- [158] Liu, J., Jiang, Y., Grierson, D. S., Sridharan, K., Shao, Y., Jacobs, T. D., Falk, M. L., Carpick, R. W. & Turner, K. T. Tribochemical wear of diamond-like carbon-coated atomic force microscope tips. *ACS Applied Materials & Interfaces* **9**, 35341–35348 (2017).
- [159] Pham-Ba, S., Brink, T. & Molinari, J.-F. Adhesive wear and interaction of tangentially loaded micro-contacts. *International Journal of Solids and Structures* (2019).
- [160] Aghababaei, R. Effect of adhesion on material removal during adhesive wear. *Physical Review Materials* **3**, 063604 (2019).
- [161] Kirkpatrick, S., Gelatt, C. D. & Vecchi, M. P. Optimization by simulated annealing. *Science* **220**, 671 (1983).
- [162] Milanese, E. & Molinari, J.-F. A mechanistic model for the growth of cylindrical debris particles in the presence of adhesion. *arXiv preprint:2003.05812* (2020).
- [163] Berthier, Y., Vincent, L. & Godet, M. Velocity accommodation in fretting. *Wear* **125**, 25–38 (1988).
- [164] Descartes, S. & Berthier, Y. Rheology and flows of solid third bodies: background and application to an MoS_{1.6} coating. *Wear* **252**, 546–556 (2002).
- [165] Cocks, M. Interaction of sliding metal surfaces. *Journal of Applied Physics* **33**, 2152–2161 (1962).

- [166] Fillot, N., Jordanoff, I. & Berthier, Y. Modelling third body flows with a discrete element method—a tool for understanding wear with adhesive particles. *Tribology International* **40**, 973–981 (2007).
- [167] Renouf, M., Massi, F., Fillot, N. & Saulot, A. Numerical tribology of a dry contact. *Tribology International* **44**, 834–844 (2011).
- [168] Maugis, D. Adhesion of solids: mechanical aspects. In Bhushan, B. (ed.) *Modern tribology handbook, two volume set*, chap. 4, 163–204 (CRC press, 2000).
- [169] Erdogan, F. & Sih, G. On the crack extension in plates under plane loading and transverse shear. *Journal of Basic Engineering* **85**, 519–525 (1963).
- [170] Johnson, K. The effect of a tangential contact force upon the rolling motion of an elastic sphere on a plane. *Journal of Applied Mechanics* **80**, 339–346 (1958).
- [171] Baney, J. & Hui, C.-Y. A cohesive zone model for the adhesion of cylinders. *Journal of Adhesion Science and Technology* **11**, 393–406 (1997).
- [172] Johnson, K. & Greenwood, J. Maugis analysis of adhesive line contact. *Journal of Physics D: Applied Physics* **41**, 199802 (2008).
- [173] Dugdale, D. S. Yielding of steel sheets containing slits. *Journal of the Mechanics and Physics of Solids* **8**, 100–104 (1960).
- [174] Chaudhury, M. K., Weaver, T., Hui, C. & Kramer, E. Adhesive contact of cylindrical lens and a flat sheet. *Journal of Applied Physics* **80**, 30–37 (1996).
- [175] Wu, J.-J. Adhesive contact between a cylinder and a half-space. *Journal of Physics D: Applied Physics* **42**, 155302 (2009).
- [176] Carter, F. On the action of a locomotive driving wheel. *Proceedings of the Royal Society of London A: Mathematical, Physical and Engineering Sciences* **112**, 151–157 (1926).
- [177] Cattaneo, C. Sul contatto di due corpi elastici: distribuzione locale degli sforzi. *Rendiconti dell'Accademia nazionale dei Lincei* **27**, 342–348, 434–436, 474–478 (1938).
- [178] Carkner, C. J., Haw, S. M. & Mosey, N. J. Effect of adhesive interactions on static friction at the atomic scale. *Physical Review Letters* **105**, 056102 (2010).

Bibliography

- [179] Moës, N., Dolbow, J. & Belytschko, T. A finite element method for crack growth without remeshing. *International Journal for Numerical Methods in Engineering* **46**, 131–150 (1999).
- [180] Barenblatt, G. I. The mathematical theory of equilibrium cracks in brittle fracture. *Advances in Applied Mechanics* **7**, 55–129 (1962).
- [181] Moës, N., Stolz, C., Bernard, P.-E. & Chevaugeon, N. A level set based model for damage growth: the thick level set approach. *International Journal for Numerical Methods in Engineering* **86**, 358–380 (2011).
- [182] Francfort, G. A. & Marigo, J.-J. Revisiting brittle fracture as an energy minimization problem. *Journal of the Mechanics and Physics of Solids* **46**, 1319–1342 (1998).
- [183] Ambrosio, L. & Tortorelli, V. M. Approximation of functional depending on jumps by elliptic functional via Γ -convergence. *Communications on Pure and Applied Mathematics* **43**, 999–1036 (1990).
- [184] Griffith, A. A. VI. The phenomena of rupture and flow in solids. *Philosophical Transactions of the Royal Society of London A: Mathematical, Physical and Engineering Sciences* **221**, 163–198 (1921).
- [185] Li, T., Marigo, J.-J., Guilbaud, D. & Potapov, S. Gradient damage modeling of brittle fracture in an explicit dynamics context. *International Journal for Numerical Methods in Engineering* **108**, 1381–1405 (2016).
- [186] Bleyer, J., Roux-Langlois, C. & Molinari, J.-F. Dynamic crack propagation with a variational phase-field model: limiting speed, crack branching and velocity-toughening mechanisms. *International Journal of Fracture* **204**, 79–100 (2017).
- [187] Borden, M. J., Hughes, T. J., Landis, C. M. & Verhoosel, C. V. A higher-order phase-field model for brittle fracture: Formulation and analysis within the isogeometric analysis framework. *Computer Methods in Applied Mechanics and Engineering* **273**, 100–118 (2014).
- [188] Tanné, E., Li, T., Bourdin, B., Marigo, J.-J. & Maurini, C. Crack nucleation in variational phase-field models of brittle fracture. *Journal of the Mechanics and Physics of Solids* **110**, 80–99 (2018).
- [189] Miehe, C., Hofacker, M. & Welschinger, F. A phase field model for rate-independent crack propagation: Robust algorithmic implementation based

- on operator splits. *Computer Methods in Applied Mechanics and Engineering* **199**, 2765–2778 (2010).
- [190] Pham, K., Ravi-Chandar, K. & Landis, C. Experimental validation of a phase-field model for fracture. *International Journal of Fracture* **205**, 83–101 (2017).
- [191] Ambati, M., Gerasimov, T. & De Lorenzis, L. A review on phase-field models of brittle fracture and a new fast hybrid formulation. *Computational Mechanics* **55**, 383–405 (2015).
- [192] Richart, N. & Molinari, J.-F. Implementation of a parallel finite-element library: test case on a non-local continuum damage model. *Finite Elements in Analysis and Design* **100**, 41–46 (2015).

Enrico Milanese

Curriculum vitae

Personal information

- Born on April 29, 1989
- Italian Citizen
- Languages: Italian (native), English (fluent), French (intermediate), Spanish and German (basic)
- email: enrico@scifilm.it

Education

- 2020 **Doctor of Philosophy (Ph.D.)**, *EPFL*, Lausanne, Switzerland.
 - Doctoral program in Mechanics
 - Thesis title: Surface roughness evolution in adhesive wear processes
 - Advisor: Prof. J.-F. Molinari
- 2014 **Laurea magistrale (M.Sc.)**, *University of Padua*, Padua, Italy.
 - Civil engineering
 - Minor in structural engineering
- 2011 **Laurea (B.Sc.)**, *University of Padua*, Padua, Italy.
 - Civil engineering

Research experience

- 2016–2020 **Doctoral assistant**, *EPFL*, Lausanne, Switzerland.
 - Numerical investigations on the surface roughness evolution in wear processes
 - Lab of Prof. J.-F. Molinari
- 2014–2016 **Researcher**, *University of Padua*, Padua, Italy.
 - Numerical development of a lattice model for two-phase porous media
 - Group of Prof. B. Schrefler

Science outreach experience

- 2019–ongoing **Co-founder, organizing team**, *SciFilmIt*, Lausanne, Switzerland.
- 2017–2019 **Organizing team**, *Exposure Science Film Hackathon*, Lausanne, Basel, and Zurich, Switzerland.

- 2019 **Organizing team**, *Young Mind's Science Film Day*, Lausanne, Basel, and Zurich, Switzerland.
- 2018 **Team member**, *Searching for love*, Short film made at Exposure Science Film Hackathon, Lausanne, Switzerland.
- 2018 **Team member**, *Wearing well*, Short film made at Symbiosis competition at Imagine Science Film Festival, New York, U.S.A..
- 2017 **Speaker**, *Better together: making a 3 minute film in 3 days*, E. Milanese, T. Blyth-Kubota, Exposure Science Film Hackathon, Lausanne, Switzerland.
- 2016 **Team member**, *Better together: of love, life, and emergent properties*, Short film made at Exposure Science Film Hackathon – Lausanne, Switzerland.

Professional experience

2014–2016 **Civil engineer**, *W.E.I.'N Venice*, Venice, Italy.

Peer-reviewed journal articles

- [1] Milanese, E., Brink, T., Aghababaei, R. & Molinari, J.-F. The role of interfacial adhesion on minimum wear particle size and roughness evolution. *Under consideration* (2020).
- [2] Milanese, E. & Molinari, J.-F. A mechanistic model for the growth of cylindrical debris particles in the presence of adhesion. *Under consideration, arXiv preprint:2003.05812* (2020).
- [3] Milanese, E., Brink, T., Aghababaei, R. & Molinari, J.-F. Emergence of self-affine surfaces during adhesive wear. *Nature Communications* **10**, 1–9 (2019).
- [4] Peruzzo, C., Cao, T. D., Milanese, E., Favia, P., Pesavento, F., Hussain, F. & Schrefler, B. Emergence of self-affine surfaces during adhesive wear. *European Journal of Mechanics-A/Solids* **74**, 471–484 (2019).
- [5] Molinari, J.-F., Aghababaei, R., Brink, T., L. Frérot, & Milanese, E. Adhesive wear mechanisms uncovered by atomistic simulations. *Friction* **16**, 245–259 (2018).
- [6] Cao, T.D., Milanese, E., Remij, E.W., Rizzato, P., Remmers, F., Joris, J.C., Simoni, L., Huyghe, J.M., Hussain, F. & Schrefler, B. Interaction between crack tip advancement and fluid flow in fracturing saturated porous media. *Mechanics Research Communications* **80**, 24–37 (2017).
- [7] Milanese, E., Yilmaz, O., Molinari, J.F., & Schrefler, B. Avalanches in dry and saturated disordered media at fracture in shear and mixed mode scenarios. *Mechanics Research Communications* **80**, 58–68 (2017).
- [8] Milanese, E., Yilmaz, O., Molinari, J.F., & Schrefler, B. Avalanches in dry and saturated disordered media at fracture. *Physical Review E* **93**, 043002 (2016).

Chapters in books

- [1] Milanese, E., Cao, T.D., Simoni, L. & Schrefler, B. Fracturing in Dry and Saturated Porous Media. In Oñate, E., Peric, D., de Souza Neto, E. & Chiumenti, M. (eds.) *Advances in Computational Plasticity*, 265-288 (Springer, 2018).

Conferences, presentations, workshops

Invited speaker

- 2018 **Science of wear international workshop**, E. Milanese, R. Aghababaei, T. Brink, and J.-F. Molinari. *Surface roughness evolution in atomistic simulations of adhesive wear: from asperity collision to three-body configuration*, Tsinghua University, Beijing, China.

Conferences

- 2018 **6th European Conference on Computational Mechanics, 7th European Conference on Computational Fluid Dynamic**, E. Milanese, T. Brink, R. Aghababaei, and J.-F. Molinari. *Fractal surfaces in adhesive wear processes*, Glasgow, United Kingdom.
- 2018 **6th European Conference on Computational Mechanics, 7th European Conference on Computational Fluid Dynamic**, L. Frérot and E. Milanese. *Continuum versus discrete approach in modeling of wear processes*, Glasgow, United Kingdom.
- 2017 **International Conference on Computational Contact Mechanics**, E. Milanese, R. Aghababaei, and J.-F. Molinari. *The role of hardness in the surface roughness evolution during adhesive wear processes*, Lecce, Italy.

Poster sessions

- 2019 **Modeling tribology: friction and fracture across scales**, E. Milanese, T. Brink, J.-F. Molinari, and R. Aghababaei. *Emergence of self-affine surfaces under adhesive three-body wear conditions*, CECAM-EPFL, Lausanne, Switzerland.
- 2019 **Emergence of surface and interface structure from friction, fracture and deformation**, E. Milanese, T. Brink, J.-F. Molinari, and R. Aghababaei. *Emergence of self-affine surfaces under adhesive three-body wear conditions*, CECAM-EPFL, Lausanne, Switzerland.

EPFL Doctoral school symposia

- 2017 December 11. *Atomistic modeling of adhesive wear and surface roughness evolution*.
- 2017 December 11. *Science films: why we need story to communicate science*.
- 2017 February 14. *Better together: of love, live and emergent properties*.

Teaching experience

Teaching assistant

- Spring 2018 **Numerical modelling of solids and structures**, by Prof. J.-F. Molinari and Dr. G. Ancaux.
- o Introductory class on the finite element method

- 14 weeks, responsible for 2 hours/week of exercise sessions and class projects supervision, grading.
- 30 students
- Fall 2017 **Continuum mechanics (for GC)**, by Prof. J.-F. Molinari, 3 ECTS credits.
 - Continuum mechanics class for civil engineering curriculum
 - 14 weeks, responsible for 2 hours/week of exercise sessions, grading.
 - 40 students
- Spring 2017 **Mathématiques 1B**, by Prof. A.-L. V. Bronstein, Prof. S. Friedli, and Prof. O. Woringer.
 - Preparatory class on calculus
 - 14 weeks, responsible for 4 hours/week of exercise sessions, grading.
 - 40 students
- Fall 2016 **Continuum mechanics (for GC)**, by Prof. J.-F. Molinari, 3 ECTS credits.
 - Continuum mechanics class for civil engineering curriculum
 - 14 weeks, responsible for 2 hours/week of exercise sessions, grading.
 - 30 students
- Spring 2016 **Numerical modelling of solids and structures**, by Prof. J.-F. Molinari and Dr. G. Ancaux.
 - Introductory class on the finite element method
 - 14 weeks, responsible for 2 hours/week of exercise sessions and class projects supervision, grading.
 - 30 students

[Co-advised master thesis \(with Prof. J.-F. Molinari and Prof. M. Violay\)](#)
- Spring 2017 Risks in nuclear waste repository: earthquakes from really low to full scale
 - Student: C. Samir

[Co-advised semester projects \(with Prof. J.-F. Molinari\)](#)
- 2019 – 2020 Development of discrete surface growth models for frictional surfaces
 - Student: T. Fry
- Fall 2018 Introduction to the material point method
 - Student: S. Ozden
- Spring 2018 Introduction to the material point method
 - Student: Z. Fouad
- Fall 2017 Introduction to dynamics with finite elements: a study of wave dynamics and applications in metaconcrete
 - Student: G. G. Bartrina
- Spring 2017 Introduction to Discrete Modeling for Engineering
 - Student: S. A. Durussel
- Spring 2017 Introduction to Discrete Modeling for Engineering
 - Student: S. Z. Wettel